Nanostructured Advanced Ceramics for Armour Applications

By

Shuo Huang

Supervisors: Prof. Jon Binner

Dr. Bala Vaidhyanathan

A Doctoral Thesis submitted in partial fulfilment of the requirements for the award of Doctor of Philosophy of Loughborough University

Feb 2013

Acknowledgements

I would like to sincerely thank my supervisor, Prof. Jon Binner and Dr. Bala Vaidhyanathan, for their continuous support, guidance and encouragement throughout my PhD study. I sincerely acknowledge Engineering and Physical Sciences Research Council (EPSRC) and Defence Science and Technology Laboratory (DSTL) for the funding support and Morgan Technical Ceramics and Dynamic Ceramics for the materials provision.

I would also like to thank the staff in Loughborough Materials Characterisation Centre (LMCC) for assistance and advice. Special thanks to Dr. Z. Zhou for giving me the training of TEM and Dr. D. Ross for his help on the XRD work. I also appreciate Dr. G.D. West for his patient assistance in the FIB work.

I am grateful to the research students in the Advanced Ceramic Group for their valuable help and advice. I would like to thank Mr. A. Lau in particular for his countless assistance during my experiments.

Finally, I am eternally grateful to my husband, Letian Li, for his constant support and patience, my parents and friends, for their enthusiasm and support.

Abstract

Ceramics have been widely used for personnel and vehicle armour because of their desirable properties such as high hardness and low density. However the brittle nature associated with the ceramic materials, i.e. low toughness, reduces their ability to withstand multiple ballistic hits. The present work is focused on ceramic armour materials made from alumina and zirconia toughened alumina (ZTA). The effects of grain size and zirconia phase transformation toughening on the mechanical and high strain rate properties in both materials were investigated in detail.

Alumina, 10%, 15% and 20% nano ZTA with 1.5 mol% yttria stabiliser were produced with various grain sizes. The processing of the materials started from suspension preparation, spray freeze drying of the suspension and die pressing to produce homogeneous green bodies with densities above 54%. Then, the green bodies were sintered using conventional single stage and/or two-stage sintering to produce the samples with full density and a range of grain sizes (0.5 to 1.5 μm alumina grains and 60 to 300 nm zirconia grains). The effects of the processing conditions on the microstructures were studied and the optimum processing route for each sample was determined.

The mechanical properties of the alumina and ZTA samples were investigated, including Vickers hardness, indentation toughness, 4-point bend strength and wear resistance. The results showed that, with an increasing amount of zirconia addition, evident increases of the toughness, strength and wear resistance properties were observed, whilst the hardness reduced slightly correspondingly. The effect of density and grain sizes on the hardness and toughness were studied as well: larger alumina grain size led to a higher hardness and negligible change in toughness, whilst the zirconia grain coarsening enhanced the phase transformation toughening effect and the samples displayed a higher toughness.

In addition to the investigation of the mechanical properties, the alumina and nano ZTA samples were subjected to high strain rate testing, including split Hopkinson pressure bar (SHPB) (8-16 $m\,s^{-1}$) and gas gun impact testing (100-150 $m\,s^{-1}$). The high strain rate performances were compared in terms of their fracture behaviours,

fragmentation process and fragment size distribution. Raman spectroscopy was used to measure the amount of zirconia phase transformation in ZTA samples after the high strain rate testing. The residual stress and dislocation density in alumina grains after testing were quantitatively measured using Cr^{3+} fluorescence spectroscopy. The results indicated that zirconia phase transformation can reduce the residual stress and dislocation densities in the ZTA samples, resulting in less damage, lower plastic deformation and less crack propagation. In addition, a nano zirconia material with 1.5 mol% yttria stabiliser (1.5YSZ) was subjected to a gas gun impact test with a very high impact speed (142 $m\,s^{-1}$); a deep projectile penetration was observed, due to the low hardness of the pure zirconia, whilst the sample stayed intact. The result further confirmed that the zirconia phase transformation toughening effect can improve the sample's high strain rate performance.

CONTENTS

List of Figures

List of Tables

1 INTRODUCTION

1.1 Background

Over the last 40 years, light weight ceramic armour has been developed for personnel, aircraft and vehicle protection in military and policing situations and has proved itself time and again against high velocity and armour piercing rounds. Globally over 5 million ceramic armour units were manufactured in 2004 in a market worth £800 million [1]. In the US market, in 2006, the market worth reached $550 million, more than a ten fold growth from 2003 [2].

Ceramic armour is a composite system incorporating a metal or polymer composite back plate as well as a hard ceramic top plate to defeat the ballistic projectiles. According to the different kinetic energies (KE) of the defeated projectiles, the armour systems are divided into two types, i.e. the thin layered ceramic/metal armour system and the thick and confined ceramic armour system. The former is used to defeat short KE projectiles and is the structure of light personnel and aircraft armours, whilst the latter can defeat long rod KE projectiles and is normally used on heavy military vehicles. The fragmentation process of the two systems are different, however, they have the same requirement in terms of the properties of the ceramic armour material [3].

The keys to high performance ceramic armour include good ceramic properties such as hardness, strength and stiffness as well as the ability to work harden under extreme stress. These properties combine to increase the impact duration allowing the ceramic to erode and blunt, or even comminute, the projectile and absorb its kinetic energy [4]. Ceramic armour systems are also designed to be able to withstand multiple hits. However, the brittle nature of ceramic materials always reduces their multihit capability. Alumina, silicon carbide and boron carbide have been used as ceramic armour materials. These materials possess very high hardness and strength, although their toughness is low [4].

Nanocrystalline ceramics which have mean grain sizes of < 100 nm, can deform plastically and extensively by grain boundary sliding. This 'superplastic deformation' is in sharp contrast to the usual brittle behaviour associated with commercial ceramics [5,6]. The various advantages of nano-ceramics can be attributed to the presence of excess grain boundaries, which result in unique physical and mechanical properties. The desirable properties of nano ceramics, such as improved hardness and toughness, could be beneficial in improving the high strain rate performance of ceramic armours, although limited relative studies have been carried out until now. On the other hand, some nanocomposites have been considered to be superior as armour materials to the conventional ones. Nanocomposites are composites with nano inclusions in a submicron or micron sized matrix. A boron carbide (B_4C) nanocomposite with nano TiB inclusions has been ballistically tested and found to provide better ballistic protection effect than a conventional B_4C composite [7]. In addition, toughened ceramics has also been considered, the aim being to use the increased toughness to improve the multihit capability of the armour. Several materials have been investigated including toughened SiC [8], Al_2O_3-Al composite [9] and ZTA composites [10,11].

In this project, the concept of using nanostructured or fine grain sized ceramics, toughened ceramics and the combination of these two are considered. The target materials for use as armour are fine grain sized alumina with grain sizes around 1 μm and nano ZTA composites, in which nano zirconia particles are included in a submicron alumina matrix made from a fine, commercial, sub-micron alumina powder (mean particle size of ~160 nm) that is available as an aqueous suspension. A processing route has been developed to produce these materials with full densities and fine grain sizes. The mechanical properties, including the Vickers hardness, indentation toughness, 4-point bend strength and wear resistance, have been measured and the effects of the grain sizes of the alumina and the zirconia in the ZTA on the mechanical properties studied. Based on the mechanical property results, selected materials with high hardness, toughness and strength were high strain rate tested. Split Hopkinson pressure bar (SHPB) and gas gun impact testing were carried out and post testing characterisation was under taken. The effect of zirconia phase transformation on the high strain rate performance was extensively studied using Raman spectroscopy and Cr^{3+} fluorescence spectroscopy.

1.2 Aims and Objectives

The main objectives of the project are:

- To investigate the potential that nano or fine grain sized ceramic materials offer for ballistic protection.
- To develop the ability to produce these materials in suitable sizes to allow high strain rate testing.
- To contribute to the development of an understanding of the mechanism(s) by which ceramic armours defeat ballistic projectiles.

Samples to be discussed in this thesis include:

Sample name	Explanation
Alumina	
10% nano 1.5Y-ZTA	10 wt% nano 1.5YSZ in alumina
15% nano 1.5Y-ZTA	15 wt% nano 1.5YSZ in alumina
20% nano 1.5Y-ZTA	20 wt% nano 1.5YSZ in alumina
10% nano 3Y-ZTA	10 wt% nano 3YSZ in alumina
Morgan composite	15 wt% submicron 3YSZ in alumina
Nano 1.5YSZ	Nano zirconia with 1.5 mol% yttria

2 LITERATURE REVIEW

2.1 Ceramic Armour Materials

The use of ceramics for ballistic protection has been considerably researched over the past 40 years. The most significant factors which make ceramics interesting for armour applications are the low density, high strength and high hardness. In this section, two ceramic armour systems are introduced in section 2.1.1 and the fragmentation process during ballistic impact is reviewed in section 2.1.2, in order to explain the role of ceramic in the whole armour system. In addition, the most commonly used armour materials and the effects of static and dynamic mechanical properties on ballistic protection are reviewed in sections 2.1.3 to 2.1.5.

2.1.1 Introduction of ceramic armour systems

Armour materials are required to possess the following properties: a) *low density* to improve the mobility of the protected system; b) *high bulk and shear moduli* to prevent large deformations; c) *high yield stress* to preserve the armour resistance to failure; and d) *high dynamic tensile strength* to avoid material rupture when tensile waves appear [12]. Metal could satisfy all the requirements except the low density, whilst ceramics are able to fulfil the first three demands but are too brittle to resist an extensive fragmentation when tensile waves appear. Therefore, a combination of ceramic and metal components is used for ceramic composite armour in order to achieve the benefits of both. Depending on the type of projectiles, the structures of the composite armour are shown in Figures 2.1 and 2.2 to prevent the attack of short kinetic energy (KE) projectiles and long rod KE projectiles, respectively. The armour system in Figure 2.1 consists of a ceramic tile top layer bonded to a ductile metallic back plate, this structure is commonly seen in body armours and aircraft or light weight vehicle amours. When a ceramic armour is subjected to the impact of a long rod KE projectile, which is usually made of a heavy metal and contains very high kinetic energy, the armour needs to be designed as in Figure 2.2. Many of these

confined, thick ceramic packets are bonded on a back plate and form an armour system. This kind of armour is mostly seen in heavy vehicle armours.

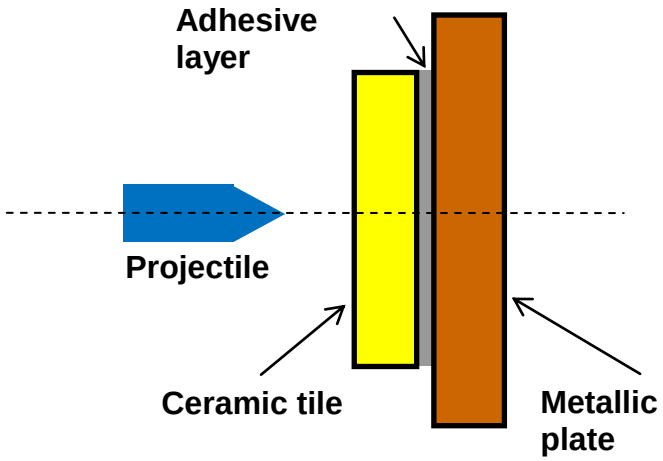

Figure 2.1 The structure of a thin layered ceramic/metal armour system.

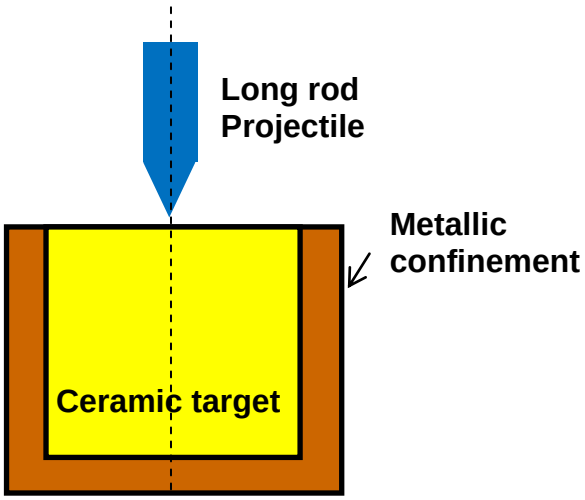

Figure 2.2 The structure of a thick and confined ceramic armour system.

2.1.2 Fragmentation of ceramics under ballistic impact

In this section, the fragmentation processes of the two ceramic armour systems shown above are discussed separately.

2.1.2.1 Fragmentation of thin layered ceramic armour

As is shown in Figure 2.3, the layered ceramic armour contains a ceramic top layer and a metallic back plate, bonded together by an adhesive layer. A significant

amount of research into ceramic armour is based on this system because of its wide spread applications [12–14]. The earliest fragmentation study was by Wilkins et al. [12], who reported the experimental results and computer simulation of the dynamic failure of alumina/aluminium layered armour under ballistic impact. He also pointed out that identification of the important material properties, along with the conditions that cause failure of the materials, is necessary.

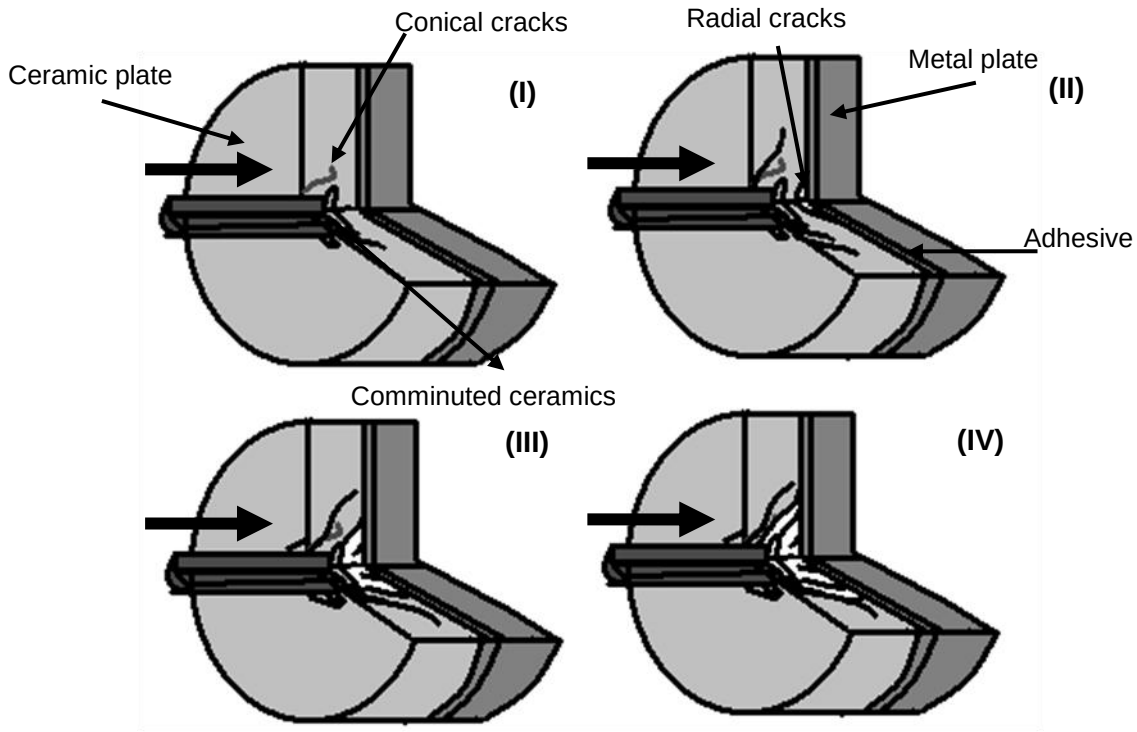

Figure 2.3 Fragmentation process of a ceramic tile during the first few microseconds of impact [12].

Figure 2.3 shows the fragmentation process of a ceramic tile during the first few microseconds of impact. Initially, high amplitude compressive stress pulses are generated both in the ceramic tile and the projectile. In the former, the compressive stress waves transmit along the thickness until they contact the back surface of the tile (Figure 2.3 I). At the interface of the ceramic tile and the metallic back plate, a fraction of the waves propagate through into the back plate, whilst the rest are reflected into the ceramic tile and become tensile waves due to the acoustic impedance mismatch of the front ceramic and the metal back plate. Compared to the compressive stress, ceramics are much weaker under tension. Therefore, cracking

in the ceramic tile propagates from the back and then forms a damaged fracture zone (Figure 2.3 II). The latter has a conical shape and grows until it reaches the impact surface. During the propagation, the tip of projectile is shattered and blunted by the hard ceramic surface, which helps to dissipate the energy generated by the projectile and spread the load over a larger area. Although the ceramic under the impact area is comminuted during the impact process, the projectile cannot penetrate until the conical fracture zone reaches the projectile (Figure 2.3 III). The time of non-penetration is known as dwell [3]. If the velocity of the projectile is low, it is possible that the projectile will be fully shattered and stopped before penetration, which is called 'interface defeat'. In other cases, the projectile will penetrate and push through the conical fracture zone in front of it. Because the area of the cone away from the projectile is larger, the impact stress can be further distributed on a larger area on the back plate (Figure 2.3 IV). During this process, the ductile back plate will deform to absorb the remaining kinetic energy of the projectile and prevent the penetration of the projectile. It was reported [10] that 10-15% of the kinetic energy is spent in deforming the projectile, the deformation process of the back plate absorbs 20-40% energy, and the rest is taken by the ejected ceramic debris. However, if the velocity of a projectile is beyond a critical value, the armour will be penetrated and cannot provide the ballistic protection effect. The critical value is related to the properties of the materials and the failure process under impact.

2.1.2.2 Fragmentation of confined thick ceramic armour

A long rod KE projectile made of a heavy metal generates a very high energy density on the impact area during ballistic attack. As opposed to the previous ballistic impact process, in which there is a dwell time, the long rod projectile can maintain its high velocity for a longer time when its front tip has been eroded and deformed by the ceramic surface. This is mainly because of its high mass and inertia. Therefore, the primary mechanism to defeat this threat is erosion, which requires a much thicker ceramic layer than a simple tile. According to the study of Hauver et al. [15], confined ceramics require a higher impact load and longer time to shatter the ceramic. Moreover, the cracked ceramic can be maintained by the metal cover and so further erodes the projectile during the penetration process. Therefore, a confined thick ceramic armour system is a better approach to defeat long rod high KE projectiles.

Figure 2.4 illustrates the process of a long rod penetrating a thick confined ceramic armour.

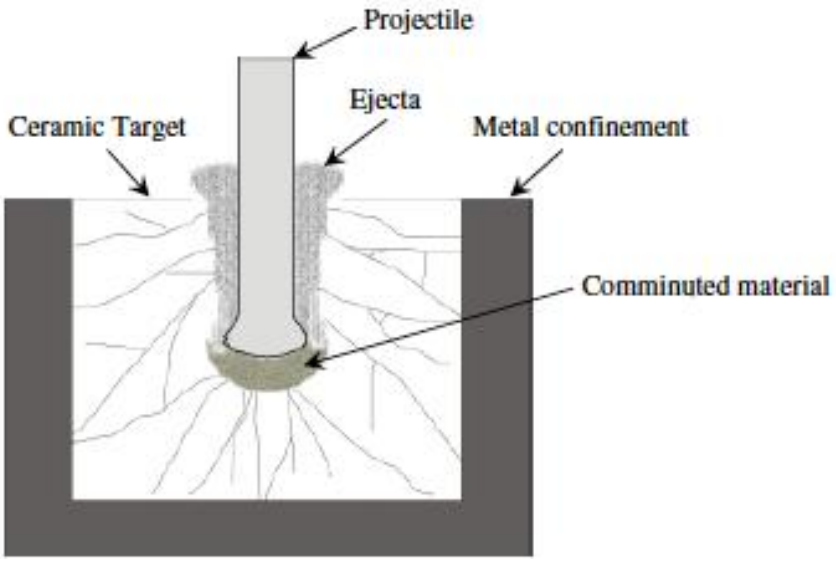

Figure 2.4 Illustration of a long rod KE projectile penetrating a thick and confined ceramic armour system [10].

This introduction to the fragmentation processes for the two armour systems indicates that the ceramic failure processes can be very complicated. Although a lot of effort has been put into this research field, the understanding of the dynamic fracture process is still limited. For example, the processes of comminution of ceramics under high pressure at ultra high strain rates are still not well understood. The relationship of the mechanical properties of ceramics to ballistic performance is also uncertain. The development of an understanding of the ballistic protection mechanism afforded by ceramics is necessary and will be a main objective in this project.

2.1.3 Introduction of ceramic armour materials

As is described in section 2.1.1, ceramics can efficiently erode projectiles and dissipate some of the energy generated by a projectile. The high hardness of the ceramic is, therefore, an essential contribution to the success of the armour. Moreover, another important reason for using ceramic as an amour material is its low density, which provides a light weight property to body armours and military vehicle

armours. Therefore, the combination of high hardness and low density is required for the currently used ceramic armour materials.

Table 2.1 summarises the properties of some ceramics used for armour applications [4,16]. Alumina (Al_2O_3), silicon carbide (SiC) and boron carbide (B_4C) are three typical ceramic armour materials. Their high hardness can be explained from their bonding and crystalline structures. Al_2O_3 has 40% covalent bond in its interatomic bonds, whilst SiC and B_4C bonds are fully covalent. The strong covalent bonds and directionally packed crystal structures result in high strength and high hardness. The low density of these materials is due to the low atomic mass of the elements and also the directional arrangement of these atoms, which makes them impossible to be close packed. The strong bonds combined with the crystalline structure also inhibit dislocation movement and result in the brittle properties of these materials [17]. According to the comparison in Table 2.1, the non-oxide materials show higher hardness and lower density. However, from an economical and technological point of view, alumina is currently the most common type of ceramics used for armour production [18].

Table 2.1Summary of properties of various ceramics for armour application [4,16]

	α-Al_2O_3	SiC	B_4C
Density (g/cm^3)	3.9-4.0	3.2	2.49
Grain size (μm)	5.7	2-5	15.69
Young's Modulus (GPa)	370	460	450
Vickers Hardness (GPa)	17-20 (10 kg)		
Knoop Hardness (GPa)	14.1 (1 kg)	24.0	26.5
Toughness (MPa m$^{1/2}$)	4-5	4.7	2.49
Flex strength (MPa)	379	600	450

On military vehicles and aircraft, transparent ceramic armour is used to make the windows in order to provide ballistic protection as well as keep the mass down. Commercially available transparent armour has a laminated structure consisting of a hard transparent ceramic top layer and an interlayer of polyvinyl butyrate backed by a layer of polycarbonate [19]. The available ceramic materials for the top layer include aluminium oxynitride (AlON), spinel ($MgAl_2O_4$) and sapphire (Al_2O_3 single crystal) [18]. It is also known that the grain size of ceramics affects the degree of transparency. According to Krell et al. [20], an alumina sample with a mean grain

size of ~0.5 µm showed visible real in-line transmission (RIT) of only 70–75% of the theoretical maximum at 0.8 -1 mm thickness, whilst the RIT increased to 84–93% when the grain size was ~0.3 µm for the same thickness.

In addition, it was found that the adhesive layer in between the ceramic tiles and the back plate affects the multihit capability [21,22]. Figure 2.5 shows a composite integral armour structure developed by United Defense Limited Partnership (UDLP) for the US Army. It mainly contains a ceramic strike face, a thin rubber layer and a glass-based composite backing plate. The rubber layer in between the top and bottom has an effect of increasing the multihit capability of armour and structural damage tolerance [21].

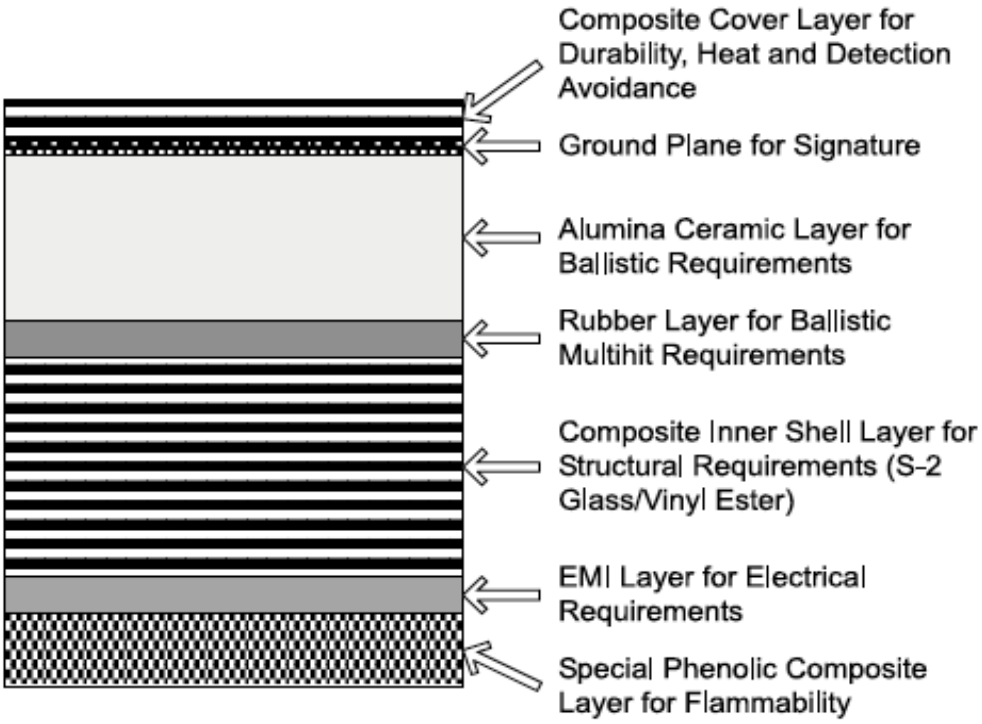

Figure 2.5 Components of composite integral armour structure [21]**.**

2.1.4 Effect of ceramic properties on armour performance

To date, limited success has been achieved in relating armour performance to a single, quasi-static mechanical property due to the dynamic nature of the ballistic event (nano to micro seconds) [10]. Instead, researchers have come to the conclusion that it is an optimum balance of several of these properties that identifies

an efficient armour material [23]. However, some fundamental mechanical properties have been studied by LaSalvia [24] to learn their commonly understood roles in resisting ballistic impact, as listed in Table 2.2.

Table 2.2 Material properties and their role in ballistic performance [24]

Properties	Roll / Effect in ballistic performance
Microstructure Grain size Minor phases Phases transformation (stress induced) Porosity	Affects all properties listed in the left-hand column below
Density	Weight of the armour system
Hardness	Damage to the projectile
Elastic modulus	Stress wave propagation
Strength	Multihit resistance
Fracture Toughness	Multihit resistance, field durability
Fracture mode (inter vs. trans granular)	Energy absorption

Hardness is considered to be a measure of resistance to deformation. As a rule-of-thumb, hardness higher than that of the projectile is desirable for armour ceramics [4]. With higher hardness, the erosion of the projectile during ballistic impact can be improved, which will help to dissipate the energy of the projectile [16,25]. Figure 2.6 [4] shows a plot of hardness of several materials as a function of their toughness. Hardness of some representative projectile materials is also shown in the plot. It can be found that the hardness and toughness follow an inverse relationship in most of the materials. This trend is also found elsewhere in the literature [9,26]. High toughness can minimize the shattering of the ceramic tile during impact, which will help to improve the ability to defeat multiple hits. In armour production, there is no standard of the best armour material, because materials with different properties can satisfy different applications. For example, the Al/SiC metal matrix composites (MMCs) with low hardness but very high toughness could be useful as a component of armour systems for defeating low hardness mild steel threats. However, to defeat tool steel and WC projectiles, higher hardness ceramics are typically needed.

It was also reported by Karandikar et al. [4] that the existence of minor phases in ceramic materials affected their ballistic performance. Figure 2.7 shows the effect of some of these on the elastic modulus of several materials, which in turn affects the ballistic performance of materials [4]. The porosity shows the biggest effect on the

reduction of modulus. This suggests that full or very high density is desirable during the production of armour materials.

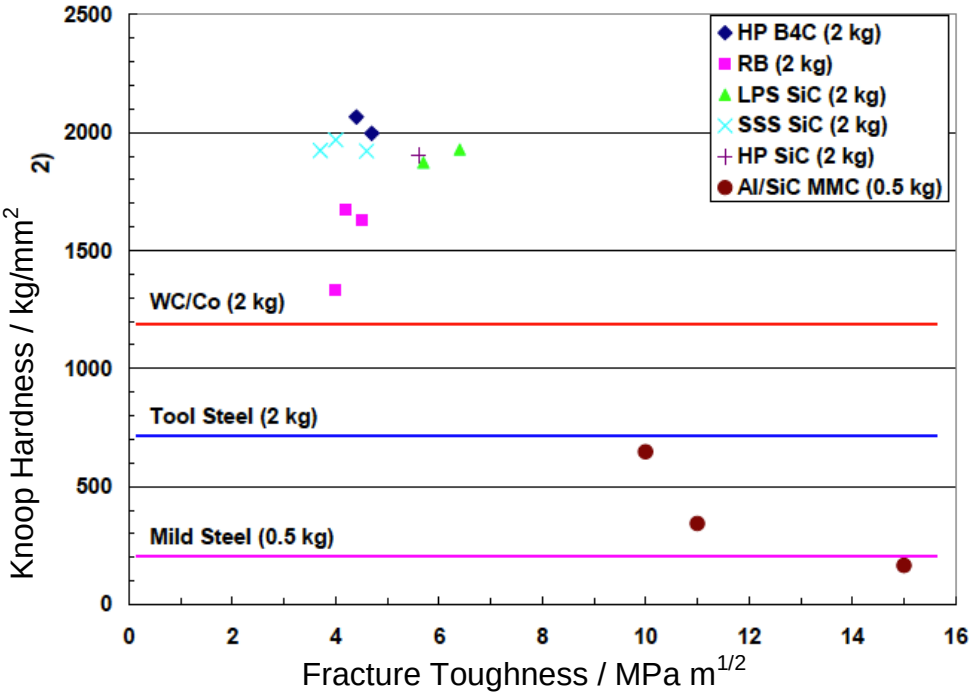

Figure 2.6 Inverse relationship between hardness and fracture toughness [4].

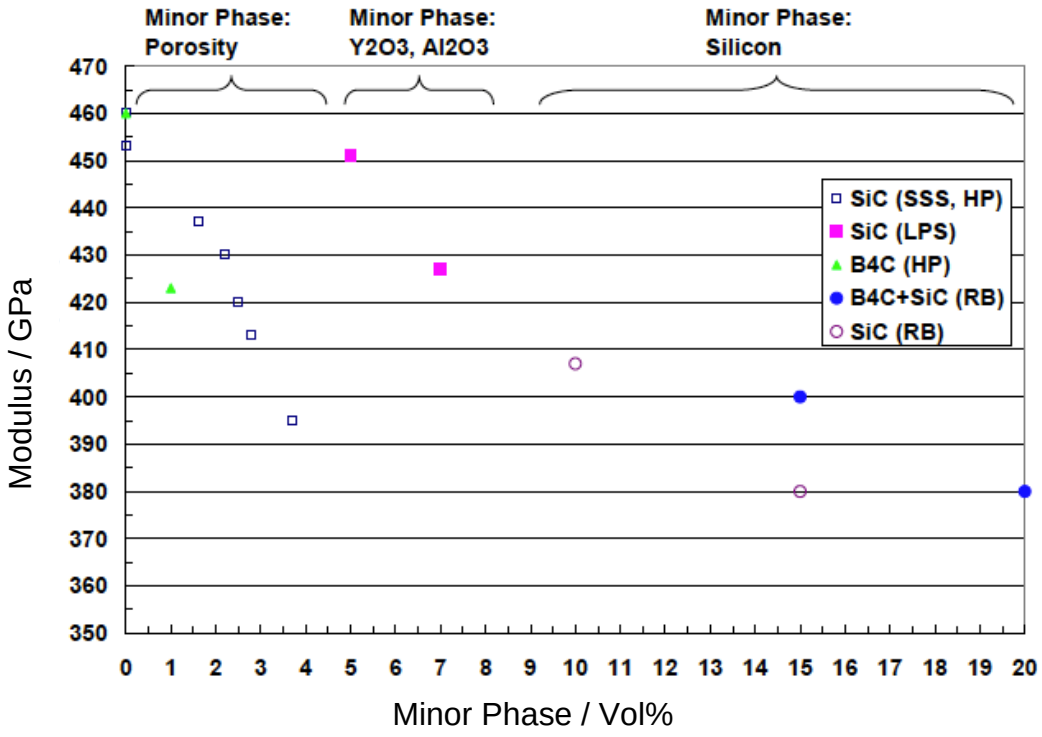

Figure 2.7 Effect of different minor phases in the ceramic on modulus [4].

2.1.5 Dynamic properties under ballistic impact

In real ballistic impact processes, ceramics undergo a very high strain rate impact. Therefore, the dynamic properties of ceramics play a critical role in the impact response of ceramic targets. It has been found that the values of the mechanical properties change when the strain rate of impact increases [3,4,27].

According to the study of Lankford [27], the strength of ceramics increased significantly when the strain rate was above 200 s^{-1}, as is shown in Figure 2.8. The result was obtained from an experiment using a split Hopkinson pressure bar (SHPB) test, which generates strain rates (ε) from 10^2 s^{-1} to 10^4 s^{-1}. The author [27] suggested that the rapid strengthening was the result of micro-crack initiation and propagation at the high strain rates. With the increase in strain rate, the fragment size decreased dramatically, which proved that the micro-cracking dominated the strengthening of the ceramics.

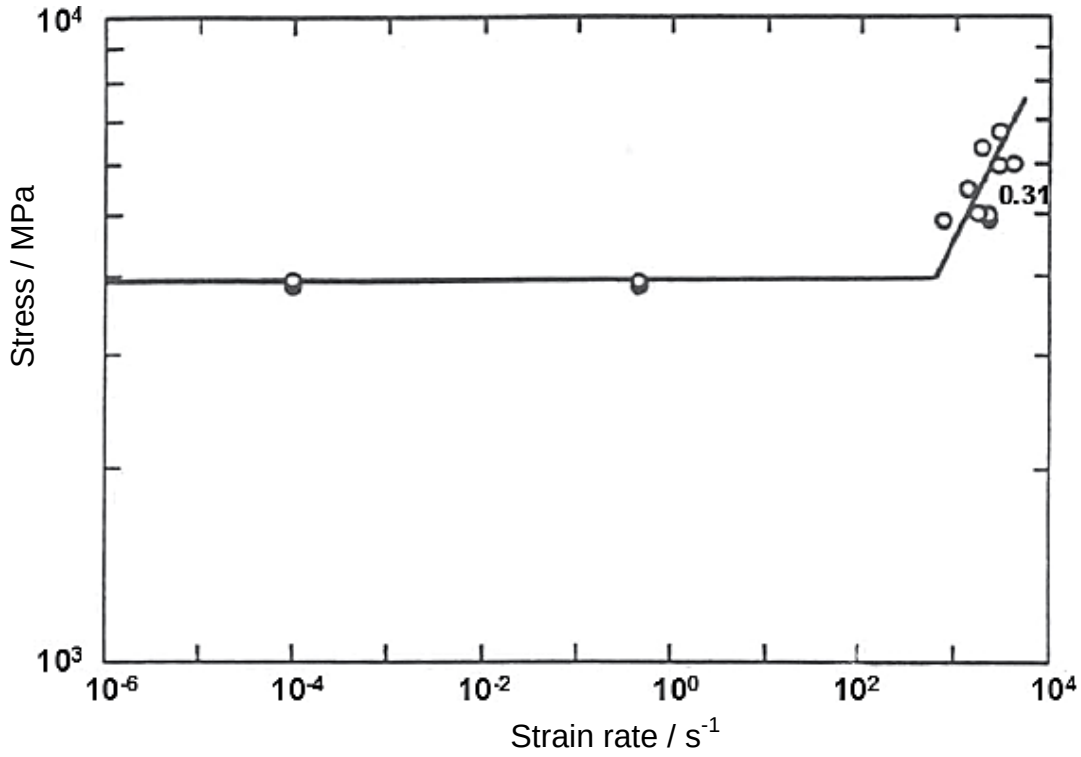

Figure 2.8 Dependence of SiC compressive strength on strain rate [27].

In addition, Chen et al. [3] studied the dynamic fracture toughness at high loading rates using a modified SHPB. As is presented in Figure 2.9, the fracture toughness of a silicon carbide ceramic increased from 4 - 6 MPa $m^{1/2}$ to 8 - 12 MPa $m^{1/2}$, indicating the rate sensitivity of the fracture toughness of the ceramic materials. This result is contradicted in the review of Karandikar [4], who suggested that most ceramics become more brittle with an increase in strain rate. The understanding of dynamic fracture toughness is still a challenge, since there is no standard experimental procedure available and the dynamic toughness test using higher strain rate (>10^4 s^{-1}) equipment has not been reported.

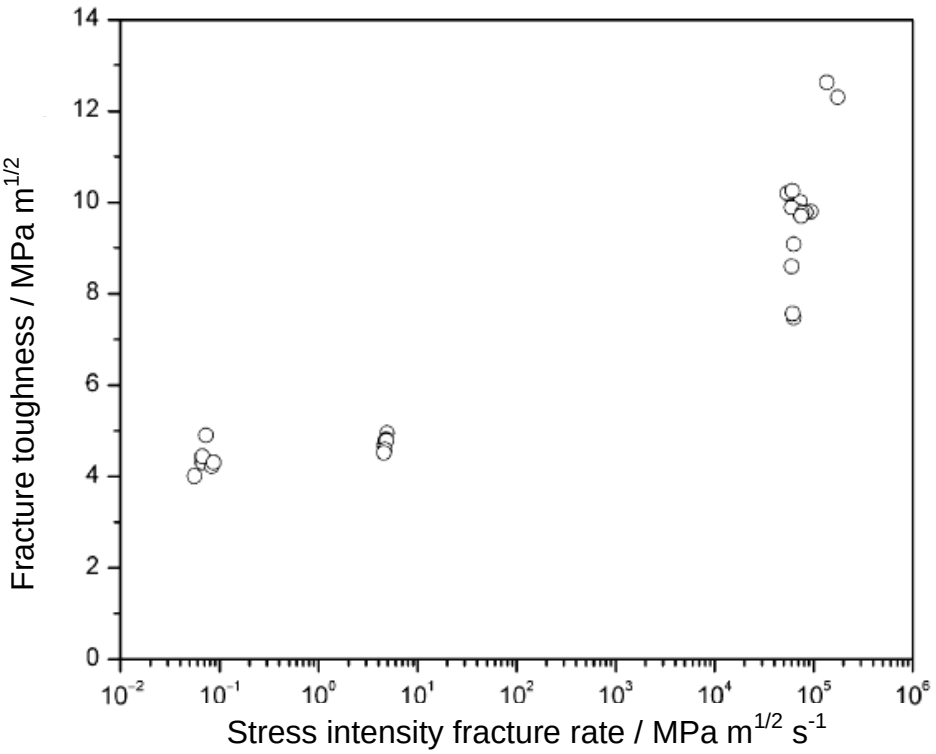

Figure 2.9 Dependency of SiC-N fracture toughness on strain rate [3].

2.2 Nano Ceramics and Composites

Tracing back to 1959, when the concept of nanotechnology was presented by Nobel laureate Richard Feynman [28], nanotechnology has attracted both scientists and industry's attention, and experienced a prosperous development over the last 50 years [29,30]. Nanotechnology has been defined by Bhushan [29] as a discipline which deals with the production and application of physical, chemical and biological systems at scales ranging from individual atoms or molecules to submicron

dimensions, as well as the integration of the resulting nanostructures into larger systems. With very fine grain size, nano materials are claimed to have superior properties to conventional materials and deliver considerable industry benefits [31–33].

Nanoceramics are ceramics with mean grain sizes less than 100 nm. The various advantages of nanoceramics can be attributed to the fact that a larger fraction of atoms reside along the grain boundaries compared to conventional micron-structured ceramics [33]. The presence of excess grain boundaries results in unique physical and mechanical properties. For example, their magnetic, electronic and optical properties are highly influenced by the smaller grain size [34]. Mechanical properties, such as toughness, hardness and wear resistance are different from their submicron sized counter parts, which attracts the attention of industry [35,36]. In addition, superplasticity at elevated temperatures has been observed in some nanoceramics, such as yttria stabilised tetragonal zirconia (YSZ) nanoceramics, which provide a possibility for overcoming the brittle nature of ceramics [5,6].

Nano materials have been applied in many areas, including information and communication technology (ICT), medicine, cosmetics, sunscreens, self-cleaning windows, ultra-strong lightweight materials, low-cost solar power generation, miniature fuel cell technology and environmental pollution monitoring and remediation [37].

For the application of ceramic armour, the literature referring to nanoceramic armours is limited. This is mainly because only limited pure nano ceramics were able to be produced and the most popular ceramic armour materials, such as Al_2O_3, SiC and B_4C, has not been able to be produced with nanostructures in large scale production, according to the current literature. On the other hand, nano-composites, i.e. a conventional ceramic matrix with nano inclusions added, have been increasingly considered for armour applications. Kremenchugskii [7] compared a B_4C nanocomposite (with 7% nano TiB+TiC) with a submicron B_4C composite in terms of their ballistic performance. A ballistic armour structure containing the new nanostructural composite ceramic displayed improved protective properties and less fragmentation, as confirmed by ballistic testing. A ZTA composite with nano YSZ is

also suggested to be a potential armour material due to its improved mechanical properties [10].

The current project is trying to produce fine grain sized pure alumina and nano zirconia toughened alumina composites as potential armour materials. Therefore, information about these two materials is reviewed in detail in sections 2.3 and 2.4.

2.3 Alumina Ceramics

Alumina is one of the most widely used ceramic armour materials. Because of its stability and its strong atomic bonds, alumina shows high hardness, high moduli of elasticity, high strength, good wear resistance and tribological properties and refractivity [38]. In this section, the phases of alumina and their stability are introduced in section 2.3.1, and the effects of grain size on the hardness and toughness of alumina are reviewed in sections 2.3.2 and 2.3.3. The high strain rate performance of alumina is reviewed in section 2.3.4. Finally, studies about the residual stress on the alumina materials after static or high strain rate testing are introduced in section 2.3.5.

2.3.1 Phases of alumina

Alumina has many different crystal structures, including α-alumina (corundum is its mineralogical term) and metastable aluminas (hydrated alumina and transition alumina) [38] . The crystal structure of α-alumina can be described as a compact hexagonal stacking of O^{2-} anions, in which the two-thirds of the octahedral interstices are occupied by Al^{3+}cations, Figure 2.10 [38]. Hydrated alumina is a variety of metastable alumina. It can be divided into trihydroxydes, corresponding to $Al_2O_3•3H_2O$ and oxyhydroxydes $Al_2O_3•H_2O$. Transition alumina has many different types (khi, kappa, rho, eta, theta, delta, gamma, etc) based on their distinction of macroscopic criteria (particularly the specific surface of the products) and crystallographic criteria (particularly the presence of numerous defects: point defects as well as extended flaws) [38]. All the transition aluminas can be classified under the collective name of gamma alumina (γ-alumina). The structure of one type of γ-alumina is shown in Figure 2.11 [36].

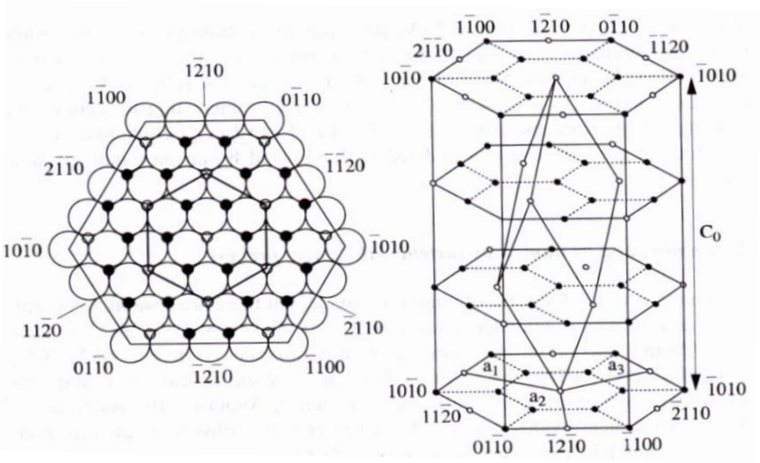

Figure 2.10 Schematic drawing of the α-alumina structure [38].

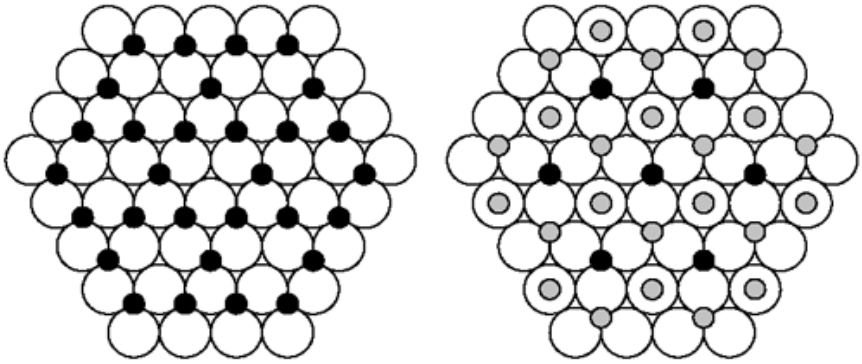

Figure 2.11 Schematic drawing of the first two layers in the γ-alumina structure, octehedral Al ions are black, tetrahedral Al ions are grey [39].

Most commercially used alumina has the α structure because it is the most thermodynamically stable phase at room temperature. However, syntheses of nanocrystalline alumina usually results in γ-alumina [40]. According to the molecular dynamics simulation study of α and γ-alumina by Blonski and Garofalini [41], the surface energies for α-alumina were significantly higher than those of γ-alumina when specific surface areas exceed ~125 m^2g^{-1}, as shown in Figure 2.12. This means that, in the nano scale, the α phase has a tendency to transform to the γ phase. Although γ-alumina powder can be made at the nanoscale, during densification, γ-alumina will transform to α-alumina at ~1075˚C. This process results in exaggerated grain growth, thus losing the benefits of the nanoscale grain size [42]. In addition, the rapid grain growth hinders densification, resulting in only 82% relative density after conventional pressureless sintering [43] Therefore, further research is required in the processing of nano-alumina. In the current research, α-Al_2O_3 with

grain sizes from 0.5 to 1.5 μm and full density will be produced using conventional pressureless sintering methods.

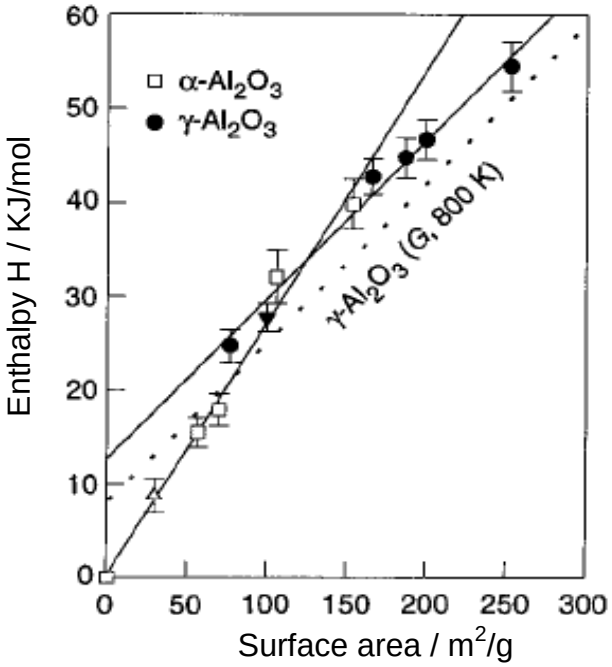

Figure 2.12 Enthalpy, H, of alumina samples relative to coarse-grained α-Al_2O_3 as a function of surface area. The γ-Al_2O_3 (●) lies at lower enthalpy than α-Al_2O_3 (□) when the specific surface areas exceeds 125m^2 g^{-1}. (Δ) Data for a 30m^2 g^{-1} sample of α-Al_2O_3 obtained from drop solution and transposed temperature drop calorimetry on diaspore. (▼) Data for a 100 m^2 g^{-1} sample of γ-Al_2O_3 obtained from drop solution and transposed temperature drop calorimetry on boehmite. The dotted line represents the free energy G of γ-Al_2O_3 relative to corundum at 800 K [42].

2.3.2 Effect of grain size on the hardness of alumina

Hardness is the resistance of a material to the mechanical penetration of another body into its surface. It is measured by investigating plastic deformation associated with the penetration behaviour of a harder indenter (usually diamond) with a known geometry. Possible influences on the hardness result associated with the material include [44]:

- Influence of the crystallographic structure and point defects;
- Influence with pre-existing dislocations (from sintering, grinding or polishing);
- Interactions with grain boundaries that restrict the free path of dislocations,

reduce the plastic deformation and hence yield an increased hardness.

Dislocation glide (or slip) is a primary mechanism for plastic deformation in crystals. In polycrystalline materials, the slip must propagate from one grain to the next to plastically deform. Stress concentrations are built up at the grain boundary and these are smaller when the length of the slip band, or the grain size, is smaller [45]. Therefore, the reduction of grain size will result in an increase of hardness, however, the influence of the grain size will disappear at grain sizes which become smaller than typical dislocation loops [44]. According to the study of Skrovanek and Bradt [46], the Knoop hardness (load: 4 N) increased for hot pressed alumina samples as the grain size decreased from 8 to 3-4 μm, whereas the hardness is independent of grain size with the further reduction of the grain size, as is shown in Figure 2.13 [46]. The microhardness at larger grain sizes showed a classic Hall-Petch behaviour, i.e. the relationship of the microhardness and grain size can be described using the equation below:

$$\text{Knoop hardness (4N)} = 1118 + 1673 \times (\text{grain size})^{-1/2}$$

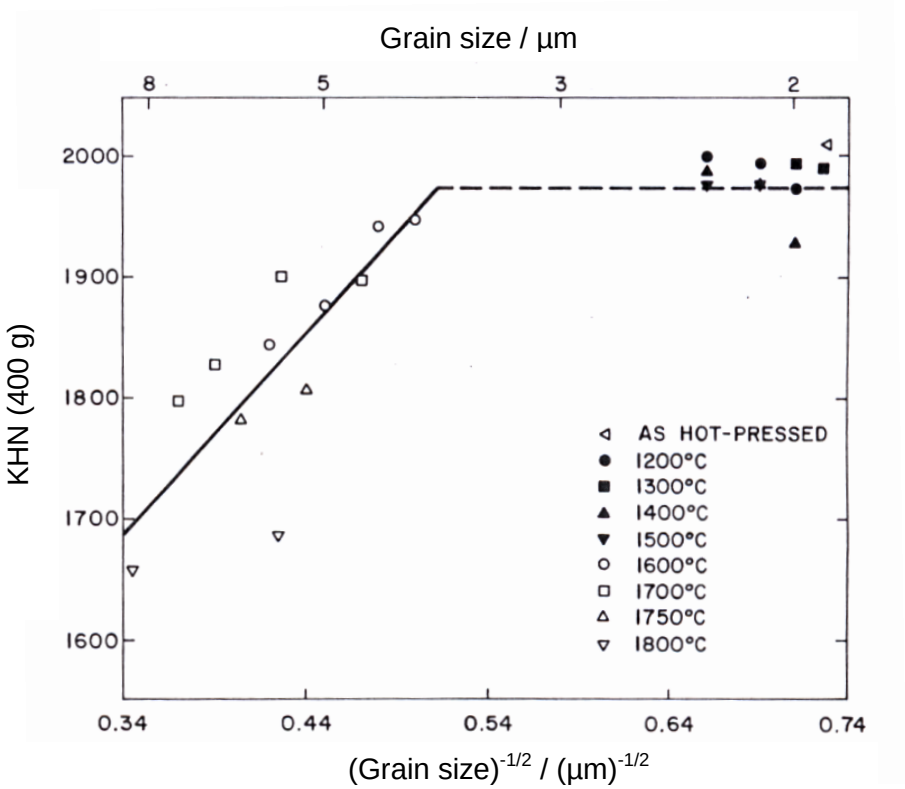

Figure 2.13 Variation of Knoop microhardness (KHN) with grain size, different symbols represent different annealing temperatures after hot pressing in order to get different grain sizes [46].

Several other researchers [44,47] confirmed the result shown above. However, Krell and Blank [44] found that, by using higher testing loads, the improvement of hardness at fine grain size appeared as well. Using a 10 N indentation load, the hardness increased from 16 to 22 GPa for ground samples with grain size decreasing from 4 μm to 0.4 μm [46]. However, it was reported that, when the grain size of materials is reduced to the nanoscale, dislocation glide is no longer the deformation mechanism and the grain size and hardness relationship becomes inverse or negative Hall-Petch. The reasons for this transition are not well understood and the transition does not appear to occur for all nanomaterials [47].

2.3.3 Effect of grain size on the fracture toughness of alumina

Fracture toughness (K_{IC}) is the energy absorbed before the fracture of a material. Various techniques have been used to determine the fracture toughness of alumina such as chevron notch beam (CVNB), single edge notched beam (SENB), double cantilever beam (DCB), single edged precracked beam (SEPB) and the indentation method [48]. The grain size of a ceramic will affect its toughness by changing the fracture stress and fracture mode.

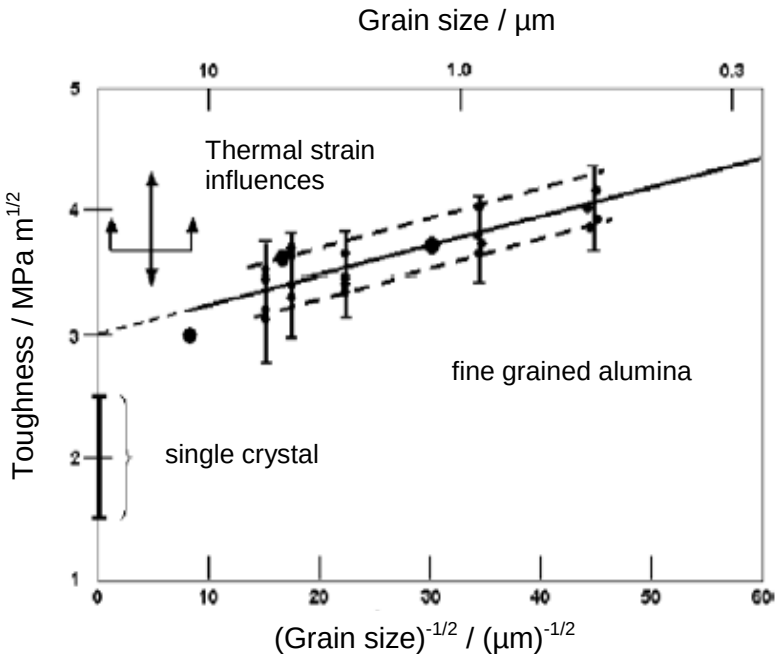

Figure 2.14 Variation of Hertzian indentation toughness with grain size [49].

Armstrong [49] reviewed the indentation toughness dependence on grain size for fine grained alumina. By using Vickers and Hertzian indentation methods, the measurements showed a Hall-Petch dependence. As discussed in section 2.1.4, the hardness and toughness have an inverse relationship when comparing with different materials. However, in case of the effect of grain size on the hardness and toughness, the latter increased simultaneously with the reduction of grain size, as shown in Figures 2.13 and 2.14. In order to explain this phenomena, Petch and Armstrong [50] investigated the dependence of fracture toughness on the yield stress change and the fracture stress change. The resultant model of Petch and Armstrong's study [50] is shown below:

$$dK_c = -\frac{K_c}{2nA}\, d\sigma_c$$

In which dK_c is the change in the fracture stress, $d\sigma_c$ is the change of yield stress, K_c is the critical stress intensity (fracture toughness), n and A are constants.

Armstrong [49] indicated that the increase of hardness with decreasing grain size resulted in an increase in the yield stress ($d\sigma_c$) of alumina, which could result in the reduction in fracture toughness. However, with the decrease of grain size, the fracture stress (dK_c) is increased to a level that is much greater compared to the increase in the yield stress ($d\sigma_c$). Therefore, the counter result of greater toughness is achieved. This suggests that grain size refinement will benefit both the increase of hardness and toughness of alumina.

The Hall-Petch relationship of toughness and grain size was also found and explained by Muchtar and Lim [51]. They reported that the main reason was the change of fracture mode with the change of alumina grain size. Using indentation loads of 300 g to 2 kg to do the toughness tests, a higher fraction of intergranular fracture was observed by SEM on finer grain size samples. For the samples with 0.5 μm grain size, intergranular cracking was evident throughout the length of the crack. The change of fracture mode with grain size is due to the increasing strength of a dislocation pile-up at the grain boundary with the decrease in grain size (which reduced the mean length of the dislocations). Therefore, the cleavage fracture toughness increases with the decrease in grain size. On the other hand, grain boundaries can be viewed as internal defects and sources of stress raiser in the

material. With the decrease of grain size, the intergranular crack is less tortuous, so the intergranular fracture toughness is decreased. Therefore, coarse grain size samples display transgranular fracture and fine grain size samples display intergranular fracture, as is shown schematically in Figure 2.15.

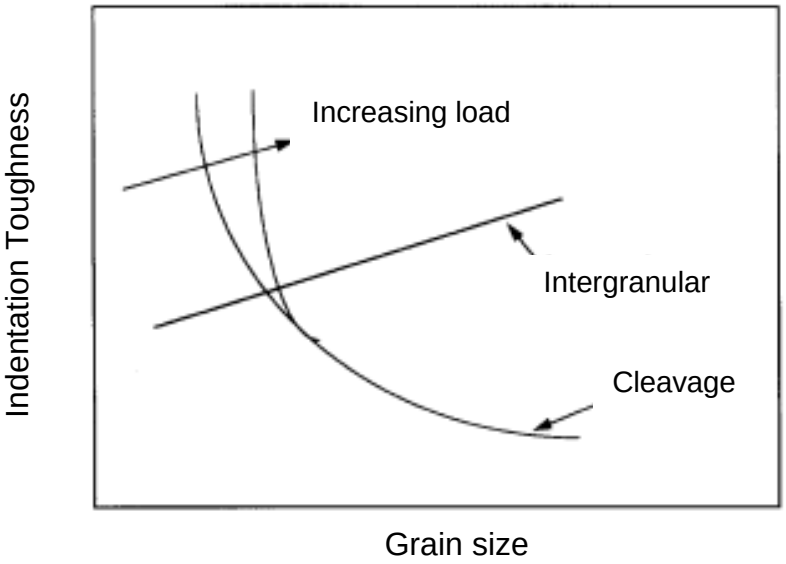

Figure 2.15 Schematic representation of the fracture toughness vs. grain size [51].

Moreover, the relationship of crack size and grain size also affects the toughness results. If the crack size is much larger than the material grain size, the plastic zone size at the tip of the larger crack should match with the material grain size and, thus, a reversed Hall-Petch dependence may occur [52].

2.3.4 High strain rate performance of alumina

As the most widely used armour ceramic, the high strain rate performance of alumina has been studied by many researchers [53–55]. From the previous literature, microstructure analysis using SEM or TEM helped to investigate the formation of plastic deformations or micro-cracks on the materials after high strain rate testing [53,54]; fragment size analysis was also used to understand the fragmentation process during impact [55].

At room temperature, the compressive strength is very sensitive to the strain rate. Rice [53] suggested that room temperature plasticity may play an important role in the compressive failure of even the most brittle ceramics. Lankford [54] measured

the strength of alumina at different strain rates using an electrohydraulic, servo controlled testing machine and SHPB and found an increased compressive strength with strain rate. By observing the microstructure of the compressed surface using SEM, they found that a few twin-like features appeared on the samples tested using 25% fracture stress. With an increase in fracture stress, more obvious twinning and microslip occurred. Moreover, at 85% fracture stress, microcracking was observed at the twin/grain boundary intersection. Many fine micro twins or possible slip bands nucleated at the grain boundary are shown in Figure 2.16. This proved that the plasticity played an important role in the crack nucleation and sample failure at high strain rate.

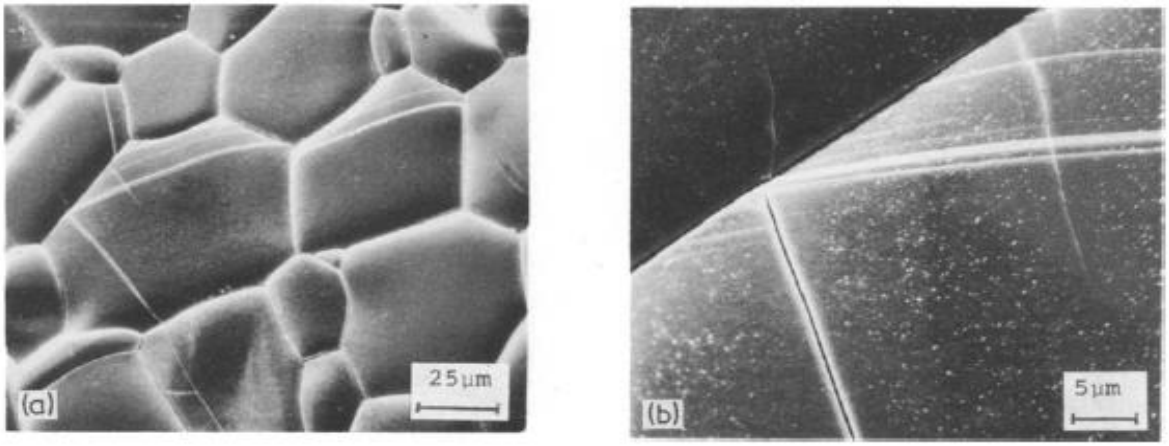

Figure 2.16 (a) Twin-nucleated axial cracking, 85% fracture stress. (b) Higher magnification of (a) [54].

At different strain rates the fragmentation process can be learned from the fragment size of the fractured ceramic samples. According to the study of Lankford and Blanchard [55], the fragment size decreased with increasing strain rate, as shown in Figure 2.17. This was explained by the fact that, under compressive loading, failure consisted of the eventual coalescence of a multitude of microcracks. It is clear that the average fragment size is directly related to the average crack size at coalescence. As the strain rate increases, the cracks nucleated at a given stress level have less time to grow, and so are smaller and less interactive at higher stresses. On the other hand, the degree of crack nucleation and the population of microcracks are larger with the increasing strain rate. Therefore, the fragments are smaller in size and more numerous at higher strain rate. It is concluded that cracking

via plastic deformation mechanisms may be important elements in the failure process.

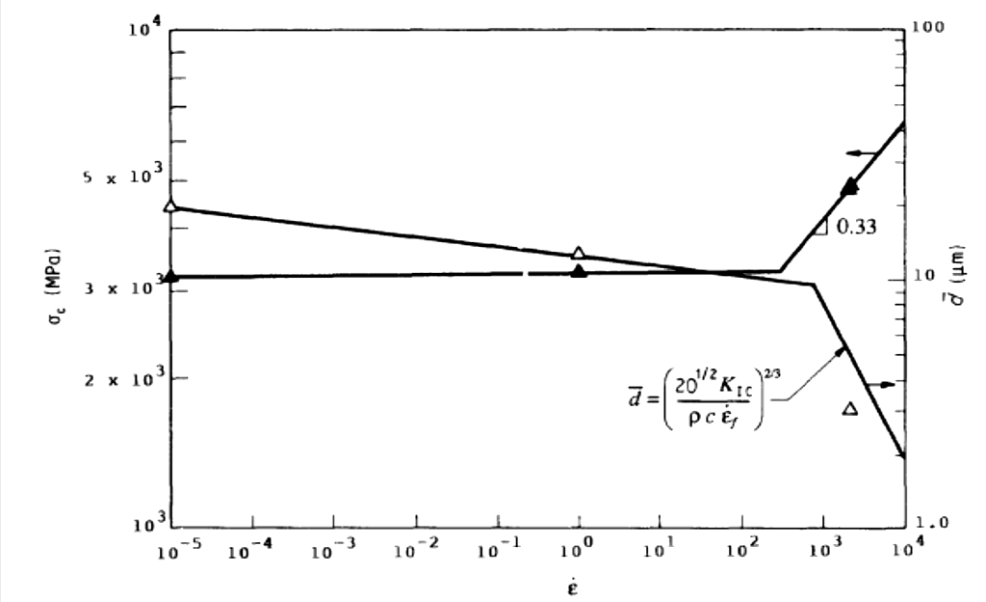

Figure 2.17 Compressive strength (σ_c) and corresponding peak frequency fragment size ($\bar{d}$) against strain rate ($\dot{\varepsilon}$) [55]**.**

2.3.5 Residual stress distribution in the alumina after static or high strain rate testing.

Cr^{3+} fluorescence spectroscopy is considered as an additional effective post test characterisation method after static and high strain rate testing [56–59].

For alumina based ceramics, the chromium ions, Cr^{3+}, are substitutional for the Al^{3+} ions and they give origin to sharp and characteristic fluorescence peaks. When the crystal of the alumina based material is subject to a certain stress, the wavelength of the fluorescence peaks in the spectrum will shift correspondingly, therefore, the stress present can be measured by analysing the Cr^{3+} fluorescence peak shift, as shown in Figure 2.18.The relationship between the peak shift and the residual stress in the crystal is given by:

$$\Delta\nu = \Pi_{ij}\sigma_{ij} \qquad \text{Eqn. (2.1)}$$

where $\Delta\nu$ is the peak shift (cm^{-1}) relative to the stress-free peak position, σ_{ij} are the stress components (GPa) and Π_{ij} is the piezo-spectroscopic coefficient, which has a value of 7.6 cm^{-1} [57].

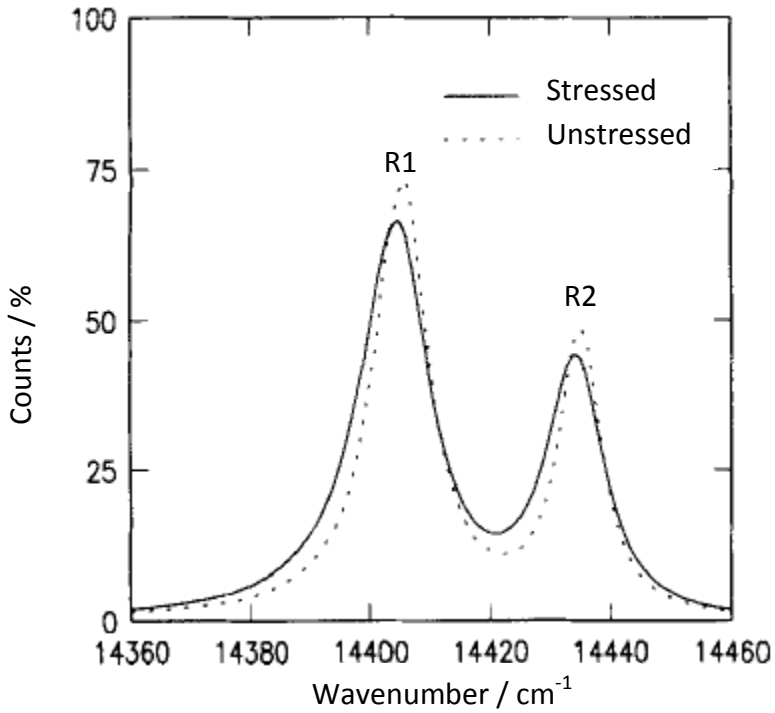

Figure 2.18 Comparison of the Cr^{3+} fluorescence peaks with and without stress, both R1 and R2 peaks have shifted and broadened [60].

In addition to the peak shift analysis, Ma et al. [57] also established that the fluorescence peaks from a plastically deformed material region, such as a plastic zone formed by an indentation, broaden significantly due to the stress variations. This was important as it demonstrated that the level of plastic deformation arising from dislocations having a large local stress field could be quantitatively determined from within a probed volume. According to an experimental and modelling study by Wu et al. [61], the R1 peak width, $\sqrt{\langle \Delta\nu^2 \rangle}$, is proportional to the dislocation density, ρ, of the probed position:

$$\sqrt{\langle \Delta\nu^2 \rangle} = kF(\rho)$$

where *k* is a constant related to the lattice parameters of the alumina crystal and the piezo-spectroscopic coefficients and *F(ρ)* is a function correlated with the dislocation density.

However, Wu et al. [61] also suggested that only when the dislocation density was less than 10^{14} m^{-2} inside the deformed layer, was the peak broadening induced by the increased dislocation density visible.

2.3.5.1 Cr^{3+} fluorescence study after static mechanical property testing

Cr^{3+} fluorescence was initially used on the alumina samples after static testing, such as indentation [60] and wearing [61]. The stress distribution caused by the compressive loading were effectively investigated. However, there are some issues that need to be noted in the case of study on an indent in an alumina-based material.

Guo and Todd [58,62] have observed that the axial resolution of the microscope and the translucency of the material can significantly affect Cr^{3+} fluorescence analysis. Studying the centre of an indent made in alumina using a 1 kg load revealed a single curve that contained four overlapping peaks, two broad peaks and two sharp peaks, Figure 2.19.

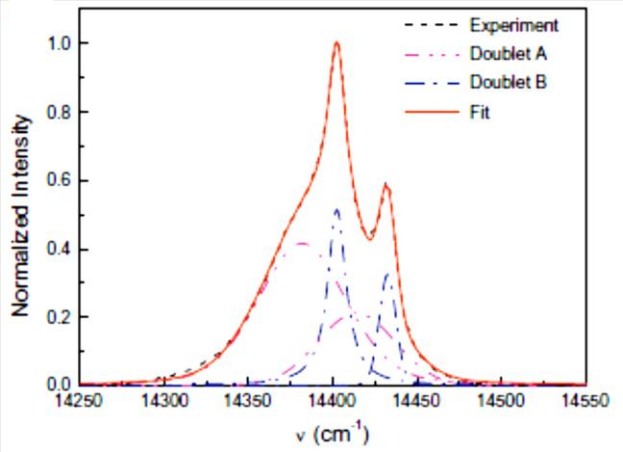

Figure 2.19 Four-peak fitting for Al_2O_3. Symbols A and B indicate the broad and narrow doublets, respectively, which correspond to the two regions shown in Fig. 2.20 using the same symbols [58].

By characterising the probe response function (PRF) and using a four peak fitting program, the two broad peaks were confirmed to originate from either the surface of or inside the plastic zone of the indentation, whilst the two sharp peaks were believed to have arisen from the subsurface region, where there was little effect from the indentation, Figure 2.20 [58]. The relatively high transparency of alumina means that the laser could penetrate below the surface on which it is focused, leading to a large sampling volume covering both the material in the plastic zone and the subsurface region. This indicates that the axial resolution of the Cr^{3+} fluorescence

spectroscopy is not only controlled by the resolution of the equipment, but also by the transparency of a material. Therefore, it is essential to determine the resolution of the microscope and the laser penetration depth so that it is possible to determine which fluorescence peaks represent the signal from the plastic zone.

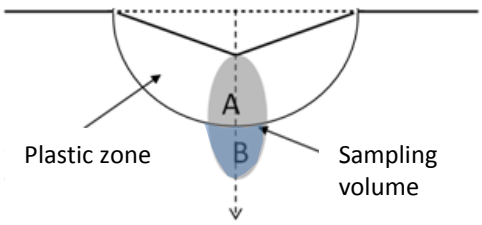

Figure 2.20 Schematic of the sampling volume at the centre of the indent in alumina, where regions both inside the plastic zone (A) and outside it (B) are sampled simultaneously [58].

2.3.5.2 Cr^{3+} fluorescence study on the high strain rate tested alumina

Cr^{3+} fluorescence analysis on high strain rate tested alumina was recently carried out by Dancer et al. [63], who investigated the residual stress distribution and plastic deformation induced by gas gun impact testing for several alumina materials with different grain sizes and glass contents. Fluorescence mapping was applied on the impact surfaces, as shown in Figure 2.21. The best performance against impact was achieved by an alumina with very low glass content (notionally 0%) and relatively small mean grain size (2.0 μm). Based on the residual stress map, a model of the stress state in the material was made, which was a combination of the stress field caused by indentation of a Hertzian indenter and a blister field which represented the plastic zone under the impact surface.

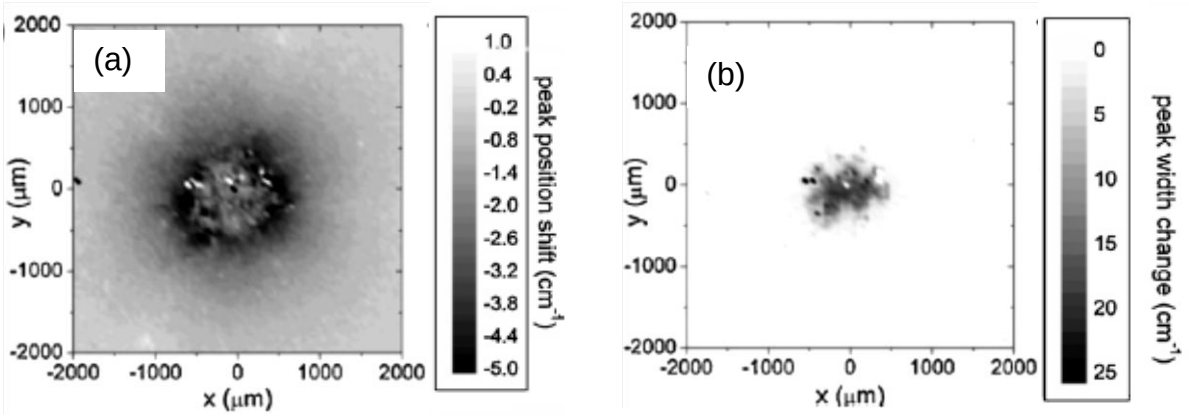

Figure 2.21 Representative Cr^{3+} R1 fluorescence (a) peak shift and (b) peak width change maps for an alumina specimen (0% glass phase, 2μm grain size) on indented region of the facing surface [63].

2.4 Zirconia Toughened Alumina (ZTA)

As indicated earlier, ceramics are considered to be suitable for armour applications because of their low density, high strength and high hardness. However, the brittle nature associated with ceramic materials can restrict their capability to resist multiple ballistic impacts. Their inherent brittleness makes special consideration necessary in designing with these materials as armour systems. Zirconia toughened alumina (ZTA) has been considered before as a candidate armour material [11]. In this section, the toughening mechanisms and different types of ZTA are introduced in sections 2.4.1 and 2.4.2; the effect of zirconia and alumina grain sizes on their mechanical properties of ZTA is discussed in section 2.4.3, and literature relevant to the high strain rate performance of toughened ceramics is reviewed in section 2.4.4. Residual stress in the ZTA composites is introduced in the last section, 2.4.5.

2.4.1 Toughening mechanism

Pure zirconia possesses a high melting temperature (T_m~2,680°C). As the temperature decreases from T_m at normal atmospheric pressure, zirconia can exhibit three crystallographic phases, viz. cubic, tetragonal and monoclinic. The transformations between these phases as a function of temperature are illustrated in Figure 2.22. The last transformation, tetragonal to monoclinic, is accompanied by a considerable volume expansion, about 4-5 vol%.

4-5 vol% change

Monoclinic ⇔ tetragonal ⇔ cubic ⇔ liquid

1170°C 2370°C 2680°C

Figure 2.22 Phase transitions in zirconia.

In a ZTA composite, the zirconia inclusions in the alumina matrix can either transform from tetragonal to monoclinic during cooling from the fabrication temperature, or they can be retained in a metastable form with the tetragonal structure. In either case, the zirconia inclusions in the ZTA matrix can toughen the material throughout different toughening mechanisms, including microcracking toughening, stress induced transformation toughening, crack deflection, crack branching, crack shielding and compressive surface stress [64]. The first three mechanisms are the more commonly observed and will be reviewed in detail.

2.4.1.1 Microcracking toughening

There are two types of microcracking toughening mechanism, which are residual microcracking and stress induced microcracking respectively [64]. If the zirconia inclusions are larger than the critical size for tetragonal retention, they can toughen the material by the residual microcracking mechanism. The large tetragonal zirconia inclusions will transform to monoclinic on cooling from the sintering temperature [65]. The volume expansion associated with the transformation generates stresses on the surrounding alumina matrix and induces microcracks at the boundaries between the inclusions and the matrix. During fracture, the stress from a propagating crack extends these microcracks and the latter may deflect the propagating crack. Therefore the fracture energy is absorbed by the microcracks on the zirconia/alumina boundary.

For stress induced microcracking toughening, the microcracks on the zirconia/alumina boundary are caused by the volume expansion and shear strain associated with the stress-induced transformation during the fracture process. It is considered [64] that residual stresses are required for the formation of the stress-induced microcracks, however the magnitude of the stresses is insufficient to cause spontaneous microcracks without the application of an external stress. Hence, when

the external stress from the propagating crack is introduced, the tetragonal to monoclinic transformation occurs and the microcracks are induced, as shown in Figure 2.23. Microcracking toughening is the most commonly occurring toughening mechanism, however the increase of toughness is at an expense of the strength due to the presence of subcritical flaws and the increase of the critical flaw size [47,64].

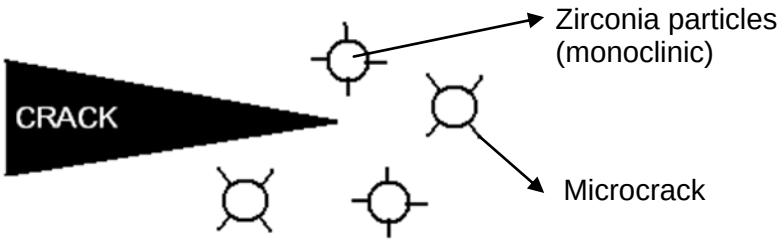

Figure 2.23 Schematic of microcracking toughening.

2.4.1.2 Stress induced transformation toughening

With a sufficiently small zirconia particle size, or with the addition of a certain amount of stabilizer, e.g. 3 mol% Y_2O_3, the tetragonal to monoclinic transformation can be suppressed on cooling from the sintering temperature of the ZTA material. Therefore, the zirconia particles in the alumina matrix are retained in the metastable tetragonal form at room temperature. When an external stress from a crack is applied to the zirconia inclusions, the metastable tetragonal zirconia around the crack tip will transform to the monoclinic form. The 4-5 vol% expansion associated with the transformation provides a compressive stress which then acts to reduce and eventually stop the propagation of the crack (Figure 2.24) [47,64,65]. The stress induced transformation toughening mechanism is considered to be superior to the microcracking toughening mechanism because the transformation toughening increases the fracture toughness of the material without introducing sub-critical microcracks [66], i.e. the strength is generally increased rather being decreased.

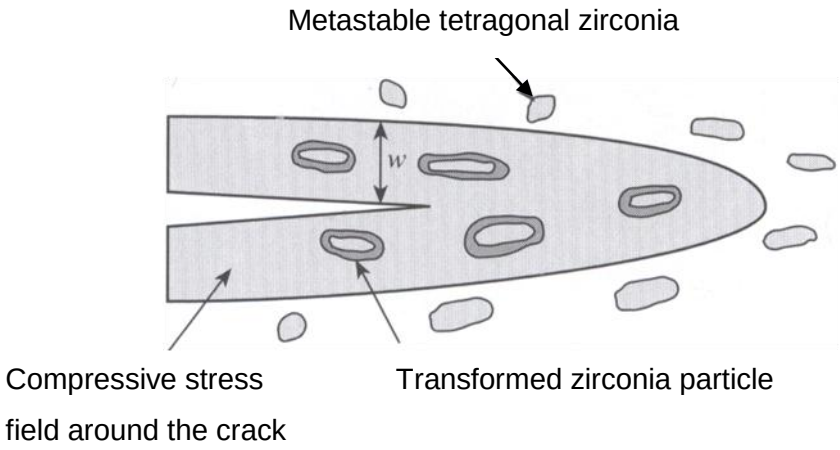

Figure 2.24 Schematics of stress induced transformation toughening [47]

2.4.1.3 Crack deflection toughening

Crack deflection toughening is found to provide an effective toughening effect without decreasing the strength of ceramics. According to several studies [67,68], cracks can be deflected either by localized residual fields or by fracture resistant secondary phases (e.g. zirconia agglomerates). The localised residual fields arise from the elastic modulus and/or thermal expansion mismatch between the matrix and the inclusion phases. The deflection by a secondary phase in the matrix is the major cause of crack deflection toughening. As is shown in Figure 2.25, when a crack approaches the secondary phase, it will tilt at an angle, θ, out of its original plane. The tilt angle depends upon the orientation and position of the second phase particle with respect to the propagating crack. Subsequent propagation and deflection of the crack result in crack front twist. All these deflections result in a degree of toughening dictated by the reduction of force on the deflected portion of the propagating crack.

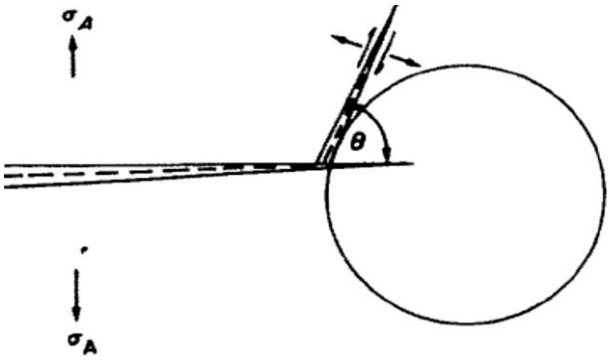

Figure 2.25 Schematics of typical crack deflection [67].

2.4.2 Microstructures of ZTA

With regard to the different microstructures, ZTA materials are divided into four types: I) alumina with dispersed unstabilized zirconia (Figure 2.26 a); II) alumina with dispersed partially stabilised zirconia (PSZ) (Fig. 2.26 b); III) alumina with PSZ agglomerates (Fig. 2.26 c); IV) alumina-zirconia duplex structures (Fig. 2.26 d) [64].

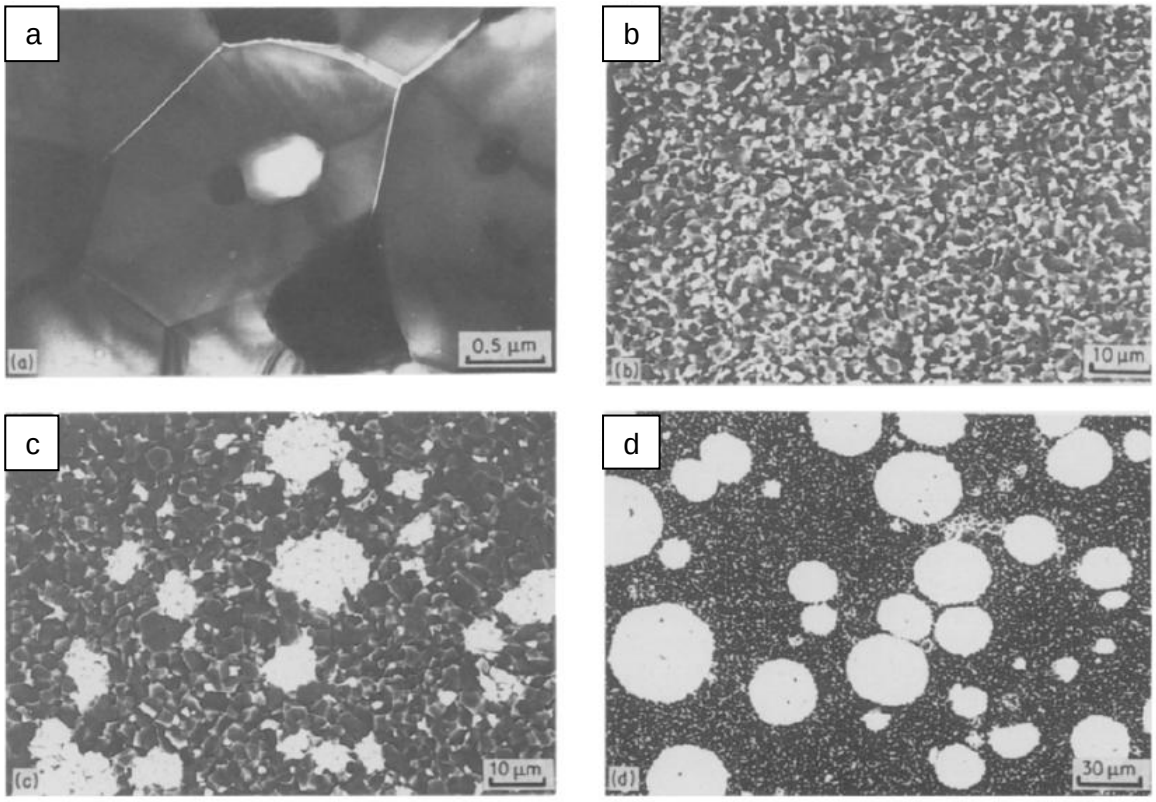

Figure 2.26 a) transmission electron micrograph showing the microstructure for alumina containing well-dispersed unstabilized zirconia particles, the microcracks at the grain boundaries are due to the volume expansion and shear strain associated with the tetragonal to monoclinic transformation of the dispersed zirconia particles; b-d) scanning electron micrographs showing the microstructures of alumina containing well-dispersed PSZ single crystals, PSZ agglomerates and alumina-zirconia duplex structured composites, respectively [64].

The toughening mechanisms of the four ZTA types are different due to their microstructural differences. The related toughening mechanisms are listed in Table 2.3. Structure I shows an increased toughness and a decreased strength as a result of the microcracking toughening. Structures II and III both exhibit increased

toughness and strength due to their different toughening mechanisms, which are stress induced transformation toughening and crack deflection toughening respectively. Structure IV, the duplex structure, contains PSZ single crystals dispersed in a matrix of PSZ agglomerates. It shows superior toughness as a result of a combined mechanism, including the stress induced transformation toughening and crack deflection. The strength increase of structures III and IV is associated with the careful control of the agglomerate size (20 to 50 μm) as well as the fine grained matrix in order to prevent large flaws in the microstructures [64]. In the current study, ZTA with structure II is selected as a potential armour material due to its benefits of the improved toughness and strength as well as the ease of fabrication. The mechanical properties of ZTA with structure II will be reviewed in detail in section 2.4.3.

Table 2.3 ZTA structures and related toughening mechanisms and their strength

ZTA Structure	**Toughening mechanism**	**Effect on the strength**
I) alumina with dispersed unstabilized zirconia	Microcracking toughening	decrease
II) alumina with dispersed PSZ	Stress induced transformation toughening	increase
III) alumina with PSZ agglomerates	Crack deflection	increase
IV) alumina-zirconia duplex structures	Stress induced transformation toughening, Crack deflection, microcracking toughening (dependent on the stabilising of the tetragonal zirconia)	increase

2.4.3 Mechanical properties of ZTA (Structure II)

The key factors that can affect the mechanical properties of ZTA are the zirconia content and zirconia particle size. The effect of the alumina matrix on the mechanical properties of ZTA is considered to be the same as for pure alumina materials [69].

2.4.3.1 The effect of zirconia content on ZTA mechanical properties

According to the study of Lange [66], the fraction of PSZ significantly affects the mechanical properties of ZTA, as shown in Figure 2.27. The fracture toughness increases with PSZ content due to the stress induced transformation toughening

mechanism. The strength increase is a result of the transformation toughening and the reduced grain size of alumina, which is caused by the hindrance of grain growth with the addition of zirconia. In addition, the Young's modulus, *E*, and hardness, *H*, of the ZTA composite obey a linear rule of matrix, which is,

$$E_{ZTA} = f \times E_{ZrO_2} + (1-f) \times E_{Al_2O_3}$$

$$H_{ZTA} = f \times H_{ZrO_2} + (1-f) \times H_{Al_2O_3}$$

where, the$f$ is the volume fraction of the PSZ [66].

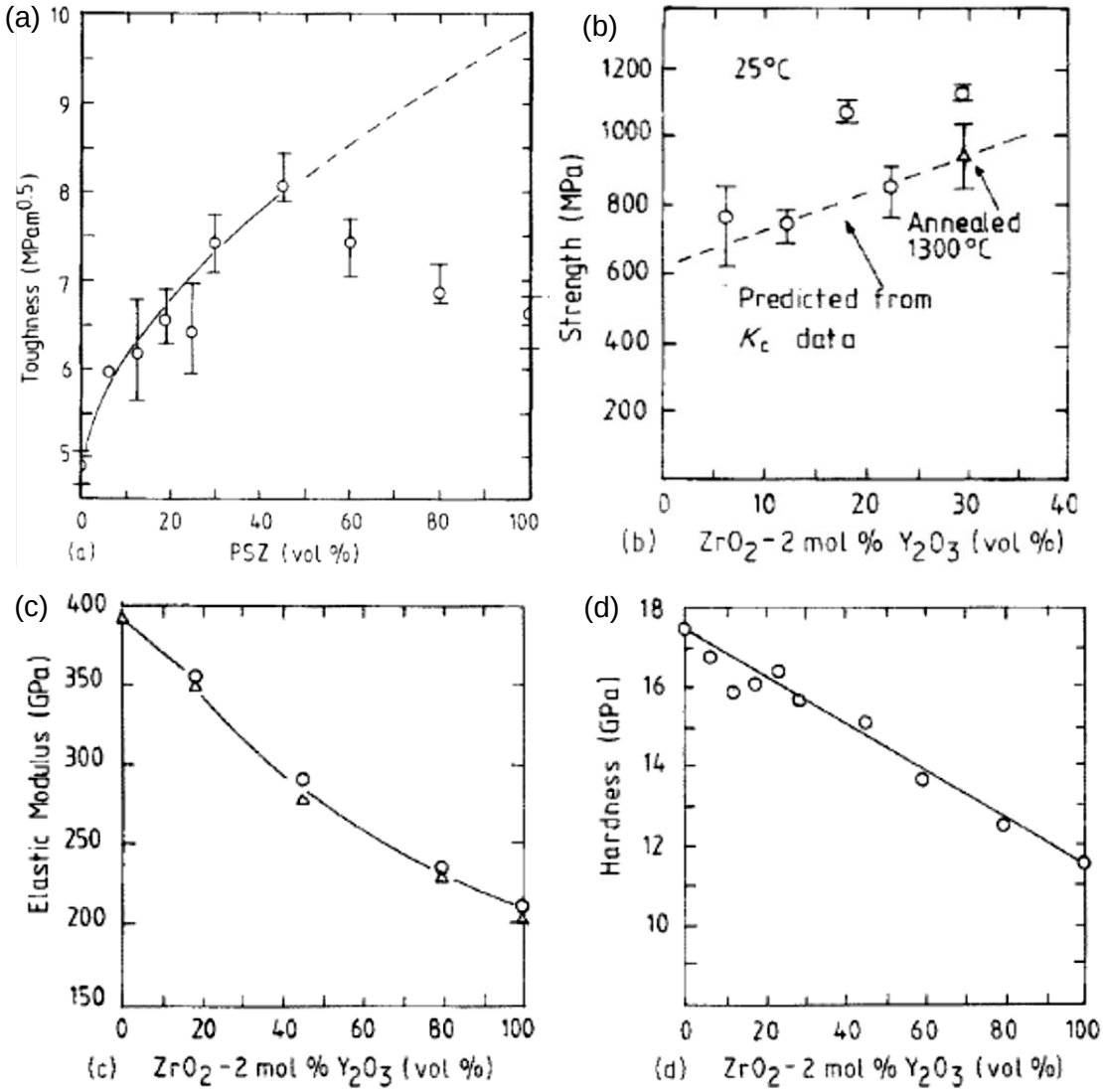

Figure 2.27 (a) The dependence of the fracture toughness on volume fraction of PSZ addition for the hot pressed ZTA composites. (b) The dependence of the fracture strength on the volume fraction of PSZ addition for the composites. (c) The composition dependence of the elastic modulus for the composites: (o) Extension (60 kHz); (Δ) flexural (9 kHz). (d) The composition dependence of hardness for the composites [66].

However, it is not that the higher the zirconia content, the tougher the material. As shown in Figure 2.27 (a), the toughness of ZTA increases until the PSZ content reaches about 45 vol%. After that, the value decreases gradually. Becher [70,71] suggested that there is a critical volume fraction for a given particle size that causes an auto transformation. This is because: the thermal expansion mismatch between tetragonal zirconia and alumina ($t\text{-}ZrO_2$ = 10.0 × 10^{-6} C^{-1}, $\alpha\text{-}Al_20_3$ = 6.0 × 10^{-6} C^{-1}) can generate internal tensile stresses; when this tensile stress is equal to the tetragonal to monoclinic transformation stress, the transformation will automatically happen and the zirconia particles will lose their tetragonal form.

2.4.3.2 Effect of zirconia grain size on the ZTA mechanical properties.

In addition to the zirconia content, the zirconia grain size in ZTA can also affect the mechanical properties [47,64,69,71]. According to Becher et al. [71], with an increase in zirconia grain size, the martensite start temperature M_s for the tetragonal to monoclinic transformation increases. The higher M_s represents a higher driving force for the transformation, hence, the applied stress required to induce the transformation reduces. On the other hand, fine zirconia grains are more difficult to transform, unless the applied force is high enough.

Casellas et al [69] measured the toughness and hardness of ZTA samples with different grain sizes. The samples were sintered at 1600˚C for 2 h and then annealed at 1600˚C for 0.5-30 h to coarsen the microstructures of the ZTA. As shown in Figure 2.28 [69], with an increase in the heat treatment time, the toughness of ZTA increased slightly, whilst the hardness decreased. Casellas suggested that the increased grain size of zirconia yielded a lower activation stress, which then led to both larger transformation zones and more pronounced shielding effects around a propagating crack. In addition, from the observation of indentation cracks, he found that crack closure always occurred when it went though some zirconia particles cluster (Figure 2.29).

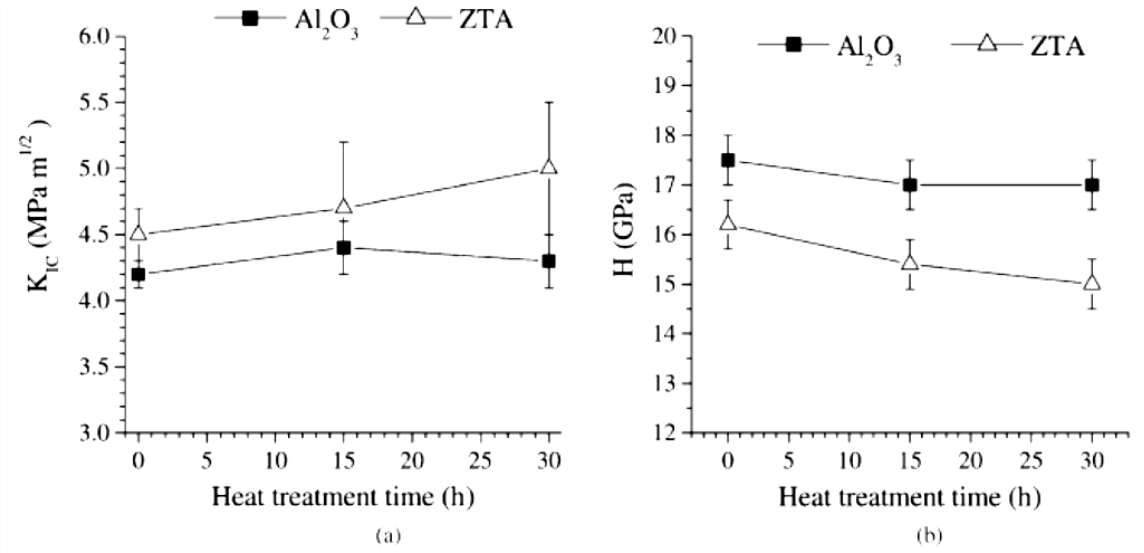

Figure 2.28 Mechanical properties of Al_2O_3 and ZTA materials: (a) fracture toughness; (b) hardness [69].

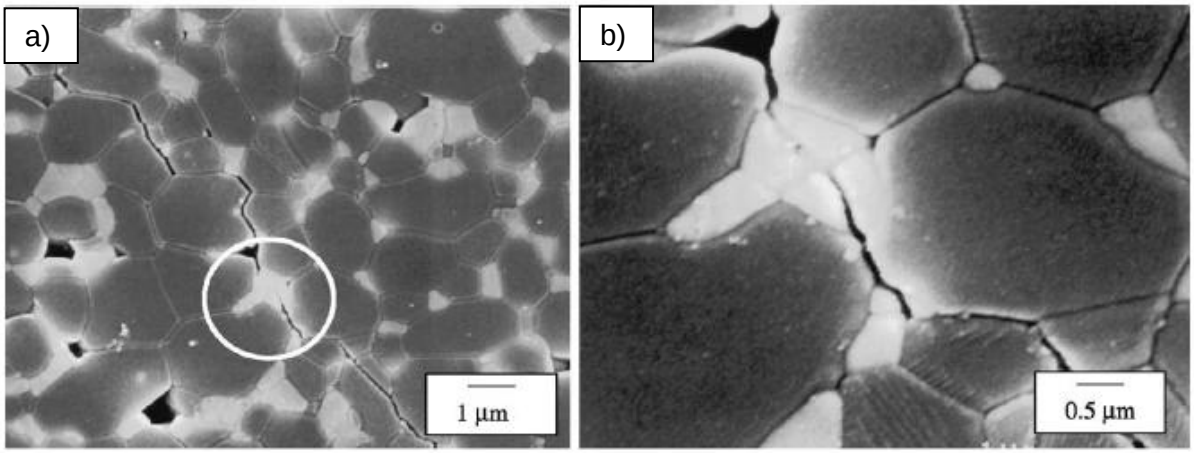

Figure 2.29 (a) Propagation of an indentation crack in heat-treated ZTA, the crack passed through a ZrO_2 particle before closure. (b) Magnification of the encircled region of (a) [69].

2.4.4 Residual stress in ZTA

The residual stress in an alumina zirconia composite material consists of three parts [72]:

$$\sigma = \sigma^{EM} + \sigma^{ATE} + \sigma^{PT}$$

σ^{EM} is the stress arising from thermal expansion and elastic mismatch between the constituent ceramic phases; σ^{EM} is due to the crystallography thermal expansion anisotropy of alumina grains, i.e. the thermal expansion mismatch of the alumina

grains with different crystallographic directions, this term is negligible and will not be further discussed; σ^{PT} is the stress induced by the tetragonal to monoclinic zirconia phase transformation after cooling or after applying a stress on to the material.

σ^{EM} has a dramatic effect on the mechanical behaviour of ZTA materials [73]. It has been observed that the grain size of the zirconia inclusions greatly affects the thermal stress in the alumina grains and that finer zirconia grain sizes leads to less stress [73,74]. In multilayer composite materials, the stress between layers caused by the different coefficient of thermal expansion (CTE) can lead to cracks on the interlayer. Portu et al. [75] successfully measured the residual stress distributions in Al_2O_3/ZTA multilayered composites by fluorescence and Raman spectroscopy, with the alumina being used as a 'stress sensor' for the stress measurement. The σ^{EM} was effectively controlled by adjusting the thickness of the layers.

Last but not least, σ^{PT} occurs when the tetragonal to monoclinic zirconia phase transformation happens in ZTA. Sergo et al. [72] measured the residual stress within a wear band in a ceria stabilised ZTA by fluorescence spectroscopy and the zirconia phase transformation contents within the band were investigated using Raman spectroscopy. They found that, although the overall residual stress in the band was compressive, a tensile residual stress induced by the zirconia phase transformation was observed, leading to the reduction of the overall stress. This result is consistent with Gregori et al.'s finding [76], in which they measured the residual stress caused by the zirconia phase transformation in ZTA materials through experimental and modelling work. They demonstrated that the monoclinic content and the stress wear linearly correlated, no matter whether the transformation had been induced thermally or mechanically. The correlation has also been theoretically modelled using a stochastic description of the residual stress field [76] and a very good agreement was achieved, as shown in Figure 2.30. These results can be explained by the fact that, during the zirconia phase transformation process, the volume expansion of transformed zirconia grains provides a local compressive stress to the surrounding alumina grains and the alumina grains provide an overall tensile stress to resist the force from the nearly uniformly distributed zirconia grains [72].

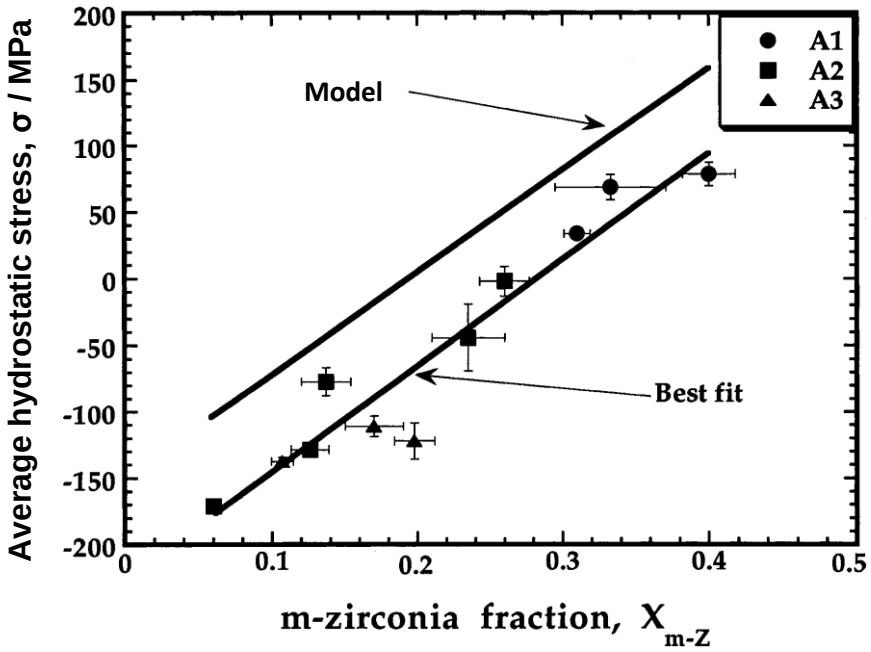

Figure 2.30 Correlation between the stress in alumina and the monoclinic content in zirconia, the experimental results and theoretically modelled line are both shown [76].

2.4.5 High strain rate performance of toughened ceramics

According to Woodward et al. [77], the toughness of ceramic tiles in an armour system significantly affects the fragmentation process. With higher toughness, the volume of fragments decreased in any size range of the fragment distribution; the volume of fragments is plotted against toughness for glass, alumina and zirconia in Figure 2.31. This provides evidence that the increased toughness could improve the multihit capability of ceramic armours, since it suggests that excessive fragmentation could be prevented.

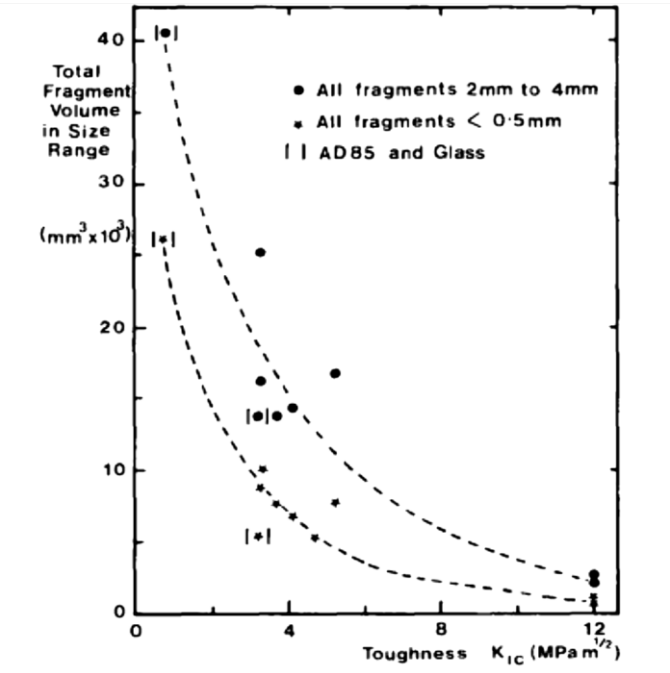

Figure 2.31 Total volume of fragments in size fractions <0.5 mm and 2-4 mm, plotted against fracture toughness, K_{IC}, for confined ceramic targets [77]**.**

On the other hand, both O'Donnell [23] and Woodward et al. [77] found that the degree of fragmentation of a ceramic has little influence on the ability of the armour system to defeat ballistic impact. Rather, the ability of the ceramic to defeat an incoming projectile is related to: 1) the ability to absorb the kinetic energy of a projectile and transfer the load to the backing plate, and 2) the ability to erode the projectile and therefore reduce the impacting mass. These abilities are considered to be related to the hardness and strength of ceramics [9].

However, Flinders and co-workers [8] pointed out that a high toughness SiC-B material showed better performance against high kinetic energy threats, whereas the depth of penetration (DOP) test velocities used in earlier research [23,77] were relatively low (~750 $m\,s^{-1}$). The authors [19] considered that the low porosity of the SiC-B combined with its ability to fracture intergranularly, and thereby absorb more energy, allowed it to outperform other materials, but the reason for the better performance at higher energy threats was not clear.

Zhang and Li [11] compared the ballistic performance of a 95% alumina ceramic (5% additives) and a 10% ZTA (10 vol.% zirconia) based on the DOP method using

impact velocities from 1100 to 1500 m s^{-1}. The relationship of the residual penetration depth against the impact velocity in Figure 2.32 shows that the penetration depth of the 10% ZTA was lower than that of the 95% alumina at impact velocities higher than 1200 m s^{-1}, and their difference in the penetration depth was more significant with the increase in the impact velocity. The results indicate that, with a lower depth of penetration, high toughness ZTA the material provides an better ballistic performance at high kinetic energy threats, which is consistent with the result found by Flinders et al. [8]. Unlike the Zhang and Li [11] work, Assis et al. [10] suggested that ZTA showed potential as an armour material, based on the study of their mechanical properties of a ZTA composite made with nanostructured YSZ. However, Assis did not undertake high strain rate tests to prove his consideration.

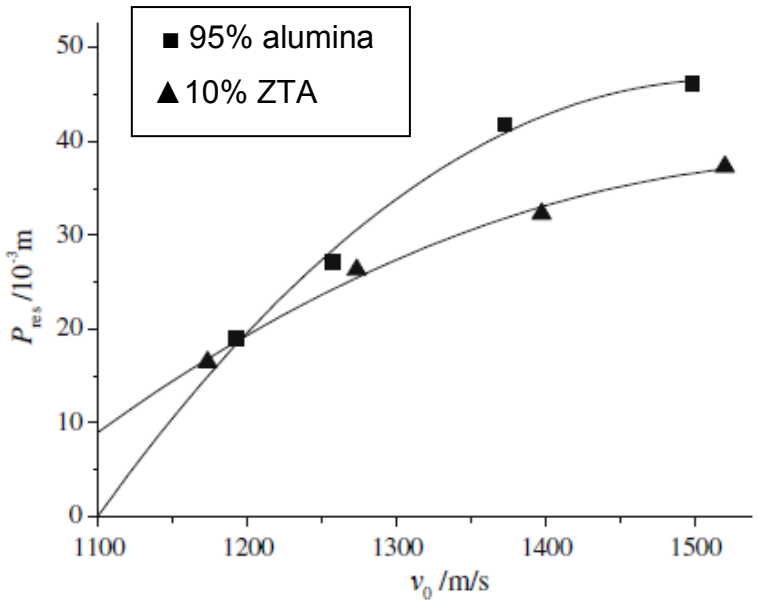

Figure 2.32 Residual penetration depth against impact velocity [11].

2.5 Processing of Nano or Fine Grain Sized Ceramics

The literature relevant to the processing of the nano or fine grain sized ceramics is reviewed in three separate sections with the regard to the three main challenges faced. In section 2.5.1, issues with regard to nanopowder and suspension preparation are introduced and compared. In section 2.5.2, studies focusing on the green forming routes are reviewed in detail. Last but not least, the sintering stage is discussed in section 2.5.3.

2.5.1 Nanopowder and nanosuspension preparation

The final grain size of the ceramic material can be significantly affected by the size of the particles used to form the green body. In this section, the synthesis of nanopowder, their agglomeration problems and nanosuspension preparation are discussed in sections 2.5.1.1 to 2.5.1.3. In addition, the problems relevant to the preparation of composite suspensions are reviewed in section 2.5.1.4.

2.5.1.1 Production of ultrafine powder

The production of ultrafine powders is the initial hurdle in the preparation of nanoceramics. The synthesis techniques include can be generally divided into chemical techniques and thermophysical methods [33].

The chemical techniques use direct chemical reactions to produce a product in powder form. By manipulating the reaction kinetics to encourage particle nucleation over particle growth, ultrafine particles can be created. The techniques, such as thermochemical synthesis, chemical precipitation and sol-gel processing, have been scaled-up for the commercial production of nanopowders, such as Y_2O_3 [33] and γ-Al_2O_3 [78].

In addition to the chemical methods, another synthesis technique is thermophysical method. The latter uses a large grained solid material as a matter source and then proceeds to apply thermal energy to reduce the solid to a powder form without a change in chemical composition. This synthesis category is dominated by the gas phase condensation technique, in which a solid is evaporated by Joule heating to form a supersaturated vapour, out of which small scale particles subsequently condense [33]. The gas phase condensation technique has been proved to be efficient in fabricating a number of ceramics, e.g. TiO_2 [79], ZnO [79], MgO [80] and ZrO_2 [81].

2.5.1.2 Agglomeration in nanocrystalline powders

Although the above methods have been used to produce dry nanopowders, the very large surface areas of the latter cause agglomeration [82]. A non-agglomerated powder will have one peak in the pore size distribution, whilst an agglomerated powder will have at least two peaks: one corresponding to the small intercrystallite pores and one corresponding to the larger interagllomerate pores, Figure 2.33. Pressureless sintering is very sensitive to the agglomeration of nanoparticles because of the driving force for surface energy reduction. Since the shrinkage rate inside agglomerates differs from that in between agglomerates, this leads to internal stresses, and appearance and the stabilisation of large pores or microcracks.

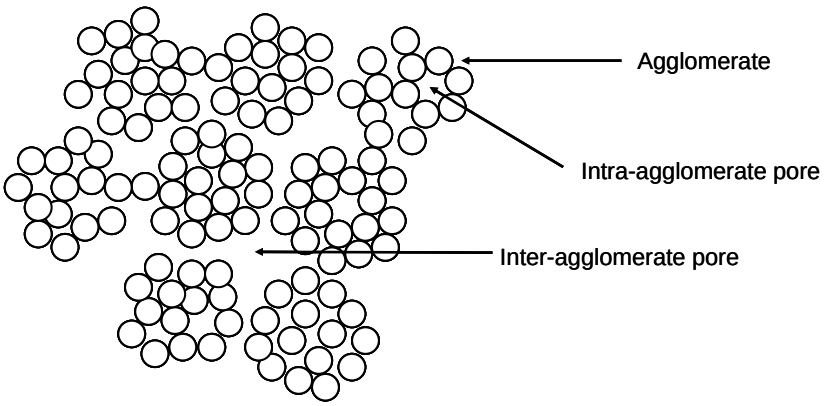

Figure 2.33 Schematic representation of agglomerates in powders [36].

2.5.1.3 Preparation of nano suspensions

The agglomeration problem can be overcome by dispersing the nanopowders into an aqueous or non aqueous suspension. Then, during green forming, the ceramic particle packing can be controlled by ability to avoid the formation of agglomeration through the use of surfactants. This leads to the ability to produce high quality green bodies with few defects [83].

The main difficulty during nanosuspension preparation is to homogeneously disperse the nano particles in the suspension. The dispersion characteristics of particles are greatly dominated by the total interparticle potential energy, V_{total}, which can be expressed as [82]:

$$V_{total} = V_{vdw}+V_{elect}+V_{steric}+V_{structural}$$

where V_{vdw} is the attractive potential energy due to long range van der Waals interactions between particles, V_{elect} is the repulsive potential energy resulting from electrostatic interactions between like charged particle surfaces, V_{steric} is the repulsive potential energy resulting from steric interactions between particle surfaces coated with adsorbed polymeric species and $V_{structural}$ is the potential energy resulting from the presence of non-adsorbed species in solution that may either increase or decrease suspension stability.

Surfactants (or dispersants) can be used to modify particle surfaces to prevent the interparticle attraction in the suspension. The particle surfaces can be modified by changing the surface charge (electrostatic repulsion), coating the particles with an organic barrier layer (steric hindrance), or the combination of the two [84]. According to Shubin and Linse [85], polyelectrolytes are an effective surfactant that can either change the surface charge or form an organic barrier layer. The plane of charge and the steric interaction length of a ceramic surface will change as a function of the pH and ionic strength.

In order to improve the dispersion of nano or submicron alumina suspensions, a polyelectrolyte, polyacrylic acid (PAA) is frequently used to increase the solid content of the suspension to 70-80 wt% [86–88]. Bowen et al [86] compared the effect of PAA on a nano γ-alumina suspension at two pH regimes (pH=6 and 10). They found that the PAA provided a “pancake” type adsorbed layer on the alumina particle surfaces at pH 6, whilst, at pH 10, a “brush” like conformation was shown on the surfaces, Figure 2.34. The authors found that the dominant mechanism of stabilization was the steric contribution according to atomic force microscopy, hence the PAA conformation at pH 10 was considered better. This suggests that both the surfactants and the pH are important to achieve a stable and homogeneous suspension with a high solid content. Other available surfactants include citric acid, polyphosphates and benzoic acid [89].

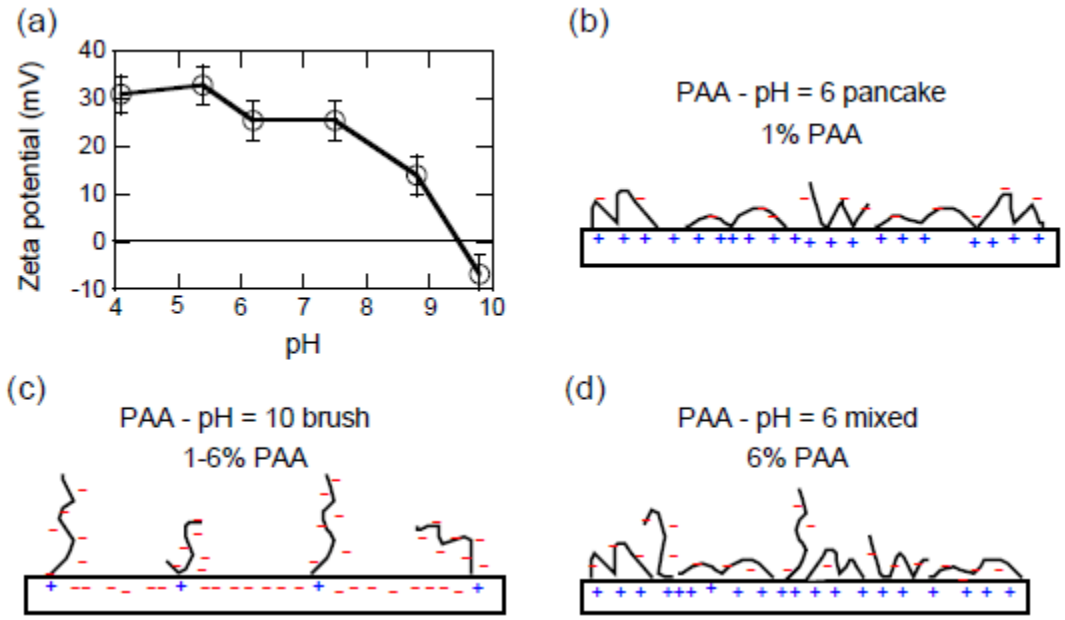

Figure 2.34 (a) Zeta potential as a function of pH for γ-Al_2O_3 before PAA addition; and schematic representations of PAA adsorption at (b) 1 wt% PAA, pH 6, (c) 1 - 6 wt% PAA, pH 10, (d) 6 wt% PAA, pH 6 [86].

The basis for the successful formation of homogeneous, fully dense, nanostructured green bodies has been shown to be the production of stable, homogeneous nanosuspensions with high solid contents and low viscosities[90]. According to a patent of Binner, et al. [91], homogeneous nanozirconia suspensions with solids contents up to 20 vol% (60 wt%) and viscosities as low as <0.05 Pa s were required. However, with an increase in the solid content, particle agglomeration becomes increasingly problematic due to the increasing interparticle forces [82]. Therefore, the surfactant triammonium citrate (TAC) was used as an anionic dispersant to further disperse the nanoparticles in the aqueous medium. Tetramethyl ammonium hydroxide (TMAH) was used to change the pH level from 2.4 of the as-received suspension to 11.5, which is the working pH for the TAC. Bursts of ultrasound were also used to ensure that any agglomerates that did form were broken up during processing [91].

2.5.1.4 Preparation of composite suspensions

Composites are made from two or more constituent materials with significantly different physical or chemical properties. The current limitations of ceramic armour materials are connected mainly with their brittleness. The most effective method for increasing toughness is the formation of a composite structure, such as the ZTA introduced in section 2.4. During the preparation of the ceramic composites, the first step is to form a mixed suspension with high homogeneity and stability. In order to learn whether two suspensions can be mixed together, their zeta-potentials need to be studied. Zeta-potential is the potential difference between the dispersion medium and the stationary layer of fluid attached to the dispersed particles. The isoelectric point (IEP) is the pH at which the value of the zeta potential is zero. Normally, stable deflocculated suspensions are observed at zeta potentials of greater than ±30 mV [92]. The more positive or negative the value is, the farther the particles are away from each other and the better dispersed the suspension is. In addition, only if two suspensions are stable in the same pH region, they are able to be effectively mixed together.

Before the preparation of ZTA suspension, the zeta-potential of zirconia and alumina suspension with or without PAA addition was studied by Zhang et al. [93], their result is shown in Figure 2.35. The two suspensions could be codispersed well at a pH below 5, where the zeta-potential was above 50 mV, and in the basic pH region. The mixed suspension with pH 2 to 3.5 was used by Aksay et al. [94] to make slip cast ZTA bodies, the sintered slip cast sample showed 1.6 times the strength displayed by samples prepared by pressing the ZTA powders due to the homogeneity of the particle distribution.

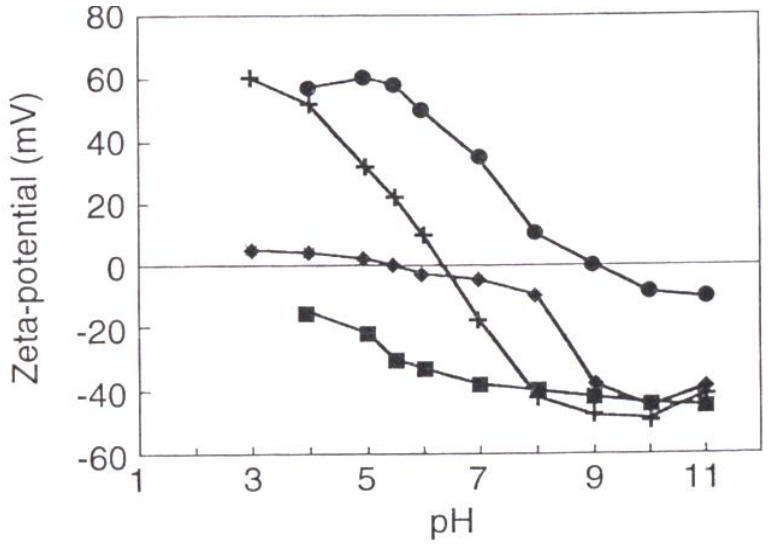

Figure 2.35 Zeta-potential of alumina and zirconia vs. pH: (●) zirconia in water, (+) alumina in water, (♦)alumina in PAA solution, (■) alumina in PAA solution [93].

2.5.2 Green forming

After the nanopowder or nanosuspension preparation, the next step is to form a cohesive body or powder compact, which is termed a 'green body' [17]. Green forming based on the use of dry powders is called dry forming, whilst the forming process using suspension as the precursor is called wet forming. There is another 'plastic forming' method, but that will not be discussed here. Some common methods are shown in Table 2.4 [40]; their main features are also listed.

Table 2.4 Feed materials and features of common ceramic forming methods [40]

Forming method		Feed material	Features
Dry forming	Die pressing	Ceramic powder with low binder content	Simple shape, mass production, low cost
Wet forming	Slip casting	Slurry with low binder content	Intricate shape, mechanization available
	Gel casting	Slurry with binders which are polymerized during solidification	Intricate shape, good powder dispersion, uniform density
Plastic deformation	Extrusion	Moist mixture of powder and binder solution	Elongate shape, mass production,
	Injection molding	Granulated mixture of powder and solid binder	Small intricate shape, dimensional accuracy

2.5.2.1 Dry forming

Dry forming (or dry pressing) is accomplished by placing the powder into a die and applying pressure to achieve compaction. Two categories of pressing are commonly used: uniaxial and isostatic.

Uniaxial pressing, or die pressing, is the most widely used pressing method. It includes compacting a powder into a rigid die by applying pressure along a single axial direction through a rigid punch [17]. Die pressing is widely used in industry because it has a very high production rate and is easy to automate. The problem of die pressing is the density variation. During pressing, the uniaxial pressure will be dissipated by the friction between the powder particles and between the powder and the die wall. Therefore, the powder on the edge will experience a much lower pressure, which results in a non-uniform density distribution. The density variation in the green compact will cause warpage, distortion or cracking during sintering.

Isostatic pressing or cold isostatic pressing (CIP) applies pressures uniformly from all directions to achieve a greater uniformity of compaction and an increased shape capability. It overcomes many of the limitations of uniaxial pressing. During pressing the power is sealed in a flexible water-tight die (usually rubber), the die is immersed in a liquid which is contained by a high-pressure chamber. When the pressure of the liquid is increased by a hydraulic pumping, the walls of the die deform and transmit the pressure uniformly to the powder, resulting in compaction. However, comparing to the uniaxial die pressing, the problems of CIP include the high cost and low production rate [17,40,47].

As a result of their small size, the problems of pressing nanopowders are much more severe. As is mentioned in section 2.5.1.2, nanoparticles agglomerate very readily due to their high interparticle forces. The agglomerates produce an inhomogeneous particle packing structure within the green body and hence achieve a poor green density. In addition to agglomeration, nanoparticles have a very large number of particle-particle point contacts per unit volume compared with a submicron powder. Each of these point contacts represents a source of frictional resistance to the

compaction of the powder and thus the total frictional resistance to compaction can be very much greater.

In order to solve these problems, firstly, the die pressing pressures used to consolidate nanopowders need to be extremely large, typically 1-9 GPa [95]. To avoid this severe limitation, the granulation of the nanopowders needs to be controlled to form granules with high crushability and flowability. This can be achieved by using methods such as spray drying, freeze drying and spray freeze drying.

Spray drying

Spray drying is the most widely used drying route to produce uniform, free-flowing powders [17]. A spray dryer consists of a conical chamber that has an inlet for hot air. The suspension is fed into the spray dryer through an atomizer and the suspension droplets are dried into roughly spherical granules by the hot air in the chamber. The spherical shape results in a good flowability of the powder. On the other hand, for nanopowders, the hot air usually results in the creation of very hard granules with low crushability. As is shown in Figure 2.36 [90], the residual agglomerates can be clearly seen in the die pressed barium titanate green body. The large agglomerates in the green body will result in abnormal grain growth, which is detrimental to the final properties.

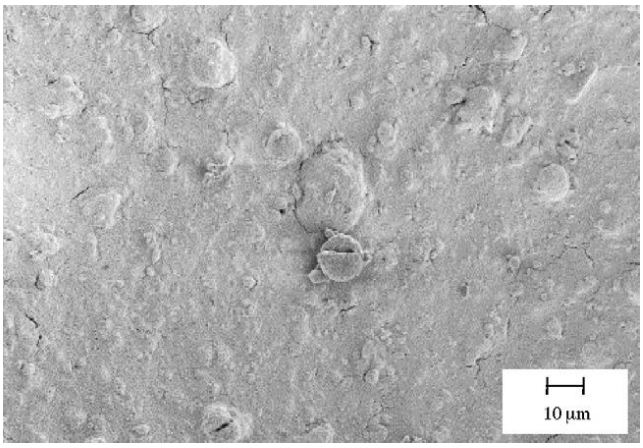

Figure 2.36 Die pressed barium titanate green body formed from a commercial spray dried nanopowder showing residual agglomerates [90].

Freeze drying

One of several alternative approaches is freeze drying, in which the suspension is sprayed into a medium such as a chilled hexane bath, which rapidly freezes the droplets into ice crystals [40]. The water is removed by sublimation during the increase of the temperature or the reduction of the pressure [96]. Due to the sublimation of water from the ice crystals, the granules obtained from freeze drying have a loose, porous structure, so these granules are relatively weak and can be easily crushed when pressed. However, the shapes of these granules are angular, so that the flowability is poor (Figure 2.37 (B) [97]).

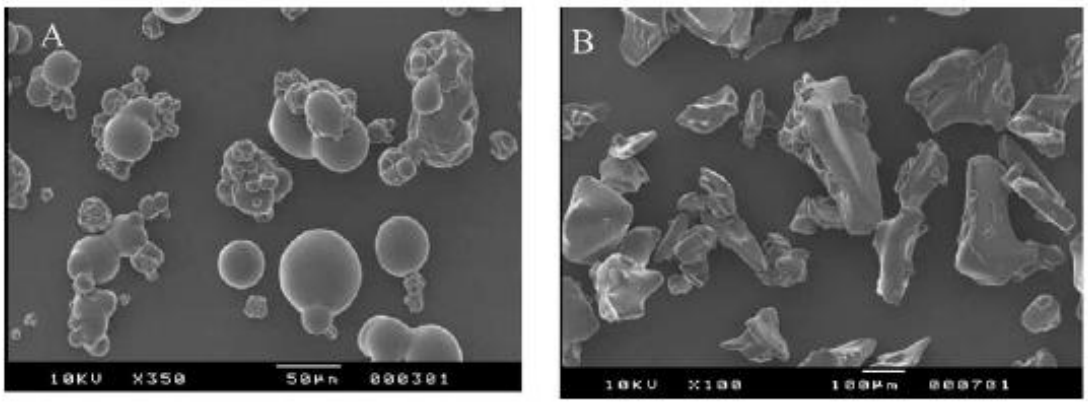

Figure 2.37 Scanning microscopic observation of powders obtained by (A) spray drying and (B) freeze-drying [97].

Spray freeze drying

Spray freeze drying is a new method that combines the benefits of spray drying and freeze drying [90]. The nanosuspensions are sprayed into liquid nitrogen and then the frozen water is sublimed off by heating at low pressure. This produces granules with high flowability, due to their spherical shape, and high crushability, due to the porous structure after water sublimation. It was observed [94,98] that the flowability of the granules increased with an increase in solid content of the suspension, whilst the crushability decreased simultaneously. In order to improve the crushability of the granules and also retain the flowability, a foaming agent, 1 wt% Freon, was added into the high solid content suspension before spray freeze drying [98]. According to Figure 2.38 [98], the size and shape of the yttria stabilised zirconia (YSZ) granules

with the Freon addition is similar to the one without the Freon, and hence the flowability is similar, whilst more voids were observed on the granule surface when the Freon was used. This had the direct effect of weakening the powder granules and, hence, allowing them to be crushed at lower pressures. The fracture surfaces of the two YSZ green bodies were compared in Figure 2.39 [94], and the more uniform fracture surface of the sample (b) is due to the improved crushability.

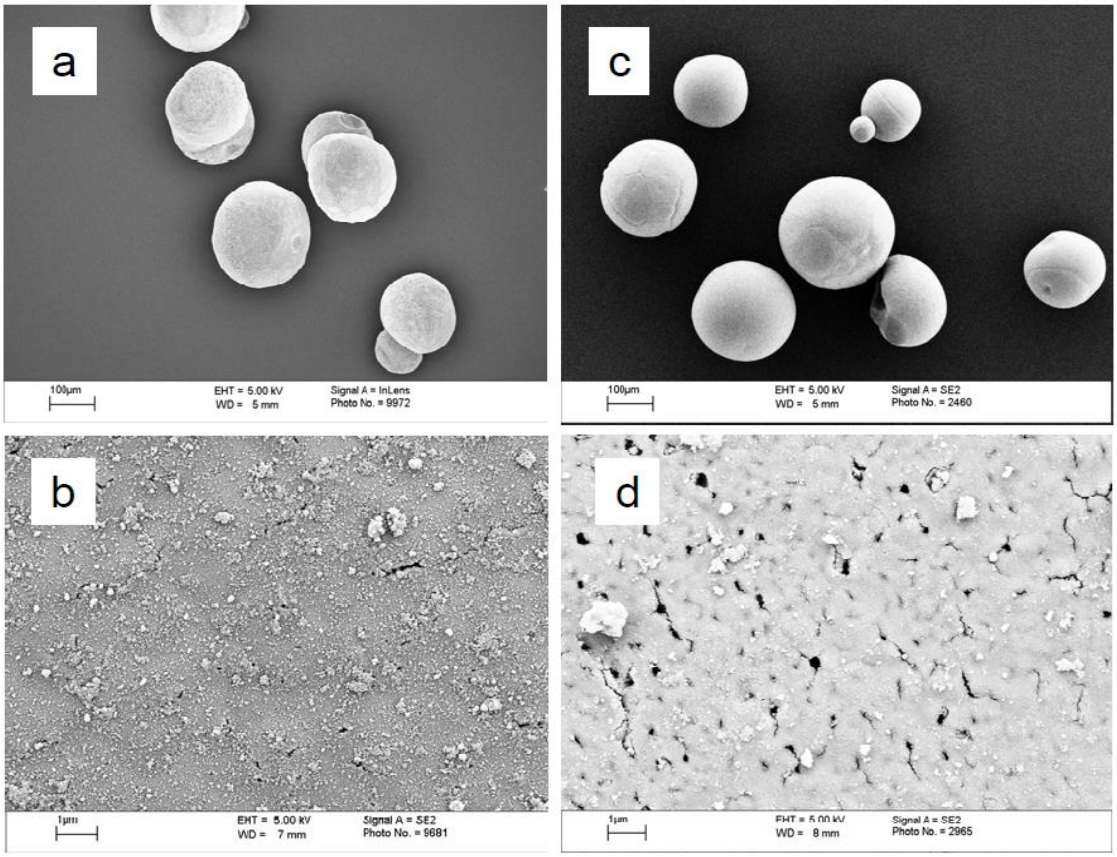

Figure 2.38 Spray freeze dried granules produced from 20 vol% solid content 3-YSZ nanosuspension, a) and b) without Freon, c) and d) with 1 wt% Freon [98].

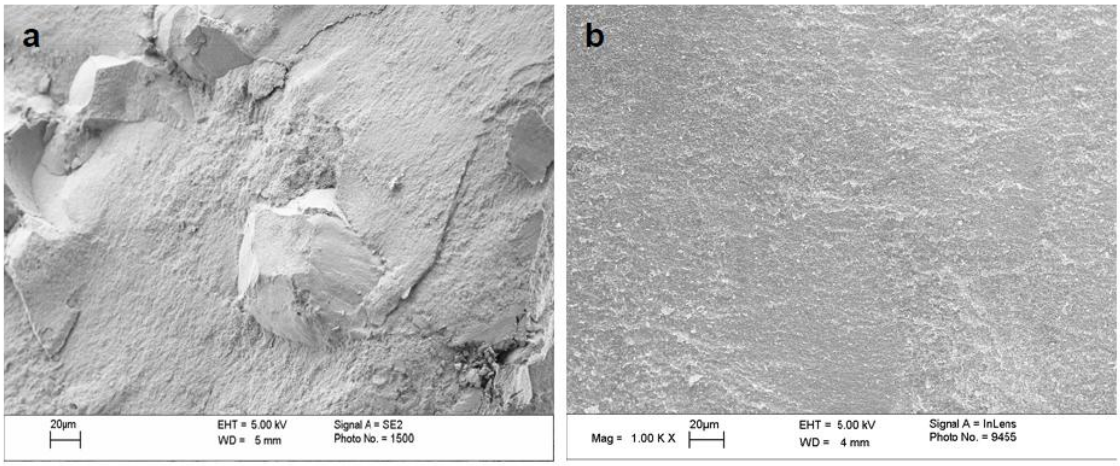

Figure 2.39 FEGSEM images of fractured surfaces of compacts pressed from sieved 3-YSZ spray freeze dried powders, (a) without Freon and pressed at 380 MPa and b) with 1 vol% Freon and pressed at 250 MPa [90].

2.5.2.2 Wet forming

Although dry forming is more widely used in industries, wet forming has the benefits of producing ceramic products with complex shape, high homogeneity, high density and high reliability. There are a large number of techniques available to prepare ceramic green bodies from a colloidal suspension, as shown in Table 2.4. Out of all these methods, slip casting is the most popular route. In slip casting, a slip (or suspension) is poured into a porous mould. Then the mould absorbs the liquid from the slip by a capillary suction process and the particles that consolidate on the surface of the mould form a cast [99]. Two factors mainly affect the properties of the slip cast body, which are the rheology of the slip (or suspension) and the drying conditions after slip casting.

During the wet forming of nano sized green bodies, there is a major problem of cracking during drying and organic burn out of the bodies as a result of the high solid content of the nanosuspension. According to the study of Binner and Vaidhyanathan [91], humidity drying results in a higher green density of the slip cast samples and the lower drying rate can prevent the formation of cracks in the green bodies during shrinkage. With conventional drying, the maximum solid content at which bodies could be dried and burnt out without any visible cracking was 14 vol%, whilst a humidity drying method effectively increased the maximum solid content from 14 vol%

to 20 vol%. They also noted that the optimum conditions were 80% relative humidity at 25°C, and the resultant higher solids content green body showed not only a higher density, but also a finer pore structure.

2.5.3 Sintering

Sintering is the process in which a heat treatment is used to covert a green body into a rigid, polycrystalline solid, which is usually very dense. For a nanoceramic powder system, the high surface area leads to a high total surface energy. Since the main driving force for sintering is surface energy reduction [92], higher surface energy means higher driving force and allows sintering processes to occur at lower temperatures. However, the high surface free energy brings a high driving force for grain growth during the sintering process, resulting in difficulties in retaining a nanostructure. It is necessary to find methods to control the grain growth during sintering. Table 2.5 [4] summarises some of the commonly used sintering method to process ceramic armour. The advantages and disadvantages are listed as well.

Table 2.5 Sintering processes for ceramic armour materials [4]

Process		Advantages	Disadvantages
Hot pressing		Lower temperature, lowest porosity	Shape limitation High cost
Pressureless sintering	***Solid state sintering***	No grain boundary phase, low porosity	Higher temperature, grain coarsening
	Liquid phase sintering	Lower temperature, fine grains, low porosity	Glass phase on grain boundaries
Reaction bonding		Low temperature, excellent complex shape capability	Residuals in the body (eg. silicon when sintering SiC)

2.5.3.1 Methods to control grain growth

There are four approaches that have been used to control the grain growth and to improve densification [90]: 1) the addition of solutes or glass phase, 2) very rapid

firing (e.g. microwave sintering), 3) pressure-assisted techniques (e.g. hot pressing) and 4) two-stage sintering. The type 1) approach is not suitable for armour material processing since the solute or glass phase significantly harm the desired properties of the final products, hence will not be discussed in detail.

For the type 2) approach, the reduction of grain growth time can result in an effective control of the grain size. Microwave sintering is a method to provide faster processing time and lower sintering temperatures than for conventional sintering [100]. According to the study of Brosnan et al. [100], a fast heating rate of 45-60˚C/min was achieved using microwave sintering of MgO-doped alumina. In addition, 95% density was reached at 1350˚C using microwave heating whilst the same density can only be achieved at 1600˚C using conventional heating. However, the rapid sintering requires extremely homogeneous green compacts and physically small components to avoid different densification rates at different locations and excessive thermal gradients [90].

By using hot pressing (type 3), samples can be sintered at much lower temperature under high pressure in order to prevent grain growth at high temperatures. Liao et al. [43] sintered nano α-alumina with grain size <50 nm and density >98% from a nano γ-alumina green body. During sintering the γ to α transformation temperature decreased from 1075˚C at ambient pressure to about 460˚C at 8 GPa. Grain growth was limited by the low sintering temperature and a multiplicity of nucleation events in the parent γ phase at high pressure created a nanoscale α grain size. The hot pressing method effectively solved the problem of exaggerated grain growth of γ-alumina during transformation. However, it brought the major disadvantage of higher processing costs and limited component shape capability.

Type 4), two-stage sintering, is another effective method to control the grain growth of alumina [86,101]. Two-stage sintering was introduced as a method by Chen and Wang [102] for the sintering of nanostructured yttria (Y_2O_3) ceramics. The key elements in this process are a) heating the green bodies to a high initial temperature, T_1,for a very short time to conduct the first-step sintering, b) achieving a high density at T_1 (>75%) to render pores unstable and c) quickly lowering the temperature to a lower temperature, T_2,to conduct the second-stage of sintering, during which there

was only densification and no grain growth according to the authors (Figure 2.40 (a) [102]). The resultant products were observed to have full density with a mean grain size of lower than 100 nm. The suppression of grain growth, but not densification, was considered to be achieved by the suppression of grain boundary migration whilst keeping grain-boundary diffusion active [102,103]. According to the kinetic study of this sintering method[103], there was a kinetic window for the second stage of sintering (Figure 2.40 (b) [103]). For each grain size, products with full density and no grain growth could only be obtained at the second-stage sintering temperatures, which were within the kinetic window.

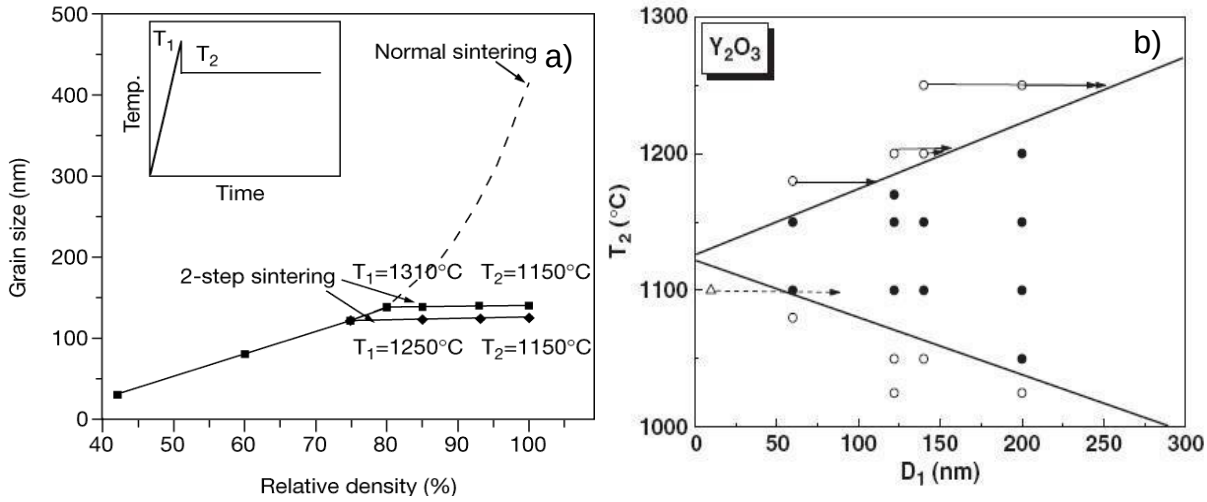

Figure 2.40 (a) Grain size of Y_2O_3 in two-stage sintering (Heating schedule shown in inset). Note that the grain size remained approx. constant in the second sintering step [102]. (b) Kinetic window for the second stage sintering of Y_2O_3. Solid symbols when full density was attained without grain growth; data above the upper boundary had grain growth. Data below the lower boundary did not fully densify. The triangle represents a one-step sintering experiment at the temperature shown [103].

As reported by some other authors [104], two-stage sintering has been proved to be effective in reducing grain growth during densification, although not all the final ceramics retain a nanostructure, which is probably due to the vary agglomerated nature of some of the precursor nanopowders used. According to a recent study of Binner et al. [34], the application of two-stage sintering successfully controlled the grain size of 3YSZ products to less than 100 nm. However, grain growth still occurred at densities above about 97%, although with a much lower grain growth

rate, which suggested that the two-stage sintering reduced the grain growth but could not fully restrain it.

2.5.3.2 Sintering of ZTA

Regarding to the sintering of ZTA, the zirconia inclusions in the ZTA have been found to suppress the grain growth of the alumina matrix [105,106]. Lange et al. [107] found that, with the zirconia content above 5 vol%, a majority (or all) of the 4-point grain junctions are occupied by the zirconia inclusions. The latter exhibits sufficient self-diffusion to move with the alumina 4-grain junctions during grain growth and, therefore, exerts a dragging force at the junction points to limit the grain growth. On the other hand, when the zirconia content is below ~2.5 vol%, the zirconia inclusions located in the junction points were not sufficient and abnormal grain growth occurred.

In addition to the effect of the grain growth inhibition, the zirconia addition in the ZTA also affects the sintering temperatures. According to the study of Bodisova et al. [108], in the two-stage sintering of pure alumina, the optimal temperatures are T_1, 1400-1500˚C, and T_2, 1150˚C. In comparison, the two-stage sintering temperature for ZTA, as found by Wang et al. [106] is about 1400-1450˚C (T_1) and 1350-1400˚C (T_2). The relatively higher T_2 is considered to be caused by the effect of the zirconia, which increased the activation energy of the densification of alumina. Wang and Raj [109] reported that the activation energy of ZTA with zirconia content from 5-95 vol% remains in the range of 700±100 kJ/mol, whilst the activation energy of pure alumina is 440±45 kJ/mol. The increase of the activation energy increases the energy required to activate grain boundary diffusion, therefore a higher temperature needs to be used during the second stage of the ZTA sintering process

3 EXPERIMENTAL

3.1 Materials

Zirconia nanosuspensions containing different amounts of yttria, viz. 1.5 and 3 mol%, were provided by MEL Chemicals, Manchester, UK. A very fine submicron alumina suspension was supplied by Baikowski, Annecy, France. Some properties of the as-received suspensions are listed in Table 3.1. These suspensions were used to prepare the 1.5YSZ, alumina and ZTA suspensions. A zirconia suspension without yttria stabiliser (MEL Chemicals, Manchester, UK) was also used to produce some 0Y-ZAC (zirconia alumina composite without yttria stabiliser) samples for residual stress analysis. A commercially available alumina zirconia composite armour material, which contained 10 wt% submicron sized 3YSZ in the alumina matrix, was supplied by Morgan Technical Ceramics, UK, for comparison with the nano ZTA samples prepared in this project.

Table 3.1 The properties of the as-received nanosuspensions

Name	Yttria content / mol%	Solid content / wt%	pH	Particle size (D50) / nm
Nano 0YSZ	0			
Nano 1.5YSZ	1.5	26.5	2.50	13
Nano 3YSZ	3	22.6	2.51	14
Alumina	/	58.8	3.52	160

Tri-ammonium citrate (TAC) (Fisher Scientific UK Ltd., Loughborough, UK) was used as a surfactant to improve the dispersion of the nano zirconia suspensions and tetramethyl ammonium hydroxide (TMAH) (Aldrich Chemicals Ltd., Dorset, UK) was used to adjust the pH of the suspension. Other chemicals, such as HCl and NaOH used to modify the pH for the zeta potential measurements and acetone and ethyl alcohol used for washing purposes, were also obtained from Fisher Scientific.

3.2 Summary of Samples to be Tested and Characterised

In this project, three related studies were undertaken, viz: the effect of processing conditions on the microstructure of the materials; the effect of the materials microstructures and the effect of zirconia phase transformation on the mechanical properties of the samples; and the effect of zirconia phase transformation on the high strain rate performance of the materials. Four materials formed the primary focus, alumina and three ZTAs. The ZTA samples were produced by adding 10, 15 and 20 wt% nano 1.5YSZ into the alumina matrix and were shorted as10, 15 and 20% nano 1.5Y-ZTA. Three further materials were used for comparison purposes, 10% nano 3Y-ZTA (10 wt% nano 3YSZ in ZTA), nano 1.5YSZ and a Morgan alumina-zirconia composite (referred to as Morgan composite) with 98% density, 1.9±0.3 μm alumina grain and 400±100 nm zirconia grain size. In order to reduce the number of samples to be tested and characterised, not all the samples were used in every part of the overall project. Table 3.2 summaries the work done.

Table 3.2 Summary of samples to be tested and characterised

		Mechanical properties				High strain rate testing		Post testing characterisation (Optical, SEM, Raman and TEM)					
	Sintering condition vs. grain sizes.	HV1	K_{IC} (Vickers)	σ_f (4-PB)	Wear resistance	SHPB	Gas gun impact test	Vickers indent	Fracture surface	Worn surface	SHPB fragments	SHPB survived samples	Impact tested samples
Alumina	×	×	×	×	×	×	×	×	×	×	×		×
10% nano 3Y-ZTA	×	×	×										
Morgan composite		×	×	×									
10% nano 1.5Y-ZTA	×	×	×	×	×	×	×	×	×	×	×		×
15% nano 1.5Y-ZTA	×	×	×	×	×	×	×	×	×	×	×	×	×
20% nano 1.5Y-ZTA	×	×	×	×	×	×		×	×	×	×		
Nano 1.5YSZ	×	×	×				×						×

×: Done Not done × Done, but not discussed in detail in this thesis.

The sintering profiles of the alumina and 1.5Y-ZTA samples were initially investigated; various sintering conditions were used to manufacture samples with different grain sizes whilst ensuring full density. For the mechanical properties measurements, Vickers hardness and Vickers indentation toughness measurements were made on all the samples with different grain sizes in order to investigate the effect of microstructures on the mechanical properties of the materials 4-point bending tests and wear resistance tests were also performed on the selected samples. Based on the results of the mechanical properties of the samples, high strain rate testing, including SHPB tests and gas gun impact tests, was then carried out.

Several post test characterisation techniques were used in this project, including optical microscopy and field emission gun scanning electron microscopy (FEGSEM) for surface and microstructural observation respectively; Raman analysis for a quantitative analysis of zirconia phase transformation and Cr^{3+} fluorescence spectroscopy for residual stress study.

Since nano 1.5YSZ has been extensively studied by other researchers in Advanced Ceramics Group, Loughborough, only its high strain rate performance will be discussed in this thesis.

3.3 Sample Processing

Figures 3.1 shows the processing and characterisation procedures of the alumina and ZTA with different zirconia contents (10 to 20 wt%). The processing route start from the suspension preparation. As received, aqueous YSZ suspension containing 1.5 or 3 mol% yttria was mixed with the as-received alumina suspension with 58.8% solid content to form suspensions containing 0, 10, 15 and 20 wt% YSZ in the final materials, followed by concentrating to about 57-60 wt% solid contents. Details of the suspension preparation process are introduced in section 3.3.1.Then the suspension was dry formed to yield green bodies. Finally, the green bodies were sintered to obtain sintered bodies with full densities and a range of grain sizes by changing the sintering conditions. The green forming and sintering processes are introduced in detail in sections 3.3.2 and 3.3.3. The microstructures of the green bodies and

sintered samples were observed using a FEGSEM. In addition, their mechanical properties, including Vickers hardness, indentation toughness, 4-point bend strength and wear resistance, were measured; the experimental details are provided in section 3.4. The high strain rate performance of the samples was investigated and the samples were extensively studied after testing; the testing process and characterisation methods were discussed in section 3.5.

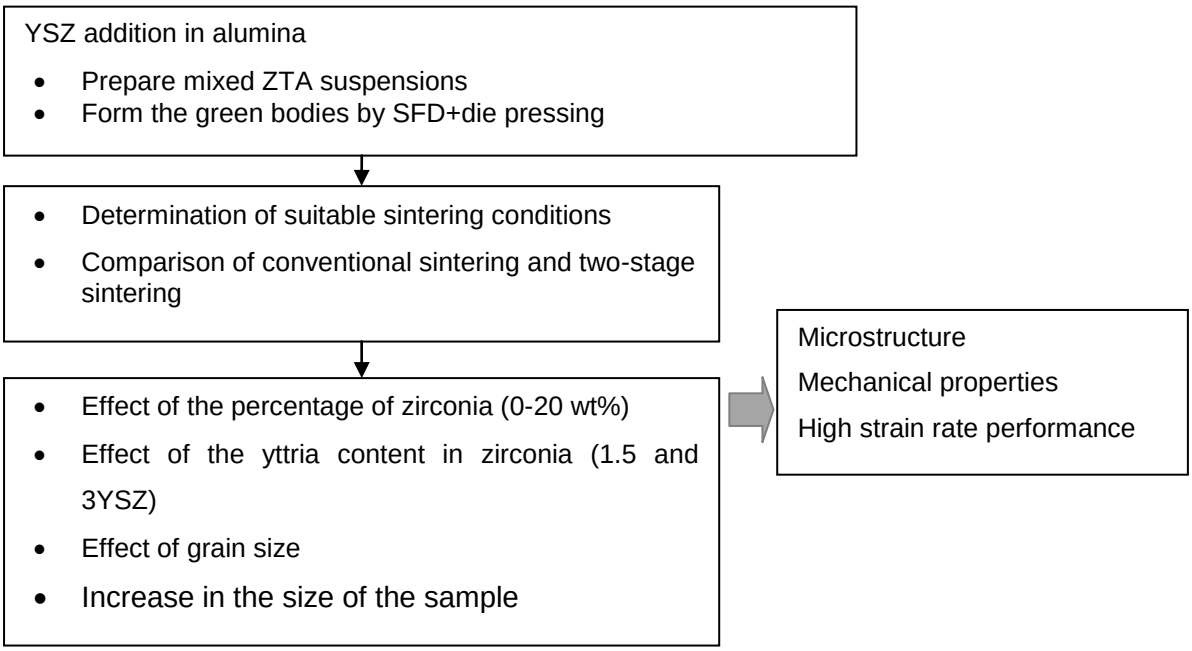

Figure 3.1 The processing and characterisation of alumina and ZTA.

3.3.1 Suspension concentration

In order to achieve a fine grain sized ceramic product after sintering, the green density needed to be above 54% theoretical [110], so that the amount of grain growth could be better controlled during densification. Achieving green bodies with a high green density in turn required use of suspensions with > 57 wt% solid content was required. However, if the solid content was too high, the viscosity of the suspension was affected, leading to dense powder granules with poor crushability after spray freeze drying or an inhomogeneous microstructure in green bodies. As a result, for all the suspensions, the solid content was kept between 57 to 60 wt% whilst the viscosity was maintained below 100 mPa s at 100 s^{-1} shear rate [91].

3.3.1.1 Alumina suspension

Since the solid content of the as-received alumina suspension was 58.8 wt% (Table 3.1), which was in the range of 57 to 60wt% solid content, in addition the viscosity of the as-received suspension was measured to be 15 mPa at 100 s^{-1} shear rate, the alumina suspension was directly used without concentration or dispersant addition. In addition, according to a TGA analysis, ~2% organic binders were contained in the suspension.

3.3.1.2 ZTA suspension

The approach for ZTA suspension preparation is shown in Figure 3.2. Firstly, a given amount of the as-received YSZ suspension was added into the as-received alumina suspension in order to achieve the required YSZ content in the final material. Three YSZ contents were used, viz. 10, 15 and 20 wt%. Taking the ZTA suspension with 10 wt% 1.5YSZ addition (10% 1.5Y-ZTA) as an example, the amount of 1.5YSZ suspension added was calculated as follow:

$$\rho_{1.5YSZ} = 6.1\ g/cm^3,\ \ \rho_{Al_2O_3} = 3.99\ g/cm^3$$

Solid content of alumina suspension = 58.8%

Solid content of 1.5YSZ suspension = 26.5%

$$m_{1.5YSZsusp.} = \frac{m_{Al_2O_3susp.} \times 58.8\%}{90\%} \times 10\% \div 26.5\%$$

Thus, $m_{1.5YSZsusp.}$ g of 1.5YSZ suspension was blended with $m_{Al_2O_3susp.}$ g of alumina suspension to yield ($m_{1.5YSZsusp.}$+$m_{Al_2O_3susp.}$) g of 10% 1.5Y-ZTA suspension.

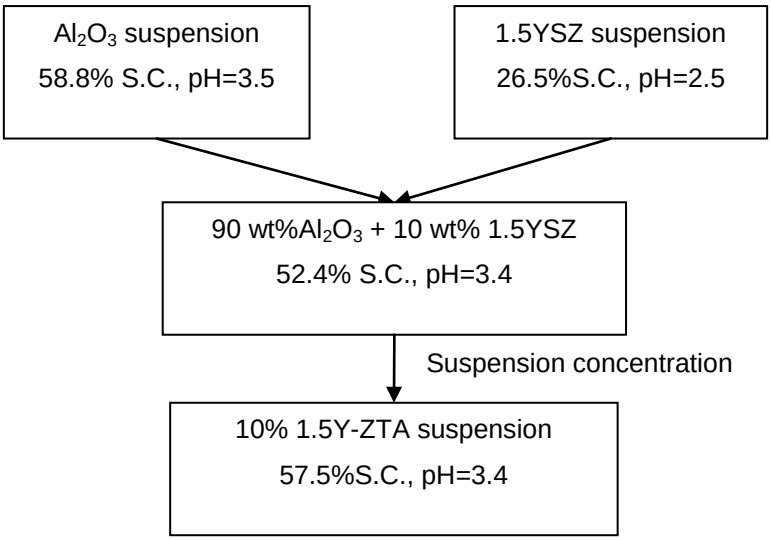

Figure 3.2 Suspension preparation route.

The suspension was stirred and concentrated to above 57 wt% without adding dispersants. The final volume of the suspension with 57 wt% was calculated as shown below in ordered to determine the time needed for the concentration process.

$$\rho_{water} = 1\ g/cm^3\ ,\ \rho_{10\%\ 1.5Y-ZTA} = 4.13\ g/cm^3$$

$$m_{10\%\ 1.5Y-ZTA} = a \times 57\%\ g$$

$$m_{water} = a \times 43\%\ g$$

$$V = \frac{m_{10\%\ 1.5Y-ZTA}}{\rho_{10\%\ 1.5Y-ZTA}} + \frac{m_{water}}{\rho_{water}}$$

where *a* is the weight of the 10%1.5Y-ZTA suspension. Thus, the volume of the 10% 1.5Y-ZTA suspension needed to be achieved after concentration is V.

To achieve concentration, the mixed suspension was heated to 60°C in a water bath under continuous stirring and the suspension was subjected to ultrasound treatment at 30 minute intervals using a Soniprep 150 ultrasonicator (MSE Scientific Instruments, Manchester, UK) to break the agglomerates that formed and hence to control the viscosity of the suspensions. No dispersant was added due to the very low viscosity of the concentrated suspension. After concentration, the solid content of the suspension was measured using the method introduced in section 3.3.1.4.

The viscosity of the suspension was measured using rheometer (Anton Paar GmbH, Österreich, Austria) before green forming and the homogeneity of alumina and

zirconia mixing was confirmed by observing the microstructure of the green bodies and sintered bodies using the FEGSEM.

3.3.1.3 Nano 1.5YSZ suspension

The concentration of the 1.5YSZ suspension followed the patented method of Binner et al. [91]. Firstly, the pH of the as-received suspensions was modified from the initial value of 2.5 (as shown in Table 3.1) to 11.5 via the addition of TMAH. Then 3 wt% TAC was added as a dispersant, which slightly decreased the pH to about 10.5. The suspension with these additives was then heated to 60°C in a water bath under continuous stirring; the suspension was also ultrosonicated regularly until it reached the required solid content.

3.3.1.4 Solid content measurement

Before and after the suspension concentration process, the exact solid contents of the as-received suspension and concentrated suspension were measured. The process involved heating about one gram of the suspension to 700°C at a rate of 10°C/min and holding for 2 hours. After cooling to room temperature, the dried sample was taken out and weighed. The exact solid content was calculated from:

$$\textit{Solid content} = \frac{m_{dried}}{m_{suspension}} \times 100\%$$

where $m_{suspension}$ is the weight of the suspension before drying (g), and m_{dried} is the weight of the sample after drying (g).

3.3.1.5 Viscosity measurement

The viscosities of the pure alumina and ZTA suspensions with different processing routes were measured using a viscometer (Anton Paar GmbH, Österreich, Austria). Before all testing, a 30 second ultrasound treatment was applied to the suspension. Due to a slight heating effect during ultrasonication, the suspension was cooled for 2 min prior to the viscosity measurement. The viscosities were recorded in a sweep cycle of continuous increasing and then decreasing shear rate ranging from 10 s^{-1} to 1000 s^{-1}. All the measurements were done at room temperature.

3.3.1.6 Zeta potential measurement

The electrokinetic behaviour of the suspensions was characterised using an AcoustoSizer II (Colloidal Dynamics, Sydney, Australia). The zeta potential curve of the suspensions was automatically measured over a wide range of pH from 2 to 12. 1 mol/l HCl and NaOH solutions were used to decrease and increase the pH respectively. An equilibration time of 100 seconds was used to ensure that the pH modifier was mixed homogeneously within the system before each zeta potential data was recorded. 5 wt% solid content suspensions were used for the measurements.

3.3.2 Green body preparation

A dry forming route was used for the green forming of the prepared samples. The concentrated suspensions were firstly spray freeze dried into spherical, porous granules and then the latter were die pressed into samples with the desired shape and size. Isostatic pressing was performed on the die pressed samples in order to achieve densities > 54 wt% of theoretical and a more homogeneous density distribution.

In addition, before spray freeze drying each suspension, 2 vol% Freon as a foaming agent was added, followed by 2 hours stirring at room temperature. The resulting powders and pressed green bodies with and without Freon were compared on their microstructures using FEGSEM.

The process of spray freeze drying consists of two stages: spray freezing and freeze drying. In the first stage, a beaker half-filled with liquid nitrogen was placed under the ultrasonic rod of an ultrasonicator (Soniprep 150, MSE Scientific Instruments, Manchester, UK). The suspension was dropped onto the ultrasonic rod using a pipette, so that very fine droplets were formed, which fell into the liquid nitrogen and froze. After most of the liquid nitrogen had evaporated, the beaker with the frozen droplets was connected to a freeze dryer (Virtis®, Benchtop SLC, New York, USA) which was itself connected to a double stage oil-sealed rotary vane vacuum pump (Leybold® D2.5B, LeyboldVacuum GmbH, Oberkochen, Germany) with an exhaust

filter. The frozen droplets were freeze dried at -50˚C under a vacuum of <100 mTorr, the process taking about 2 days. The resulting granules were sieved to achieve a fraction of 125 to 250 μm [98].

These powders were then used for die pressing. Three green sample sizes were needed for the different measurements; 10 mm Ø pellets, 40 mm Ø discs and rectangular tiles measuring 40×15×3-7 mm^3. The 10 mm small pellets were mainly used to investigate the sintering profiles and the effect of sintering condition on the microstructure. To make them, about 0.6 g of powder was slowly poured into a single-action, hardened steel die with a diameter of 10.6 mm. The die punch was unixially driven using a mechanical testing machine (L10000 Tensometer, Lloyds Instruments, Fareham, UK) to achieve a ram speed of 1 mm min^{-1} and the sample held at a consolidation pressure of 360 MPa for 1 min. Each pellet was then slowly ejected from the die. For the 40 mm Ø disc samples, which were used for gas gun impact testing, ~16 g powder was used to make a green body of 5 mm thickness. Due to the large surface and the limitation of loading, the samples were die pressed at about 65 MPa. The rectangular tile shape samples were pressed using a rectangular die sized 40×15 mm^2 and 120 MPa applied; the thickness of the tile samples could be varied from 3 to 6 mm by adjusting the amount of powder used (3.5 to 7 g). Tiles with 3 mm thickness used for bend test bars or wear testing, whilst the 7 mm thick tiles (5 mm thick after sintering and polishing) were cut to split Hopkinson pressure bar test samples, which had a size of about 3×3×5 or 4×4×5 mm^3. The green densities for the small pellets, large discs and tiles were approximately 52, 40 and 42% of theoretical, respectively, after die pressing.

In order to prevent the powder sticking to the die surfaces, a reusable hydrophobic Teflon sheet (Teflon cooking mat, Dupont, US) was used, the sheets being cut into the shape of the die and attached to the punch surfaces, as shown in Figure 3.3. These Teflon sheets effectively prevented the sticking of the powders on the punch surfaces and any contamination from the used of traditional lubricants.

Figure 3.3 Teflon sheets attached on the Ø 40 mm die surfaces to prevent the powder sticking.

Since the green densities achieved after die pressing were relatively low, a further isostatic pressing stage was used for large disc and tile samples. Each sample was placed in a clean latex bag and the air was extracted to form a low vacuum before sealing. It was then immersed in the pressure chamber of an isostatic press and 250 MPa applied. After 1 min, the pressure was released and the tiles were taken out for further processing. Finally, green densities about 52-55% were achieved for all the green bodies. Figure 3.4 shows a green tile before and after the isostatic pressing stage.

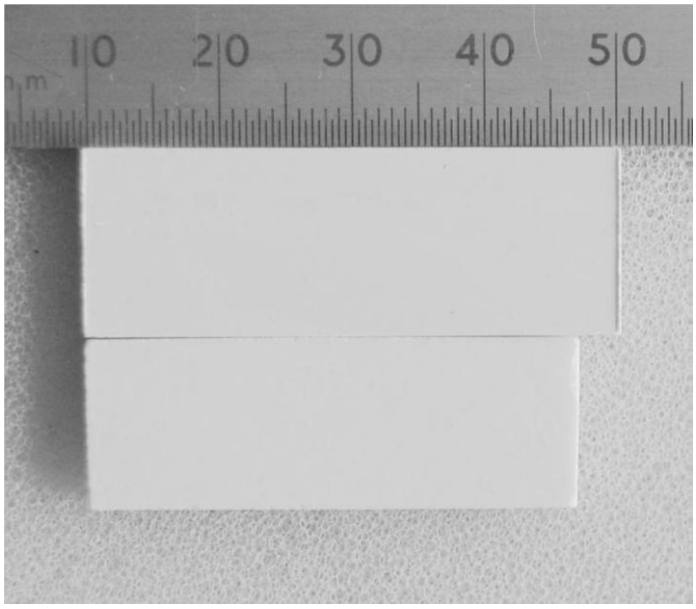

Figure 3.4 Tiles before and after isostatic pressing.

As a result of the presence of organics in the as-received and concentrated suspensions (2 wt% in alumina suspension and 2 wt% in YSZ suspension), binder removal was required prior to sintering. The samples were heated at a rate of 0.5°C min^{-1}, held at 100°C, 200°C, 300°C and 400°C for 30 min each and finally held at 700°C for 2 h. The samples were then cooled down to room temperature using a cooling rate of 0.5°C min^{-1}. After binder removal, the samples were visually inspected for any defects/cracks. Only the samples without any defect were sintered.

The green density was measured before and after binder removal using the Archimedes principle in mercury. The green density (ρ_g) was calculated from:

$$\rho_g = \frac{M_s \times \rho_l}{M_s + M_l}$$

Where M_s is the weight of the green body in air (g), M_l is the weight of sample in mercury (g) and ρ_l is the specific gravity of mercury at the measurement temperature (g cm^{-3}).

3.3.3 Densification

Sintering experiments were carried out using a conventional furnace box manufactured by Carbolite UK Ltd. and consisting of SiC heating elements, the temperature was controlled using a Eurotherm 902 controller (Eurotherm UK Ltd., West Sussex, UK) connected to a thermocouple inside the furnace chamber. The sintering methods used include conventional single stage sintering and two-stage sintering. The two sintering cycles are shown schematically in Figure 3.5. The aim was to prepare samples with densities above 99% and a range of different alumina and zirconia grain sizes.

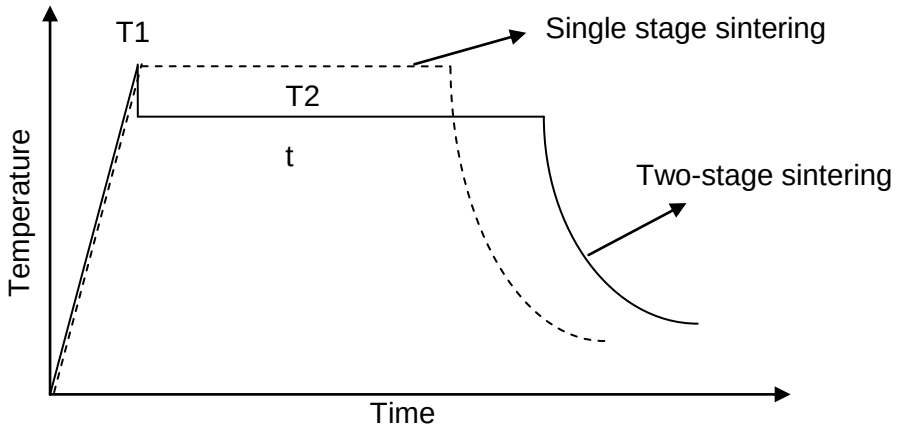

Figure 3.5 The heating cycle of two-stage sintering.

For the single stage sintering of alumina, the temperature was varied from 1300°C to 1400°C and the sintering time from 0.1 min to 10 hours. During two-step sintering, the above temperatures were used as the first step temperature, T_1, based on trials and T_2 was varied from 1150°C to 1250°C to achieve optimal densification and the finest grain sizes achievable. The time at the second stage was varied from 2 hours to 20 hours. A similar study was carried out for the densification of the ZTA samples. Temperatures from 1450°C to 1550°C and a sintering time of 2 to 10 hours were used as the single stage sintering conditions; the two stage sintering conditions investigated were 1450°C for T_1 and 1300 to 1400°C for T_2 with dwell time from 10 to 20 hours at T_2.

The density was measured using the Archimedes principle in water. The sintered density (ρ_s) was calculated from:

$$\rho_s = \frac{M_s \times \rho_w}{M_s - M_w}$$

where M_s is the weight of the sintered body in air (g), ρ_w is the density of water at the measurement temperature (g cm^{-3}) and M_w is the weight of the sample in water (g).

3.3.4 Processing of other materials

The sintering conditions for the nano 3Y-ZTA samples were selected to be single stage sintering at a temperature of 1450°C for 10 hours on the basis of trials whilst the nano 1.5YSZ samples were sintered using a two stage sintering route. The

sintering conditions were T_1=1250°C, T_2=1150°C and the dwell time was 5 hours. This resulted in a final mean zirconia grain size of ~110 nm, but the density was only 97% of theoretical. Despite the latter, these conditions avoided the formation of any monoclinic zirconia occurred at higher sintering temperatures.

In addition, some zirconia alumina composites without yttria stabiliser (0Y-ZAC) were made in order to study the residual stress generated by the zirconia phase transformation, this is outlined in more detail in section 5.2.2. Samples with different zirconia contents were made, including 15%, 20% and 27% 0Y-ZAC, which developed different tetragonal to monoclinic phase ratios after sintering. The processing route was the same as that for the 1.5Y-ZTA samples and the sintering conditions used are listed in Table 3.3.

Table 3.3 Sintering conditions of the 0Y-ZAC samples

Sample code	Sintering T / ˚C	Dwell time / h
15% 0Y-ZAC	1500	5
20% 0Y-ZAC	1500	5
27% 0Y-ZAC	1500	5
	1400	5
	1300	5

3.4 Mechanical Properties

The main objective of the mechanical properties measurements was to investigate the effect of zirconia content, amount of yttria addition, and alumina and zirconia grain sizes on the mechanical properties of the alumina and ZTA samples. Four properties, which are potentially related to the high strain rate performance, were studied in this project, including Vickers indentation hardness, Vickers indentation toughness, 4-point bend strength, and wear resistance. The samples tested and characterised were listed in Table 3.2.

3.4.1 Mounting and polishing of sintered samples

Before any mechanical and high strain rate testing, the sample surfaces needed to be polished. The sintered samples were mounted using epoxy resin and epoxy

hardener (Epofix, Struers Ltd., Solihull, UK) mixed in a volume ratio of 15:2 in a beaker for 30 seconds. After the resin solidified, the sample was polished using a semi-automatic polishing machine (Struers TegraForce-5, Catcliffe, UK) with grinding discs and grinding suspensions, following a programme shown in Table 3.4.

Table 3.4 Programme of polishing

Polishing material	Resin bonded diamond grinding disc			Suspension		
Grit/particle size	220	600	1200	Plan (9 µm)	Dac (3 µm)	Colloidal silica (~0.04 µm)
Time / min	10-15	3	3	5	4	4

Between each polishing step, the samples were removed from the specimen holder and cleaned thoroughly with water. After polishing, the samples were cleaned using water and then acetone using ultrasound for 2 min. The resin mount was removed by heating to 150ºC for 10 minutes in an oven to make it soft.

3.4.2 Vickers indentation hardness

Before the final colloidal silica polishing step, the Vickers hardness was measured on the polished surface of the sample using a Vickers micro indentation hardness tester (Mitutoyo HM-124, Mitutoyo Corporation, Kawasaki, Japan). A square-based pyramidal-shaped diamond indenter with face angles of 136° was used to determine the hardness with a load of 1 kg being applied for 15 s. After removal of the load, a square indent was formed on the sample surface. The lengths of the diagonals of the indent were measured with the help of a microscope. The Vickers hardness of the sample was then calculated using:

$$HV\ (GPa) = 0.0018544 \times P/d^2$$

Where, *P* is the applied force (N) and *d* is the average length of the diagonals of the indentation (mm).

3.4.3 Vickers indentation toughness

The indentation toughness of the samples was determined using a hardness tester (Mitutoyo AVK-C2, Mitutoyo Corporation, Kawasaki, Japan). The indents on the samples were created using a Vickers pyramidal indenter by applying a 10 kg load for 15 s. After indenting the sample, the diagonal length of the indent and the length of the cracks were recorded. The indentation toughness was calculated using the formula suggested by Anstis et al. [111]:

$$K_{Ic} = a \times (\frac{E}{H})^{1/2} \times \frac{P}{c^{3/2}}$$

Where E is the Young's modulus of the material (GPa), *H* is the Vickers hardness (GPa), *P* is the indentation load (N), and *c* is the crack length (m). *α* is a constant: for alumina samples the value is 0.016; for ZTA the value is 0.025 [69]. The value of E was assumed to be 392 GPa for all the alumina samples [112], the E for the ZTA samples with different zirconia contents were calculated as below

$$E(xZTA) = 210 \times x + 392 \times (1 - x)$$

Where the x is the volume percentage of the zirconia. The *E* of YSZ is 210 GPa [69,113].

3.4.4 Residual stress distribution and zirconia phase transformation

In order to study the effect of indentation load on the residual stress distribution and zirconia phase transformation around an indent, a range of loads, viz. 1, 5, 10 and 20 kg, were applied using the AVK-C2 hardness tester. At least 5 indents were made for each load/sample combination.

To allow the plastic zone around each indent to be examined, two polished samples were bonded together using superglue and then the top, joined surface was polished again to a1 μm diamond grit size. Indents were then made along the join line and the two samples separated by dissolving the glue in acetone. A schematic drawing is shown in Figure 3.6 (a). The plastic zone was observed using optical microscopy, as shown in Figure 3.6 (b), and its size confirmed to be similar to the half-length of the diagonal of the indent.

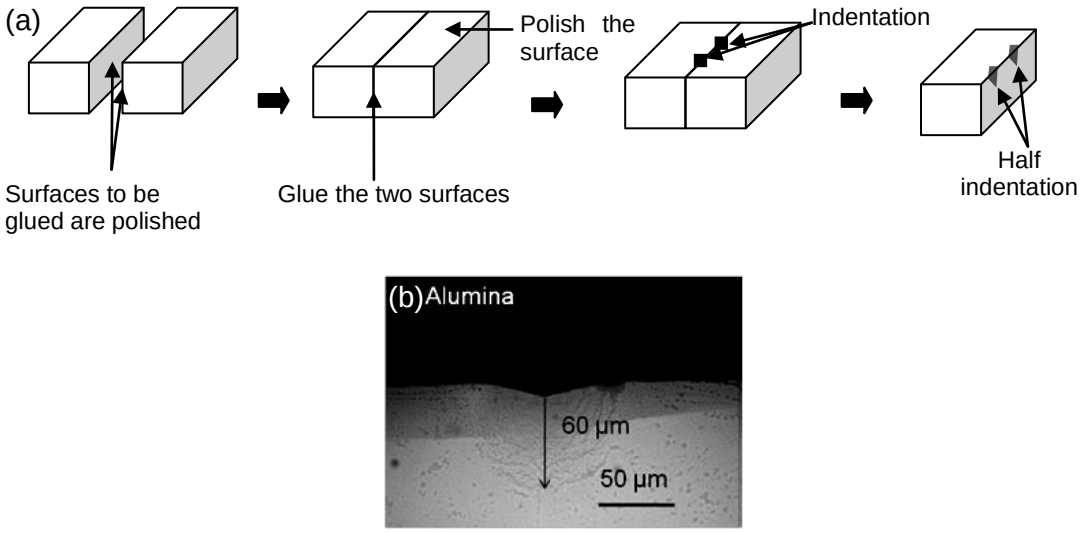

Figure 3.6 (a) Sample preparation for plastic zone observation and (b) optical microscopy image showing the plastic zone of an alumina sample.

3.4.5 4-point bend strength

4-point bend fracture strength measurements were carried out on samples measuring 2.5×2×30mm^3 according to the guidelines in ASTM C1161-02c. Test-pieces were prepared by cutting the tile samples mounted in mounting wax using an automatic cutting machine (Struers, Catcliffe, UK) with a diamond saw. The lowest cutting speed, 0.005 mms^{-1}, was used in order to prevent any damage to the samples. 7 bars were cut from one or two tiles sized 12×30×2.5 mm^3. For each bar, all the surfaces were polished.

The sample bars were tested using a LR50K materials testing machine (LLORD, West Sussex, UK). A monoblock design of semi-articulating four-point flexural strength jig was employed with 2.5 mm diameter tungsten carbide rollers. The design allowed free movement of the support rollers during loading. A schematic of the 4-point bend jig is shown in Figure 3.7. Tests were conducted at a cross-head displacement rate of 0.3 mm min^{-1}. Peak force at fracture was captured and nominal flexural strength computed using:

$$\sigma_f = \frac{3F(L_0 - L_i)}{2wh^2}$$

where σ_f is the fracture stress of the material, (Pa), F is the applied force (N), L_0 is the outer span of the supports (m), L_i is the inner span (m), w is the beam width (m)

and *h* is the beam height (m). 7 samples were tested for each composition and the mean was calculated.

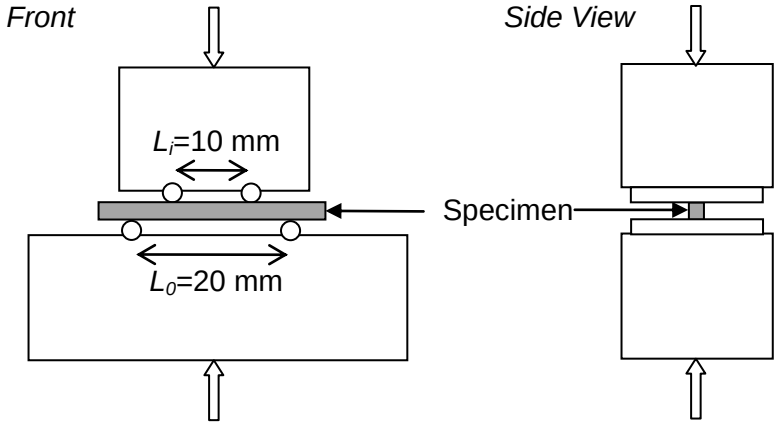

Figure 3.7 Jig for 4-point bend test.

The fractured samples were analysed using FEGSEM to identify their fracture modes and critical flaws. Weibull modulus for each sample was calculated in order to quantify the reliability of its quoted strength. The test results were assigned a rank by strength and the equation below was used to calculate the ceramics probability of survival under a given stress [114]:

$$P_s = 1 - \frac{n}{N+1}$$

Where P_s is the probability of survival at a given stress σ, n is the rank of the sample, N is the total number of samples. The P_s is related to its material strength:

$$P_s = \exp\left(-\left(\frac{V}{V_0}\right)\left(\frac{\sigma}{\sigma_0}\right)^m\right)$$

Where V is the stressed volume, m is the Weibull modulus of the material. V_0 and σ_0 are nominal quantities with no physical meaning.

Re-arranging the above equation yielded:

$$lnln(1/P_s) = lnV - ln({V_0}{\sigma_0}^m) + mln\sigma \qquad \text{Eqn. (3.1)}$$

A linear relationship between $lnln(1/P_s)$ and $ln\sigma$ is achieved according to the above equation, and the gradient of the line is the Weibull modulus.

3.4.6 Wear resistance property

Both dry and wet wear testing was carried out using a linearly reciprocating ball-on-flat sliding wear tester as per ASTM G 133-05. The test set up was similar to the one shown schematically in Figure 3.8.

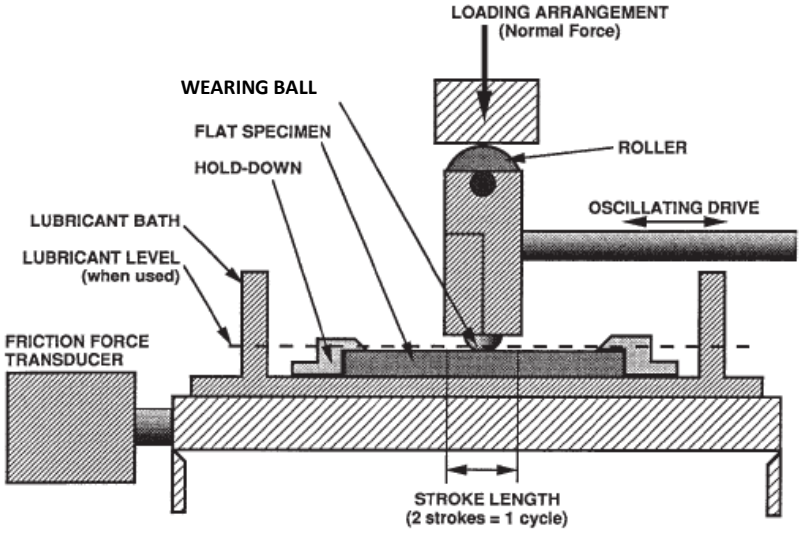

Figure 3.8 Schematic of the wear testing machine (from ASTM G 133-05).

The samples were mounted in epoxy resin and polished to a 1 µm surface finish, 12 mm diameter tungsten carbide–cobalt balls (5-7% cobalt) were used to wear on the sample surface. A constant load of 20 N was applied on all the samples, whilst a 25 N load was also applied on a batch of 10% 1.5Y-ZTA samples. The total number of cycles was 100,000 with a 2.5 cm stroke length, equivalent to a total sliding distance of 5 km. After wear testing, the samples were cleaned using ultrasound in distilled water, followed by acetone. Then, the weight loss of each sample was measured and the wear volume was calculated. The wear scar on the zirconia specimens was analysed using optical microscopy, FEGSEM and micro-Raman spectroscopy.

3.5 High Strain Rate Testing

Two high strain rate test techniques were employed in this project. The first was split Hopkinson pressure bar (SHPB) testing, which provided 10-20 m s^{-1} impact speeds. The second involved a gas gun that generated impact speeds of 100 to 150 m s^{-1}.

The samples after testing were characterised using various characterisation techniques and the effect of zirconia phase transformation on the high strain rate performance was extensively studied.

3.5.1 Split Hopkinson pressure bar testing

The split Hopkinson pressure bar (SHPB) testing was carried out on small cuboid samples (3× 3 × 5 mm^3 to 4 × 4 × 5 mm^3). The samples were cut from the tile samples that had been polished on both sides. The SHPB setup consisted of a maraging steel elastic striker and incident and transmission bars, each with a diameter of 10 mm, Figure 3.9. A copper pulse shaper was placed in between the striker and the incident bars, in order to provide a ramp-loading pulse. To prevent the ceramic specimen from indenting into the bar end faces and thus causing stress concentrations, a pair of high stiffness tungsten carbide conical shaped anvils (5 and 10 mm Ø on two surfaces and 5 mm thickness) were placed in between the sample and the bars [15]. The impact speeds used in the work were from 8 to 16 m s^{-1}.

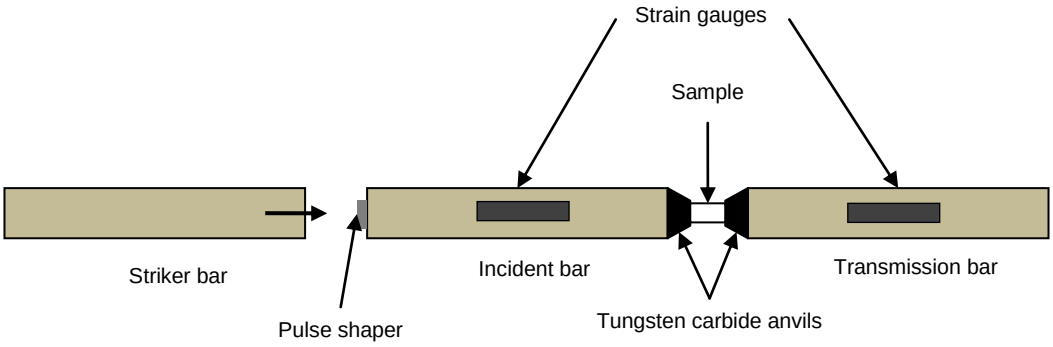

Figure 3.9 Setup of SHPB test.

3.5.2 Gas gun impact testing

The gas gun impact tests were carried out by firing sharpened tungsten carbide, WC, projectiles at the polished ceramic disc samples, Figure 3.10. The projectiles were machined from 3 mm diameter WC rods to conical shapes with 45° sharp tips and tip diameters smaller than 30 µm. The sharpness of the tips for all the projectiles was checked using a 3D optical microscopy (Alicona Infinite Focus, Kent, UK) before use. A 3D image and profile of a projectile is shown in Figure 3.11. The impact surface of

the test samples was polished to a 1 µm finish in order to reduce the size of surface defects. The back surface was also ground to ensure there was good attachment to the steel backing bar; the latter was achieved using a small amount of vacuum grease. The projectile was stuck onto a nylon sabot with the same diameter as the gas gun barrel. The sabot and projectile were separated before impact by a splitter. The impact speed was measured using two light gates; velocities in the range 100 to 150 m s^{-1} (±7 m s^{-1}) were used. For each type of material, three samples were tested and a high degree of reproducibility was observed.

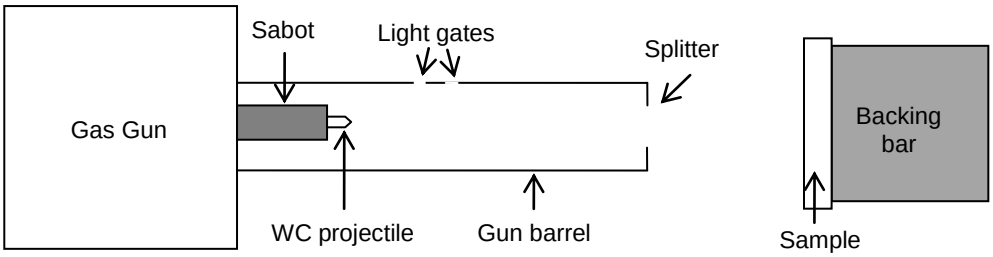

Figure 3.10 Schematic of the gas gun impact test.

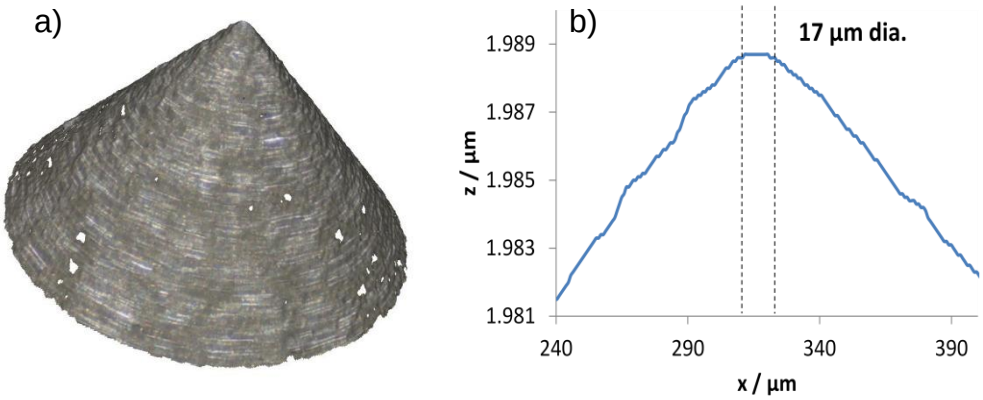

Figure 3.11 a) 3D image and b) surface profile of a WC projectile.

3.5.3 Post testing characterization

SHPB tested samples

After the SHPB testing, most of the samples had fragmented completely; the fine fragments were analysed using Raman spectroscopy to determine the zirconia phase present and Cr^{3+} fluorescence spectroscopy to analyse the residual stress

and dislocation density on the fractured surfaces. For the 15% nano 1.5Y-ZTA, some samples were survived after the high strain rate testing and so the impact surfaces were analysed using the same methods. In addition, the fracture surfaces of the fragments were observed using FEGSEM to determine their fracture modes. The fragment size distribution was also studied and the relationship between the fragment sizes and the fracture modes was investigated. In addition, FIB lift-out was carried out on some fragments and intact sample surfaces in order to observe the dislocations and microcracking using TEM.

Gas gun impact tested samples

After the gas gun impact testing, the indented surface topography was analysed. The zirconia phase transformation after impact was studied using Raman analysis, whilst Cr^{3+} fluorescence mapping was carried out to measure the residual stress distribution around the impact areas and the dislocation density change.

In order to observe the plastic deformation and crack propagation below the impacted surfaces, the samples were cross sectioned at the impact region. The sample was first cut along a cutting line (line 1) very close to the impact region, Figure 3.12; this was followed by another cut further away and on the other side of the impacted region. This yielded a relatively small sample, making preparation easier. The sample was then mounted using the epoxy resin and gently polished on the cut surface next to the impacted region until the centre of damaged region was reached. The lowest cutting speed (0.005 m s^{-1}) and fine polishing (1-3 µm grit) were used to prevent any damage to the impact region.

The cross-section of the impacted region was observed using FEGSEM and Raman and Cr^{3+} fluorescence mapping were carried out. TEM was also used to observe very small samples lifted out from the impact region using the focused ion beam (FIB) technique.

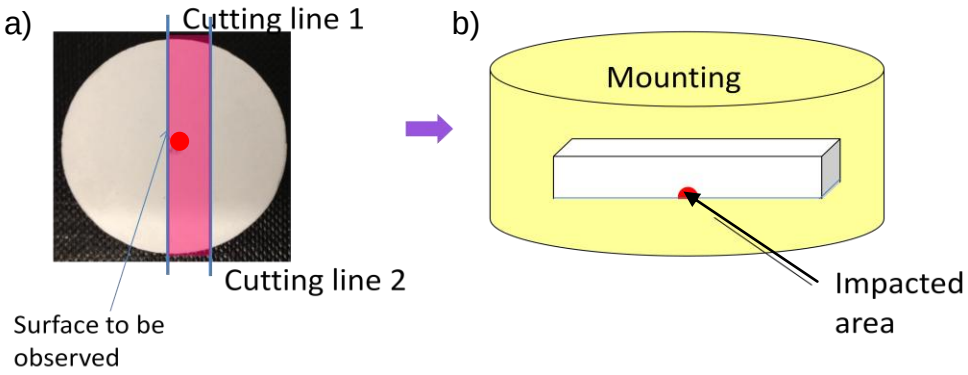

Figure 3.12 Schematic of sample preparation for cross-section observation for the impact tested samples: a) a sample with the impact region was cut from the disc; b) the sample was mounted and polished until reaching the cross-section of the impact region.

3.6 Characterisation Techniques

3.6.1 XRD

X-ray diffraction patterns of the alumina and ZTA samples before and after sintering were recorded using a diffractometer (Model D8 diffractometer, Bruker AXS GmbH, Karlsruhe, Germany) with a quarter-circle eulerian cradle. The testing conditions were as follows:

- CuKα radiation with a wave length of 1.5406×10^{-10} m.
- Step size 0.02° increment in 2θ, step time 1 s.
- 2θ range: 20° to 80°.

High temperature XRD patterns were recorded for a 15% 1.5Y-ZTA powder and a 20% 0Y-ZAC powder to determine the phases present at different temperatures. The XRD patterns were recorded from 25° to 35° 2θ at room temperature, 700°C, 800°C, 900°C, 1000°C, 1100°C, 1200°C, 1300°C, 1400°C, 1500°C and then back to room temperature. Each temperature was held for 5 minutes before recording.

3.6.2 FEGSEM observation and grain size measurement

Field Emission Gun Scanning Electronic Microscopy(Leo 1530VP FEGSEM, LEO Elektronenskopie GmbH, Oberkochen, Germany) was used for the microstructure observation, the measurement of the grain size of the sintered bodies, determination of the wearing mechanisms of the wear tested samples and the fracture modes of the bend test samples.

For all the ceramic samples, gold coating was required to make the surface electrically conductive before observation using the FEGSEM. In order to measure the grain size of the sintered samples, the surface of the specimen was initially polished followed by thermal etching before gold coating, in order to obtain a high quality image. Thermal etching was accomplished by heating the sample to 1200ºC for alumina and 1250ºC for ZTA and holding for 6 minutes.

The grain size was determined using the linear intercept method (ASTM E 112-96). The two dimensional grain size was converted to three dimensional using a conversion factor of 1.56. At least three micrographs and a total of 300 grains were evaluated to determine the grain size for each sintering batch. The method involved determining the mean grain size from the number of grains/grain boundaries intersecting one or more lines of known length superimposed on a micrograph. The mean grain size was calculated by the equation,

$$D = \frac{L \times A_1}{M \times N}$$

Where *D* is the equivalent mean grain diameter, *L* is the length of superimposed lines, A_1 is the shape correction factor, 1.56, *M* is magnification (dimensionless) and *N* is the quantity of intercepts or intersections.

3.6.3 Optical microscopy

An optical microscope (Reichert Jung MeF3 optical microscope, Cambridge, UK) was used to measure the size of the Vickers indents and the crack lengths. It was also used to check the surface of the samples after the gas gun impact testing. The magnification ranged from 20× to 1000×.

A 3D Optical microscopy (Alicona Infinite Focus, Kent, UK) was also used to observe the topography of a sample surface. The observation was carried out on the surfaces of the impact tested samples and it was also used to measure the sharpness of the WC projectile tips. Both 3D mapping and line scanning were used on the sampling areas.

3.6.4 Micro-Raman spectroscopy

The zirconia phases were investigated using a high-resolution confocal Micro-Raman spectrometer (Horiba Yvon Raman LabramHR, Horiba JobinYvon SAS, Villeneuve d´Ascq, France) equipped with a liquid nitrogen cooled CCD detector and incident radiation from a He red laser at 633 nm. The laser power was 20 mW, the spectrum integration time was 40 s and an objective lens with ×100 magnification was used. Raman spectra between 100 and 400 cm^{-1} were recorded. This range was selected as the main monoclinic bands are at 181 and 192 cm^{-1}, whilst the primary tetragonal bands are at 148 and 264 cm^{-1} [115,116].

3.6.4.1 Determination of zirconia phase transformability

According to McMeeking and Evans [116], the fracture toughness, K_{Ic}, is a function of the transformability of a zirconia based material, $V_f d^{1/2}$, according to the following equation:

$$K_{Ic} = K_{Ic}^{m} + \eta V_f \Delta V E \times d^{\frac{1}{2}}/(1-\nu) \qquad \text{Eqn. (3.2)}$$

where K_{Ic}^{m} is the fracture toughness of a matrix, V_f is the highest transformable zirconia content, ΔV is the volume dilation associate with the transformation, E is Young's modulus, ν is poisson ratio, η is a constant and d is the plastic zone size. Since K_{Ic}^{m}, ΔV, E, ν and η are constant for a selected material, a linear relationship can be expected between the toughness, K_{Ic}, and the transformability, $V_f d^{1/2}$, with the change of grain sizes for a zirconia based material. The $V_f d^{1/2}$ can be determined by means of Raman analysis following the method proposed by Katagiri et al. [115], which is based on a spatial mapping of the sample performed in the direction perpendicular to the crack, as illustrated in Figure 3.13 (a).

The transformed monoclinic zirconia concentration (*m*) along the mapping line was quantitatively calculated according to the following equation [72]:

$$m = \frac{1/2(I_m^{181} + I_m^{192})}{0.97(I_t^{148} + I_t^{264}) + 1/2(I_m^{181} + I_m^{192})} \quad \text{Eqn. (3.3)}$$

Where *I* is the intensity of the peaks and the subscript indicates the corresponding phase, whilst the superscript indicates the peak position in reciprocal centimetres.

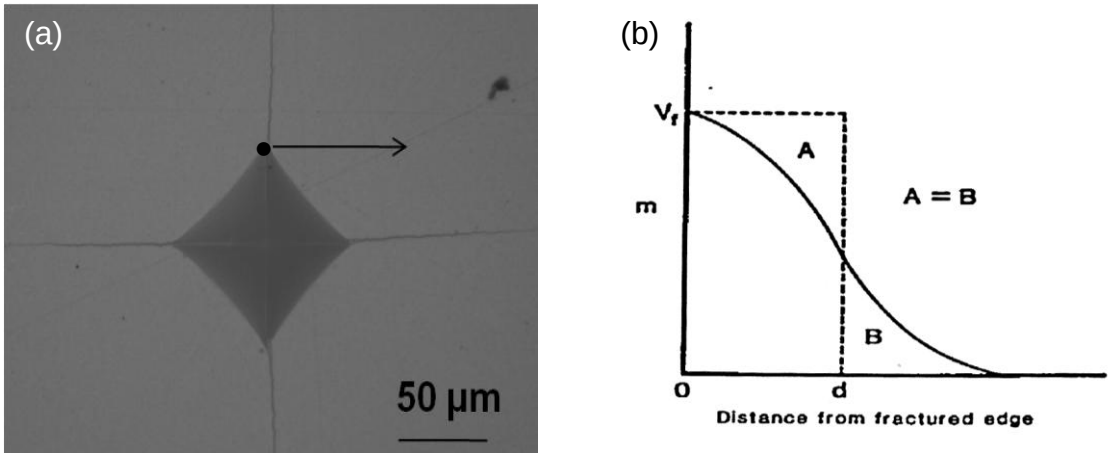

Figure 3.13 Image of an indent, the arrow indicates the mapping path from the fractured edge outwards to away from the crack; (b) transformed monoclinic zirconia concentration along the mapping line [115].

By mapping the degree of monoclinic zirconia transformation, a curve of *m* as a function of the distance to the fracture edge could be drawn, as shown in Figure 3.13 (b). Then, V_f is the value at the fracture edge, because the highest degree of phase transformation occurred at this position. The transformation zone size (*d*) is defined as the distance at which the areas of A and B become equal, Figure 3.13 (b), which can be determined using Origin software. After calculating the value of $V_f d^{1/2}$, the transformability of a ZTA material was quantitatively measured and its relationship with the K_{Ic} was investigated.

Line maps of the degree of zirconia phase transformation around the different indents were made by measuring the fraction of each zirconia phase present along a line from outside the indent to its centre, Figure 3.14. The laser was first focused on the polished surface and then scanned towards the indent centre; the scanning lines were 60 µm long with a step of 3 µm and the laser was auto-focused at each step.

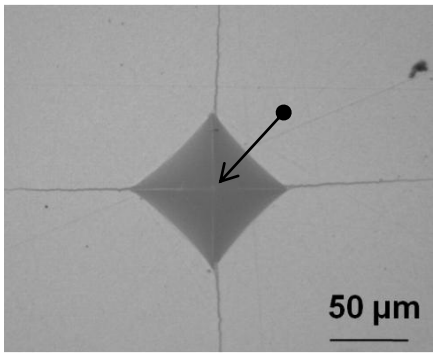

Figure 3.14 Location of a typical line map obtained across an indent formed in a ZTA sample.

3.6.4.2 Raman analysis on the high strain rate tested samples

The degree of zirconia phase transformation was investigated on the high strain rate tested samples using Raman analysis. The samples included the fragments and surviving surfaces from both the SHPB and gas gun tested samples. Line maps and/or area maps were obtained. For the former, at least 25 points were collected 3 times across an area of interest, whilst for the latter a typical area about 3×3 mm^2 and 25×25 mapping points were used.

3.6.5 Cr^{3+} fluorescence spectroscopy

Cr^{3+} fluorescence spectra were obtained using the same Raman equipment and the same laser. The highest spatial resolution of 1.5 µm was achieved using a ×100 objective lens and a laser aperture of 20 µm diameter. The exposure time was 1 s at each point. For each measurement, a region of interest was selected using the optical microscope with white light. Cr^{3+} fluorescence spectroscopy was used to obtain two sets of results, viz. the residual stress change and dislocation density change after either mechanical or high strain rate testing.

The Cr^{3+} fluorescence analysis on the indentations in the alumina and ZTA samples was carried out in two stages. First, a depth scan [62] was performed to investigate the degree of laser transparency of each sample. To achieve this, the laser was initially focused on each polished sample surface at a remote location from the indents, this position was set as zero; then the specimen stage was moved upward

by 100 μm, so that the laser focal plane was the same distance below the surface. Mapping was then carried out in the direction normal to the sample surface in 2 μm steps from the starting position, from -100 μm to +50 μm above the surface with the Cr^{3+} fluorescence spectra being collected at each step. Secondly, line mapping was again performed as described Figure 3.14, but this time collecting the Cr^{3+} fluorescence spectra. Note that for both the depth scanning and line mapping, the results were repeatable.

The collected data were subsequently analysed using a constrained 4-peak fitting method [58] and Auto2Fit 5.5 (7-D software, China) software. Essentially, the two doublets of the R1 and R2 peaks were fitted using a mixed Lorentzian and Gaussian function with a constraining parameter, which is the R1 to R2 peak area ratio for any individual doublet, being constrained to be 2.0. This is derived from the fact that the mean piezo-spectroscopic coefficients (see Eqn. 2.1) are similar for the R1 and R2 peaks. Finally, the peak position and width were identified and used to investigate the residual stresses and dislocation densities after each indentation test. Since a certain amount of residual stress could be generated during the sintering process and, particularly, surface polishing, all the peak shifts and broadenings of the indentation-tested samples were compared with data obtained after sintering and polishing but before indenting.

3.6.6 FIB lift-out and TEM analysis

In order to observe the microstructure inside an indent or within the high strain rate tested samples and resulting fragments, transmission electron microscopy (TEM, JEOL 2000FX) was carried out on thin foil samples lifted out from the centre of the relevant damaged regions.

To prepare the lift-out samples, a focused ion beam system (Nova Nanolab 600, FEI, Netherlands) was used and the lift out procedures from an indent centre are illustrated in Figure 3.15 (a) to (f). Initially, a platinum protective layer was deposited on the diagonal of the indent, with an area of 20×1.5 μm and a thickness of ~1.5 μm, Figure 3.15 (a). Then, a 20 nA ion beam was used to cut two trenches measuring ~25×15 μm in area and ~10 μm in depth on each side of the platinum layer, Figure

3.15 (b). A U-shaped cut was performed on the slice-shaped material with one side not fully cut through, in order to prevent the sample from falling off, Figure 3.15, (c). A sharp tungsten probe was welded to the edge of the slice using platinum deposition and then the bridge connecting the slice to the rest of the sample was cut and the sample was lifted out, Figure 3.15 (d). The sample was attached onto a TEM copper grid using a platinum weld and then cleaned and thinned using a reduced ion beam current of 0.5 or 1 nA, to prevent sample damage, Figure 3.15 (e). The final TEM sample measured ~20 µm in width, 3-5 µm in length and ~100 nm in thickness, Figure 3.15 (f).

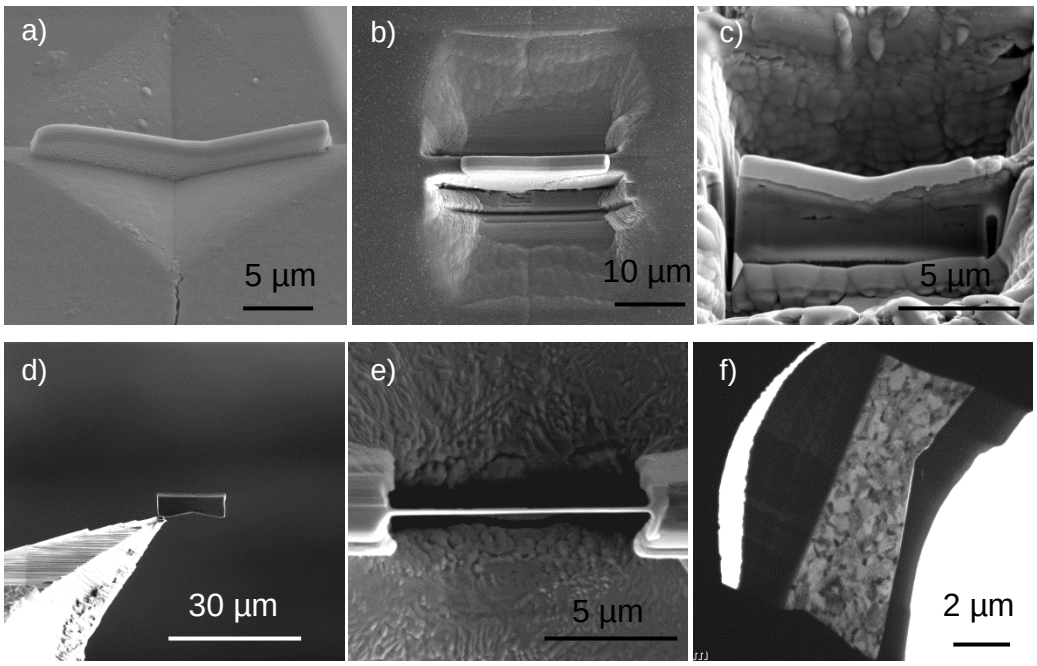

Figure 3.15 Images illustrating the procedures of ion beam-assisted in-situ TEM thin foil sample preparation: a) platinum protective layer deposited on the area of interest; b) two trenches were milled on the two sides of the platinum layer; c) U-shape cutting on the slice sample; (d) sample lift-out using a sharp tungsten probe; (e) the final thinning using the ion beam to achieve electron transparency. f) lift-out of the TEM sample.

The dislocation and microcrack distribution of each FIB sample were analysed using high magnification transmission electron microscopy. The microcrack density was quantitatively determined by taking 10 TEM images at above ×120k magnification of each sample and then 12 vertical lines with equal spacing and length were drawn across each image, Figure 3.17. The number of times the lines intersected with

cracks was counted yielding the number of cracks per unit length of test line, *i.e. micro*crack density (ρ) [117]:

$$\rho = n/L \qquad \text{Eqn. (3.2)}$$

Where n is the number of intercepts and L is the overall length of the lines.

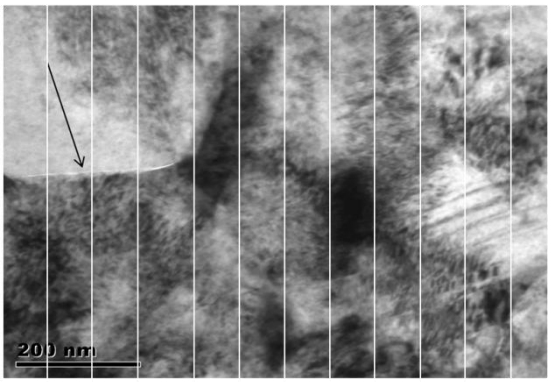

Figure 3.16 TEM image used to measure the microcrack density. The number of times the white lines intersected with microcracks was counted and turned into a microcrack density, see the text.

4 PROCESSING OF ALUMINA AND NANO ZTA

The mechanical properties and ballistic performance of a ceramic amour are determined by the microstructures, including the porosity, mean grain size, grain size distribution and any inclusions, each of which are controlled by the manufacturing process. In order to find the optimal materials for amour applications, work has been focused on developing methods to produce alumina and ZTA materials with full densities and different grain sizes. Section 4.1 is focused on the characterisation of the as-received and concentrated suspensions, followed by a phase analysis of the ZTA powders in section 4.2. Section 4.3 investigates the effect of manufacturing parameters associated with the green forming process, including the employment of Freon used as a foaming agent for granules used in dry forming; the green structure, density and homogeneity were all investigated. Sections 4.4 and 4.5 focus on the sintering conditions of the alumina and nano ZTA, respectively; both single stage and two stage sintering were investigated to produce samples with varied grain sizes and also to find the optimised sintering conditions.

4.1 Characterisation of the Suspensions

The mean particle size of the suspension highly affects the achievable grain size of the sintered samples, therefore it is crucial to identify the former and TEM was used to observe the particles and particle size distribution in the suspensions. In addition, the zeta potential affects the stability of the suspension during suspension preparation; the possibility of mixing two suspensions at a given pH can also be confirmed through zeta potential measurements. Thorough mixing could help to form green bodies with homogeneously distributed microstructure. The suspension viscosity is another crucial factor that affects the homogeneity of the green bodies; if the viscosity is too high, the powder formed from the suspension could be too dense to crush during die pressing, leading to agglomerates in the green bodies. Therefore, before processing, the as-received suspensions were characterised in terms of their particle sizes, zeta potential and viscosity for the concentrated suspensions.

4.1.1 TEM studies

TEM images of the particles from the suspensions of 1.5YSZ, 3YSZ and alumina suspensions are shown in Figure 4.1 (a) – (c). From the images, it can be observed that the nano zirconia particles in the 1.5YSZ and 3YSZ suspensions were uniformly dispersed without significant agglomeration and a narrow particle size distribution was achieved. It is very clear that the individual crystallites of the nano sized zirconia were of the order of ~20 nm. On the other hand, the alumina suspension showed a wider range of particle size distribution, as shown in Figure 4.1 (c). The particle size distribution for the alumina particles in the suspension is shown in Figure 4.2, the measured mean alumina size is 150±50 nm.

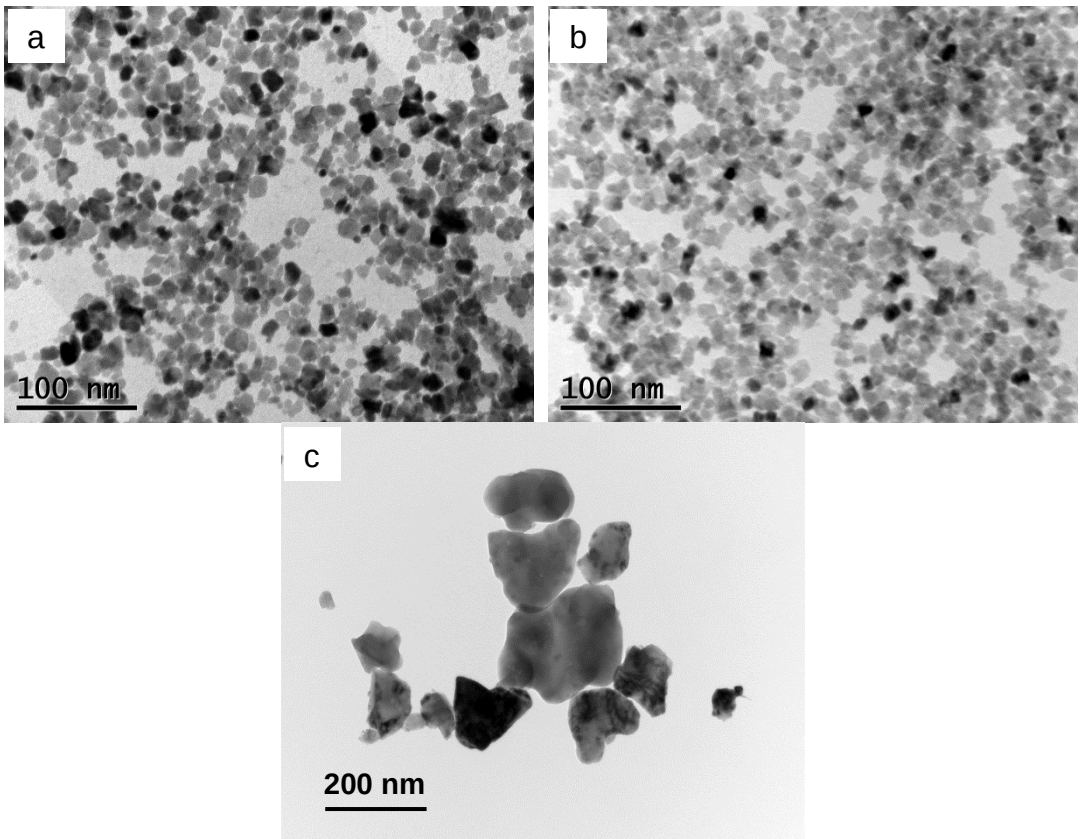

Figure 4.1 TEM images of the as-received suspensions: (a) 1.5YSZ, (b) 3YSZ (c) alumina.

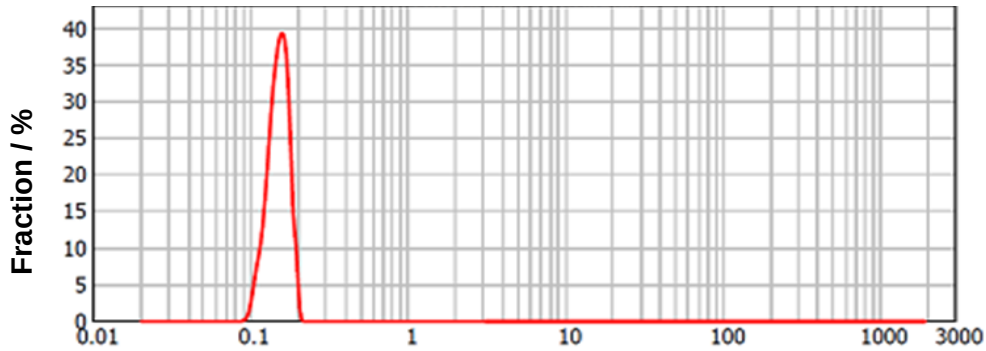

Figure 4.2 Particle size distribution of the alumina suspension.

4.1.2 Zeta potential

The zeta potential of the alumina suspension, nano 1.5YSZ suspension and the mixed suspension of these two at a ratio of 9:1 (10% 1.5Y-ZTA) were measured and are shown in Figure 4.3. The isoelectric points (IEP) of the above suspensions were 9.6, 9.1 and 8.8, respectively. The zeta potential was above 30 mV for all the suspension in the acidic region, indicating that they can be considered stable when their pHs were in this region. The pHs of the as-received YSZ and alumina suspensions were 2.5 and 3.5. After mixing to form the ZTA suspension, the pH became 3.4. From the zeta potential measurement, the mixed suspension can be considered to be stable at pH 3.4. This suggests that the suspension could be acceptable for the further green forming.

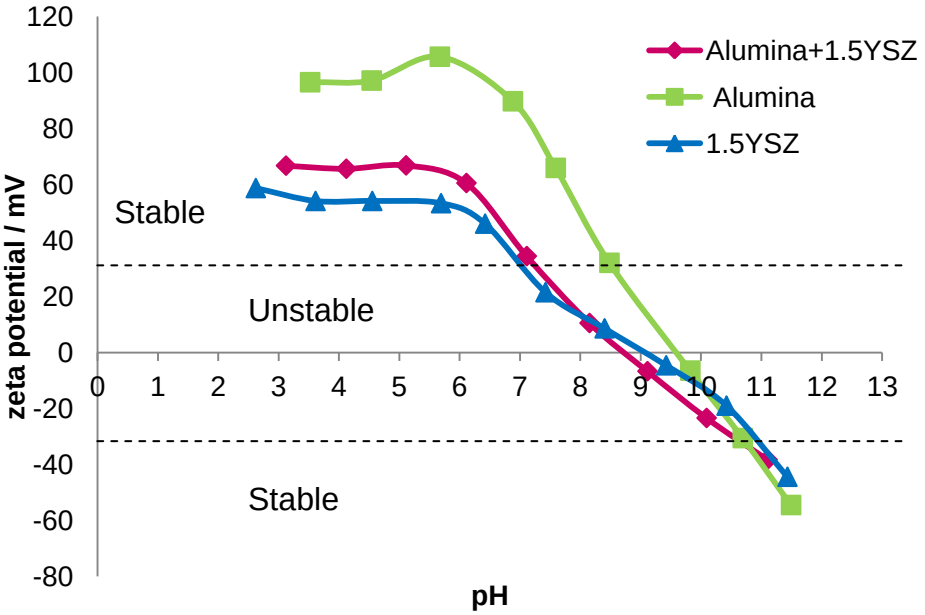

Figure 4.3 Zeta potential measurement of the as-received alumina suspension (the error bar for each point is ±5 mV).

4.1.3 Viscosity

From the zeta potential measurements, the alumina suspension and the mixed ZTA suspension were stable and well dispersed at their pHs (3.5 for alumina, 3.4 for ZTA). However, another requirement of the suspension, before confirming their applicability for green forming, is the viscosity. As mentioned in section 3.3.1, after concentrating to a solid content around 57-60 wt%, a viscosity below 100 mPa s at a shear rate of 100 s^{-1} were required.

Based on the above consideration, the viscosities of the as-received alumina suspension, which had a solid content of 58.8%, and the ZTA concentrated suspensions (10% 1.5Y-ZTA with 58.0% solid content as an example) were tested and are shown in Figure 4.4. The viscosities of the above suspensions were both below 15 mPa s at the shear rate of 100 s^{-1}. Therefore, the suspensions were confirmed to be well dispersed and of low viscosity, therefore acceptable for green forming. A table of the viscosities of all the concentrated suspensions are listed in Table 4.1.

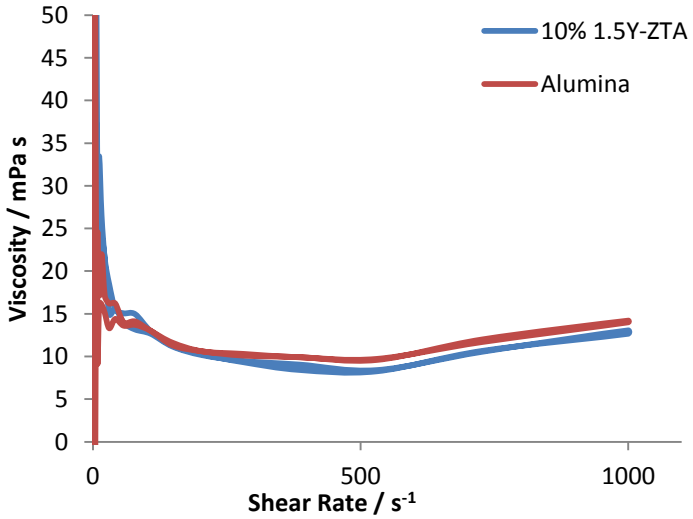

Figure 4.4 Viscosity measurement of the as-received alumina suspension and concentrated 10% 1.5Y-ZTA suspensions.

Table 4.1 Viscosities of concentrated suspensions with solid contents of 57-60%

Suspension	Alumina	10% ZTA	15% ZTA	20% ZTA	1.5YSZ
Viscosity / mPa s at 100 s^{-1} shear rate	14	14	14	14	15

4.2 Phase Characterisation

It is important to study the phases in alumina grains before and after sintering, and in addition, metastable tetragonal zirconia phases in ZTA provide a phase transformation toughening effect, which is desirable. Therefore, the phases in both the alumina and ZTA materials before green forming and after sintering were investigated using XRD.

The XRD patterns of the 15% 1.5Y-ZTA powder and a sample sintered at 1500℃ for 10 h are shown in Figure 4.5. The indexed crystal structures are labelled above the corresponding peaks.

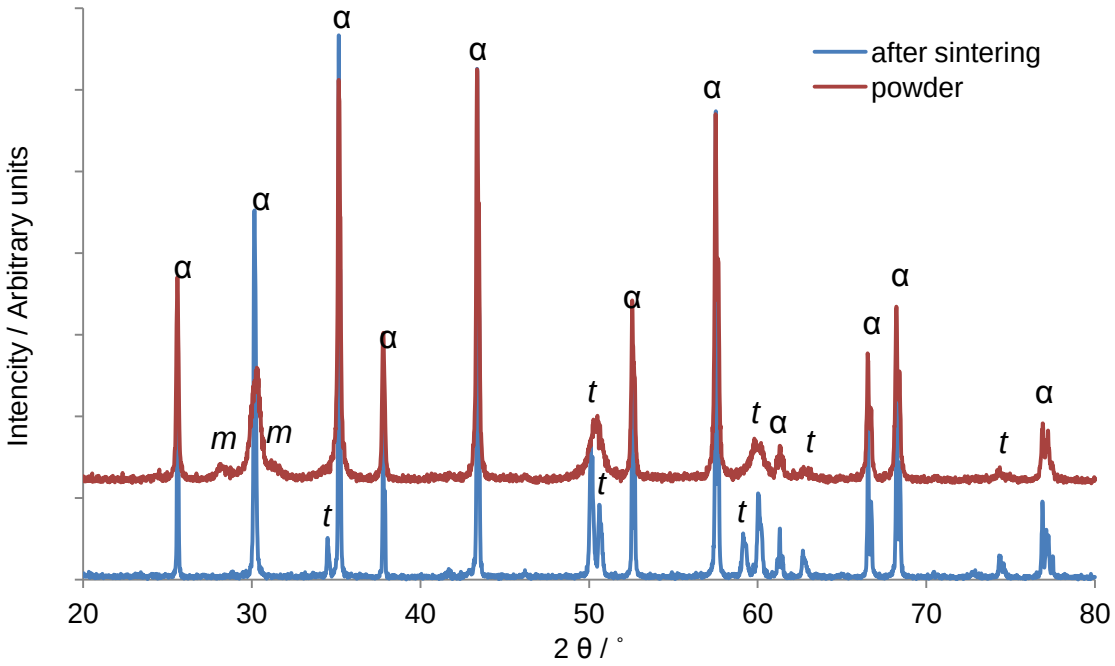

Figure 4.5 XRD pattern of the 15% 1.5Y-ZTA powder and a sample sintered at 1500℃ for 10 h. α represents α alumina, *m* and *t* stand for monoclinic and tetragonal zirconia phases.

The powder and sintered samples both showed a pure α alumina phase. In case of the zirconia phases, some very low monoclinic peaks were observed on the diffraction pattern of the powder, whilst they disappeared after sintering. A nano 1.5YSZ XRD analysis performed by Paul [36] showed that the monoclinic content in the nano 1.5YSZ particles before sintering was about 32 vol%. Although the

monoclinic peaks in Figure 4.5 are very low, due to only 15wt% 1.5YSZ addition in the alumina matrix, it proves that some monoclinic zirconia particles exist in the powder. These were transformed to metastable tetragonal zirconia in the ZTA sample during sintering and maintained in the latter form after cooling, therefore, the final sintered samples showed no monoclinic phase.

In order to produce a full tetragonal ZTA, the sintering temperature needs to be higher than the temperature at which the monoclinic zirconia transforms to its tetragonal phase. With the purpose of finding out the transformation temperature of the zirconia phases, high temperature XRD was performed. Figure 4.6 shows the results for the same ZTA powder used above. The monoclinic to the tetragonal phase transformation occurred at ~1200°C, indicating that sintering performed at a higher temperature yielded ZTA samples with fully tetragonal zirconia, which was needed for the subsequent zirconia phase transformation toughening.

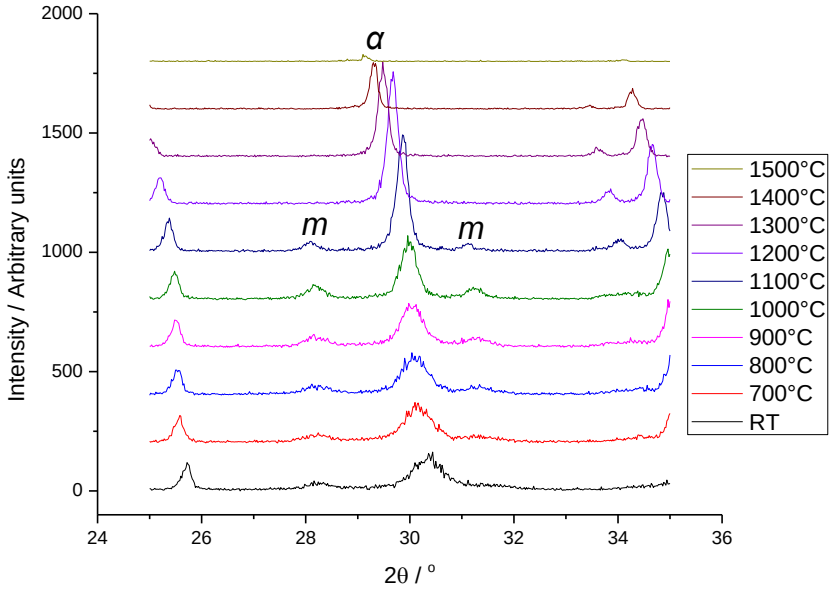

Figure 4.6 High temperature XRD patterns of the 15% 1.5Y-ZTA powder.

4.3 Green Forming

4.3.1 Effect of Freon on the powder structure and green densities

The green forming process was divided by two steps, i.e. spray freeze drying to produce powders from the suspensions and subsequent sample pressing, including

die pressing and iso-pressing. During the first step, one of the reasons for using spray freeze drying was to produce spherical powder granules that possessed enhanced flowability. The addition of Freon as a foaming agent during the spray freeze during process has been proven to be effective in improving the crushability of the powders by producing large amount of pores in the granules in nano YSZ powder [98]. In this study, the comparison of the powders and green bodies with and without Freon was also investigated in order to learn whether the addition of Freon in the alumina and ZTA could provide the same benefit. The results for the alumina powder are reported in this section, since the ZTA powders showed the same behaviour with respect to Freon additions.

The SEM images of the spherical granules with and without Freon and produced by spray freeze drying are shown in Figure 4.7. It is evident that the former showed very dense surfaces with some large pores, whilst the latter showed a higher degree of pores but with a finer pore size.

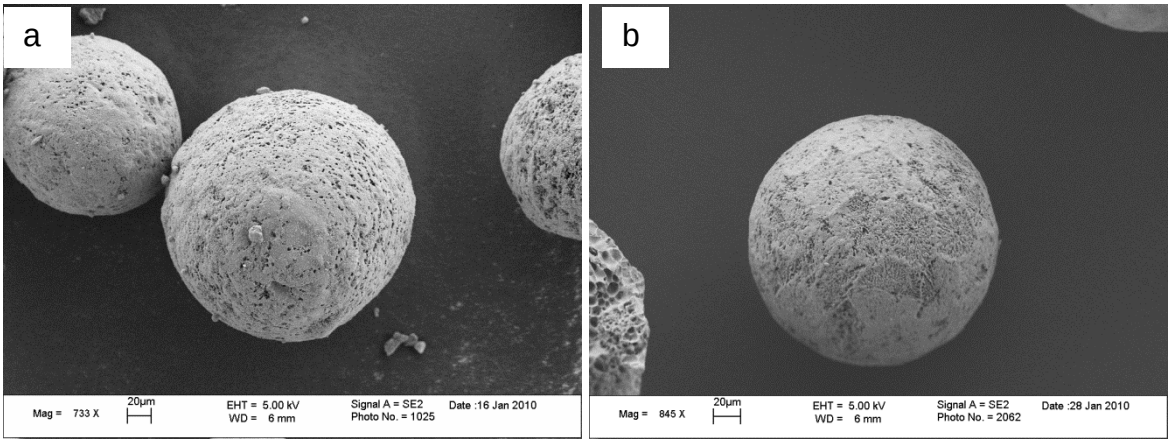

Figure 4.7 Granulated alumina powders prepared by spray freeze drying (a) without Freon, (b) with Freon.

By cutting the granule in half, the structure inside the granule was revealed, Figure 4.8. For the granule without Freon, the pore size was large and it showed a wide pore size distribution. However, for the granule with Freon, the pore size was much smaller and more uniform. The structure difference indicates that a more homogeneous microstructure could be achieved with the assistance of Freon, yielding a powder that could be crushed more easily during die pressing, reducing the number of residual agglomerates present in the green bodies.

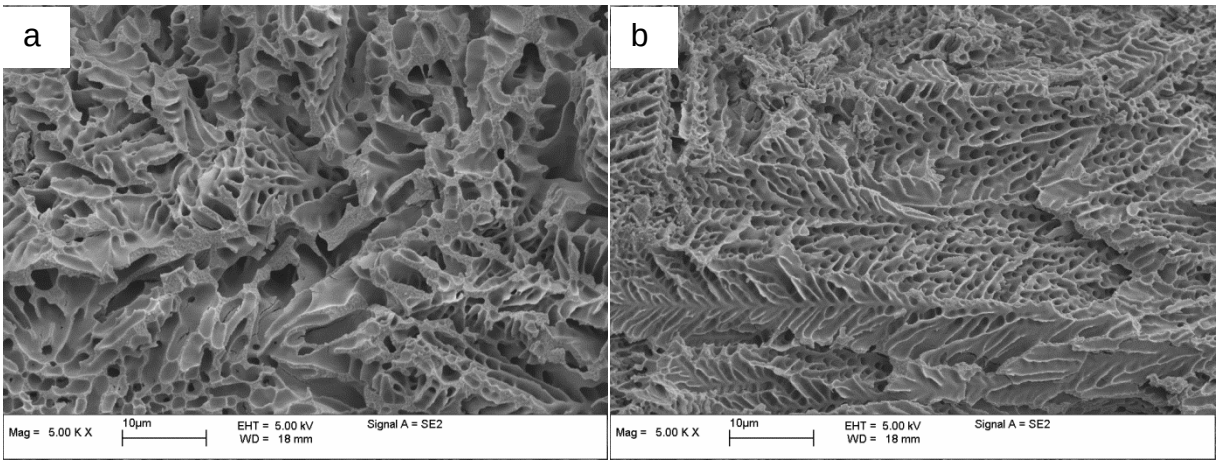

Figure 4.8 Fracture surfaces of the alumina powders a) without Freon, b) with Freon.

The flow rate measurements of the granulated alumina powders are shown in Table 4.2; the data for the powders with and without Freon were very similar, viz. 0.23 and 0.26 g s^{-1}, respectively. The slight reduction for the powder with Freon was probably due to the more porous surface and less densely packed powder surface, but it was negligible in terms of affecting the overall flow rate.

Table 4.2 Flow rate of alumina powder sieved to 125-250 µm

	Flow rate / g s^{-1}
No Freon	0.26±0.01
2% Freon	0.23±0.01

Figure 4.9 shows the green densities of the alumina samples die pressed under the loads ranging from 150 MPa to 550 MPa; it was found that the density of the samples increased with increasing pressure to until about 52% of theoretical at ~ 360 MPa. The comparison of the samples with and without Freon revealed no significant difference with respect to the density obtained across the whole range of pressures. A similar green density could be caused by the porous structures in both powders shown in Figure 4.7 and 4.8.

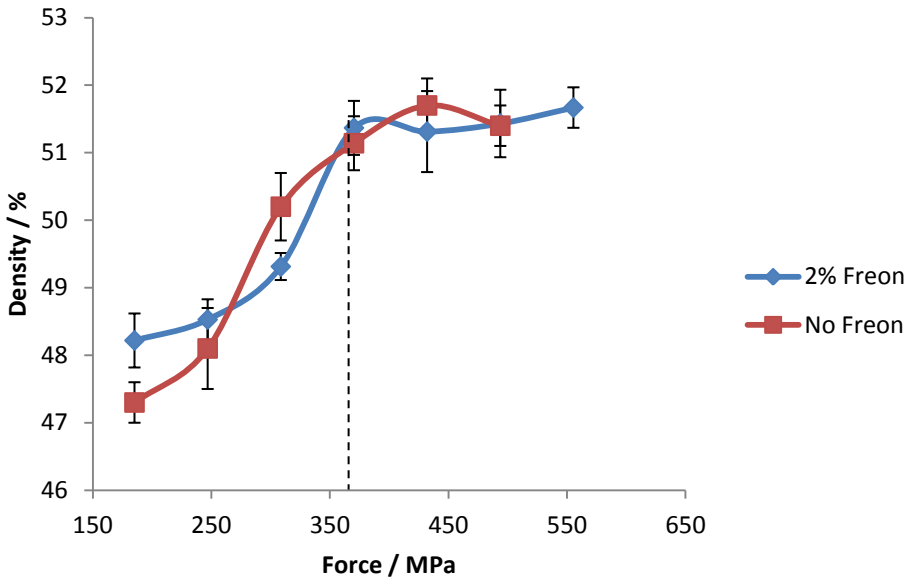

Figure 4.9 Densities of the die pressed alumina samples.

Using the same pressing load, 360 MPa, the fracture surfaces of the green bodies with 2% Freon revealed an obvious improvement in the homogeneity of the microstructure than the one without Freon, Figure 4.10. This result suggests that the crushability was significantly improved by the addition of Freon, leading to very homogeneous microstructure and no residual agglomerates, even though it did not show a benefit with respect to the density of the die pressed samples.

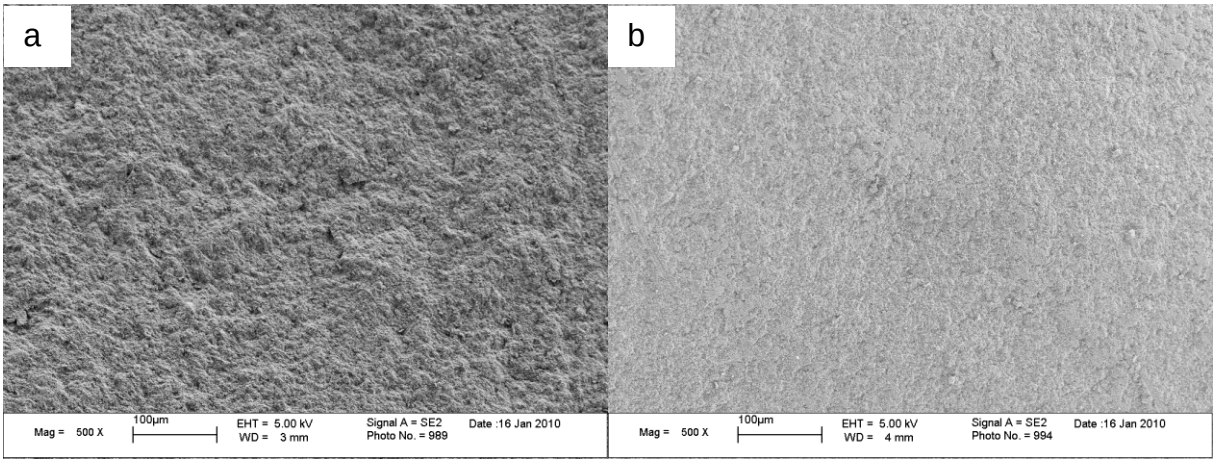

Figure 4.10 Green microstructures of the die pressed samples: a) Die pressed without Freon; b) Die pressed with 2 vol% Freon.

Moreover, the density measurement shows that the maximum density of the die pressed alumina samples was only ~ 52%. The density was further improved by using isostatic pressing at 250 MPa, which increased the density to about 54%.

4.3.2 ZTA powder and die pressing

In a nanocomposite material, the homogeneity of the second phase in the matrix highly affects the mechanical properties of the composite. Therefore, it is of critical importance to learn the microstructure and zirconia distribution in the matrix of the ZTA green body. From the EDX analysis of the 10% 1.5Y-ZTA granules and the fracture surface of the green body, the YSZ contents in the granules and the fracture surfaces were both very consistent at 10 wt% YSZ content, Figure 4.11. This suggests that any inhomogeneity of the zirconia particle distribution was at a scale smaller than the size of the particles.

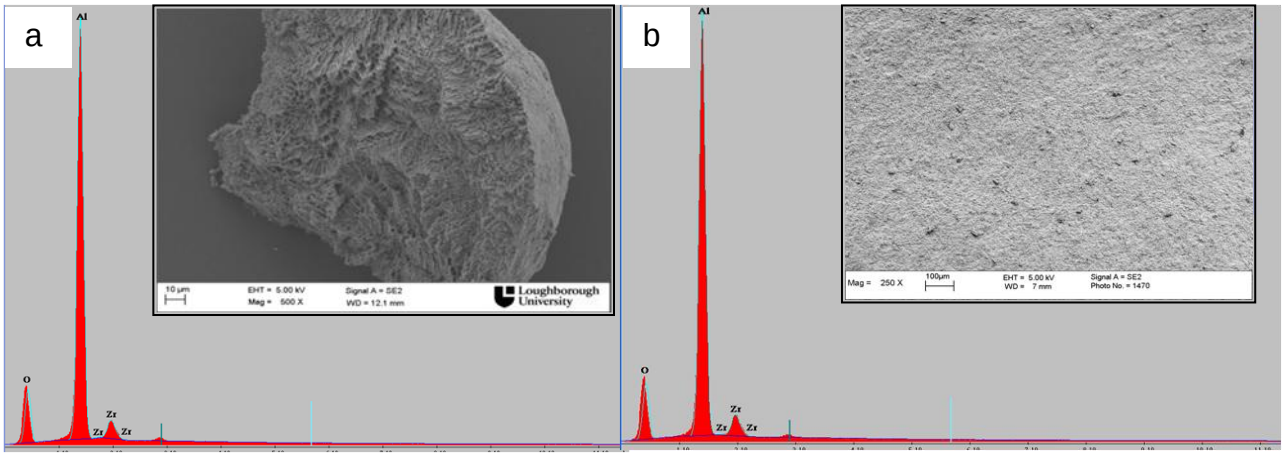

Figure 4.11 EDX analysis and the microstructures of a) the 10% 1.5Y-ZTA powder surface and b) the green fracture surface.

The densities of the die pressed 10% 1.5Y-ZTA samples are compared with those of the alumina in Figure 4.12; a 2-3% increase in the green density was observed for the ZTA samples across the full pressing range. The possible explanation for this increase may be that the nano sized 1.5YSZ particles were able to fill the voids between the alumina particles, therefore resulting in higher packing efficiency. Figure 4.13 shows the comparison of the green densities of the ZTA samples with different 1.5YSZ contents and using the same die pressing pressure, 360 MPa. Although

there are relatively large error bars, an increasing trend of the green density with the zirconia content was observed, which could be another indication that the nano sized zirconia particles provided the effect of improving the dense packing of the green pellets. Before binder removal and sintering, an additional iso-pressing process of 250 MPa was applied to all the samples in order to improve the homogeneity of the density.

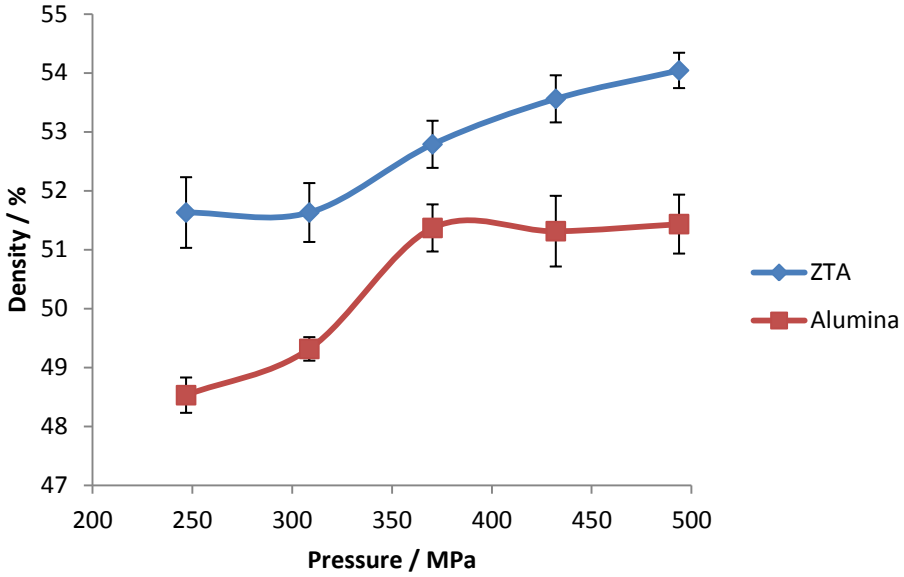

Figure 4.12 Densities of the die pressed 10% 1.5Y-ZTA and alumina samples.

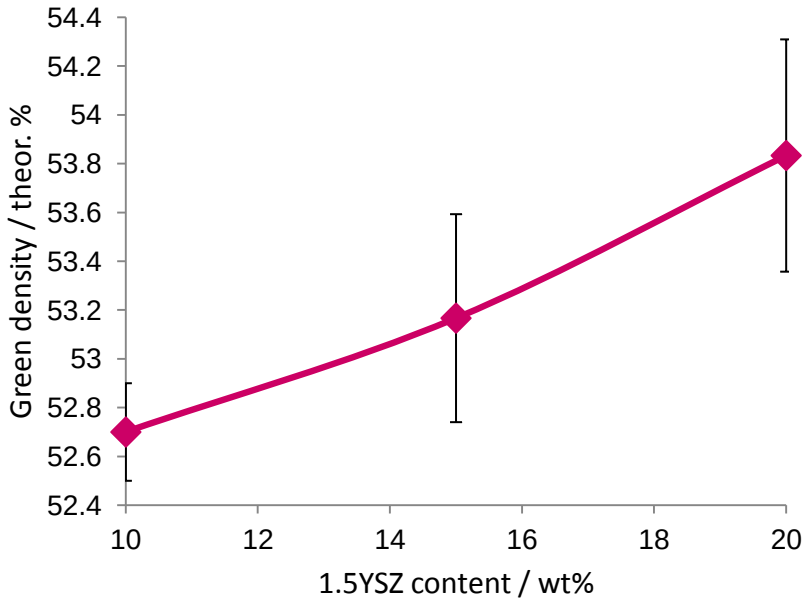

Figure 4.13 Effect of 1.5YSZ content on the green densities of the ZTA die pressed samples.

4.4 Sintering of Alumina

In order to produce the alumina samples with a range of grain sizes and full densities, single stage and two-stage sintering were performed. Comparing the two sintering methods, the two-stage sintering had the benefit of providing better control of the grain growth during densification and so samples with much finer grain sizes could be produced, although the process was more time and energy consuming than single stage sintering.

4.4.1 Single stage sintering

The densities and grain sizes of the samples sintered using single stage sintering cycles are summarised in Table 4.3. To exclude the effect of heating rate on the density and grain growth, all the sintering experiments were conducted at a constant heating rate of 10°C/min.

Table 4.3 Densities and grain sizes of alumina after single stage sintering, the results shown in bold represents the optimal conditions identified

Sample	T / ˚C	t / h	Density / % TD	Mean grain size / µm
Al_2O_3-CSS-1400-2*	**1400**	**2**	**99.1±0.2**	**1.2±0.1**
Al_2O_3-CSS-1400-10		10	98.8±0.5	1.6±0.2
Al_2O_3-CSS-1350-2	1350	2	97.8±0.3	0.8±0.1
Al_2O_3-CSS-1350-5		5	98.3±0.2	1.4±0.2
Al_2O_3-CSS-1300-2	1300	2	97.2±0.3	0.6±0.1
Al_2O_3-CSS-1300-5		5	97.5±0.3	0.7±0.1
Al_2O_3-CSS-1300-8		8	97.9±0.5	0.8±0.1

* CSS stands for “conventional single stage” followed by the sintering temperature, °C, and time, h.

In Table 4.3, the results show that the density of the alumina samples increases with the sintering temperature, as expected. The required density of above 99% was achieved at the sintering temperature of 1400˚C. For the samples sintered at 1300 and 1350˚C, even with an increase in the sintering time, full density still could not be achieved. This result indicates that the effect of sintering duration on the resultant sample density is less significant than the effect of sintering temperature as

expected. The microstructures of the samples sintered under different conditions are shown in Figure 4.14. The observed microstructure actually confirms the density measurement shown in Table 4.3, as large amount of unsealed pores were observed in the images of alumina samples sintered at 1350 and 1300˚C for 2 hours. From the above observation, the condition at 1400˚C for 2 hours (bolded in Table 4.2) is considered to be the optimal single stage sintering condition for the alumina material from the current trials, achieving 99.1±0.2% density and a mean grain size of ~1.2 μm.

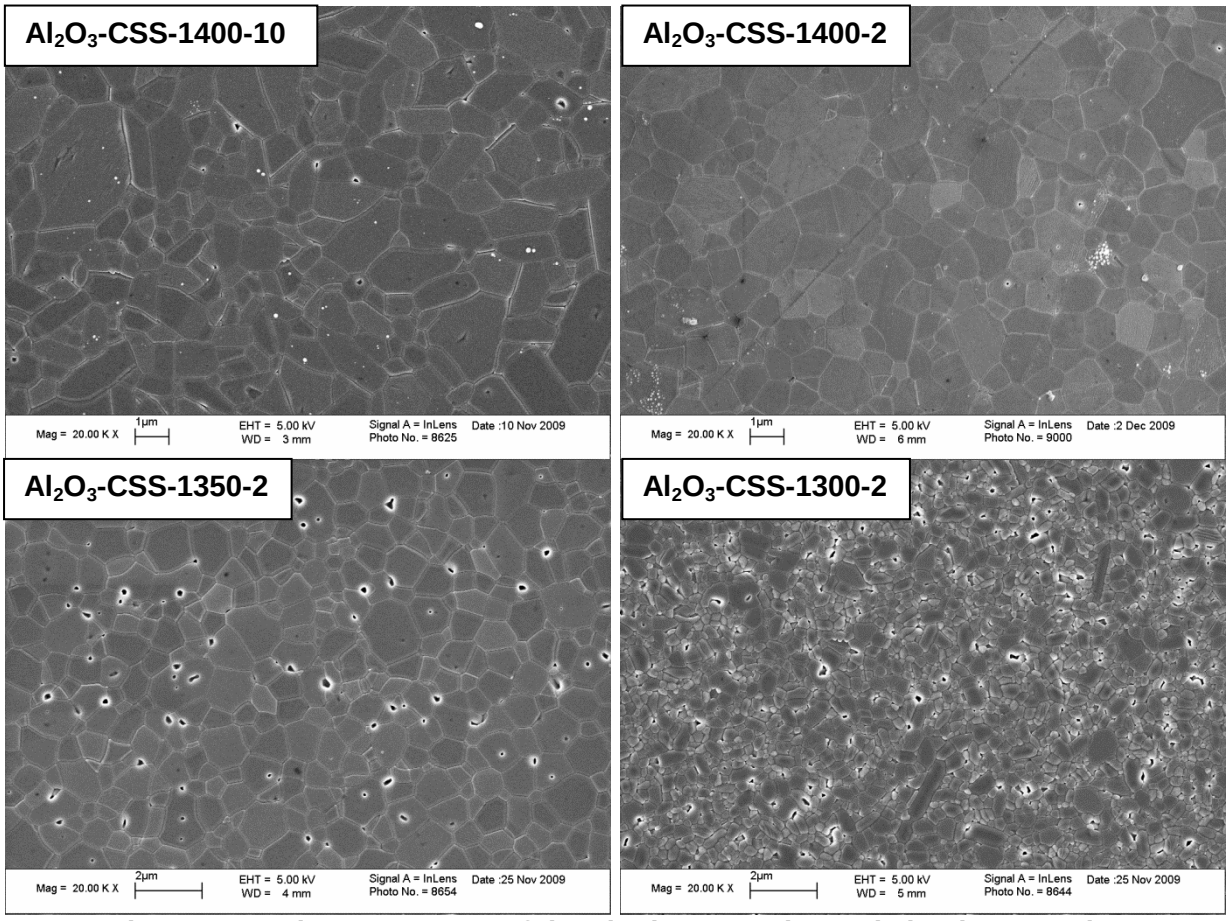

Figure 4.14 Microstructures of the single stage sintered alumina samples.

4.4.2 Two stage sintering

As mentioned before, two-stage sintering can produce samples with much finer grain sizes due to the restraint of grain growth during the second sintering step. In the first sintering step, the sample needs to achieve a relatively high density to render pores unstable. In order to simulate the first step in the two-stage sintering cycle, the green

samples were heated to 1300, 1350 and 1400°C for a very short time (0.1 min) and the densities of these samples were listed in the last three rows of Table 4.4. As explained in several publications [9,88,94], a density of ≥ 80% is required after the first sintering step. Therefore, a first stage sintering temperature of 1300°C was considered to be sufficient to achieve full density after two-stage sintering. However, as the density above 90% after the first stage is suggested by other researchers [108] for alumina sintering, the temperature 1400°C was needed to meet the 90% density requirement. Therefore, all three temperatures, 1300, 1350 and 1400°C, were used in the first stage of the two-stage sintering to investigate the best sintering condition. The temperature for the second sintering step was selected in a range from 1150 to 1300°C.

Table 4.4 Density and grain size of slip cast alumina after two-stage sintering, the results shown in bold represents the best conditions identified.

Sample	T_1 /°C	T_2 /°C	t_2 /h	Density / % TD	Mean grain size /μm
Al_2O_3-CTS-1300-1200-5*	1300	1200	5	93.2	0.32±0.04
Al_2O_3-CTS-1350-1200-5	**1350**	**1200**	5	96.7	0.55±0.08
Al_2O_3-CTS-1350-1200-10			10	96.8	0.56±0.08
Al_2O_3-CTS-1350-1200-20			**20**	**98.0**	**0.59±0.07**
Al_2O_3-CTS-1350-1250-5		1250	5	98.0	0.65 0.13
Al_2O_3-CTS-1400-1150-5	1400	1150	5	95.5	0.64±0.07
Al2O3-CTS-1400-1150-10			10	95.7	0.68±0.16
Al_2O_3-CTS-1400-1150-20			20	97.7	0.88±0.05
Al_2O_3-CTS-1400-1250-2		1250	2	96.3	0.53±0.04
Al_2O_3-CTS-1400-1250-5			5	97.4	0.56±0.05
Al_2O_3-CTS-1400-1250-10			10	98.3	0.68±0.02
Al_2O_3-CTS-1400-1300-5		1300	5	97.8	0.59±0.02
Al_2O_3-CTS-1400-1300-10			10	98.7	0.73±0.04
Al_2O_3-CSS-1400-0.1	1400			91.1	0.43±0.05
Al_2O_3-CSS-1350-0.1	1350			86.4	0.31±0.03
Al_2O_3-CSS-1300-0.1	1300			83.9	0.34±0.05

*CTS stands for “conventional two stage”, the following numbers represent the sintering temperatures T_1 and T_2 and the sintering time t_2

Based on the trials using different sintering temperatures and dwell time in Table 4.4, the sample with the smallest grain size and a relatively high density was ‘Al_2O_3-CTS-1350-1200-20’, which was sintered using 1350°C as T_1 and 1200°C as T_2 and was

held at T_2 for 20 hours. The density achieved was 98% theoretical and the grain size was as fine as 0.6 μm, which was about half of the grain size of the single stage sintered samples. Figure 4.15 shows the density-grain size relationships of the two sintering methods (single / two-stage sintering) used in this thesis. It can be observed that, in the case of the two-stage sintering, with the increase of the density from 96% to 98%, the grain size only increased from 0.55 to 0.59 μm, which is much less significant compared to the case in the single stage sintering. With the further increase in the density to ~98.7%, the grain size increased from 0.59 to 0.73, however, the increase was still lower than that of the single stage sintering. It is considered that the application of hybrid two-stage sintering could help to control the grain growth during densification.

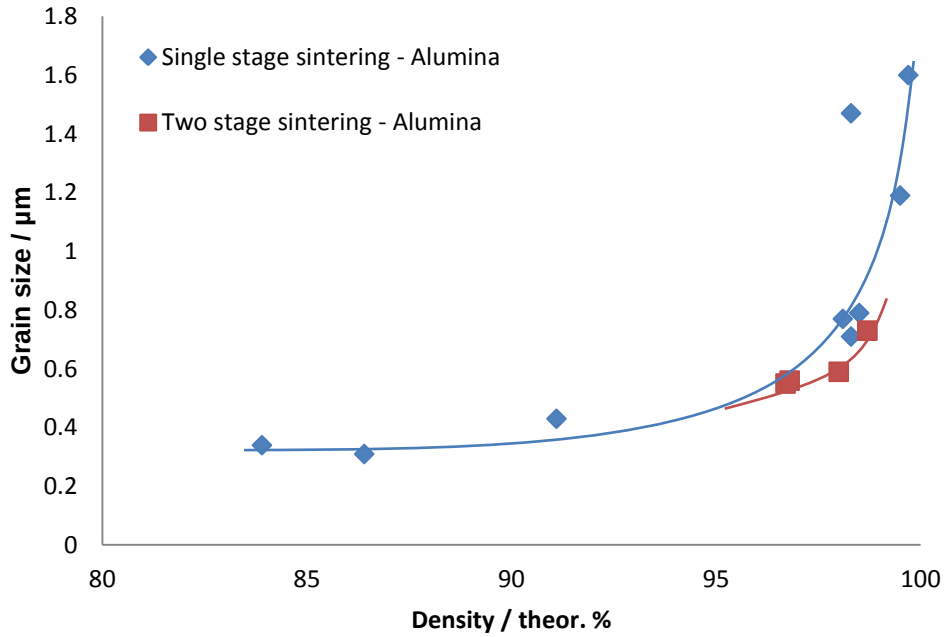

Figure 4.15 The grain size change with density of the samples sintered using single stage sintering and two-stage sintering.

4.5 Sintering of ZTA

4.5.1 Single stage sintering

Single stage sintering trials were also carried out on ZTA samples, the sintering conditions and the densities and grain sizes of the 1.5Y-ZTA are listed in Table 4.5. The best sintering conditions for the 10% to 20% 1.5Y-ZTA specimens from the trials

were‘10ZTA-CSS-D-1450-10’, ‘15ZTA-CSS-1500-10’, ‘20ZTA-CSS-1500-10’ as highlighted in Table 4.5.

Table 4.5 Density and grain size of 1.5Y-ZTA samples after sintering, the results shown in bold represents the best conditions identified.

Sample	T /°C	t / h	Density / % TD	Mean Al_2O_3 grain size /μm	Mean YSZ grain size /μm
10ZTA*-CSS-1450-2	1450	2	98.2	0.72±0.05	0.14±0.06
10ZTA-CSS-1450-10	**1450**	**10**	**98.8**	**0.95±0.10**	**0.15±0.08**
10ZTA-CSS-1475-2	1475	2	97.5	0.78±0.06	0.16±0.06
10ZTA-CSS-1500-2	1500	2	98.6	0.93±0.08	0.17±0.07
10ZTA-CSS-1500-5	1500	5	98.7	1.07±0.09	0.16±0.06
10ZTA-CSS-1550-2	1550	2	99.1	1.20±0.09	0.19±0.08
15ZTA-CSS-1450-10	1450	10	98.2	0.9±0.1	0.15±0.06
15ZTA-CSS-1450-20	1450	20	99.3	1.1 ±0.1	0.16±0.05
15ZTA-CSS-1500-5	1500	5	99.8	0.9±0.1	0.18±0.06
15ZTA-CSS-1500-10	**1500**	**10**	**99.3**	**1.0±0.1**	**0.16±0.05**
15ZTA-CSS-1500-15	1500	15	99.1	1.1±0.1	0.24±0.10
15ZTA-CSS-1500-20	1500	20	99.2	1.3±0.1	0.29±0.10
20ZTA-CSS-1450-10	1450	10	97.3	0.8±0.1	0.22±0.10
20ZTA-CSS-1500-5	1500	5	97.4	1.0±0.1	0.22±0.11
20ZTA-CSS-1500-10	**1500**	**10**	**98.8**	**1.1±0.1**	**0.28±0.10**

*10ZTA stands for 10% 1.5Y-ZTA

It was found that the YSZ content in ZTA can affect the density after sintering. As mentioned in section 4.3.2, the green densities of the ZTA samples increased with increased zirconia contents. However, high green body density does not necessary result in high density after sintering. On the contrary, it has been found that the densification process was more difficult for the ZTA samples with higher zirconia contents. As shown in Figure 4.16, when the identical 1450˚C, 10 hours condition was applied to the ZTA samples with different zirconia additions, the measured density after sintering decreased as the zirconia content. For the 10% 1.5Y-ZTA sample, for example, above 99% density could be achieved using the sintering condition 1450˚C for 10 hours, whilst a sintering condition of 1500˚C for 10 hours was required for the 15 and 20% 1.5Y-ZTA. In addition, this trend was also obvious when comparing the sintering temperatures of the alumina, which has 0% zirconia content, and ZTA samples. The more demanding sintering conditions required by the ZTA was considered to be due to the increase in the activation energy for the

densification of alumina caused by the zirconia grains sitting at the three point junctions of the alumina grains [86].

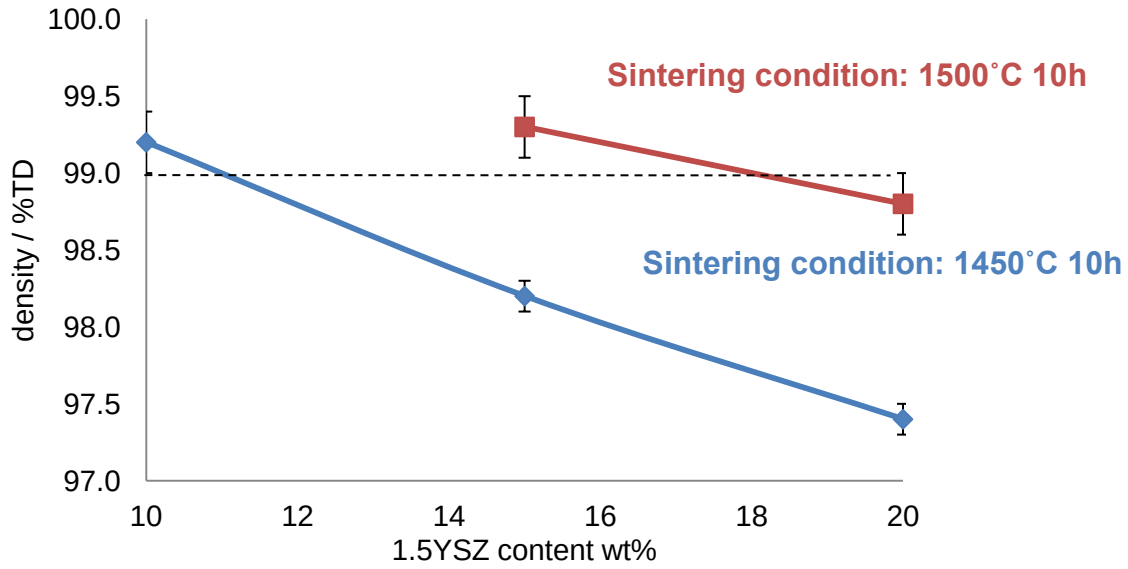

Figure 4.16 Effect of 1.5YSZ content on the sintered density of the ZTA die pressed samples, the dash line shows the level of the 99% density.

The microstructures of the above samples with full density and around 1 μm alumina grain sizes are shown in Figure 4.17. The difference of the zirconia grain size was mainly caused by the different amount of zirconia added in the ZTA. In should be noted that the micrograph at the bottom right of the Fig 4.17 corresponds to the microstructure of a two-stage sintered 15% 1.5Y-ZTA sample, which will be discussed in the next section.

It was also found that, for the ZTA samples with the different yttria contents in the YSZ, the sintering conditions required were not affected. For instance, the 10% 3Y-ZTA samples achieved a density above 99% and a mean grain size of 0.9 μm using the sintering conditions of 1450˚C for 10 hours, which is also the most suitable sintering condition for the 10%1.5Y-ZTA. This is probably because it is the alumina matrix that is undergoing densification in both cases.

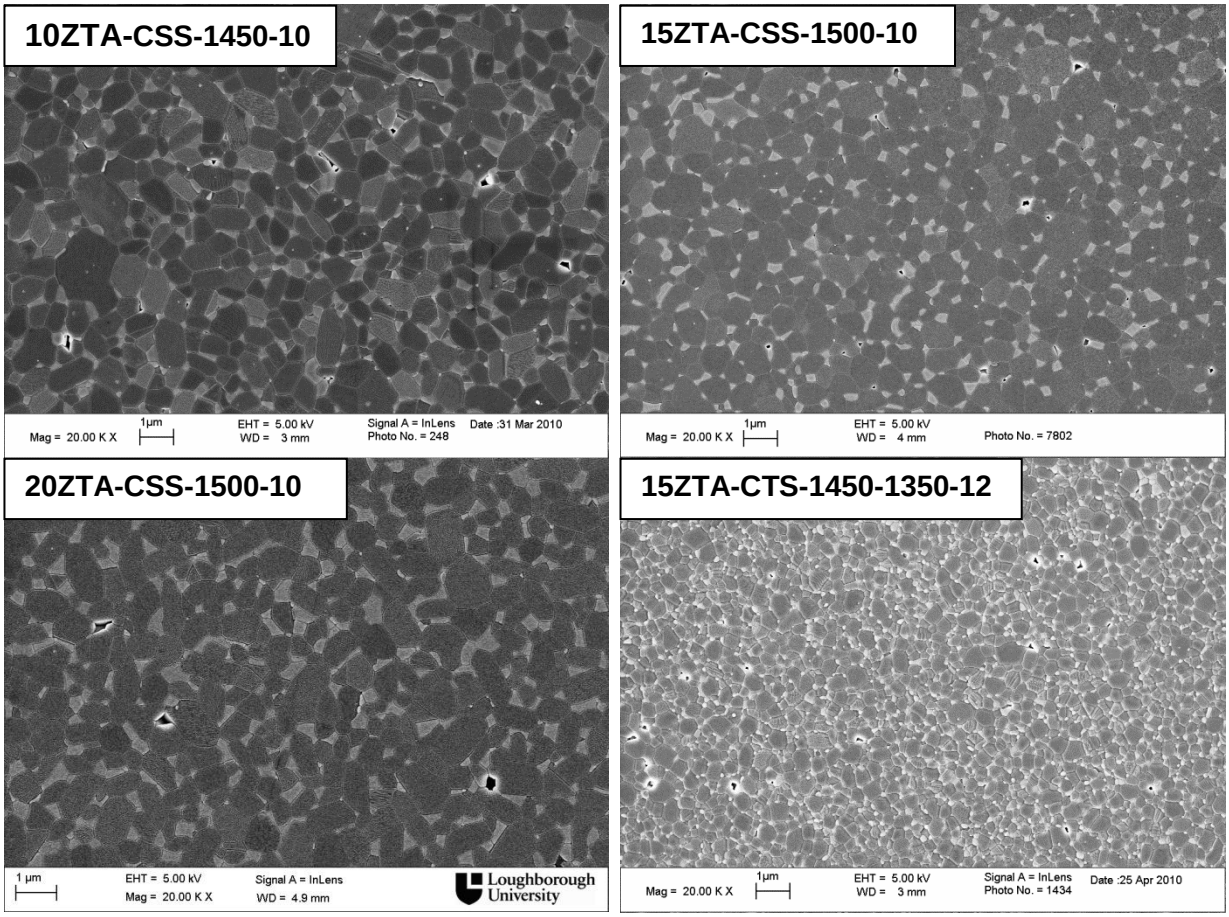

Figure 4.17 Micrographs of the ZTA sintered samples.

4.5.2 Two-stage sintering

As already shown in Figure 4.17, the two-stage sintered 15% 1.5Y-ZTA sample showed much finer grain sizes compared to the single stage sintered samples. The detailed sintering trials and the densities and alumina grain sizes achieved are listed in Table 4.6. The temperature of the first step was set constant at 1450°C, which is adequate to reach full densification according to [106], meanwhile different combinations of T_2 and holding time were used in the second stage. It should be noted that the two-stage sintering was only carried out on the 15% 1.5Y-ZTA, this is because the mechanical properties and high strain rate performance studies, which will be discussed in chapter 5 and 6, both showed that 15% 1.5Y-ZTA were superior to the other ZTA materials.

Table 4.6 Results of sintering 15%1.5Y-ZTA samples

Sample code	T_1 / °C	T_2/°C	t /h	Density / % TD	Alumina grain size /nm
15ZTA-TSS-1450-1300-10	1450	1300	20	95.5	402±18
15ZTA-TSS-1450-1350-8		1350	8	97.9	487±14
15ZTA-TSS-1450-1350-12		**1350**	**12**	**99.3**	**519±25**
15ZTA-TSS-1450-1350-20		1350	20	99.3	559±20
15ZTA-TSS-1450-1400-8		1400	8	99.2	551±15
15ZTA-CSS-1450-0.1	1450	/	0.1	90.0	350±15

The sample failed to achieve full densification after holding at 1300°C for 20 hours, indicating that 1300°C was too low to activate grain boundary diffusion. On the other hand, the sample still maintained a fine grain size when T_2 was 1350°C or 1400°C. The most suitable sintering condition to achieve a full density and fine grain size was considered to be '15ZTA-TSS-1450-1350-12'. The alumina grain size was about half of that achieved using the single stage sintering.

Figure 4.18 shows the density-grain size relationships of the alumina and 15% 1.5Y-ZTA samples using single-stage and two-stage sintering. The comparison between the alumina grain sizes of alumina and ZTA after single stage sintering shows that the grain sizes are constantly lower in the ZTA samples across the whole range of the densities. As has discussed in section 4.5.1, the densification was found to be more difficult for the ZTA samples, due to the higher activation energy required. On the other hand, the zirconia grains located on the three point junction of the alumina grains helped to suppress the grain growth of the alumina grains, resulting in smaller grain sizes. This result is consistent with the previous researches [43,100,101]. In addition, by comparing the two-stage sintering with the single stage sintering, the grain size-density curve representing the former revealed a notable decrease in the degree of grain growth.

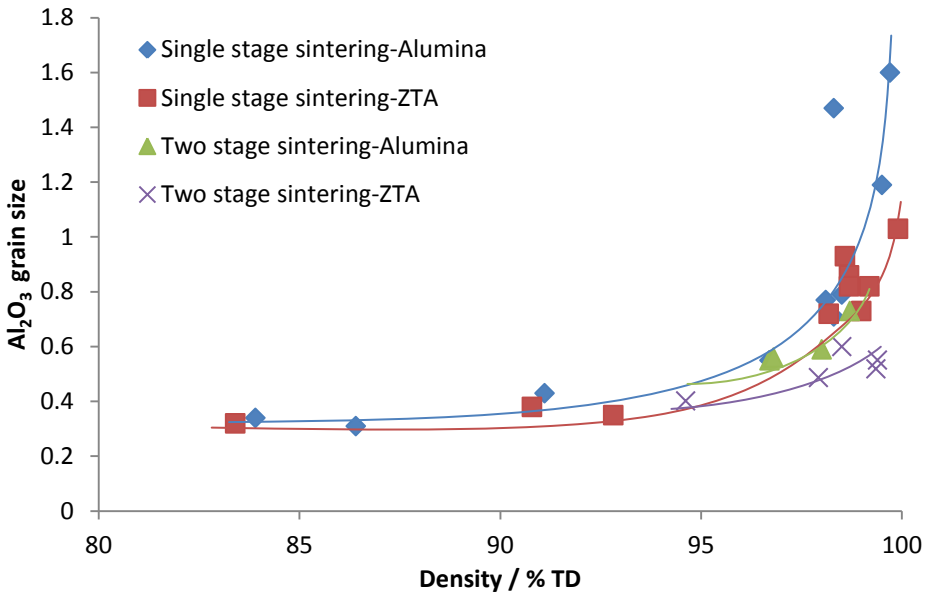

Figure 4.18 The grain size change with density of the alumina and ZTA samples sintered using single stage sintering and two-stage sintering.

4.5.3 Zirconia distribution in the ZTA sintered samples

Uniform zirconia grain sizes are considered to be essential to prevent stress concentration during static or high strain rate applications. Due to the contrast difference between the zirconia grains and the surrounding alumina matrix, the nano 1.5YSZ grain size was measured by manually extracting the zirconia grains from the ZTA FEGSEM image using a gray scale segregation method. The zirconia grain size distribution as well as the area percentage of zirconia were measured using UTHSCA Image Tool 3.0 software. This work was repeated on ten images collected from different positions of the sample and an example was shown in Figure 4.19. The measured area fraction of the zirconia grains for a 10% 1.5Y-ZTA sample was about 6.2%. Since the volume content of zirconia was about 6.8 vol% (corresponding to 10 wt%), the two values were considered consistent, which confined the homogeneous distribution of the YSZ grains.

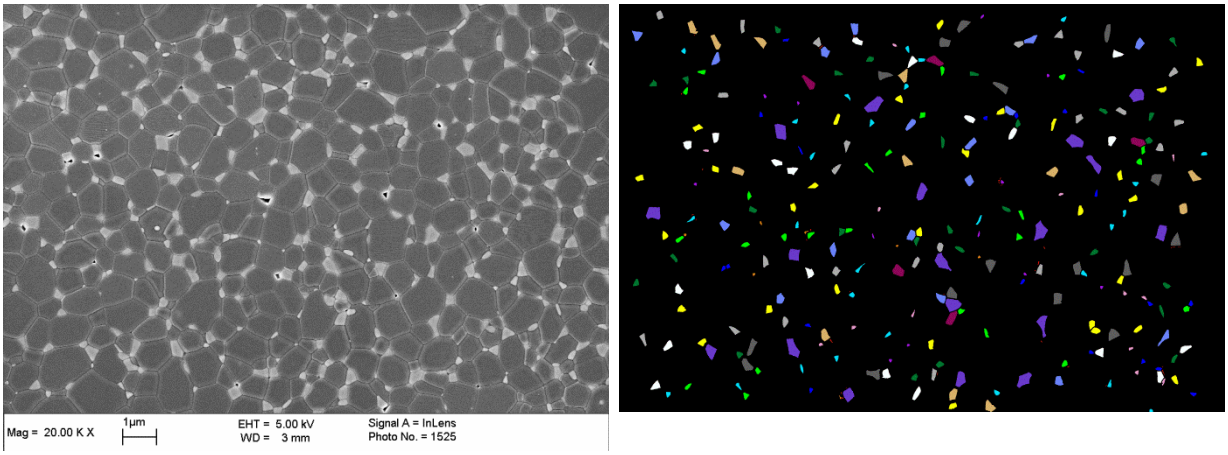

Figure 4.19 (a) The original FEGSEM image of a 15% 1.5Y-ZTA; (b) Extraction of the YSZ particles from the image (a), the different colours suggest the different zirconia grain size levels.

The zirconia grain size distribution was investigated, as shown in Figure 4.20. The 10% and 15% ZTA showed reasonably narrow distributions, whilst the 20% ZTA showed a slightly larger grain size distribution. However, comparing to the grain size distribution of the commercially available Morgan composite with coarser alumina and zirconia grain sizes, the ZTA samples prepared in this work showed much narrower grain size ranges.

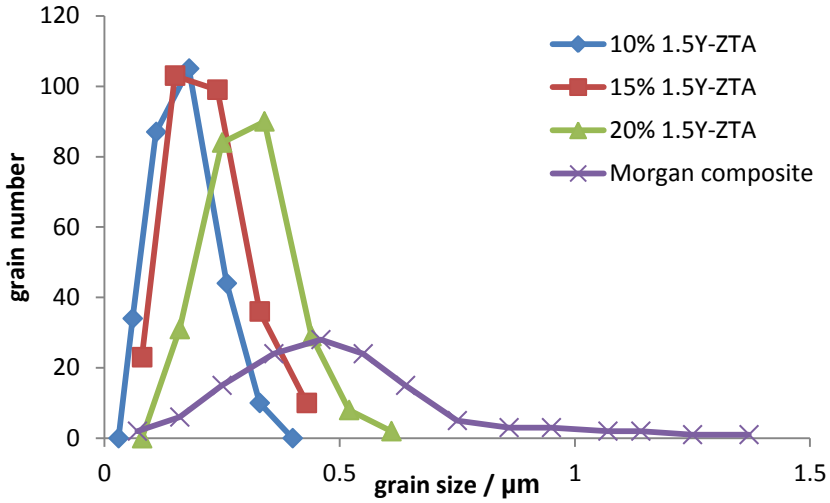

Figure 4.20 Grain size distribution of the ZTA samples.

4.6 Other Samples

In addition to the alumina and 1.5Y-ZTA samples, other samples listed in Table 3.2 were also prepared. The Morgan composite was provided by the company using a

confidential (and unknown) processing route. The 10% 3Y-ZTA and nano 1.5YSZ were sintered using the sintering conditions listed in Table 4.7. The samples were used for comparison with the alumina and nano 1.5Y-ZTA materials for their mechanical and/or high strain rate performances.

Table 4.7Sintering conditions of the samples and their densities and grain sizes

Sample code	Sintering T / ˚C	Heating time / h	Density / theor.%	Mean grain size	
				Al_2O_3 / μm	YSZ / nm
10% 3Y-ZTA	1450	10	98.8±0.5	0.9±0.2	150±50
Morgan composite	/	/	98.4±0.3	1.9±0.32	460±120
Nano 1.5YSZ	T_1 1250 $T_2$1150	5	96.7±0.4	/	110±15

4.7 Summary

- The particle sizes, zeta-potential and viscosities of as-received suspensions were studied to make sure the suspensions were sufficiently stable to be used and to produce granulated powders with a nano particle size. The phases of the alumina and zirconia grains before and after sintering were also analysed using XRD.

- Fine submicron alumina and ZTA die pressed samples were prepared from spray freeze dried powders with high flowability and crushability. It has been found that the addition of 2 vol% Freon in the powder improved the crushability of the powder and also the homogeneity of the green microstructure, whilst not affecting the flowability.

- Sub-micron alumina samples have been successfully produced, yielding mean grain sizes in the range from 0.6 to 1.6 μm, with full density, using the single and two-stage sintering methods. The grain growth control effect for the two-stage sintering has been demonstrated. The ZTA samples were also sintered using both single stage sintering and two-stage sintering. The mean alumina grain sizes were in the range of 0.5 to 1.2 μm and full density was achieved.

- The zirconia content has shown effects on the densities of the die pressed bodies and the sintering conditions. With the increased zirconia content in ZTA, the green density increased, this might be explained by the nano zirconia particles occupying the voids between the alumina particles during pressing. However, densification became more difficult with increasing zirconia content and higher sintering temperature was required to achieve full density. According to literature, this could be because the zirconia grains at the three-point junction of the alumina grains increased the activation energy of grain boundary diffusion; this effect also resulted in the restriction of grain growth during the densification. The homogeneity of the zirconia grains distribution was studied using FEGSEM observation and EDX analysis and it was measured to be very homogeneous.

5 MECHANICAL PROPERTIES AND POST TESTING CHARACTERISATION

Mechanical properties such as hardness, toughness, strength, fracture mode and wear resistance can affect the performance of armour ceramics. Therefore, it is of great importance to understand how these mechanical properties can be altered to suit its service environment. Since the mechanical properties are controlled by the microstructures of the materials, the purpose in this chapter is, first, to find out the relationship between the microstructure and the hardness and toughness properties, which is introduced in section 5.1. In addition, due to the importance of the zirconia phase transformation on the improved mechanical properties in ZTA, the zirconia phase transformability of the ZTA samples with different grain sizes and zirconia contents is investigated in section 5.2. Based on the above study, selected alumina and ZTA samples with similar alumina grain sizes (1 μm) were tested using 4-point bend and wear testing, which is analysed in sections 5.3 and 5.4; the most suitable materials for the subsequent high strain rate testing are suggested. In section 5.5, a case study on the residual stress induced by the zirconia phase transformation in ZTA is studied, in order to investigate the contribution of the transformation on the residual stress formation under static and high strain rate stresses. By analysing the stress change and distribution after a static indentation testing, it is possible to understand the materials' behaviour under high pressure impact and its ability to resist deformation; this work is discussed in section 5.6.

5.1 Vickers Hardness and Indentation Toughness

The hardness and toughness of ceramic materials are related to their microstructures, including the densities and the grain sizes. For ZTA materials, the zirconia content and the amount of yttria stabiliser can also highly affect the mechanical properties due to the different transformability.

5.1.1 Variation in hardness and toughness with density, zirconia content and the amount of yttria stabiliser

The Vickers micro-indentation hardness values are plotted against the densities of the various samples in Figure 5.1. The samples to be compared include alumina, 1.5Y-ZTA with zirconia contents from 10 to 20 wt%, 10% 3Y-ZTA and the Morgan composite samples. All the samples were densified to above 98% of theoretical and the samples were all single stage sintered, in order to exclude the effect from the grain size.

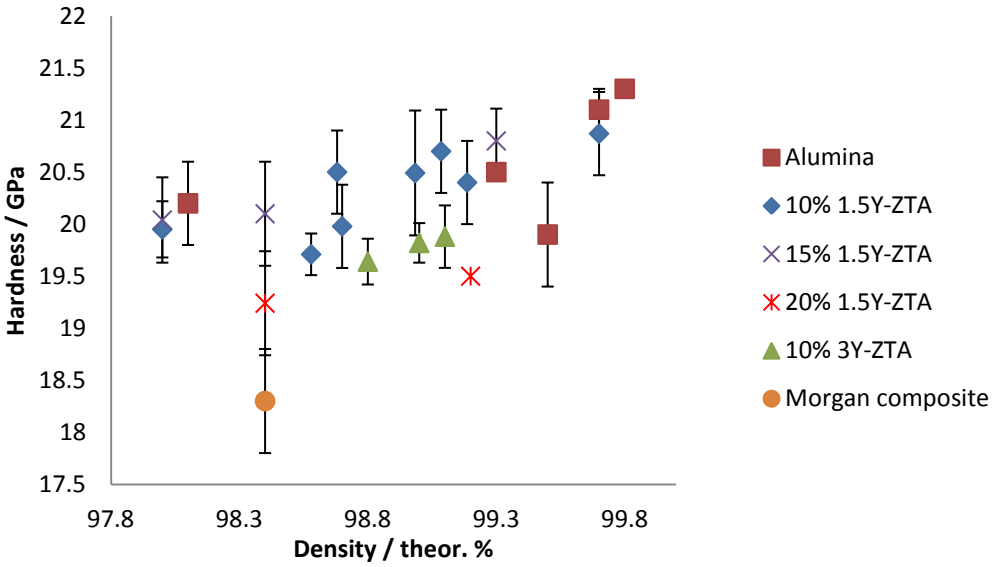

Figure 5.1 Variation in hardness with density.

With the exception of the Morgan composite, for which there is only one data point, there is a gradual increasing trend of hardness with increasing density. This is as expected because the porosity is one of the most important defects that could result in stress concentration and lead to crack generation, and therefore, causes less resistance to plastic deformation. However, it should be noted that most of the hardness values (except for the Morgan composite) were within a range of 19 GPa to 21 GPa, which means the effect of increasing density on the sample's hardness is very limited.

Comparing the hardness values of the samples with different zirconia content, the pure alumina showed the highest hardness (21.5 GPa) and the 10% and 15% nano

1.5Y-ZTA both showed their maximum hardness values of 21.4 and 20.8 GPa, respectively. The 20% 1.5Y-ZTA showed the lowest hardness (19.2 GPa). Therefore, a general reduction of hardness with the increasing zirconia content was also observed; again this was expected because the zirconia inclusions were softer than the alumina matrix. However, the reduction was more significant for the 20% 1.5Y-ZTA, which could be related with the formation of larger zirconia grain sizes when the zirconia content was higher. Casellas [69] suggested that the increased zirconia grain size yielded a higher transformability of the grains due to a lower activation stress required by the zirconia phase transformation. When the zirconia grains can transform easily, m-ZrO_2 tends to be formed under a low load level and when the load is fully applied, the material turns to display less resistance to plastic deformation. This could explain the significant hardness reduction for the 20% sample.

Comparing the ZTA samples with different yttria stabiliser content, i.e. 10% 1.5Y-ZTA and 10% 3Y-ZTA, the latter showed a slightly lower hardness (19.9 GPa), which could also be explained by their different zirconia transformation ability. However, the difference is within the error bar, and, therefore, is negligible. In addition, all the fine grain sized alumina and ZTA samples showed significant improvement on the hardness in comparison to the benchmark sample, the Morgan composite.

The variation in toughness with density is plotted in Figure 5.2. For all the ZTA samples, it was observed that the toughness increased slightly with the sample's density. Comparing the alumina and the 1.5Y-ZTA samples, the increased zirconia content from 0 to 20 wt% has significantly increased the toughness value from ~3.0 in alumina to ~5.5 MPa $m^{1/2}$ in 20 wt% ZTA, which is due to the contribution from the zirconia phase transformation toughening effect as the zirconia content increases.

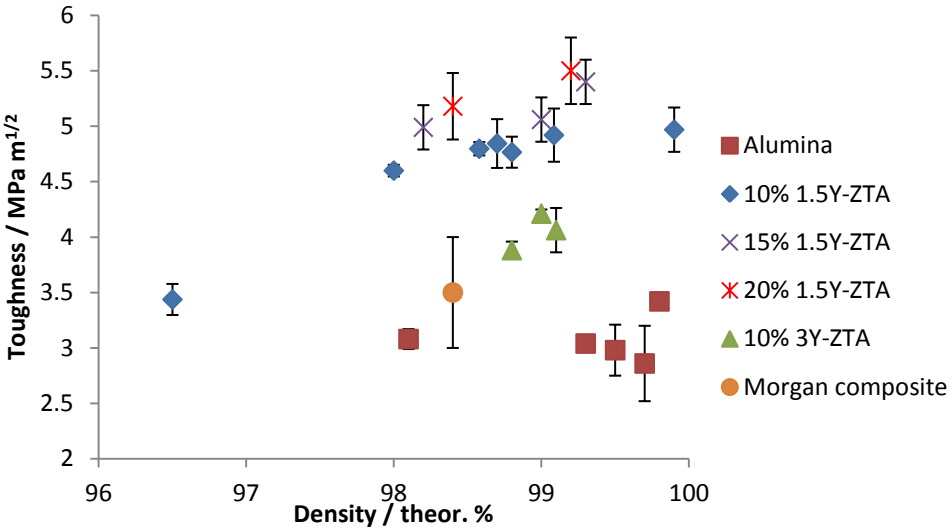

Figure 5.2 Variation in toughness with density.

On the other hand, it can be observed that the toughness of the ZTA increased as the yttria content in the YSZ additive decreased; the 10% 3Y-ZTA showed a toughness of 4.1 MPa $m^{1/2}$, whilst the toughness of 10% 1.5Y-ZTA was 4.7 MPa $m^{1/2}$. The reason for the difference is probably related to the different transformability of the zirconia additions. It is expected that the transformability of the zirconia grains in 1.5Y-ZTA is higher compared to that in 3Y-ZTA [118], which will, therefore, have resulted in the increased transformation toughening effect.

To confirm this, the Raman spectra of the 10% 3Y and 1.5Y-ZTA samples before (Figure 5.3 (a)) and after indentation toughness tests (Figure 5.3 (b)) were compared. In Figure 5.3 (a), it can be observed that the spectra of both samples showed the distinctive peaks of the tetragonal structure before the test. In Figure 5.3 (b), it is evident that the intensities of the two monoclinic peaks at 175 and 188 cm^{-1} as a result of zirconia phase transformation were much more significant in the 1.5Y-ZTA sample compared to those in the 3Y-ZTA sample. Therefore, it is evident that the transformability of the YSZ in the 1.5Y-ZTA is higher than that in the 3Y-ZTA. Several researches [118,119] have observed that the critical grain size of zirconia phase transformation for different yttria contents in YSZ are different; the critical grain sizes are 1.2 µm for 3YSZ and a much reduced critical grain size of 110 nm was observed in 1.5YSZ. In the present work the mean zirconia grain sizes were 150-170 nm, which is much smaller than that required for 3Y-ZTA but is very close to

that required for 1.5Y-ZTA, hence the latter showed a higher transformability than the former.

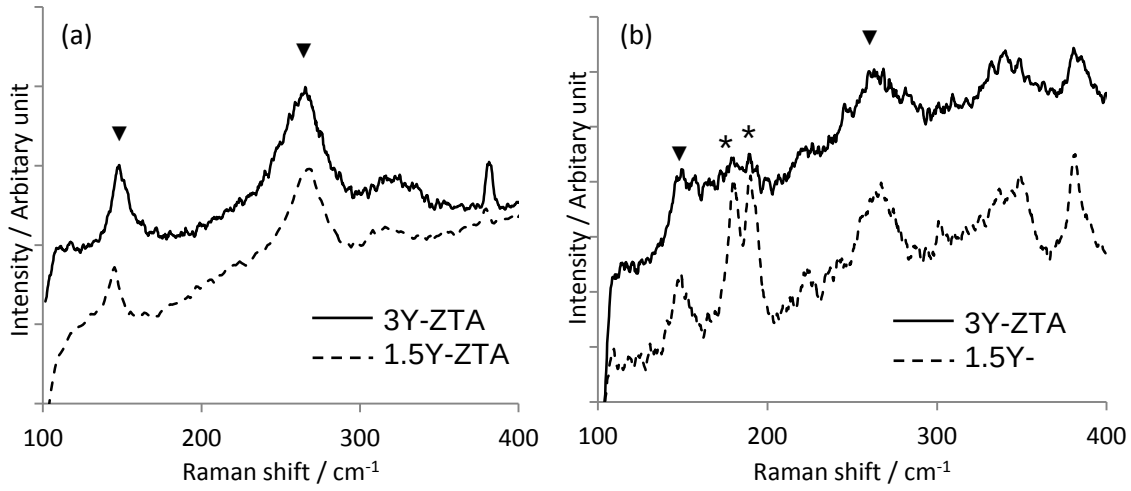

Figure 5.3 Raman spectra of 10% 3Y-ZTA and 10% 1.5Y-ZTA before (a) and after (b) indentation test, ▼ zirconia tetragonal peaks, * zirconia monoclinic peaks.

5.1.2 Hardness and toughness with grain sizes

The alumina and 15% 1.5Y-ZTA samples with alumina grain sizes ranging from 0.5-1.6 μm and densities above 98% were produced using various sintering and heat treatment conditions as discussed in Chapter 4. The relationship between the alumina grain size and the indentation hardness and fracture toughness values are shown in Figure 5.4 (a) and (b), respectively, whilst the relationship between the alumina grain size and the YSZ grain size is shown in Figure 5.5.

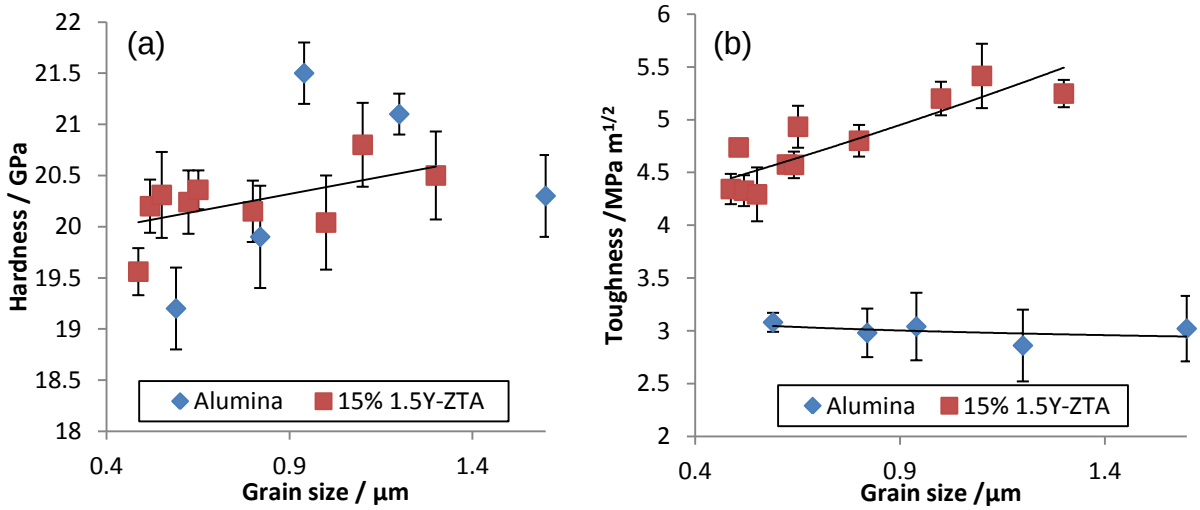

Figure 5.4 Variation in (a) hardness and (b) toughness with mean Al_2O_3 grain size for alumina and 15% 1.5Y-ZTA samples.

From Figure 5.4 (a), the hardness of alumina increased with the increasing grain sizes from 20 to 21.5 GPa, however, it is considered that the relationship between the grain size and hardness was affected mainly by the density difference in the case of the alumina samples. The sample with 1.6 μm grain size and 99.8% density showed the highest hardness, 21.5 GPa, whilst the sample with 0.6 μm grain size and 98.0% density showed the lowest hardness value of 20 GPa. It is very difficult to clearly separate the effect of grain size from the effect of density for the alumina samples. A similar trend between the hardness and grain size was observed for the ZTA samples, as shown in Figure 5.4 (a). However, it should be noted that the hardness difference for both alumina and ZTA materials in the available grain size range is not significant.

Figure 5.4 (b) shows that there is a negligible change in toughness for pure alumina with grain size over the range investigated, whilst the addition of zirconia particles resulted in an increase in toughness with the alumina grain size in the ZTA samples. For the pure alumina samples, although the increasing grain size increased the crack bridging force, which could have toughened the material, a change of fracture mode from intergranular to transgranular fracture was observed with the increase in the grain size and this is considered to be the main effect. On the other hand, the reason that the ZTA samples did not follow the same trend as the alumina should be due to the change in the zirconia grain sizes. As shown in Figure 5.5, the increase in alumina grain size in the ZTA samples was accompanied by a coarsening of the zirconia grains. As suggested by Casellas [69], the zirconia grain size increase lead to the increased transformability. This suggests that although the increasing alumina grain size can be potentially harmful to the toughness of the material, the increased zirconia grain size provided a stronger toughening effect due to the increased zirconia phase transformability.

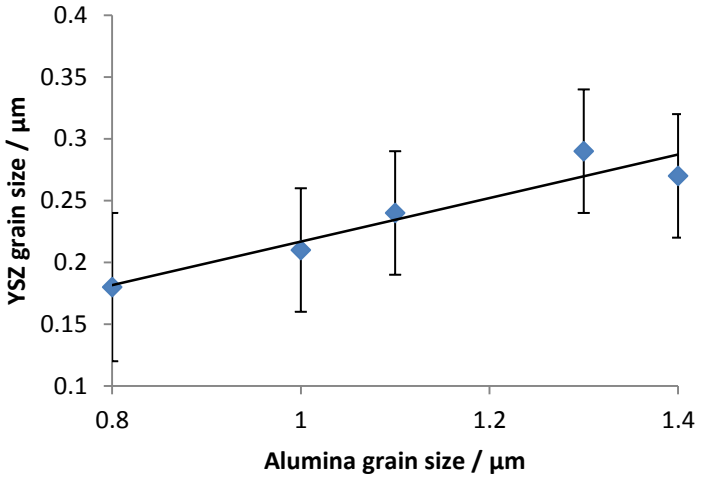

Figure 5.5 Relationship between YSZ and alumina grain sizes in 15% 1.5Y-ZTA

By observing the crack propagation using FEGSEM, it was found that in the 15% 1.5Y-ZTA samples the cracks were mainly intergranular, but transgranular fracture always occurred when the cracks met larger alumina grains, as shown in Figure 5.6. As transgranular fracture requires less energy to proceed compared to that required by the intergranular fracture, it is suggested that a finer alumina grain size and a narrow grain size distribution is desirable for increasing the toughness.

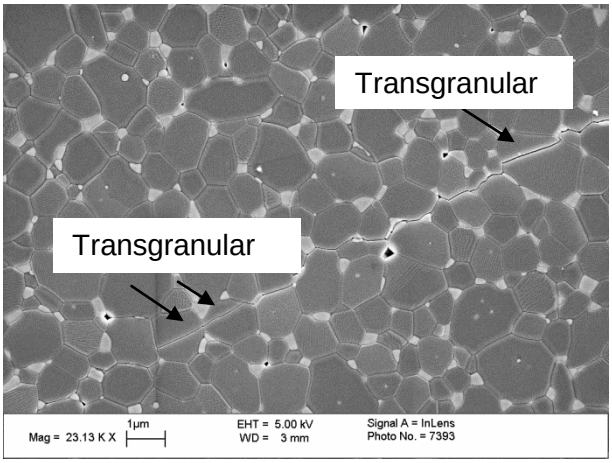

Figure 5.6 Crack propagation in a 15% 1.5Y-ZTA, the arrows indicate the transgranularly fractured grains.

In summary, the density and grain size can affect the hardness and toughness. With increased zirconia content, the hardness reduced but the toughness increased. The increase of zirconia grain size improved the transformability, leading to a higher

toughness in ZTA materials. In addition, the toughness of the 3Y-ZTA sample was lower than that of the 1.5Y-ZTA sample due to the lower transformability. The samples which showed a combination of high hardness and toughness are listed in Table 5.1. These samples are considered to be the most suitable potential armour materials and are further studied in terms of their strength, wear properties and high strain rate performance in sections 5.4 and 5.5.

Table 5.1 Processing, microstructural and mechanical properties of the samples showing both high hardness and toughness

Sample code	Sintering T / ˚C	Hold time / h	Density /theor. %	Mean grain size		Hardness / GPa	Toughness / MPa $m^{1/2}$
				Al_2O_3 / μm	YSZ / nm		
Alumina	1400	10	99.0±0.2	1.2	/	21.5±0.5	3.0±0.3
10% 1.5Y-ZTA	1450	10	99.0±0.2	0.9±0.1	170±60	21.4±0.8	5.1±0.4
15% 1.5Y-ZTA	1500	10	99.3±0.3	1.0±0.1	210±60	20.8±1.1	5.4±0.6
20% 1.5Y-ZTA	1500	10	98.8±0.3	1.1±0.1	280±60	19.3±2.3	5.5±0.3

5.2 Zirconia Phase Transformation in ZTA

As suggested in section 5.1.2, the increased zirconia grain size lead to an increase in toughness, which could be due to the higher transformability of the larger zirconia grains. Therefore, a quantitative measurement of the transformability is carried out in this section, in order to get a better understanding of the reason leading to this relationship.

As is mentioned in section 3.6.4.1, there is a linear relationship between the toughness (K_{Ic}) of a zirconia based material and its transformability ($V_f d^{1/2}$) [116]. According to Eqn (3.2), this relationship can be explained as a function of:

$$K_{IC} = A + B \times V_f d^{1/2}$$

where A and B are constants for a selected material. Using Raman analysis, the transformability of the ZTA ($V_f d^{1/2}$) was quantitatively measured by studying the zirconia phase transformation across a crack generated by a Vickers indentation, as illustrated in section 3.6.5.1. An example of Raman spectra obtained at different distances from an indentation is shown in Figure 5.7. The monoclinic fraction has been estimated from the relative intensities of the monoclinic doublet at 181 and 192 cm^{-1} with respect to the tetragonal peaks at 145 and 264 cm^{-1}. The calculated $V_f d^{1/2}$

value with respect to the different grain sizes and toughness of the 15% 1.5Y-ZTAs are listed in Table 5.2.

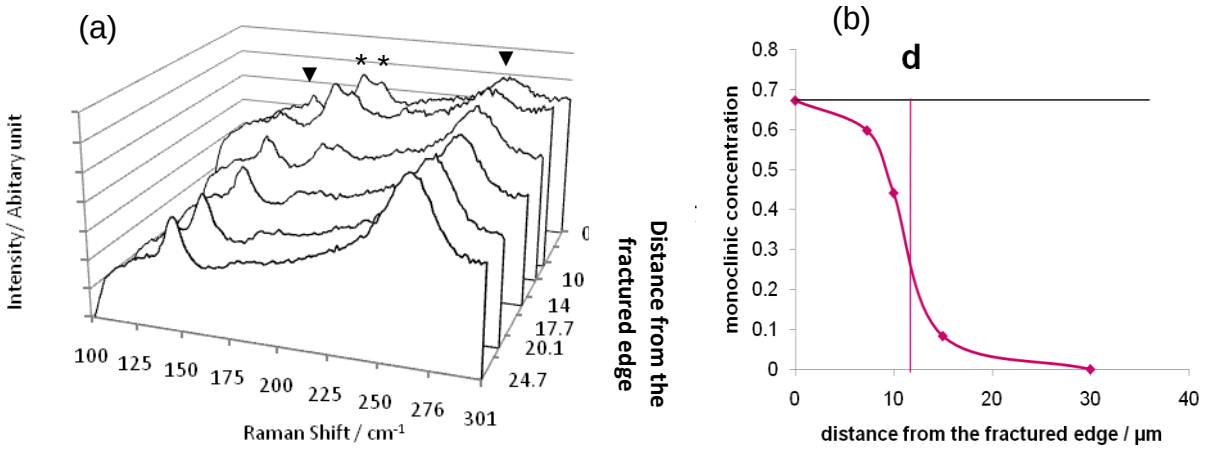

Figure 5.7 (a) Raman spectra acquired at different distances from the crack. The mapping line is shown in Figure 3.14 (a);(b) relationship between the monoclinic concentration measured from the spectra in (a) and distance to the fracture edge.

Table 5.2 Transformability parameters and the mechanical properties of 15% 1.5Y-ZTA sintered at different conditions

Material	Mean grain size		*HV* / GPa	K_{Ic} / MPa m$^{1/2}$	V_f	*d* / μm	$V_f d^{1/2}$ / (μm)$^{1/2}$
	Al_2O_3 / μm	YSZ / nm					
Sample 1	0.8±0.1	180±60	19.8±0.4	5.0±0.4	0.69	8	1.95
Sample 2	1.0±0.1	210±50	20.8±0.3	5.1±0.3	0.71	8.5	2.07
Sample 3	1.2±0.1	250±50	20.8±0.4	5.4±0.3	0.67	12	2.32
Sample 4	1.4±0.2	270±60	20.2±0.8	5.5±0.2	0.68	16	2.72

From the above table, a linear relationship between the toughness and the $V_f d^{1/2}$ was observed and is shown in Figure 5.8. This quantitative measurement further confirmed the suggestion that the transformability increased with increasing zirconia grain size. By comparing the V_f value, i.e. the highest transformable zirconia content, for the different samples, it was found that the V_f is independent of the effect from the zirconia grain size; the increased transformability was achieved by a larger transformation zone (*d*), which caused a more pronounced shielding affect around a propagating crack. Therefore, the current results indicate that the transformation toughening effect induced by the increasing YSZ grain sizes outperforms the detrimental effect of increasing the alumina grain size in the ZTA samples. It is therefore expected that the toughness of the ZTA could be improved further if the

alumina grain size could be further limited whilst the large zirconia grain size could be maintained.

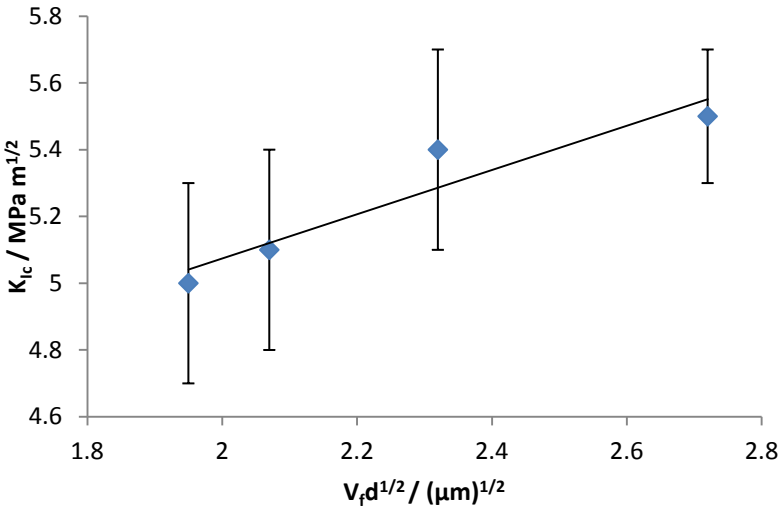

Figure 5.8 Relationship between toughness and transformability.

5.3 4-Point Bend Strength

The 4-point bend fracture strength of the alumina and 1.5Y-ZTA samples and the Morgan composite are listed in Table 5.3. The Weibull modulus of each sample was measured as well. 7 specimens were tested for each material to get a statically valid result.

Table 5.3 Average fracture strength and Weibull modulus of each sample tested

Sample	Avg. fracture strength / MPa	Weibull modulus
Alumina	355±54	4.2
10% 1.5Y-ZTA	429±67	4.6
15% 1.5Y-ZTA	528±44	8.5
20% 1.5Y-ZTA	500±62	6.6
Morgan composite*	360±36	8.4

*The results was obtained at Oxford University using a different, but similar, 4-point bend facility

It can be seen from Table 5.3 that, with the increasing zirconia content, the average fracture strength increased from 355 MPa for the alumina to above 500 MPa for the 15% and 20% 1.5Y-ZTA. This suggests that the zirconia phase transformation could help to improve the fracture strength. The phase transformation was confirmed by the Raman spectroscopy results as shown in Figure 5.9, all the 1.5Y-ZTA samples showed a certain amount of zirconia phase transformation on their fracture surfaces

after testing. An improvement of the fracture strength for the nano ZTA samples, compared to the Morgan composite sample, was also observed, which could be due to their different microstructures, including densities and grain sizes, as discussed in the previous sections.

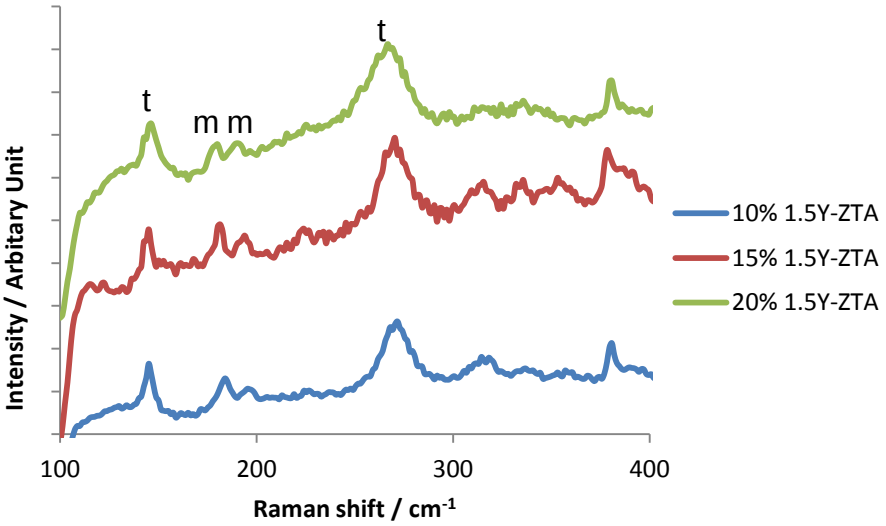

Figure 5.9 Raman spectra on the fracture surfaces after 4-point bend test.

The results show that there was a slight decrease in the fracture strength when the zirconia content was increased from 15% to 20%. According to the modified Griffith equation [120], strength should be proportional to the fracture toughness if the processing defects are unchanged. Lange [121] observed that, with the increasing zirconia content, the strength reflected the increase in fracture toughness of ZTA. However, he also noted that the materials that offered the highest toughness were generally not those that offered the highest strength. The latter normally requires a more stabilised zirconia than those offering the highest toughness. This is because the critical transformation stress determines the failure strength. If the material can transform easily, its critical transformation stress is low, which leads to a lower strength. Comparing the 20% 1.5Y-ZTA with the 15% 1.5Y-ZTA, the former had a larger zirconia grain size and a wider grain size distribution, as shown in Figure 4.20. A certain fraction of the zirconia grains even possessed grain sizes above 400 nm, which could transform very easily upon loading, as they are far larger than their critical grain size for phase transformation, ~110 nm. As a result, the highly transformable zirconia could cause a reduction in the critical transformation stress and could not effectively contribute to the fracture strength. It is considered that the

larger zirconia grain size could be the reason for the slight strength reduction for the 20% 1.5Y-ZTA.

5.3.1 Weibull modulus and fracture surface observation

The Weibull moduli of the materials were determined via Eqn (3.1) in section 3.4.6.1. the investigation was limited to 7 specimens to obtain some idea of repeatability of strength. There was a reasonably good fit with the lines fitted to the data, as shown in Figure 5.10. The Weibull modulus values, i.e. the gradient of the fitting lines, are listed in Table 5.4. It was found that the 15 and 20 % 1.5Y-ZTA and the Morgan composite had relatively high Weibull moduli, which suggests that their strength results are fairly reliable and the defects in the materials are relatively consistent. On the other hand, the alumina and 10% 1.5Y-ZTA showed much lower Weibull moduli, only ~4.5,which indicates the presence of less uniform defects in the samples.

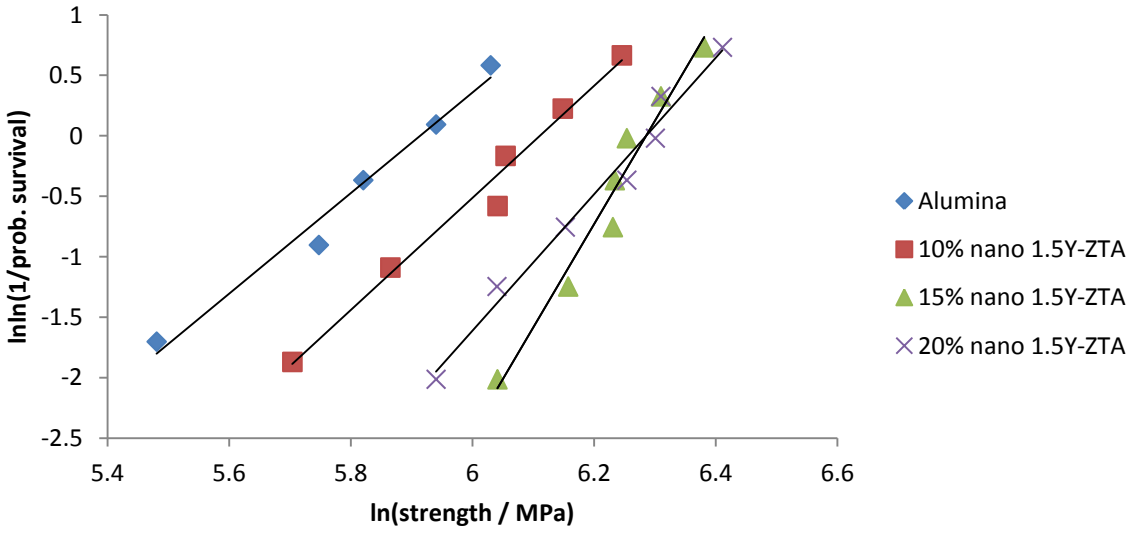

Figure 5.10 Weibull modulus plot of the materials

The existence of critical defects was confirmed by the microstructure observation and selected images are shown in Figure 5.11. It was found that the alumina and 10% 1.5Y-ZTA samples that displayed minimum strength values are likely to have failed from surface flaws. These defects were considered to arise from the processing stages and were found on the bottom surfaces, which were exposed to tension during the test. It is considered that the defects on the top surfaces did not

contribute to the failure due to the local compressive stress involved during the test. For the other samples with higher strength values, no visible defect was observed on the fracture surfaces. This suggests that it is essential to eliminate the defects formed during the processing stages so that the fracture strength, and Weibull modulus, can be improved.

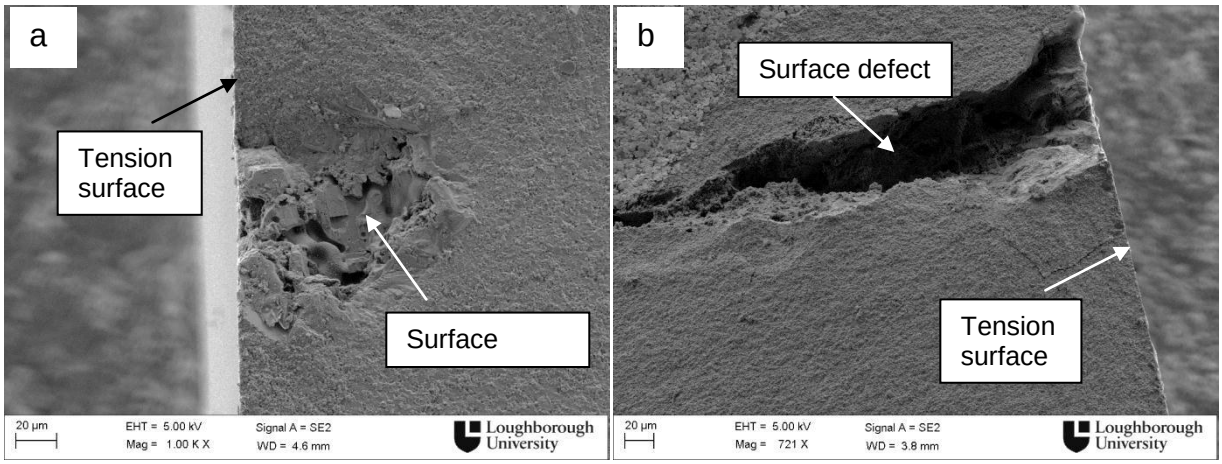

Figure 5.11 Surface defect caused by processing observed in (a) an alumina and (b) a 10% 1.5Y-ZTA with the lowest strength values.

A comparison of the fracture modes between the alumina and the ZTA materials was also performed; their fracture surfaces are shown in Figure 5.12. It was found that the alumina sample showed mainly intergranular fracture with a small amount of transgranular fracture, whilst the ZTA showed fully intergranular fracture. The area fraction of transgranular fracture was measured from 5 micrographs for 5 randomly selected positions on the fracture surfaces, the alumina showed ~17% of transgranular fracture whilst the value for the 15% 1.5Y-ZTA was 0. The different fracture mode could be another reason that led to the different strength between the alumina and ZTA samples.

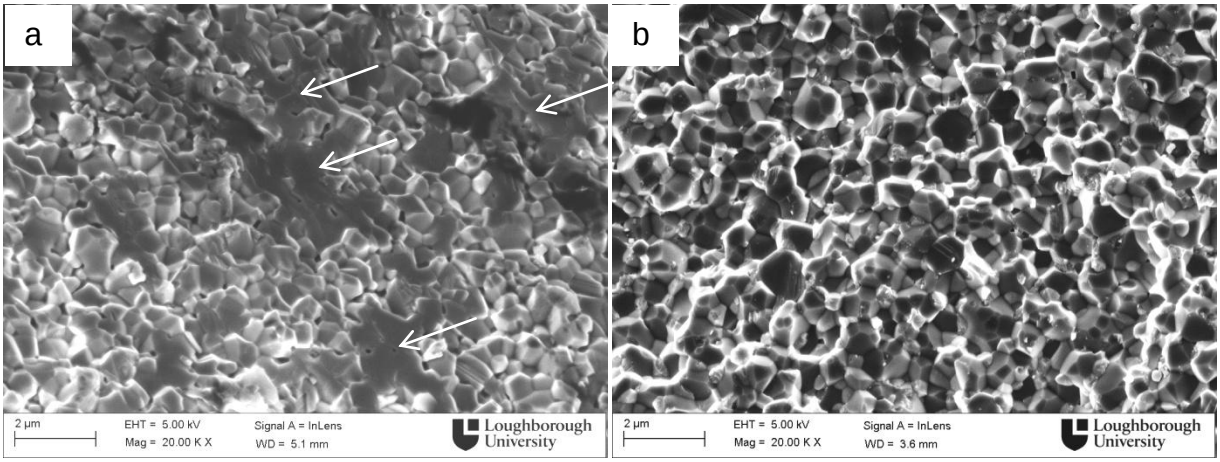

Figure 5.12 Fracture surfaces of samples after bending test (a) alumina, (b) 15% 1.5Y-ZTA, the arrows pointed the transgranular fractured grains.

5.4 Wear Resistance Testing

The wear resistance testing was performed on the alumina and 1.5Y-ZTA samples. The results are summarised in Table 5.4.

Table 5.4 Wear testing results

Sample	No. of wear cycles	Load / N	Sample volume loss/ mm^3
Alumina	100,000	20	1.59±0.50
10% nano 1.5Y-ZTA	100,000	20	0.63±0.32
15% nano 1.5Y-ZTA	100,000	20	0.32±0.11
20% nano 1.5Y-ZTA	100,000	20	0.22±0.10

From the above table, the volume loss of alumina after the wear test was much higher than for the ZTA samples. In addition, with increased zirconia content, the volume loss gradually decreased indicating that the wear resistance increased significantly with the addition of zirconia second phase particles.

5.4.1 Surface observation after wear resistance testing

FEGSEM images of the worn surfaces were taken after the wear tests to determine the wear mechanism for the alumina and ZTA samples, Figure 5.13 and 5.14. In Figure 5.13, the micrographs of the turning point (a) and the area in the centre of the wear lines (b) for the alumina sample are shown. The turning point is the position

where the wear ball reaches its full stroke during a wear cycle and then changes its moving direction, whilst the centre of the wear line is at the middle part between the two turning points. A large amount of material pull-out (c) and a large number of cracks on the worn surfaces (d) were observed as well.

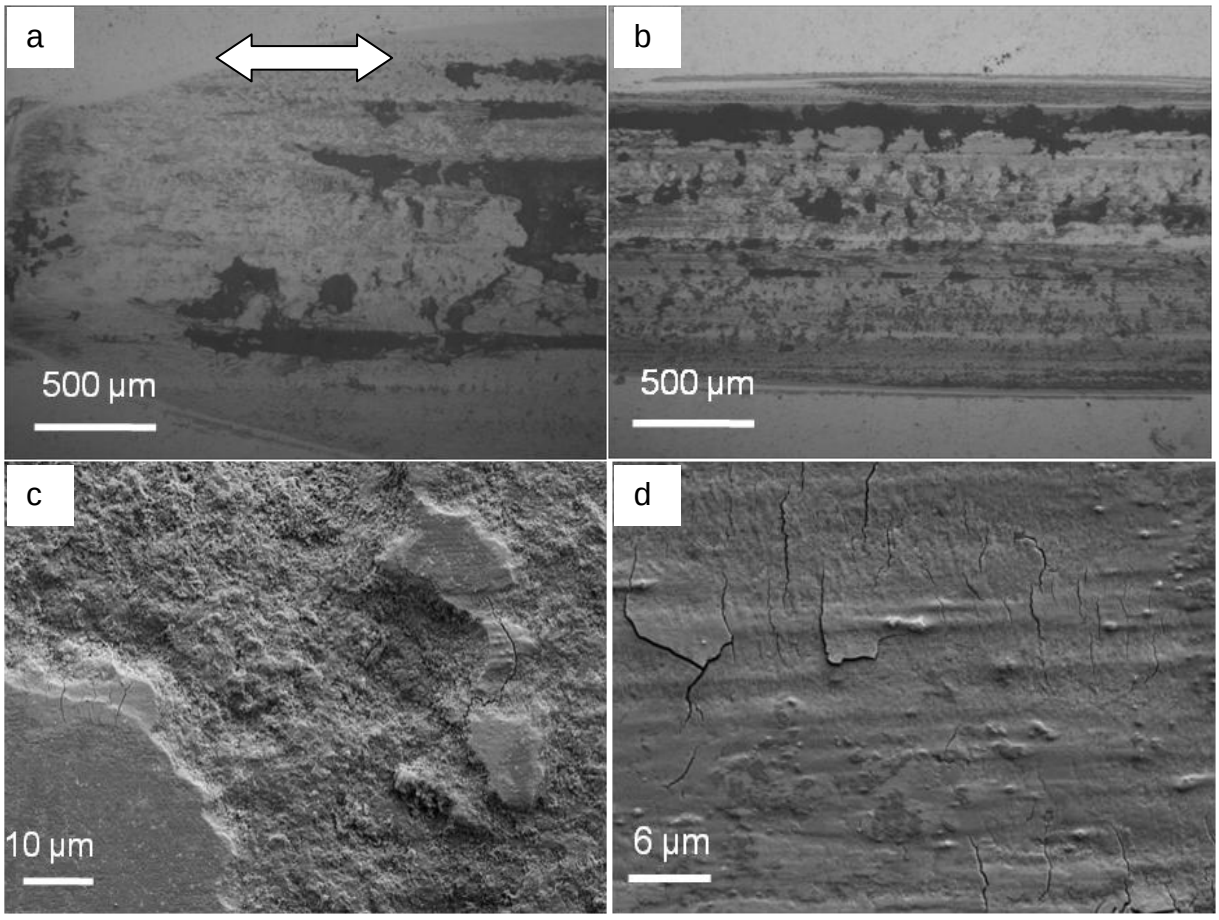

Figure 5.13 Worn surface of alumina. a) turning point of the wear line; b) centre of the wear line; c) material pull out; d) cracks on the wearing line. The arrow indicates the wear direction.

As shown in Figure 5.13, material pull-out is significant in the alumina sample along the wear line. The extent of the damage was more significant at the turning point and at the edge of the wear line due to the stronger shearing stress and less compressive force at these positions. The material pull-out was probably generated by the occurrence of significant microcracking at the contact surface and in the subsurface. With more debris adhering to the surface, the local contact stress was concentrated and grinding by the pull-out debris occurred, which further increased the surface roughness and hence resulted in greater deterioration of the wear

resistance of the material. These high local stresses could further result in crack propagation near and/or beneath the wear debris regimes. In addition, the wear scar, as shown in Figure 5.13 (b), which looked like fish scales, could be related to the perpendicularly propagated cracks formed during the wearing. According to these details of the microstructure of the worn surface, the wear mechanism for the alumina samples is considered to be intergranular fracture dominated chipping wear.

Figure 5.14 (a) and (b) shows the worn surface of the 10% 1.5Y-ZTA samples after the same wear cycles as that for the alumina samples. Material delamination is observed at the turning point area, Figure 5.14 (c), and zirconia grain pull-out on the worn surfaces is shown in Figure 5.14 (d).

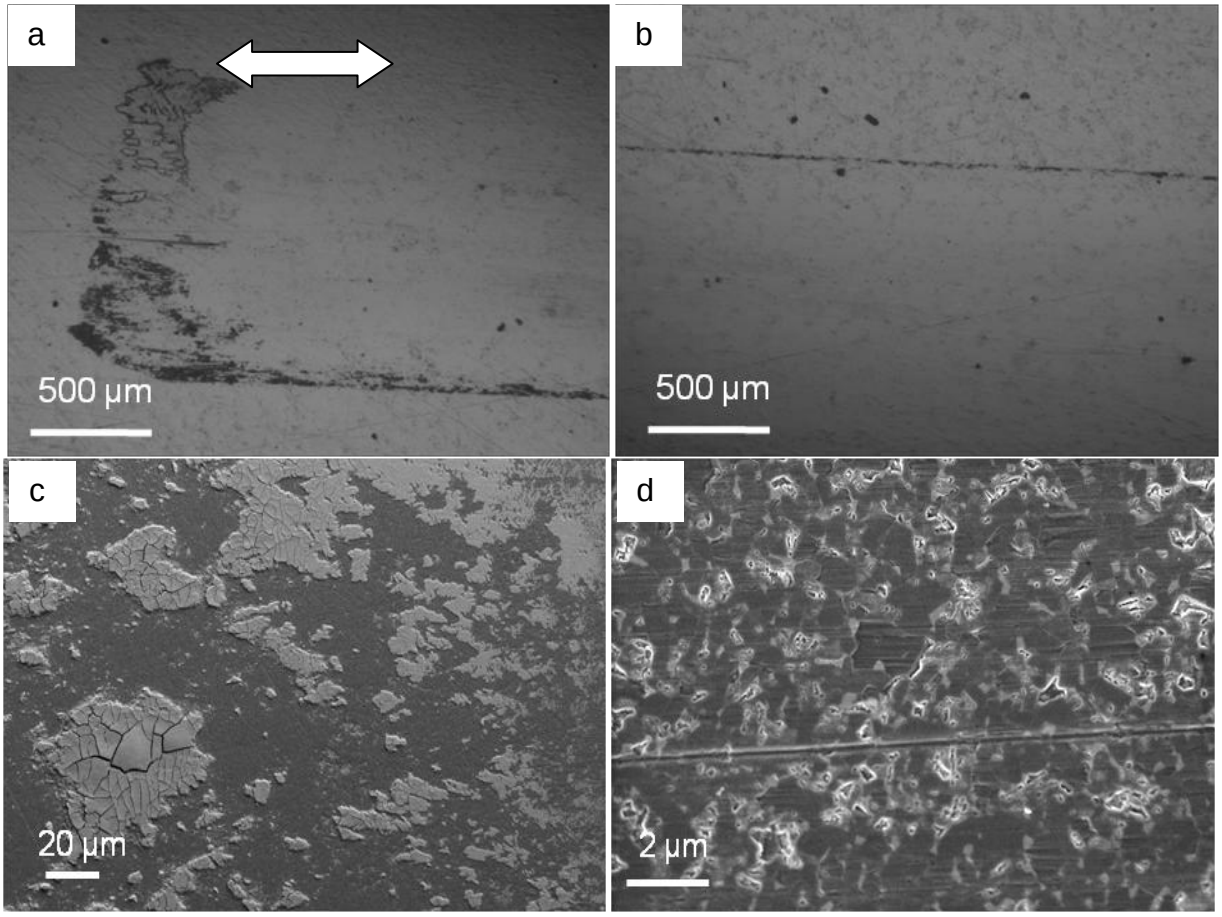

Figure 5.14 10% nano ZTA after testing. a) tuning point of the wear line; b) centre of the wear line; c) delamination on the surfaces at the turning point; d) zirconia grains pull out. The arrow indicates the wear direction.

It is evident that, compared to that observed for the alumina samples, the wearing line in the ZTA is much less intense after the same number of wear cycles. The much reduced surface damage observed in the ZTA may indicate that the zirconia transformation may be active during the wear process. The stress induced by the wear test could trigger phase transformation toughening at the crack tip, which may help the material to resist crack propagation and hence reduce wear [122]. The zirconia phase transformation demonstrated proved by a Raman analysis on the worn surface of a 10% 1.5Y-ZTA sample. The monoclinic peaks were observed in the Raman spectra, Figure 5.15, indicating that the zirconia phase transformation occurred during the wear test.

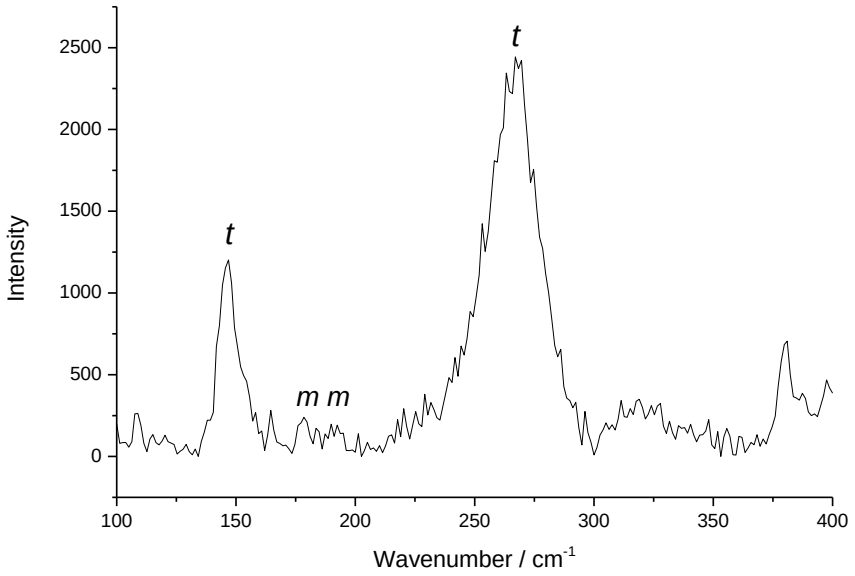

Figure 5.15 Raman spectrum on the centre of the worn surface of a 10% 1.5Y-ZTA

As shown in Figure 5.14 (c), the sample showed delamination and detachment of a surface layer at the turning point. In addition, cracking net was observed on the surface layer. At the turning point of the wear lines, the materials experienced a higher shear stress and sudden wear rate change. This resulted in a large amount of shear induced zirconia phase transformation, which is accompanied by volume expansion. It is considered that, as a result of this transformation, a compressive layer was formed at the worn surface, however, a tensile stress can develop beneath the compressive layer, forming internal stresses in local areas. These local stresses

promote microcrack nucleation at pores and grain boundaries [36]. These cracks, in turn, could mechanically weaken the parts and lead to premature failure of the components. In addition, the stress variation at the turning point is very high which lead to the high level of crack generation and materials deformation. This phenomenon was also observed by Paul [36] on a submicron grain size 3YSZ material.

On the worn surfaces at the centre of the wear line, Figure 5.14 (d), the wearing surface was different from that at the turning point. There was nearly no significant bulk material pull-out, but some zirconia grain pull-out was observed. The reduced level of surface damage was mainly due to the less shear stress and higher compression from the wearing ball, which inhibited the materials pull-out. However, the shear stress could easily remove the transformed zirconia grains with volume expansion. The zirconia grain pull-out could help to release the stress on the surrounding alumina grains caused by the zirconia phase transformation and therefore prevented further damage. From the image, the alumina grains were mainly abrasively worn, generating microcracks and plastic deformations. The different wear mechanisms between the alumina and the ZTA materials could be an important reason that led to their different surface damage after the same wear cycles.

5.4.2 Cr^{3+} fluorescence mapping after wear test

The residual stress and dislocation change in the alumina grains after stress, such as wearing, can be detected using Cr^{3+} fluorescence spectroscopy. Cr^{3+} fluorescence mapping was carried out on the wear tested alumina and ZTA samples, the mapping line was perpendicular to the wear line at the central position of the wear scar, as illustrated in Figure 5.16 (a). The Cr^{3+} fluorescence peak shift and peak broadening are shown in Figure 5.16 (b) and (c).

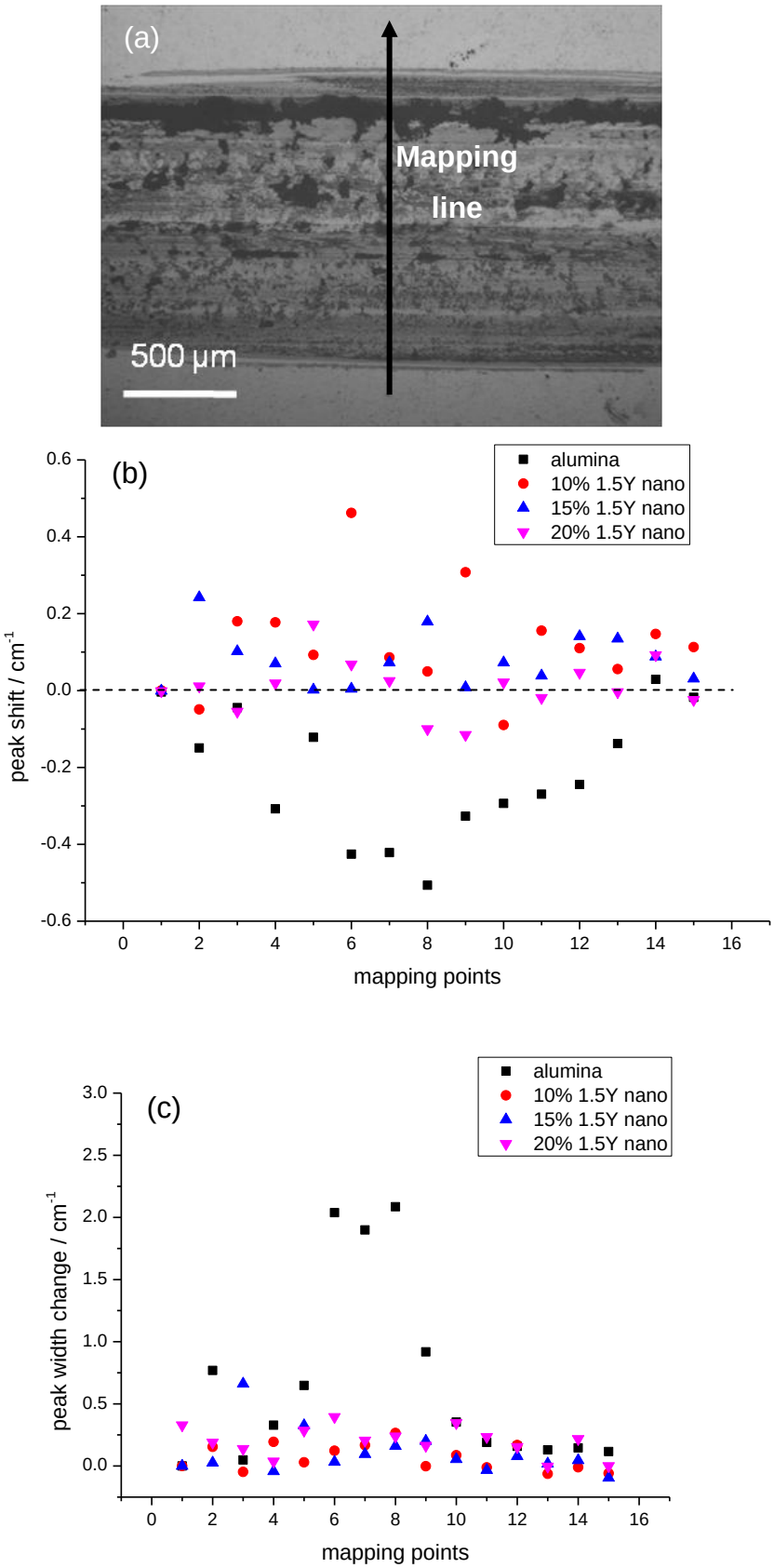

Figure 5.16 a) Mapping line on the worn surface; b) peak shift representing residual stress of the samples; c) peak broadening indicating the dislocation density change after testing.

The peak shift indicates the changes in the residual stress on the samples after wearing. For the alumina sample, a significant amount of negative peak shift was observed, which suggests a compressive residual stress caused by the wearing process. On the other hand, the ZTA samples showed limited compressive stress or a small amount of tensile residual stress, which indicates that the residual stress change in the samples after the wear tests was very limited. The much lower residual stress in the ZTA samples must be related with the zirconia grains and their phase transformation during wear. It is considered that a certain amount of residual stress in the alumina grains could be generated during the zirconia phase transformation due to the accompanied volume expansion. Therefore, it is crucial to investigate the residual stress induced by the zirconia phase transformation, which will be discussed in section 5.5 in detail; after that, the reason for the different residual stress of the alumina and ZTA samples after wearing can be better explained.

From the peak width change map in Figure 5.16 (c), significant peak broadening was observed on the alumina sample, which could be an indication of significant plastic deformation and dislocation generation during wearing. On the other hand, the ZTA samples showed nearly no peak width change across the wear line, indicating that no significant dislocations remained after the wear test. However, the current results suggest that the changes in the zirconia content in the ZTA materials did not significantly affect the amount of changes in the peak shift and peak broadening, i.e. residual stress and dislocation densities, after the wear test.

5.5 Case study on the residual stress induced by the zirconia phase transformation

The changes in the residual stress can be a good indicator of the materials' reaction to static or dynamic loading and also to the changes in the internal stress conditions, such as zirconia transformation in ZTA. With zirconia phase transformation, the volume expansion of the transformed zirconia grains causes a compressive stress in the surrounding alumina matrix, and, therefore, a certain reflective stress in the alumina grains. Therefore, before the investigation of the role of the phase transformation toughening on the mechanical and high strain rate performance of a

ZTA material, it is important to study the residual stress caused by the transformation in the ZTAs.

This work has been previously investigated in the [72,123] using Raman and Cr^{3+} fluorescence spectroscopy. However, most of the phase transformation in the previous literature was induced by grinding, scratching, indentation or other mechanical stressing methods. In these cases, according to a recent study by Guo and Todd [58], the Raman signal collected from the plastically deformed zone (which is the area of interest) is always superimposed on the signal from the area beneath the deformation zone due to the large sampling area associated with the Raman technique. In this study, the residual stress caused by the zirconia phase transformation was measured by investigating the stress change for several 0Y-ZAC materials, before and after sintering.

Using a high temperature XRD, Figure 5.17, the monoclinic zirconia phase in the 0Y-ZAC materials was recorded up to 1200°C, above which all the zirconia grains were transformed to the tetragonal phase. After cooling from the high temperature to room temperature, the tetragonal phase was retained until below 700°C and the material after sintering showed mixed tetragonal and monoclinic phases. The result indicates that, in the 0Y-ZAC materials, because no yttria stabilisation effect exists, the tetragonal phase cannot be maintained in the samples after cooling. However, it was considered that the amount of monoclinic to tetragonal phase ratio could be controlled by changing the mean zirconia grain size by using different sintering conditions. This is because, the larger the zirconia grain size, the easier the phase transformation occurs. In addition, by changing the amount of zirconia in the alumina, the energy required for fully phase transformation can also be changed, because the alumina grains provide less restriction effects on the volume change during phase transformation when the zirconia content increases.

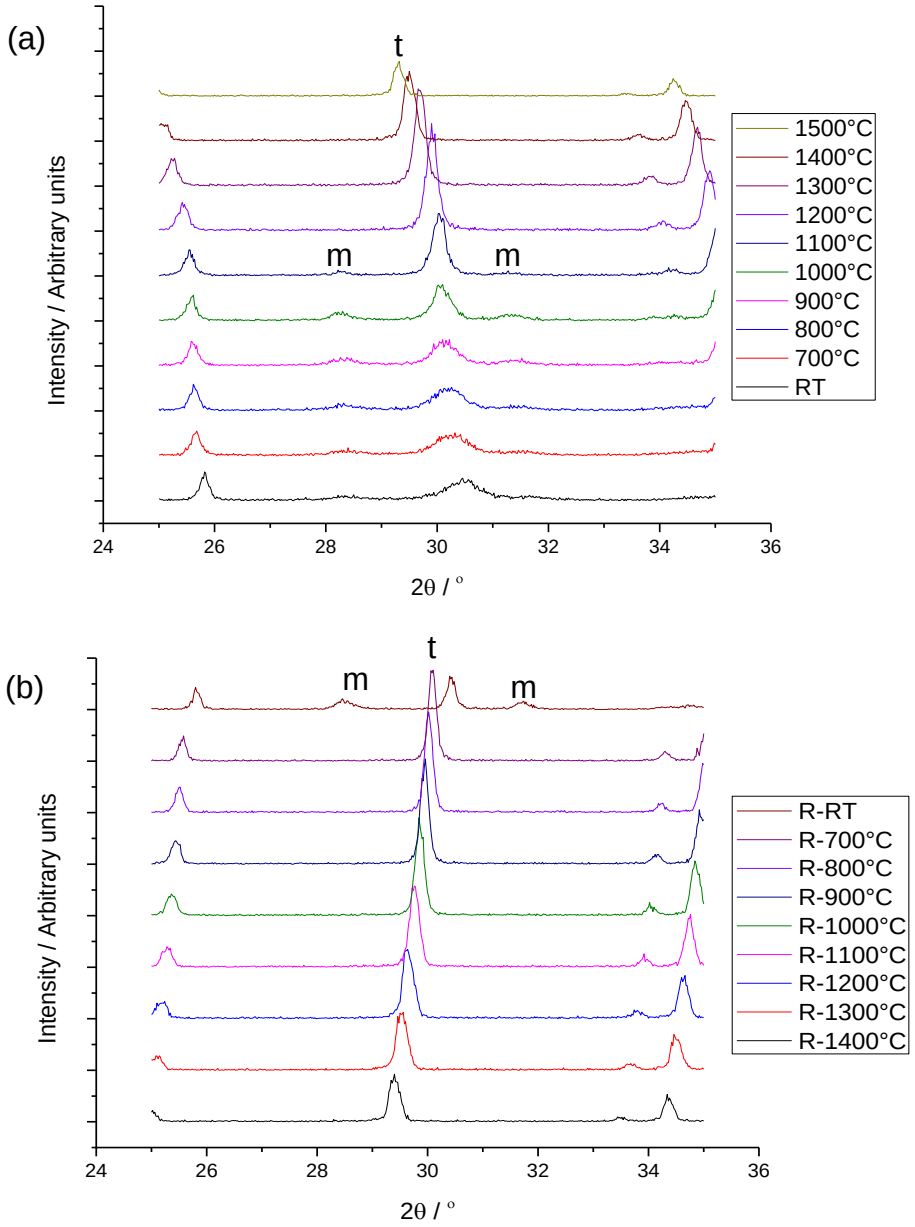

Figure 5.17 High temperature XRD on the 20% 0Y-ZAC (a) during temperature increase and (b) temperature decrease.

Based on these considerations, the 0Y-ZAC materials with different zirconia contents and varied sintering conditions were prepared to quantitatively study the stress change caused by the zirconia phase transformation. Three 0Y-ZAC samples with different zirconia contents, 15, 20 and 27 wt%, were prepared and sintered using several sintering routes; various monoclinic zirconia contents were achieved in these samples, as listed in Table 5.5. The monoclinic zirconia content was measured by studying the intensities of the tetragonal and monoclinic zirconia peaks in the Raman spectra, as shown in Figure 5.18. The 27% sample showed the highest amount of

monoclinic zirconia after sintering, 96%, due to the reduced restriction of the zirconia phase transformation by the alumina grains. With reduced sintering temperatures, the samples showed a reduced monoclinic zirconia content due to the reduction of the zirconia grain sizes.

Table 5.5 Sintering conditions of the 0Y-ZAC samples and their m-ZrO_2 contents

Sample code	Sintering T / ˚C	Heating time / h	Zirconia grain size / nm	m-ZrO_2 content
15% 0Y-ZAC	1500	5	170±60	9
20% 0Y-ZAC	1500	5	210±60	68
27% 0Y-ZAC	1500	5	280±50	95
27% 0Y-ZAC	1400	5	210±30	86
27% 0Y-ZAC	1300	5	130±40	48

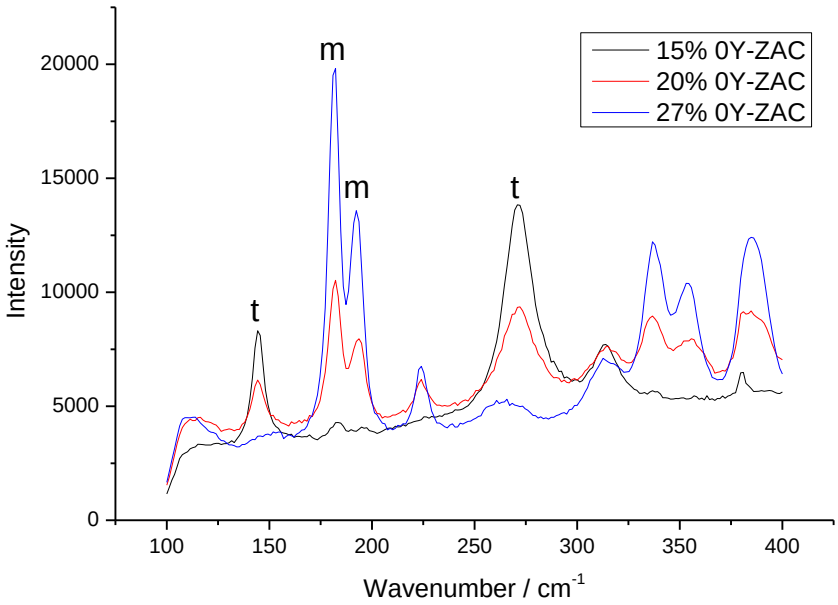

Figure 5.18 Raman spectra showing the zirconia phases in the 0Y-ZAC.

The very significant zirconia phase transformation during cooling caused some stress change in the alumina grains, which were measured using Cr^{3+} fluorescence spectroscopy. Figure 5.19 (a) shows the Cr^{3+} fluorescence peak position change for the 27% 0Y-ZAC samples with 95 and 48% transformed zirconia, compared to a fully tetragonal 27% 1.5Y-ZTA. It is clear that the two peaks positively shifted with increasing zirconia phase transformation, which suggests that a certain amount of tensile residual stress was generated during the phase transformation process. In Figure 5.19 (b), the 0Y-ZAC samples with 9 to 95% zirconia phase transformation

resulted in tensile stresses from ~50 to 600 MPa. An increasing trend of the residual stress with the zirconia phase transformation was evident. This result is in a good agreement with previous work [72,76]. This study confirmed that the zirconia phase transformation resulted in a tensile residual stress in the alumina grains and the highest stress caused was around 600 MPa.

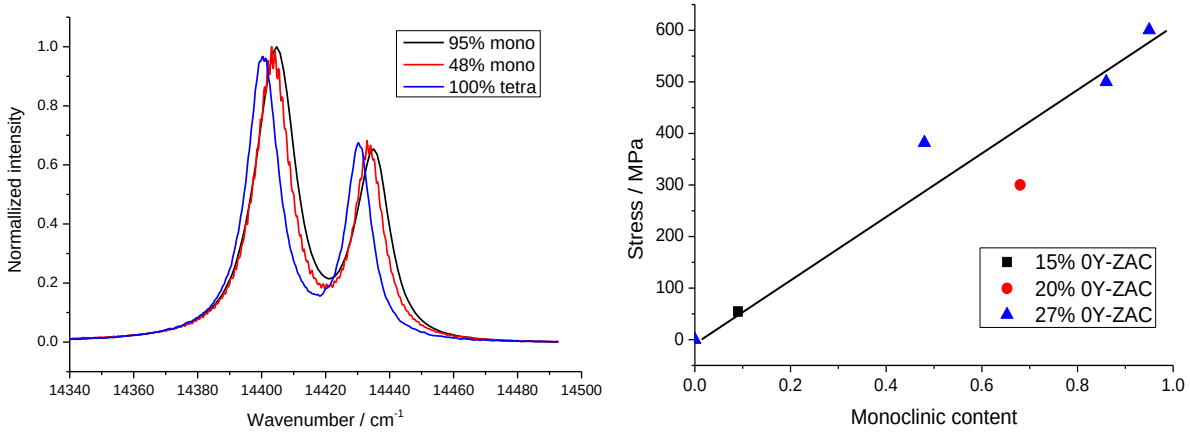

Figure 5.19 (a) Cr^{3+} fluorescence spectra of the 27% 0Y-ZAC with 95% and 48% transformed monoclinic zirconia and a 25% 1.5Y-ZTA with full tetragonal zirconia. (b) Residual stress variation with zirconia phase transformation.

From the above, the for the difference in the residual stresses in the alumina and ZTA samples after wear testing was evident; the residual stress caused by the zirconia phase transformation was tensile, which cancelled the compressive residual stress induced by the wear process. The significantly reduced compressive or tensile residual stress on the worn regions of the ZTA samples indicates the effect the zirconia phase transformation has reduced the stress change after surface damage. With little stress change or stress concentration, the deformation on the surface would be much lower than for samples with high stress changes, such as the alumina.

5.6 Residual Stress Distribution around Vickers Indents

In this section the residual stress distribution around the Vickers indents of the samples in Table 5.6 were investigated in order to understand the effect of zirconia phase transformation on the ability of the materials to resist deformation. The study could give an instruction of the stress change and distribution during a high strain

rate impact. A depth scanning on the polished surface of the samples was firstly studied in section 5.6.1, in order to find out the laser scattering in different samples, which will help to determine the sampling volume of the laser during the Cr^{3+} fluorescence analysis. Then, the four peak fitting technique was verified in section 5.6.2. After that, the residual stress distribution and dislocation density distribution around the indents were studied in section 5.6.3 and 5.6.4, the zirconia phase transformation around the indents was also identified. Finally, in section 5.6.5, TEM study was carried out to compare the dislocations in the indents of alumina and ZTA, as well as their microcrack densities.

Table 5.6 Materials to be studied in this section

Sample	sintered density / %	Alumina grain size / μm	Zirconia grain size / nm	Hardness / GPa	Toughness / GPa
Pure alumina	98.3±0.3	1.2±0.1	N/A	21.5±0.5	3.0±0.3
10% 1.5Y-ZTA	98.8±0.5	0.9 ±0.1	170 ±60	21.4±0.8	5.1±0.4
20% 1.5Y-ZTA	99.3 ±0.3	1.1 ±0.1	280 ±60	19.3±2.3	5.5±0.3

5.6.1 Depth scanning and laser penetration

The depth scanning results of the Cr^{3+} fluorescence are shown in Figure 5.20, which plots the R1 peak intensity, normalized using the maximum intensity, covering stage displacements from -100 μm (i.e. focus is below the surface) to +50 μm. For all the three materials, alumina, 10% ZTA and 20% ZTA, the results show a sharp peak with the highest intensities near the surface, as expected. For the alumina, very little signal was collected once the focusing position was greater than 40 μm from the surface, whilst for the ZTAs, much broader shoulders were observed. This suggests a much larger sampling volume in the ZTAs. The results indicate that the addition of nano zirconia inclusions induced a very strong laser scattering effect, which increased with increasing zirconia content. The elastic scattering of light could have been caused by the larger number of particles and interfaces, resulting in a degradation of the confocal optics and therefore the illumination of a larger volume of the matrix and the scattering of more luminescent radiation towards the confocal aperture. Similar observations have been made in alumina/silicon carbide

nanocomposites [58] but the effect is much stronger in the present alumina/zirconia nano-ZTAs. This suggests that the light scattering in nano-ZTA is even stronger.

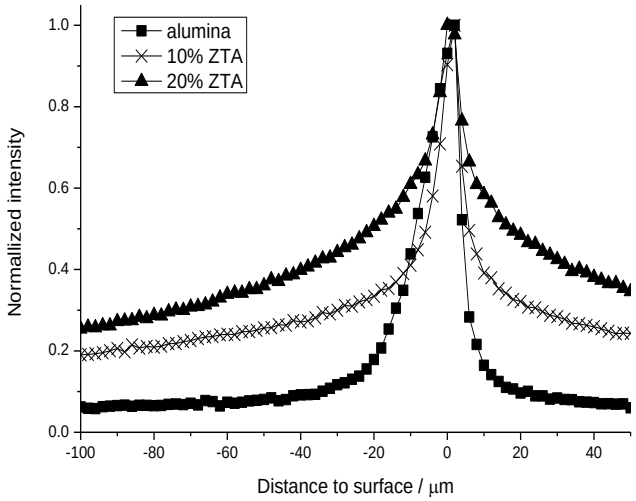

Figure 5.20 Depth scanning on the polished surfaces of alumina, 10% ZTA and 20% ZTA; the intensity corresponds to the normalized intensity of the R1 fluorescence peak.

5.6.2 Cr^{3+} fluorescence analysis on the indentation centre - origin of the sharp peaks and broad peaks

The Cr^{3+} fluorescence spectra from the indent centres of the three materials are shown in Figure 5.21. All the spectra were 4-peak fitted to separate the two doublets; examples of the curve fitting are shown in Figure 5.22, which shows one doublet with broad R1 and R2 peaks and the other doublet with sharp R1 and R2 peaks in each example. The broad peaks, which displayed very significant negative peak shift and peak broadening, are believed to originate from within the plastic zone as the materials experienced extensive plastic deformation caused by the high compressive load during indentation. On the other hand, very limited peak shift and peak broadening were observed for the sharp peaks from each sample, which suggests that these peaks may have originated from outside the plastic zone.

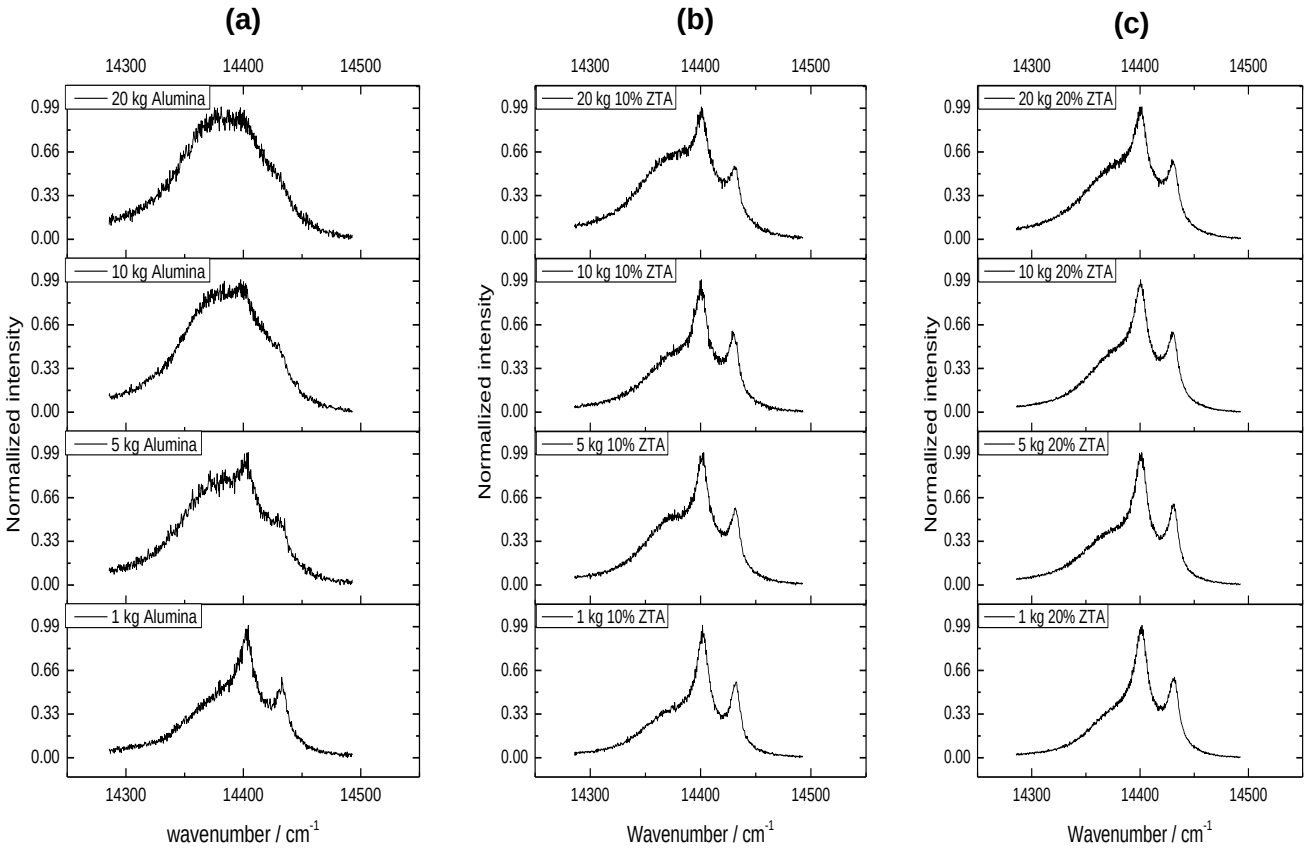

Figure 5.21 Cr^{3+} fluorescence spectra collected from the indent centre for (a) alumina, (b) 10% ZTA and (c) 20% ZTA with indentation loads of 1, 5, 10 and 20 kg.

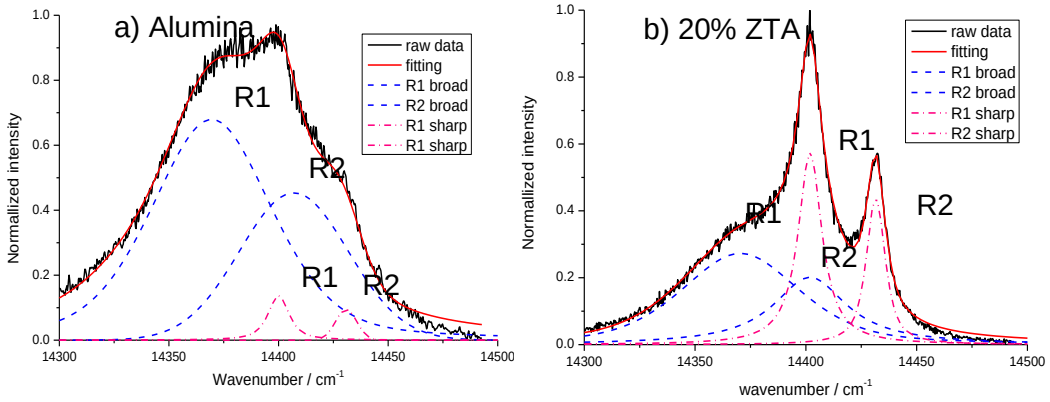

Figure 5.22 Comparison of the 4-peak fitting results for the Cr^{3+} fluorescence spectra from the indent centres of (a) alumina and (b) 20% ZTA, both with the 10 kg indentation load.

Measurements of broad peak percentage, peak shift and peak width were made on the broad peaks from the alumina, as a baseline material, and are listed in Table 5.7. The broad peak percentage was measured by calculating the area ratio of the broad

R1 peak compared to the sum of the broad and sharp R1 peaks. When a 1 kg indentation was used, about 79% of the signal was collected from the plastic zone; the data also showed a ~32 cm^{-1} peak shift and peak broadening of ~56 cm^{-1}. This result is very consistent with that of Guo and Todd [58], also with a 1 kg indentation, confirming the validity of the 4-peak fitting and similar resolution of the Raman equipment used in Guo's and the present studies. With increasing indentation load, the plastic zone size increased significantly from 15 to 100 μm. The percentages of broad peak in alumina were increased from 79% (1 kg) to 99% (20 kg); there was a sharp increase between 1 kg and 5 kg, which indicating that the plastic zone was large enough by the latter load to result in nearly all the collected signal originating from inside it. The comparison further demonstrated that the origin of the two doublets in the indentation area, i.e. the broad peaks, represented the signal from the plastic zone, whereas the sharp peaks were generated from the materials outside the plastic zone. In addition, with the increasing indentation load, the peak shift and peak width were observed to increase slightly in the broad peaks, i.e. from 56 (1 kg) to 70 cm^{-1} (20 kg), respectively. This variation was limited in comparison to the extent of the increase in the indentation load and the size of the plastic zone, as is expected since the mean pressure is believed to remain constant in the yield zone. During the indentation process, the plastic zone size increases as the load increases, continuously forming freshly yielded zones outside the previously formed plastic zone, without affecting the stress level beneath the indenter significantly [124]. The result also confirmed that the fitted broad peaks are physically meaningful and that the fitting work was applicable to the full range of indentation loads used in this study.

Table 5.7 Quantitative analysis of the size of the plastic zone, broad peak percentage, peak shift and peak broadening condition on the indentation centre for a range of indentation loads for alumina.

Indentation load / kg	Size of plastic zone / μm	Measured broad peak / %	Peak shift / cm^{-1}	Peak width change / cm^{-1}
1	15	78.8±3.2	32.4	56.4
5	35	94.8±5.0	32.8	56.9
10	60	96.3±3.7	37.7	57.0
20	100	98.8±2.5	39.3	70.4

The same broad peak analysis was also performed on the ZTA samples. Compared to the case for alumina, the broad peak percentages were significantly reduced for the ZTA indentations for all the indentation loads. The values as a function of plastic zone size are shown in Figure 5.23, confirming that the strong, sharp peak doublets in the ZTA originated from the material outside the plastic zone due to the much greater laser scattering with the ZTA samples.

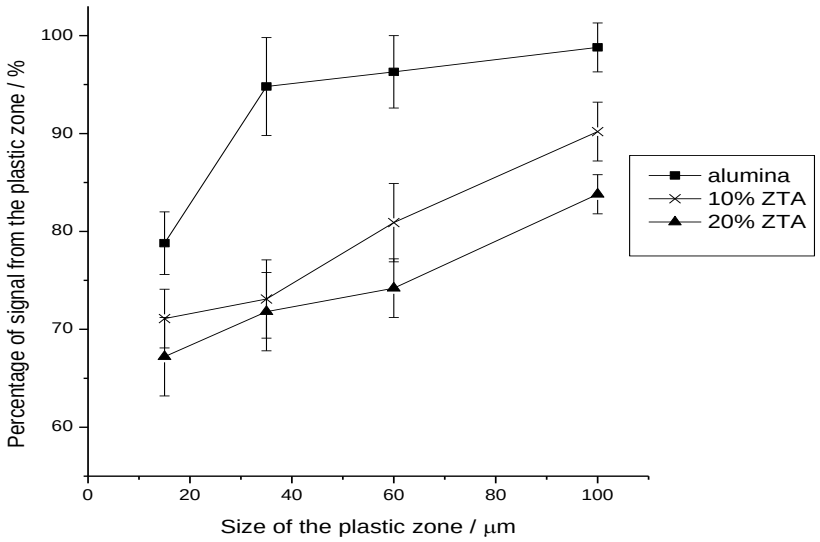

Figure 5.23 Effect of indentation load on the broad peak percentage for the three different materials as a function of plastic zone size.

5.6.3 Effect of zirconia phase transformation on the residual stress distribution around indents

After confirming the origins of the sharp and broad peaks in alumina and ZTA, the residual stresses at the indent centres formed under different loads were studied based on the peak shift of the broad R1 fluorescence peaks, as shown in Figure 5.24. An increase in peak shift with increasing indentation load may be observed for all three materials, however, no significant difference can be observed in terms of their peak shift between alumina and ZTAs, which suggests that either the zirconia phase transformation did not happen at the indent centre or, if it did, it had a very limited effect on the residual stress change in the alumina grains. Determining which explanation was valid was achieved via Raman analysis of the zirconia phases inside and around the indents.

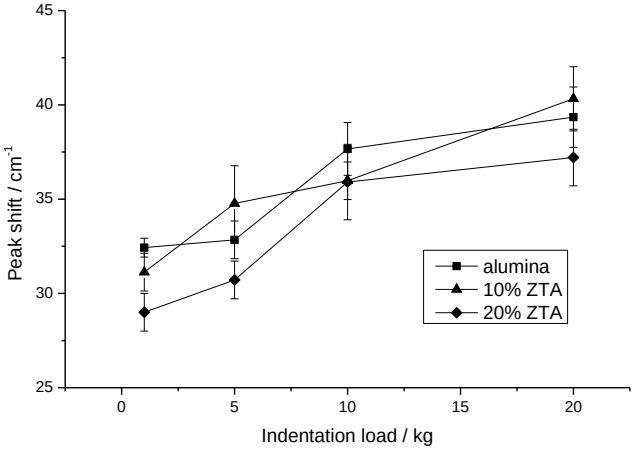

Figure 5.24 R1 broad peak shift at the indent centres for the alumina, 10% ZTA and 20% ZTA specimens, with increasing indentation loads.

Figure 5.25 (a) shows an example of the line map obtained for the transformed monoclinic zirconia concentration from outside a 10 kg indent in 20% ZTA to its centre. The Raman spectra from three locations, viz the indent centre, on the inclined surface inside the indent and at the surface outside the edge of the indent, are shown in Figure 5.25 (b). It may be seen that significant monoclinic peaks were observed around the indent, whilst their intensity reduced when focusing on the inclined surface of the indent and virtually no monoclinic peak was observed in the indent centre itself. It should be noted, however, that the intensity of the Raman signal reduced significantly when close to the indent centre. This will have affected the accuracy of the quantitative measurement. The reduction in intensity will have been caused by several factors, including the surface formed by the compression of the indenter being both concave and very rough compared to a polished surface, resulting in the refraction of the incident radiation, and plastically deformed, disrupting the phonons responsible for the Raman effect. In addition, the relatively low zirconia contents (10-20%) meant that the intrinsic intensity of the Raman signal was very low.

Nevertheless, the trend of a reduction in the degree of zirconia phase transformation towards the indentation centre was very clear; a similar result was obtained by Paul et al. [65] for nano zirconia. The cause is believed to originate in the increasingly high compressive stresses towards the indent centre, which will have suppressed the volume expansion that occurs during the phase transformation. However, the

high monoclinic content near the edge of the indentation, where there are tensile stress components [124], demonstrates unequivocally that the tetragonal to monoclinic transformation did take place in the region where permanent deformation was occurring as the indentation load increased. We tentatively suggest, therefore, that some of the monoclinic zirconia formed around the indenter during loading may also have transformed back to tetragonal zirconia as the indentation expanded and enveloped this initially transformed material in the highly compressive region beneath the indenter. Previous results on 3Y-TZP with conventional grain size [125] do not show this effect. This may reflect differences between the transformability of nanosize zirconias and conventional materials and clearly merits further investigation. The same experiments were carried out on the 10% ZTA and the indents with different loads. The same trend of reduction in the degree of zirconia phase transformation towards the indentation centre was observed. The results are listed in Table 5.8, in which only the content of transformed monoclinic zirconia phase on the edge of the indent and in the indent centre was displayed. It should be noted error about ±5% was observed, due to the factors mentioned before which affecting the accuracy of the quantitative measurement; within the error bar, no significant difference was observed.

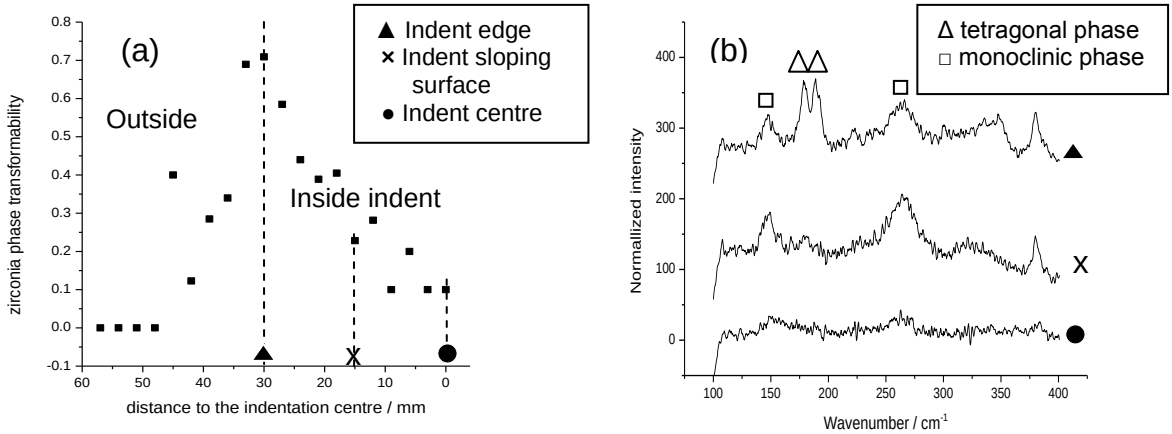

Figure 5.25 (a) Raman line map obtained around a 10 kg indentation in 20% ZTA; (b) Raman spectra obtained at three locations on the same indent shown in (a).

Table 5.8 m-ZrO_2 contents on the indent of 10 and 20% ZTA with 5, 10 and 20 kg indent loads.

Material		10% ZTA			20% ZTA		
Indent load / kg		5	10	20	5	10	20
m-ZrO_2 content / %	Indent edge	62	65	65	65	70	69
	Indent centre	10	12	9	11	11	14

A line scan of the R1 peak shift with the distance to the indent centre was made and the results are shown in Figure 5.26. For all the samples, the compressive residual stress increased significantly from the unloaded surface to the indent centre owing to the constraint on the expanded indentation region from the unyielded material surrounding it. The peak shift inside the indent, in the range of 30 to 10 μm from the indent centre, displayed consistently lower values for the ZTA samples compared to the alumina, Figure 5.26. The mean difference was ~4 cm^{-1}, corresponding to a hydrostatic stress of ~500 MPa. Although there was virtually no zirconia monoclinic phase at the centre of the indent, the amount of transformation increased significantly on the inclined indent surface, particularly from 10 to 30 μm away from the centre (Figure 5.25 (a)). Therefore, it is very likely that the observed lower residual stresses in the ZTAs compared to the alumina originated from the zirconia phase transformation.

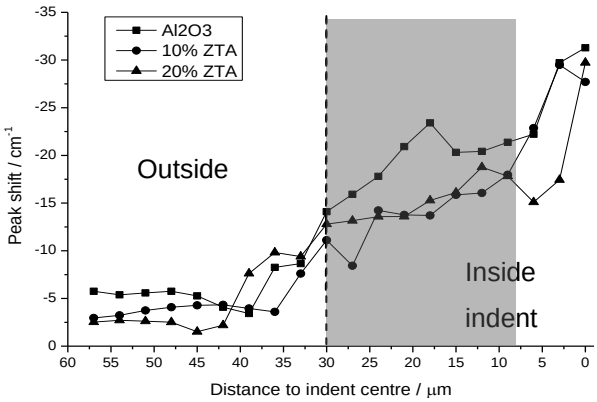

Figure 5.26 R1 broad peak shift along a line from the sample surface to the indentation centre for the alumina, 10% ZTA and 20% ZTA specimens using a 10 kg load to create the indents. The dash line separated the mapping positions inside and outside the indent, the grey area indicates the positions showing different peak shift between the alumina and ZTA samples

Gregori et al. [76] found that there was a linear relationship between the degree of zirconia phase transformation and the residual tensile stress produced in the alumina matrix of ZTA. The explanation is that during the zirconia phase transformation process, the volume expansion of transformed zirconia grains is resisted by the surrounding alumina matrix putting the zirconia into compression and the alumina into tension [72]. Therefore, for ZTA materials after indentation testing, some

alumina grains around the phase transformed zirconia received a certain amount of the tensile stress which cancelled part of the compressive stress induced by the indentation, resulting in the lower net residual stresses at the positions with zirconia phase transformation. According to the modelling results of Gregori et al. [76], the maximum tensile stress provided by 100% zirconia phase transformation was about 600 MPa for ~20 vol% zirconia. This value is of a similar level to the measured difference in the residual stresses on the indentation surfaces of the alumina and ZTA samples. It is also interesting that there was little difference in residual stress between the 10% and 20% ZTA, probably because the difference in zirconia content was not significant given that the degree of phase transformation inside the indent was relatively low for both materials. The similar stress levels outside the indentation for all three ceramics can be understood in terms of their similar hardness values. This implies that the extra volume of the indentation that needs to be accommodated by elastic strains in the material around it is approximately the same.

5.6.4 Effect of zirconia phase transformation on the dislocation density distribution in the alumina around indents

The dislocation density at the centre of the indents formed under different loads were compared using the peak width changes in the broad R1 fluorescence peaks, as shown in Figure 5.27 (a). In each case there was a clear increase in the peak broadening between the 10 and 20 kg indents, though it was less in the ZTA samples than the alumina. Assuming that dislocation formation was the dominant source of broadening, this indicates that the alumina dislocation densities at the indent centres of the ZTA materials were lower than in the pure alumina.

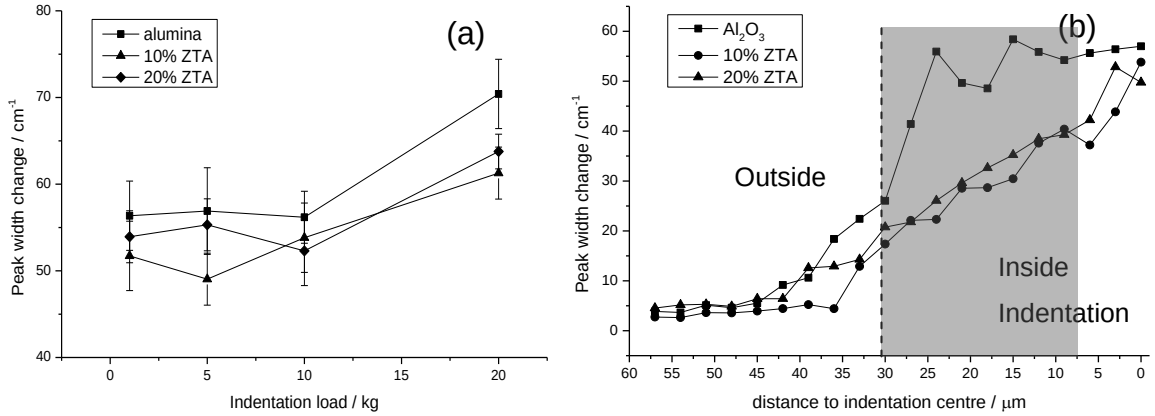

Figure 5.27 R1 broad peak width change (a) at the indent centre and (b) along a line from the sample surface to the indentation centre of the alumina, 10% ZTA and 20% ZTA specimens using a 10 kg load to create the indents. The dash line separated the mapping positions inside and outside the indent, the grey area indicates the positions showing different peak width change between the alumina and ZTA samples

Following the same mapping points illustrated in Figure 5.26, the peak width change from the unloaded surface to the indent centres for the 10 kg indentations are shown in Figure 5.27 (b). The alumina sample showed a sharp increase in the values around the edge of the indent and the change of peak width, from about 10 to 55 cm^{-1}, remained fairly constant within the indent. For the ZTAs, however, the peak width increased reasonably smoothly along most of the mapping route, until reaching a similar value to that of the alumina at the indent centre. This more gradual peak broadening associated with the ZTAs could also have originated from the zirconia phase transformation inside the indentations. It can be observed that the peak width difference between the ZTAs and alumina was gradually reduced nearer to the indent centre, which is again consistent with the trend of a reduced zirconia transformation, i.e. the fraction of monoclinic phase, from the edge of the indentation to its centre, as discussed in section 5.6.3. The volume change during transformation could directly contribute to the deformation at the edge of the plastic zone during loading but could be magnified considerable when the large shear deformation (~0.16) also occurring is taken into account. In isotropic conditions, the net shear is effectively removed by twinning [126] but in the presence of a deviatoric stress, such as exists at the edge of the indentation [124], the twinning will occur so as to minimise the mechanical energy of the system, producing potentially large net shear strains that can also contribute to the deformation process, leaving less requirement

for dislocation and twinning mediated plastic deformation in the alumina matrix. Even if some reverse transformation does occur as indentation progresses, a residual ferroelastic switching may remain, preserving the shape of the indentation and again reducing the plastic strain contributed by the alumina matrix.

5.6.5 TEM analysis

As indicated earlier, in order to observe the microstructure inside the plastic zone, FIB lift-out was performed on the indent centre of a 10% ZTA and an alumina sample, the samples were then characterised using TEM. The results are shown in Figure 5.28. For both the samples, it was observed that there were very many dislocations inside the plastic zone, as expected. In the alumina sample, dislocation entanglements were observed across the whole lift-out sample area and the grain boundaries were not easily observed because many dislocations propagated across them, Figure 5.28 (a) and (c). The situation was different for the 10% ZTA sample, however, where only the indent centre had a high dislocation density and across the rest of the lift out sample the grain boundaries could be observed clearly, Figure 5.28 (b) and (d). This observation is consistent with the peak broadening mapping shown in Figure 5.28 (b). According to the change of peak width, which is about 55 to 60 cm^{-1} for both alumina and ZTA samples, the dislocation density in the plastic zone was as high as about $10^{16} – 10^{17}$ m^{-1} [61]. Therefore, it was difficult to quantify the difference in dislocation density between the alumina and the ZTA from the TEM observation. Using the high magnification TEM images, it was calculated that the microcrack densities of the alumina and 10% ZTA were 600±50 and 350±50 m^{-1}, respectively. The lower microcrack density in the ZTA confirmed the effect of the zirconia phase transformation on restricting crack propagation.

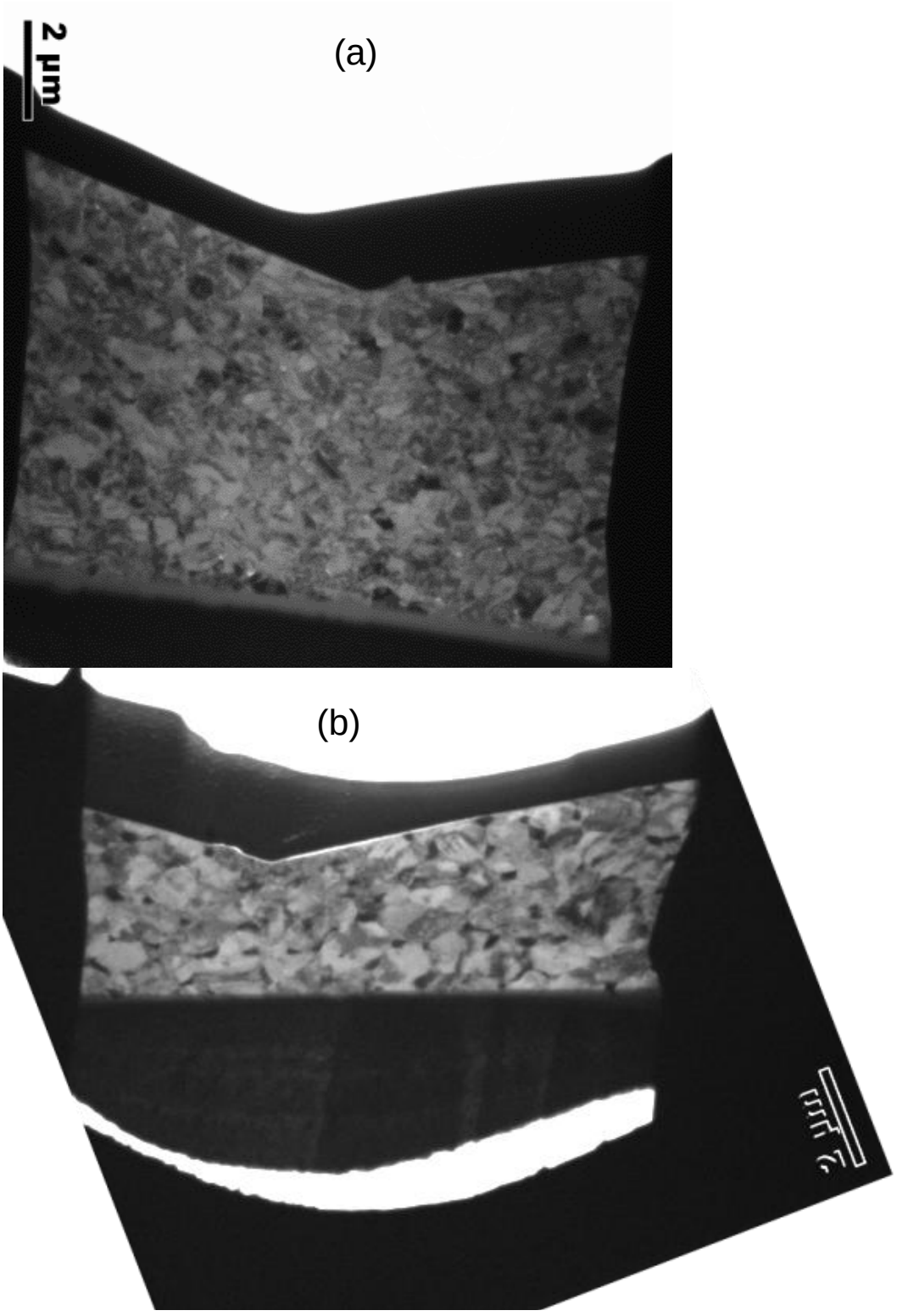
(a)
2 µm
(b)
2 µm

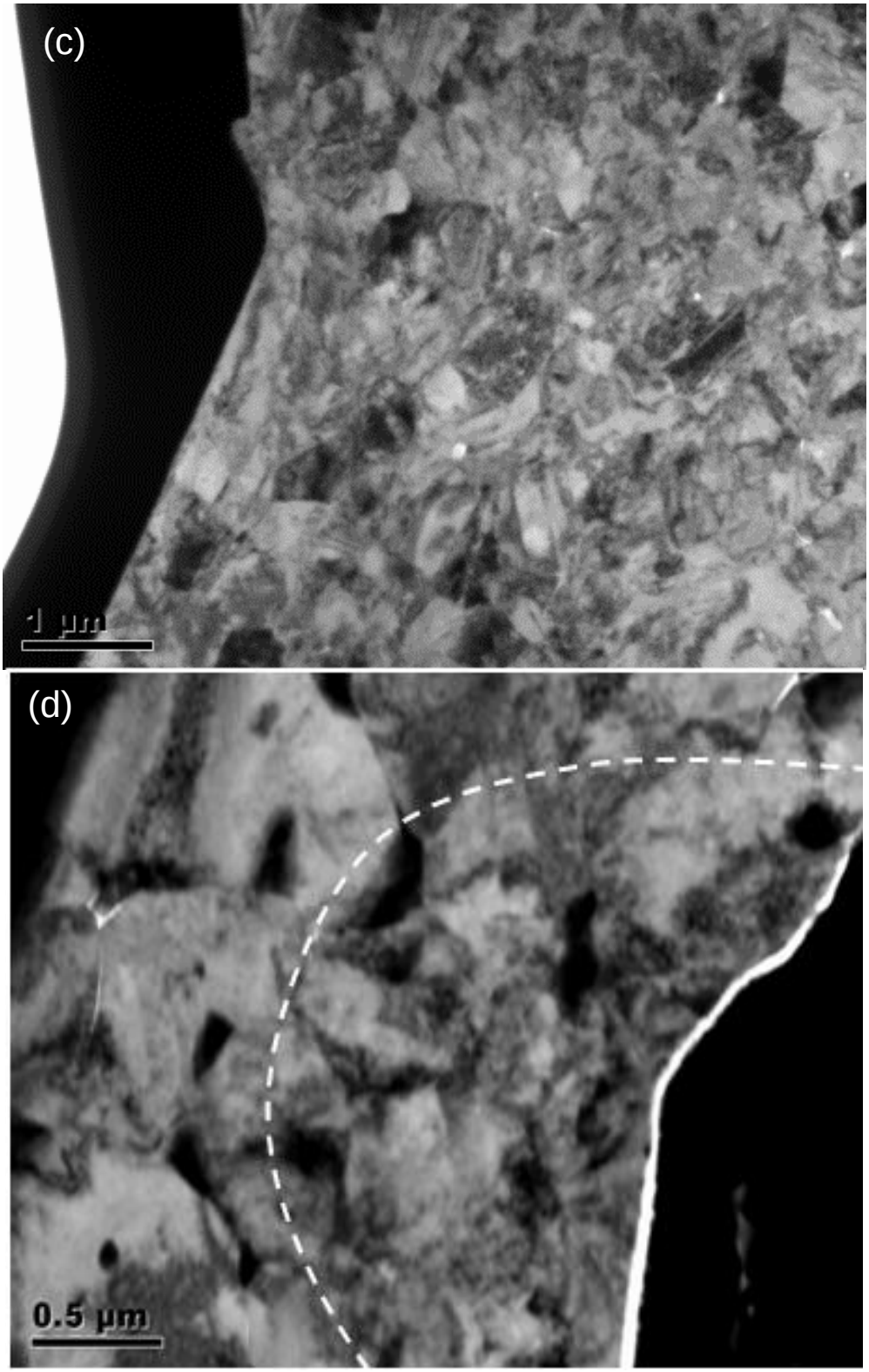

Figure 5.28 TEM images of the FIB lift out sample taken from a 1 kg indentation of (a) alumina and (b) 10% ZTA, (c) and (d) are higher magnification images of (a) and (b), respectively, at the indent centre.

5.6.6 Conclusions

The residual stresses around 1 to 20 kg indentations in alumina and 10% and 20% nano ZTA have been measured using Cr^{3+} fluorescence microscopy. According to depth scanning of the Cr^{3+} fluorescence peak intensity, a significant laser scattering effect in the ZTA samples was observed. The broad peaks were confirmed to be generated inside the plastic zone, due to the consistency of the measured percentage of R1 broad peak and the calculated percentage of signal from inside the plastic zone.

The peak shift analysis on the three materials showed no significant difference in the residual stresses in the indent centres between alumina and ZTA samples. This is believed to be because, in the ZTA samples, the zirconia phase transformation at the indent centre was suppressed by the high compressive load. The degree of zirconia transformation increased, however, towards the edge of indent and the ZTA samples showed ~500 MPa reduction in the compressive residual stress compared to the alumina sample. This was probably caused by the generation of tensile residual stresses in the alumina grains due to the zirconia phase transformation.

In addition, it was found that the ZTA materials displayed lower dislocation densities on the indentation surfaces away from the centre, where the zirconia phase transformation occurred. This effect was caused by the restriction of crack propagation and the energy absorption during the phase transformation process. The relatively lower microcrack density in the plastic zone for the ZTA materials was confirmed by examining the plastic zone microstructure using TEM.

5.7 Summary

- The density showed a slight effect on the hardness and toughness of the materials, but the effect was not significant when the densities were above 98% of theoretical. For alumina, with the increase of the alumina grain size, the hardness increased slightly whilst the toughness showed no significant change. The effect of the grain size on the hardness was not clearly observed due to the influence of the different densities. The toughness of the ZTA

samples increased with the increasing zirconia grain sizes due to the higher transformability.

- The alumina samples showed a slightly higher hardness than the ZTA samples, but much lower toughness. With increased zirconia content in the ZTA, the hardness decreased whilst the toughness increased. In addition, the 1.5Y-ZTA samples showed much higher toughness than the 3Y-ZTA. According to the Raman analysis, the tetragonal to monoclinic transformation toughening effect was higher in the 1.5Y-ZTA than in the 3Y-ZTA.

- The transformability of the ZTA samples were quantitatively measured using Raman spectroscopy. The increased transformability with the increasing zirconia grain size was confirmed to be caused by a larger transformation zone and better shielding effect on the cracks. The residual stress caused by the phase transformation was studied by sintering some 0Y-ZAC samples, about 600 MPa tensile residual stress happened on the alumina grains after the zirconia phase transformation.
- The fracture strength of the ZTA samples were much higher than the alumina samples due to the benefit of zirconia phase transformation, which reduced the crack propagation, as well as led to different fracture modes. The alumina showed a certain amount of transgranular fracture, whilst the ZTA samples were fully intergranularly fractured.

- Comparing the wear testing results of the alumina and ZTA samples, the wear resistance was significantly improved by the zirconia phase transformation. Much less surface damage was observed on the ZTA samples and different wearing mechanisms were identified between them. In addition, the reduced residual stress change could be an important reason that led to the less plastic deformation and surface damage of the ZTA samples.

- The residual stress distribution around indents of the alumina and ZTA samples were analysed in details. The work helped to understand the effect of zirconia phase transformation on the residual stress distribution and dislocation density change under a high pressure static impact and after

materials deformation. Although the effect from the zirconia phase transformation was not significant due to the very high stress from the indentation, the reduced residual stress and dislocation density was still observed. The microcrack density in the plastic zone was much less in the ZTA than in the alumina samples.

6 HIGH STRAIN RATE TESTING AND POST TESTING CHARACTERISATION

The previous studies about the effects of microstructure and composition on the mechanical properties have shown that ZTA materials can provide superior properties including, toughness, strength and wear resistance, whilst the alumina samples showed higher hardness values. However, it is important to learn, under dynamic compression, which material can show a superior high strain rate performance. In section 6.1, the results of split Hopkinson pressure bar test on ZTA and pure alumina samples at impact speeds of 8 to 16ms^{-1} are reported. The degree of zirconia phase transformation in the ZTA samples after the SHPB testing was investigated and Cr^{3+} fluorescence analysis was undertaken to investigate the effect of phase transformation on the residual stress and dislocation density in the post tested samples. TEM observation was carried out to characterise the dislocations and plastic deformation on the impacted area. Based on the initial data from the high strain rate performance of the samples, gas gun impact tests were used to investigate selected materials under a much higher impact speed, 100 m s^{-1}, the results of which are presented in section 6.2. Raman and Cr^{3+} fluorescence studies were also used for the post testing characterisation. Finally, 15% 1.5Y-ZTA samples were further tested using increased impact speeds at 130 and 150 m s^{-1}, the effect of impact speeds on the high strain rate performance of the ZTA materials is reported in section 6.3. In addition, the impact tests on the nano grain sized 1.5YSZ samples were carried out and are discussed in section 6.3 as well.

6.1 SHPB Test

Split Hopkinson pressure bars (SHPB) can be a useful tool in testing relatively small samples under a controlled high strain rate (10^3 to 10^6 s^{-1}) in laboratories. In the present work, a range of 1.5Y-ZTA (zirconia addition in 10, 15 and 20 wt%) and alumina samples sized 4×4×5 mm^3 were tested using SHPB; the impact velocity varied from 8 to 16 m s^{-1} (strain rate from 2×10^3 to 4×10^4 s^{-1}) and the results are

listed in Table 6.1. At least 5 samples for each material were tested under the same impact velocity. The results showed a very high consistency.

Table 6.1 Fracture conditions of the SHPB tested samples

Sample	Hardness / GPa	K_{Ic} / MPa $m^{1/2}$	Fracture strength / MPa	Impact velocity / m s^{-1}	Degree of fracture
Al_2O_3	21.5±0.5	3.1±0.4	355±54	8	Fractured into pieces
				11	Fractured into pieces
10% 1.5Y-ZTA	21.4±0.8	5.1±0.3	429±67	8	Mainly intact, 2-3 small fragments
				11	Fractured into pieces
				16	Fractured into pieces
15% 1.5Y-ZTA	20.8±1.1	5.4±0.2	528±44	8	Intact
				11	Intact
				16	Fractured into 3 large pieces
20% 1.5Y-ZTA	19.3±1.3	5.5±0.1	500±62	11	Mainly intact, 2-4 small fragments

The results showed that at the lowest velocity, 8 m s^{-1}, only alumina fragmented into pieces. With the 11 m s^{-1} SHPB tests, the pure alumina and the 10% 1.5Y-ZTA samples shattered into pieces, those containing 20% YSZ resulted in mainly intact samples but with some small fragments, whilst the 15% 1.5Y-ZTA samples were all intact. When the impact velocity was increased to 16 m s^{-1}, the failure of the 15% ZTA occurred, resulting in several large broken pieces. From the comparison, it was found that the samples with a higher zirconia content or zirconia phase transformation effect showed a better performance to defeat the high strain rate impact, although the 20% 1.5Y-ZTA did not show any improvement compared to the 15% samples. It is considered that the high strain rate performance is related to several mechanical properties, including hardness, toughness, fracture strength, etc, as listed in Table 2.5. The hardness represents the ability of the material to resist deformation; high toughness means less crack propagation and higher ability to retain the fracture locally without full fragmentation; a higher bend strength indicates a higher stress or energy required to cause the failure of the material. Therefore, these properties were combined to affect the high strain rate performance and, from the Table 6.1, it is difficult to point out which one is the dominate contribution to the materials' high strain rate performance.

In order to investigate the effect of zirconia phase transformation on the high strain rate performance of the ZTA samples after the SHPB tests, the 10% and 15% 1.5Y-ZTA were selected to be mainly studied in the following sections, including their stress strain curves, amount of zirconia phase transformation, residual stress and dislocation density changes and fragmentation behaviours.

6.1.1 SHPB impact process

Under the same impact speed, 11 m s^{-1}, the stress-strain relationships of a fractured 10% 1.5Y-ZTA sample and an intact 15% 1.5Y-ZTA sample were compared in Figure 6.1. The former sample showed a stepped curve with each step representing a fracture activity in the sample during impact. The fracture process released the stress and hence resulted in the flat steps in the curve. The latter showed a much smoother curve without the periodic stress releases. As a consequence, it withstood a much larger strain, ~4% versus <2.5% for the sample that fractured, although the maximum stress was quite similar.

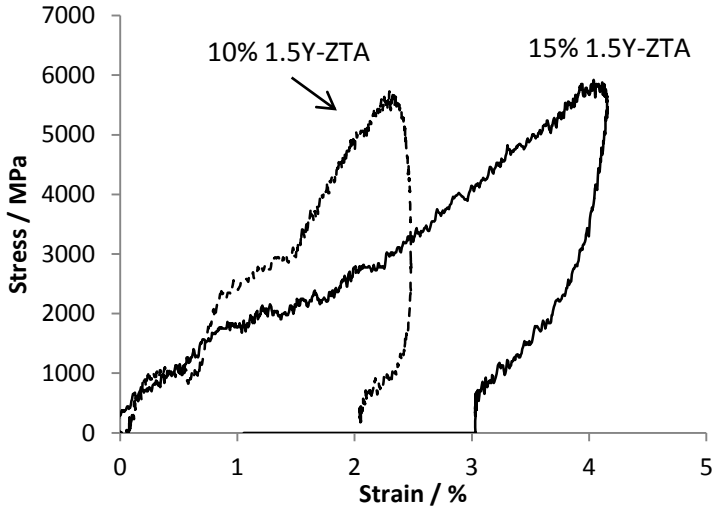

Figure 6.1 Stress-strain relationships of 10% 1.5Y-ZTA and 15% 1.5Y-ZTA SHPB tested using an impact velocity of 11 m s^{-1}.

The impact process was also recorded using a high speed camera (Phantom 7, Vision Research, USA). Figure 6.2 shows the images of the SHPB impact process for a 15% 1.5Y-ZTA sample, which survived after the test. The recorded signal from the transmission bar, which represents the loading process, is shown in Figure 6.3. The images in Figure 6.2 were all taken during the impact process, as highlighted in Figure 6.3. It was observed that the first crack initiated at the back surface (circled in

the third image) at 0.0179085 s. Comparing this with the recorded signal in Figure 6.3, a small step was observed at this point, which suggested that the crack initiation released a small amount of stress from the impact. Finally, the crack propagated locally and formed a small chip (circled in the last image), during this process, the signal curve showed that impact stress was smoothly applied onto the sample until reaching the highest load.

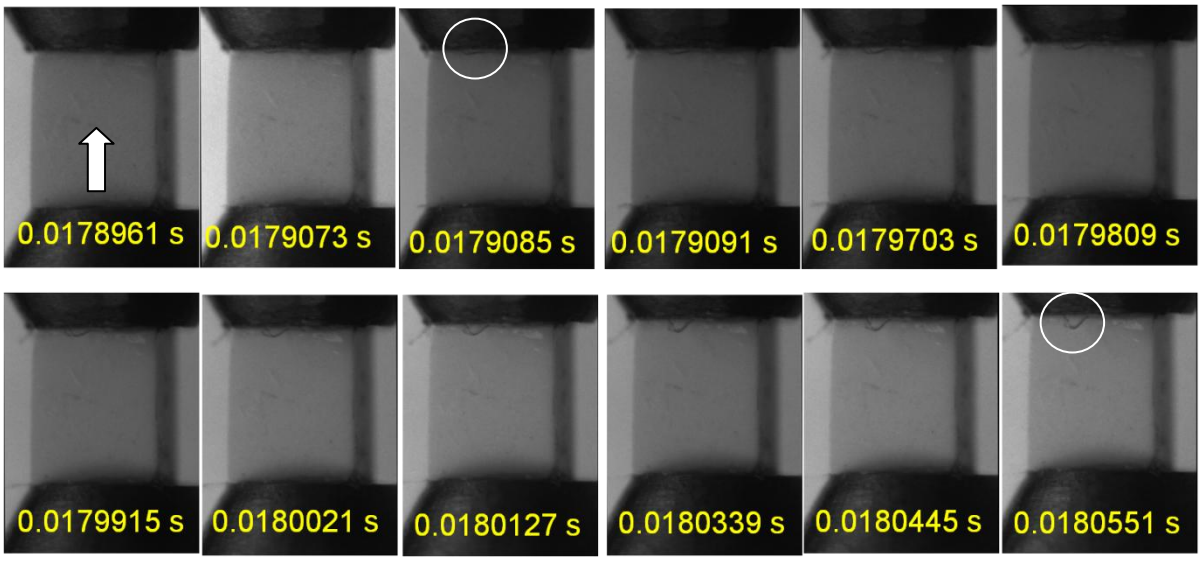

Figure 6.2 Impact process of a 15% 1.5Y-ZTA sample under the SHPB test, the arrow indicates the direction of impact. Crack initiation on the back surface is highlighted in the third image, which propagated and chipped from the sample in the last image.

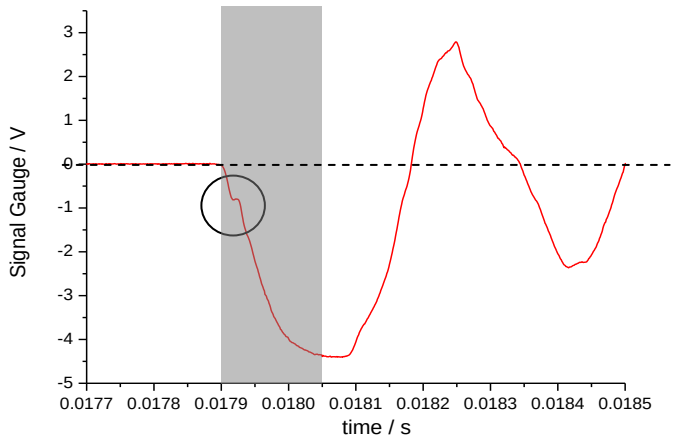

Figure 6.3 Signal recorded during the SHPB impact process of the 15% 1.5Y-ZTA, the grey area indicates the range in which the high speed camera photos in Figure 6.2 were taken. A step on the curve was highlighted, which was caused by the crack initiation during the impact.

The same sample was re-tested with the intention of breaking it. Using the same impact procedure, the sample still survived without any further damage, as shown in Figure 6.4. The results suggest that although microcracks could be introduced during the first SHPB test, the sample was still strong enough to withstand another test without fragmentation. This result also indicates that the impact speed provided for this sample with this size would not be sufficiently high to cause failure.

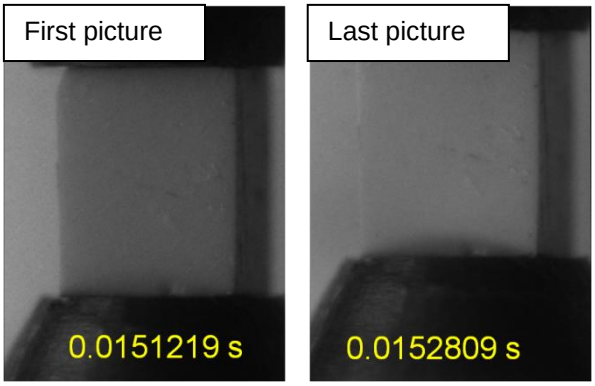

Figure 6.4 The first and last image of the re-tested 15% 1.5Y-ZTA.

In comparison, the 10% 1.5Y-ZTA samples with the same sample size and the same testing impact speed, 11 m s^{-1}, were fragmented into fine debris. The fragmentation process was recorded and is shown in Figure 6.5. The corresponding loading signal is shown in Figure 6.6.

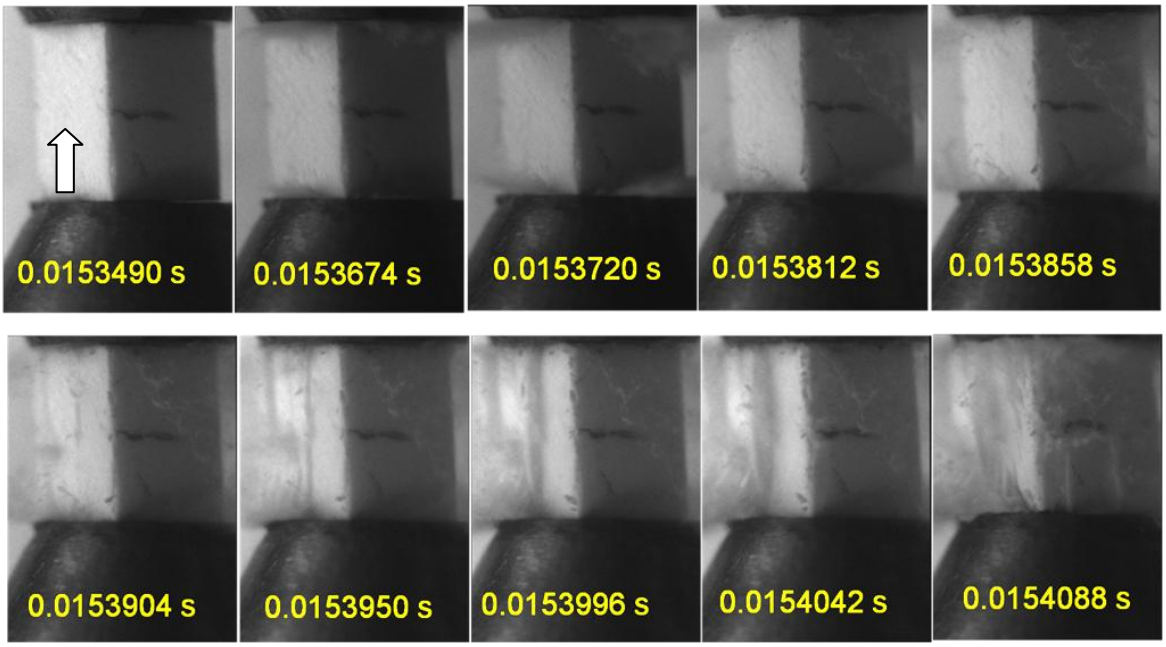

Figure 6.5 Impact process of a 10% 1.5Y-ZTA sample under the SHPB test, the arrow indicates the direction of impact.

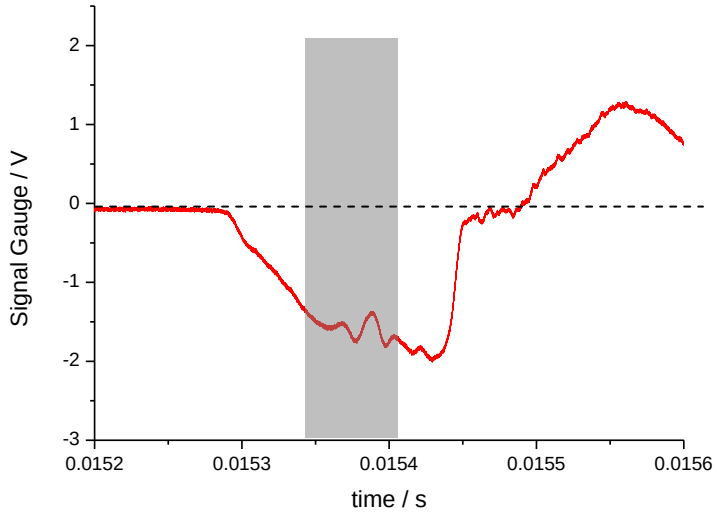

Figure 6.6 Signal recorded during the SHPB impact process of the 10% 1.5Y-ZTA, the grey area indicates the range in which the high speed camera photos in Figure 6.5 were taken.

A large number of cracks were observed on both the impact and back surfaces; they propagated along the impact direction, resulting in the fragmentation of the sample. The fragmentation resulted in the fluctuation in the stress signal gauge, as shown in Figure 6.6. The same phenomena were observed on the alumina samples, which fragmented into pieces after the SHPB tests.

It was also found that, for samples that remained mainly intact after testing or that fractured into large pieces, they did not fracture during the initial impact process when the incoming impact wave hit the samples, since the failure was not observed on the high speed photos. Instead, the sample fractured during the lateral process, during which the waves reflected between the two bars. This suggests that these samples survived the initial impact but could not withstand the continuous waves of compression and tension afterwards.

6.1.2 Residual stress on ZTA upon loading

The residual stress of alumina grains upon loading is considered to be caused by the superposition of stress fields from a number of independent mechanisms [61]:

$$\langle\sigma\rangle = \langle\sigma\rangle^{ATE} + \langle\sigma\rangle^{MTE} + \langle\sigma\rangle^{DL} + \langle\sigma\rangle^{MC} + \langle\sigma\rangle^{LE} + \langle\sigma\rangle^{PT}$$

where $\langle\sigma\rangle^{ATE}$ is due to the crystallographic thermal expansion anisotropy of the alumina phase, $\langle\sigma\rangle^{MTE}$ is the stress from the mismatch in thermal expansion coefficient between the alumina and zirconia,$\langle\sigma\rangle^{DL}$ represents the stress field around dislocations, $\langle\sigma\rangle^{MC}$ is the perturbations to the stress field introduced by the presence of microcracks, $\langle\sigma\rangle^{LE}$ is a large-scale elastic stress, and $\langle\sigma\rangle^{PT}$ is the additional stress created from the tetragonal to monoclinic phase transformation of the zirconia grains. The $\langle\sigma\rangle^{ATE}$, $\langle\sigma\rangle^{DL}$ and $\langle\sigma\rangle^{MC}$ are negligible due to the condition of stress equilibrium and the relatively large volume of material illuminated. The $\langle\sigma\rangle^{MTE}$ is constant for the ZTA materials with the same zirconia content, whilst it increased with increasing zirconia fraction, leading to the R1 peak position without stress moving from 694.33 nm to 694.44 nm when the zirconia content increased from 0 to 27%. Except for the above stress mechanisms, the $\langle\sigma\rangle^{LE}$ and $\langle\sigma\rangle^{PT}$ are the largest contribution to the residual stress and are the main focus in this study.

In pure alumina materials, the residual stress after an indentation test or high strain rate impact test is compressive [63], and the R1 peak obtained from Cr^{3+} fluorescence mapping yields a negative shift (in wavenumber), which means the $\langle\sigma\rangle^{LE}$ contributes a negative / compressive stress to the material after the impact. By studying the residual stress caused by the zirconia phase transformation in ZTA, see section 5.5, it was found that a tensile residual stress was formed as a function of the zirconia phase transformation. Therefore, if the zirconia phase transformation occurs after stressing, the $\langle\sigma\rangle^{PT}$ should be in tension, which cancels the contribution from the compressive stress of the $\langle\sigma\rangle^{LE}$.The different stress conditions of the $\langle\sigma\rangle^{LE}$ and $\langle\sigma\rangle^{PT}$ provides a method to study the contribution of the phase transformation under the high strain rate loading conditions, i.e. analysing the residual stress change and zirconia phase transformation condition in the samples after SHPB testing.

6.1.3 Phase transformation of the post tested ZTA samples

Figure 6.7 shows the Raman spectra of the 10% and 15% 1.5Y-ZTA samples and the corresponded images that recorded their final breaking conditions at the end of testing, under the same impact velocity, 11 m s^{-1}. The Raman analyses were carried

out on the impact surfaces to measure the amount of zirconia transformation upon impact. To achieve statistically valid data, five Raman analyses were performed on each sample. The existence of zirconia phase transformation during the SHPB test was confirmed from this analysis and it was observed that the 15% 1.5Y-ZTA samples showed a higher monoclinic intensity than the 10% samples. In addition, the higher intensity of the monoclinic peaks for the 15% compared to the 10% sample occur for two reasons: first, the higher amount of zirconia led to a higher transformability, which led to a greater transformation toughening effect during high strain rate testing; second, the 10% sample shattered during the SHPB test because the majority of the impact energy was consumed by the shattering process rather than by the zirconia phase transformation.

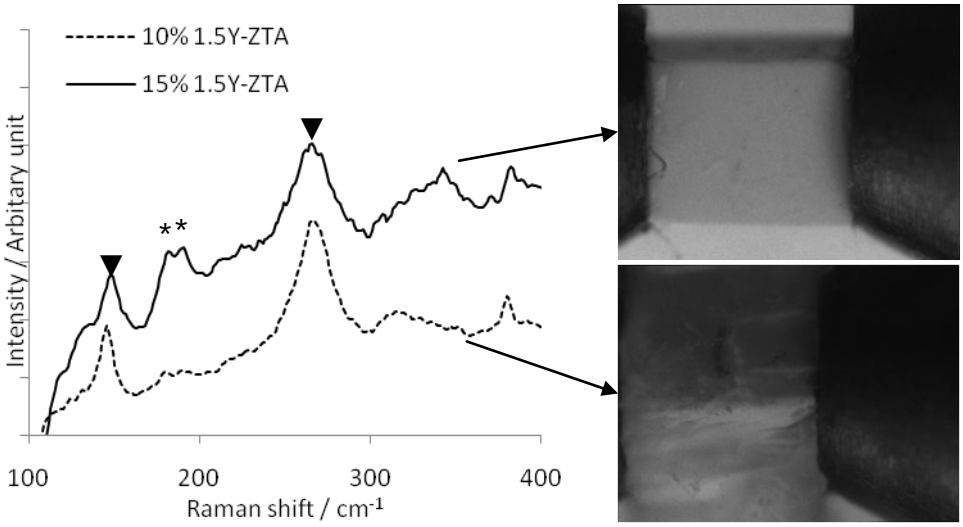

Figure 6.7 Raman spectra acquired from the SHPB impacted surfaces of 10% and 15% ZTA samples using 11 m s^{-1} impact velocity. Images of the SHPB tested samples taken near the end of the impact.

In order to exclude the effect of the zirconia contents and find out which reason dominated, 15% 1.5Y-ZTA fragments were needed. Since the available impact speeds (8 - 16 m s^{-1}) could not shatter the 15% 1.5Y-ZTA, the same material with a smaller sample size (3×3 mm cross section area and 5 mm length) was tested using 11 m s^{-1}. The 10% sample with the same smaller size was also tested for comparison and the results are listed in Table 6.2.

Table 6.2 Fracture condition the SHPB tested samples

Sample size / mm^2	15%: 3×3	15%: 4×4	10%: 4×4 and 3×3
Fracture condition	Fragmented into small debris	Intact	Fragmented into small debris

With a smaller size, the impact energy is concentrated into a smaller volume, which is equivalent to increasing the impact energy on a sample with a correspondingly larger size. It was found that the 15% 1.5Y-ZTA with the reduced size fragmented successfully whilst the 10% samples fragmented for both sizes as expected. The surviving samples and fragments of the 15% 1.5Y-ZTA were compared in terms of their degree of zirconia phase transformation, Figure 6.8. By comparing the Raman spectra acquired from their impact surfaces, it was observed that the (large) samples that survived showed a higher monoclinic peak intensity than the (small) samples that shattered. In addition, the degree of phase transformation was not uniform in the latter, some fragments or areas showed monoclinic peaks, as shown in Figure 6.8, whilst other fragments were free of phase transformation. The phase transformation in the former was expected since the crack propagation can promote the tetragonal to monoclinic transformation. For the positions where the phase transformation did not occur, it may be that the crack propagation occurred too quickly to produce any phase transformation. Comparison between the spectra from the impact surface and the transformed fractured surfaces of the fractured sample showed that a higher monoclinic peak intensity was observed on the fracture surface. However, both the impact surface and fracture surface possessed less zirconia phase transformation compared to the intact sample, which confirmed that the energy from the impact was mainly consumed by the materials' fragmentation. If fracture occurs, correspondingly, only a small amount of the impact energy is consumed by the zirconia phase transformation.

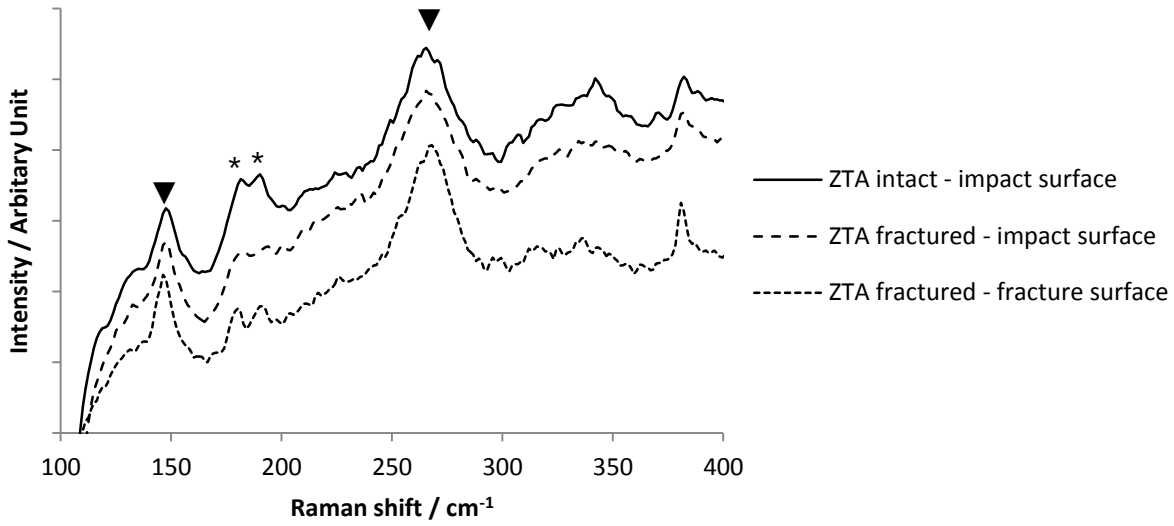

Figure 6.8 Raman spectra acquired from different surfaces of the 15% 1.5Y-ZTA samples. Note that the zirconia phase transformation was observed on certain fracture surfaces, whilst other surfaces showed pure untransformed tetragonal zirconia phase.

6.1.4 Residual stress distribution in the surviving 15% 1.5Y-ZTA samples

With the purpose of further confirming that the zirconia phase transformation affected the high strain rate performance of the ZTA samples, the residual stress distribution in the post tested ZTA samples were analysed out using the Cr^{3+} fluorescence technique. The intact and fragmented 15% 1.5Y-ZTA samples discussed in section 6.1.3 were investigated. A surviving sample is analysed in this section, whilst the fragments will be discussed in section 6.1.5.

It was observed that no obvious cracking occurred across the majority of the impact surface, although the corner areas showed some short cracks, which were due to the stress concentration that occurs for the cubic shaped samples. The image of the cracked surface is shown in Figure 6.9 (a). Cr^{3+} fluorescence mapping was carried out on the same area, as shown in Figure 6.9 (b) for the R1 peak shift map and (c) for the R1 peak width map.

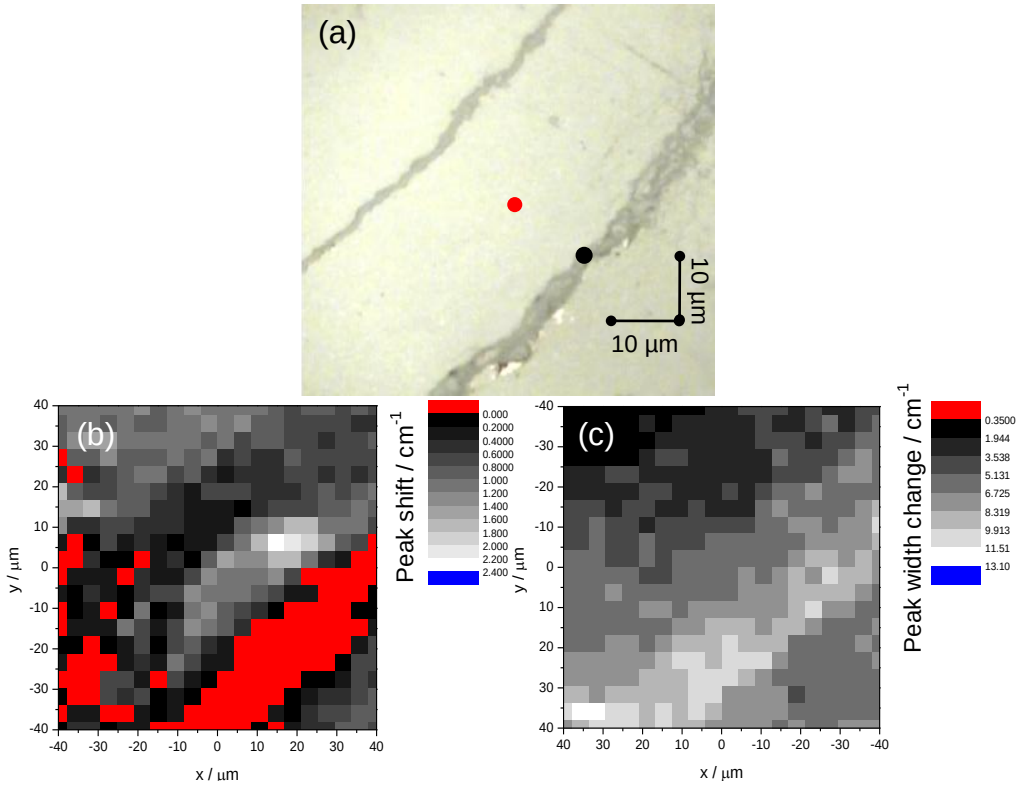

Figure 6.9 (a) The cracks on a corner of the impact surface of the 15% 1.5Y-ZTA. The Cr^{3+} fluorescence mapping on the same area: (b) the R1 peak shift mapping and (c) the R1 peak width change mapping. The red and black points in (a) are the Raman data collecting locations, the Raman data are shown in Figure 6.10.

It was observed that the R1 peaks on the cracks were slightly negatively shifted and the larger the crack the more negative the peak shift observed (red in Figure 6.9 (b)). On the surface remote from the cracks, a positive peak shift was obvious and the highest peak shift was about 2.4 cm^{-1}, representing a 315 MPa tensile residual stress. A comparison between the peaks arising from the crack, an uncracked region of the surface and from before the SHPB test was shown in Figure 6.10 (a). The difference between the peaks arising from the crack and from before SHPB testing was very limited, whilst a significant positive peak shift was observed on the impact surface remote from the cracks after the SHPB test, which indicates the presence of tensile residual stresses. The monoclinic peaks from the uncracked and cracked regions of the surface are shown in Figure 6.10 (b), which suggests that the phase transformation occurred as a result of the impact. The slight compressive residual stress or much lower tensile stress in the cracked region was due to the high density of materials deformation and the stress release during cracking. The volume

expansion of the transformed zirconia grains reduced the compressive stress in the alumina grains caused by the impact and helped to absorb the energy from the impact. Therefore the fragmentation of the sample was prevented. In addition, as is discussed in section 6.1.2, the residual stress of the impacted area was formed by the combination of $\langle\sigma\rangle^{LE}$, which is in compressive form, and $\langle\sigma\rangle^{PT}$, which is in tensile form. The final residual stress suggests that the $\langle\sigma\rangle^{PT}$ was larger than $\langle\sigma\rangle^{LE}$, and therefore resulted in a tensile stress on the impact surface. This indicates that the phase transformation could be a primary mechanism for consuming the impact energy in the intact samples and preventing the 15% 1.5Y-ZTA samples breaking.

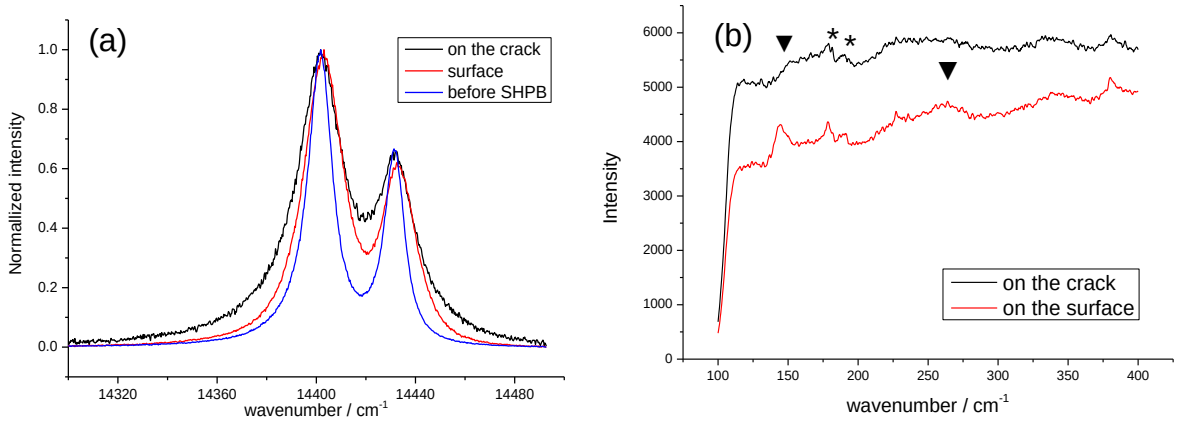

Figure 6.10 (a) The fluorescence R1 peaks before and after the SHPB testing; (b) the zirconia Raman bands for the post tested survived 15% 1.5Y-ZTA sample. For both figures, the black and red curves represent data collected on the crack and on the surface away from the crack, correspondingly; examples of the collecting locations are shown as black and red points in Figure 6.9 (a). The blue curve is a Raman spectrum collected on a random position of the sample before SHPB test.

In addition to the peak shift study, the degree of peak broadening was also observed in the mapping area. As shown in Figure 6.9 (c), the peak broadening was very significant around a relatively thick crack, whilst a thinner one did not show any signs of broadening. The latter is because the peak broadening is detectable only when the dislocation density is above 10^{14} m^{-2} inside the deformed layer [61]. A TEM analysis was undertaken on a focused ion beam (FIB) lift-out sample collected from a cracked area of the intact sample to characterise the dislocations, Figure 6.11. A large number of alumina grains with dislocations were observed, examples are shown in Figures 6.12 and 6.13.

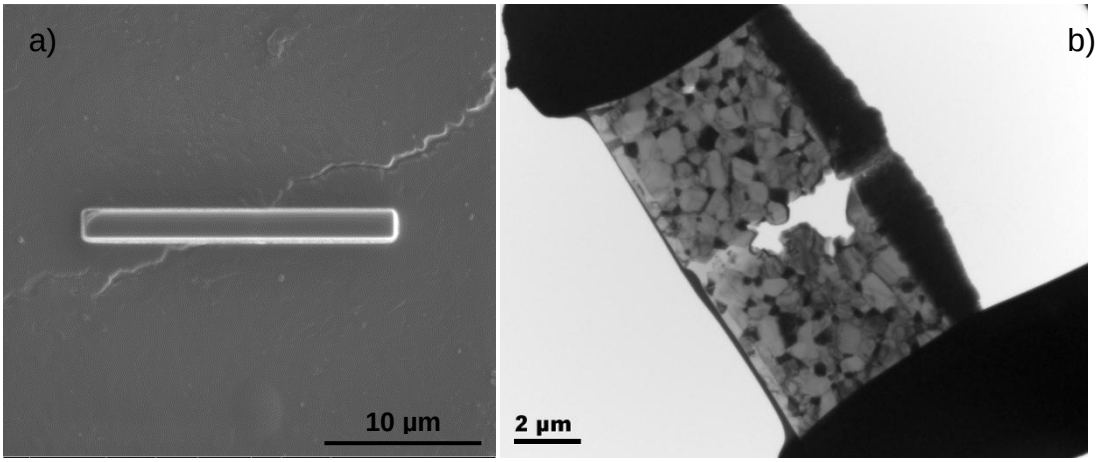

Figure 6.11 (a) FIB lift out from a cracking area of the post tested 15% 1.5Y-ZTA sample, (b) the sample showed a cracked region under the TEM observation.

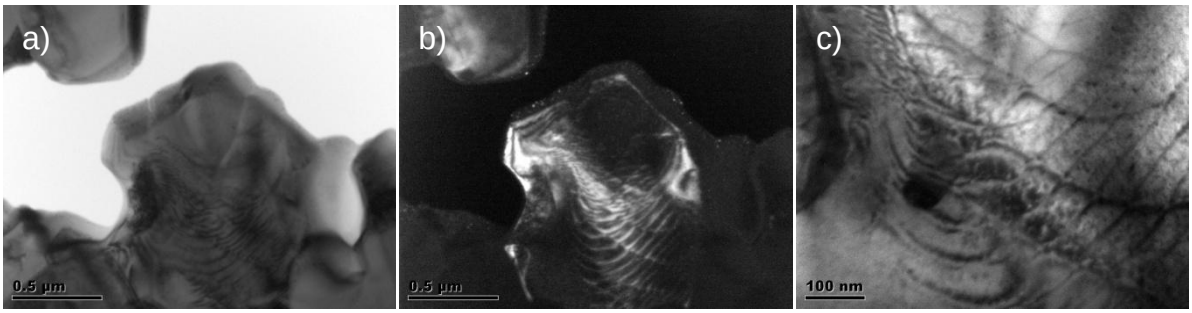

Figure 6.12 The bright field (a) and dark field (b) images of an alumina grain with dislocations, c) an enlarged image showing a small zirconia grain 'swallowed' inside the alumina grain and the dislocations generated from this grain.

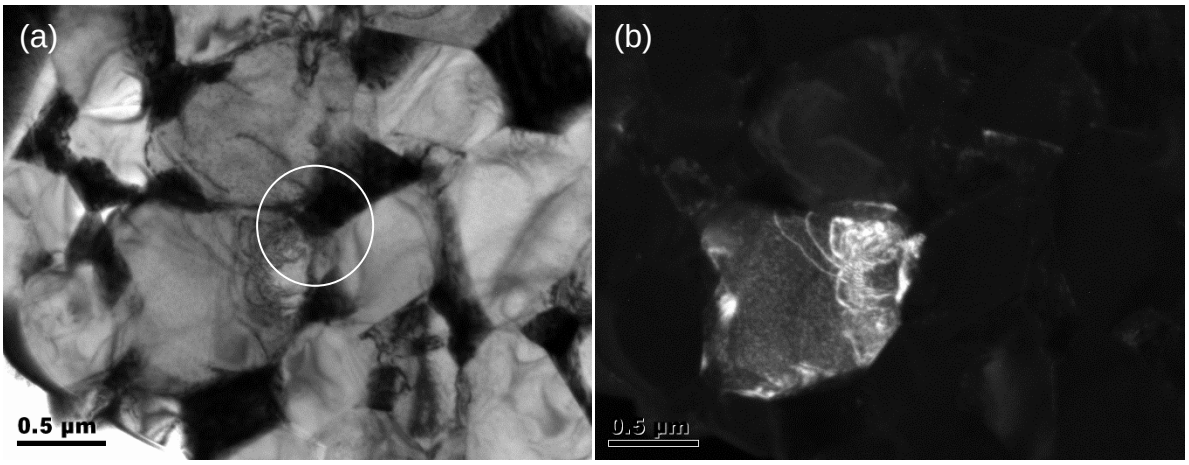

Figure 6.13 The bright field (a) and dark field (b) images of an alumina grain with dislocations, showing that the dislocations were generated from a zirconia grain next to the alumina grain.

In Figure 6.12, a very small zirconia grain has been ‘swallowed’ into an alumina grain during sintering and the dislocations were observed to be generated from this zirconia grain. For most of the other alumina grains that had dislocations, it was found that the dislocations were generated from zirconia grains near them, as shown in Figure 6.13. This suggests that the dislocation generation in the alumina grains probably originates from nearby zirconia grains. The diffraction pattern was collected on 8 zirconia grains in the vicinity of the alumina grains with dislocations and nearly all of the zirconia grains showed monoclinic crystalline structure, as shown in Figure 6.14. This result suggests that these dislocations could result from the volume expansion associated with the transformation of the zirconia grains. The formation of dislocations is another mechanism of energy absorption during the SHPB test, which helped to improve the high strain rate performance of the ZTA samples.

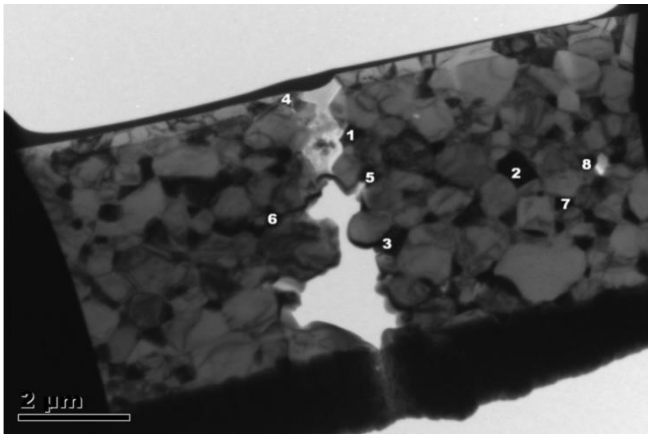

ZrO_2 grain No.	Phase	Grain size / nm
1	M	105
2	M	170
3	M	134
4	M	80
5	M	100
6	T	90
7	M	70
8	M	80

Figure 6.14 Zirconia phase study.

In addition, signs of crystallographic twinning were observed on many transformed zirconia grains. An example is shown in Figure 6.15, the parallel black lines in the zirconia grains indicates the existence of the twinning deformations. The twinning was also confirmed by the diffraction pattern from the deformed zirconia grain, shown in Figure 6.15 (b). The symmetrical shifting of the patterns on the two sides from the central line was caused by the symmetrical slipping of the crystal structure. In addition, in Figure 6.15 (a), dislocations were observed in the nearby alumina grain. It is considered that the volume expansion during the zirconia phase transformation caused the deformation of the zirconia grains, which led to twinning,

and further affected the surrounding alumina grains, resulting in the formation of the dislocations.

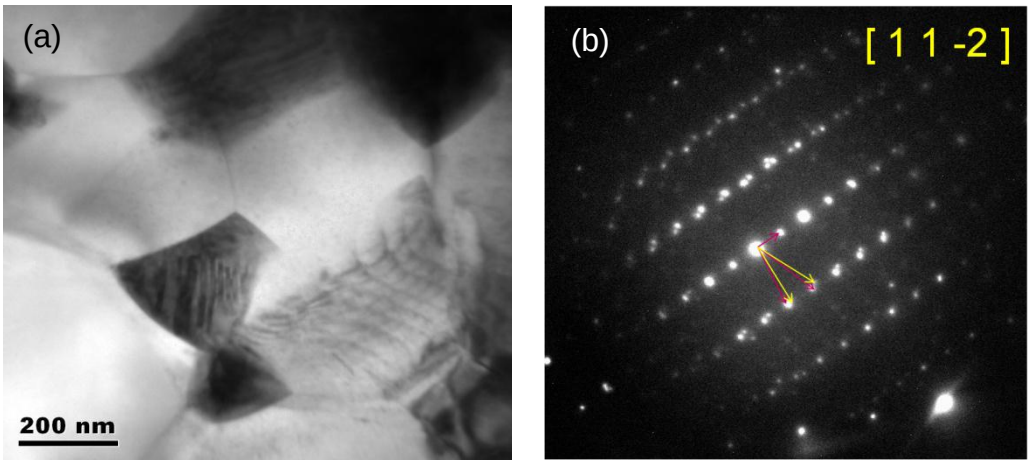

Figure 6.15 (a) Twins in the zirconia grain and dislocations in the nearby alumina grain; (b) diffraction pattern of the zirconia grain showing the twinning pattern.

6.1.5 ZTA fragments analysis

For the 15% 1.5Y-ZTAfragments, the fracture surfaces of fragments with different sizes were studied. Raman spectra were collected from the fracture surfaces to investigate the degree of zirconia phase transformation and the results showed that was not very uniform, Figure 6.16 (a). Monoclinic peaks were found on some of the fragments, whilst others showed no sign of phase transformation.

A Cr^{3+} fluorescence spectroscopy study was carried out on the fragments with a range of fragment sizes from 50 to 450 μm to investigate the relationship between the residual stress and the fragment size. The result is shown in Figure 6.16 (b), which plots the measured peak shift against the fragment size. More than 20 fragments were studied and a line map with 5 points was made on each fragment (>100 mapping points in total). It was observed that, with increasing fragment size, the measured residual stress reduced significantly. Moreover, the fragments with monoclinic zirconia phases are plotted with a cross in Figure 6.16 (b), a relatively lower residual stress may be observed for these fragments, which was believed to be caused by the tensile residual stress contribution associated with the phase transformation. However, there is no clear trend showing a relationship between the degree of zirconia phase transformation and the fragment size. This suggests that

the fragmentation was not highly affected by the zirconia phase transformation. The observation, therefore, suggests that the very fast fragmentation process lead to insufficient zirconia phase transformation.

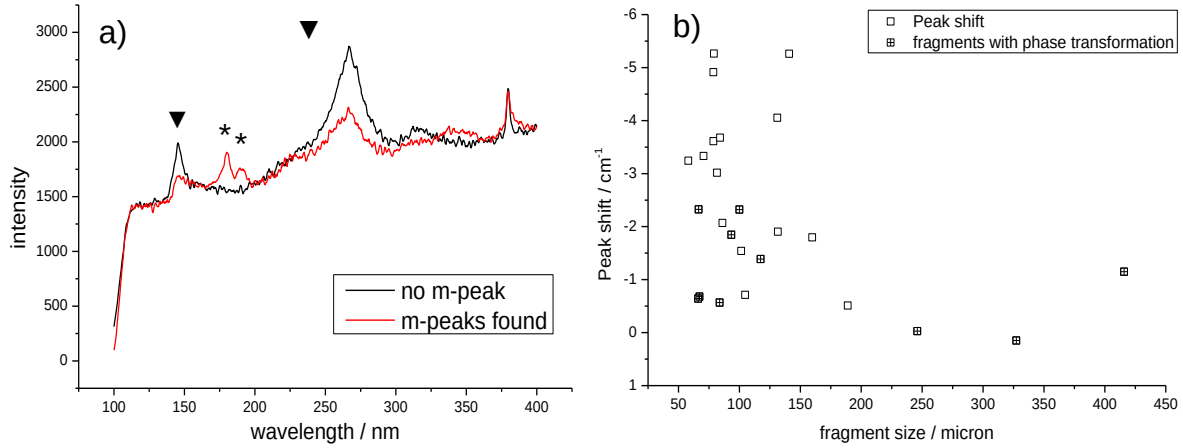

Figure 6.16 a) The zirconia Raman bands on the fracture surface of the SHPB tested 15% ZTA; b) relationship between R1 peak shift and fragment size.

In order to further investigate the difference between the large and small fragments, the fracture surfaces and fracture modes of the fragments sized from 3 to 700 μm were investigated using FEGSEM. Three fracture modes with different fracture surfaces were observed, including intergranular fracture, transgranular fracture and ductile fracture surfaces, as shown in Figure 6.17. On the intergranular fractured surface, the crack propagated along the grain boundaries and the crack could be initiated from a large surface or internal defect. For the transgranular fractures, the surfaces were very smooth; this type of fracture is considered to be generated by the dislocations in the grains. When the dislocations propagated across the grain, transgranular fracture occurred. Last but not least, ductile fracture surfaces were observed and there were considered to originate from the wearing of the fragments or the accumulation of high dislocation densities that caused the fracture of the material. The last two modes were basically related to the dislocations generated during the high strain rate testing.

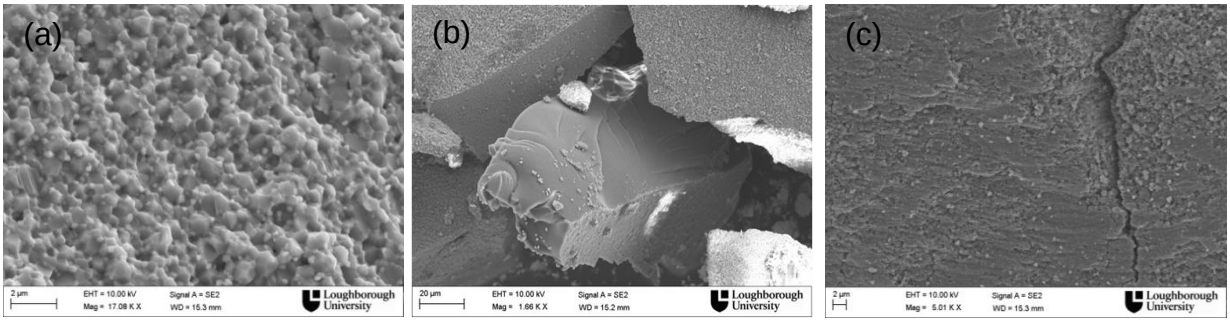

Figure 6.17 Fracture surfaces of the fragments with three fracture modes: (a) intergranular fracture, (b) transgranular fracture and (c) ductile fracture surface.

By measuring the area fraction of a fracture mode across the whole fracture surface of a fragment, the distribution of fracture modes with fragment sizes were mapped, as shown in Figure 6.18. It can be observed that fragments above 160 µm in size and between 50 to 100 µm were dominated by intergranular fracture failure, whilst the fragments from 100 to 160 µm were mainly fractured transgranularly. When the size was below 50 µm, ductile fracture surfaces were observed on nearly all the fragments. A general trend is that, with the decrease of the fragment sizes, the fracture modes changed from intergranular fracture, which was defect controlled, to transgranular fracture and ductile fracture surface, which were dislocation controlled.

The different fracture behaviour and fragmentation process could explain the reason for the different residual stresses on the fragments with different sizes, as shown in Figure 6.16 (b). For large fragments, the cracks initiated from large defects and passed through the grain boundaries, leading to less effect on the alumina grain interiors and hence resulting in lower residual stresses, whilst the much finer fragments could be generated from some highly plastically deformed locations created during the impact and which had a high dislocation density. The material was then fragmented along the dislocation lines, resulting in transgranular fracture and very fine fragments. This dislocation controlled process could consume much higher amount of energy than the former, and therefore, resulted in higher residual stresses in these fine fragments.

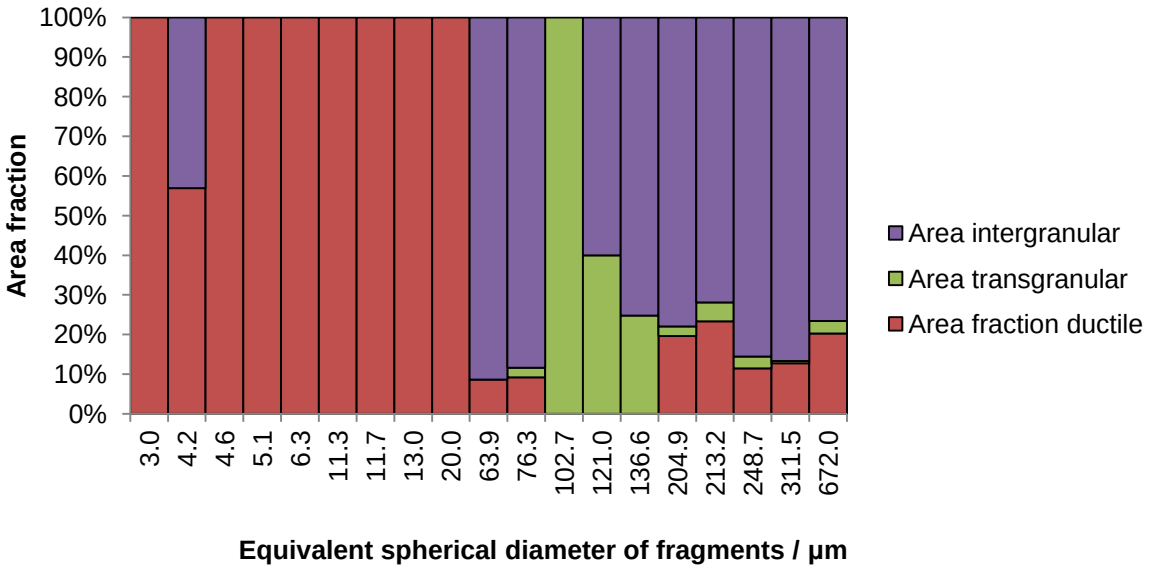

Figure 6.18 Relationship between the fracture modes and the fragment sizes.

Finally, a comparison of the intact and fragmented 15% 1.5Y-ZTA and the fragmented 10% samples was carried out, in order to investigate the effect of the zirconia content on the fragmented samples. As listed in Table 6.3, the samples were compared in terms of the zirconia phase transformation results and the residual stresses after the tests. As mentioned before, the samples with a smaller size (3×3×5 mm^3) experienced a higher impact energy level than the larger samples (4×4×5 mm^3).

Table 6.3 Fracture condition the SHPB tested samples tested at 11 m s^{-1}

Sample size / mm^3	15% ZTA 3×3×5	15% ZTA 4×4×5	10% ZTA 4×4×5 and 3×3×5
Fracture condition	Fragmented into small debris	Intact	Fragmented into small debris
Monoclinic level	30% Occurred on certain fragments	50% Occurred around cracks activated by the impact	20% Occurred on certain fragments
Residual stress / MPa	-700 to 0 (compressive)	-80 to 315 (tensile)	-700 to 0 (compressive)

The 10% sample fragmented with both sizes, whilst the 15% sample survived when the size was larger. This comparison indicates that the 15% ZTA with higher phase transformability can withstand higher impact energy without fragmentation. On the

other hand, the results also showed that for the same material, 15% ZTA, the amount of phase transformation and residual stresses were very different between the intact and fragmented samples. The intact sample showed a very high level of zirconia phase transformation, 50%, leading to a significant tensile residual stress and a much lower compressive stress on the impact surface. However, when the sample was fragmented, the level of phase transformation was reduced and the total residual stress observed on the fragments was dominated by the compressive component originating from the impact. This suggests that the effect of zirconia phase transformation was largely reduced when the sample was fragmented. Comparing the 10% and 15% fragments, their degrees of zirconia phase transformation and the residual stresses were similar, indicating that the zirconia content did not have any effect on the fragmented samples.

6.1.6 Conclusions

In general, the SHPB results suggest that the ability to withstand high impact energy by a 1.5Y-ZTA was related to the materials' phase transformation effect. For the 15% 1.5Y-ZTA which survived after the test, a high degree of transformation was observed. Most of the energy was consumed by the transformation and the formation of dislocations in the alumina grains, which prevented the fragmentation of the ZTA samples. On the other hand, when the energy exceeded a certain limit, the samples fragmented, less zirconia phase transformation was produced during the impact test, probably because the fragmentation process was too quick for the zirconia grains to transform, and, therefore, most of the impact energy was consumed by the breaking process.

6.2 Gas Gun Impact Test

6.2.1 Process recorded using high speed camera

The gas gun impact test provided a much higher impact speed, about 100-200 m s^{-1}, than the SHPB test. The samples, alumina, 10% and 15% 1.5Y-ZTA, were initially tested using the same impact speed, 100 m s^{-1}. 20% 1.5Y-ZTA was not used in this

part of work, based on the consideration that it had not offered improved high strain rate performance during the SHPB tests. The loading process during impact was recorded by detecting the voltage change in the strain gauges attached to the backing bar and the high speed camera was used to record the process in which the WC projectile was defeated by the ceramic discs. A typical force-time profile of a 15% 1.5Y-ZTA sample and the corresponding high speed photos are shown in Figure 6.19.

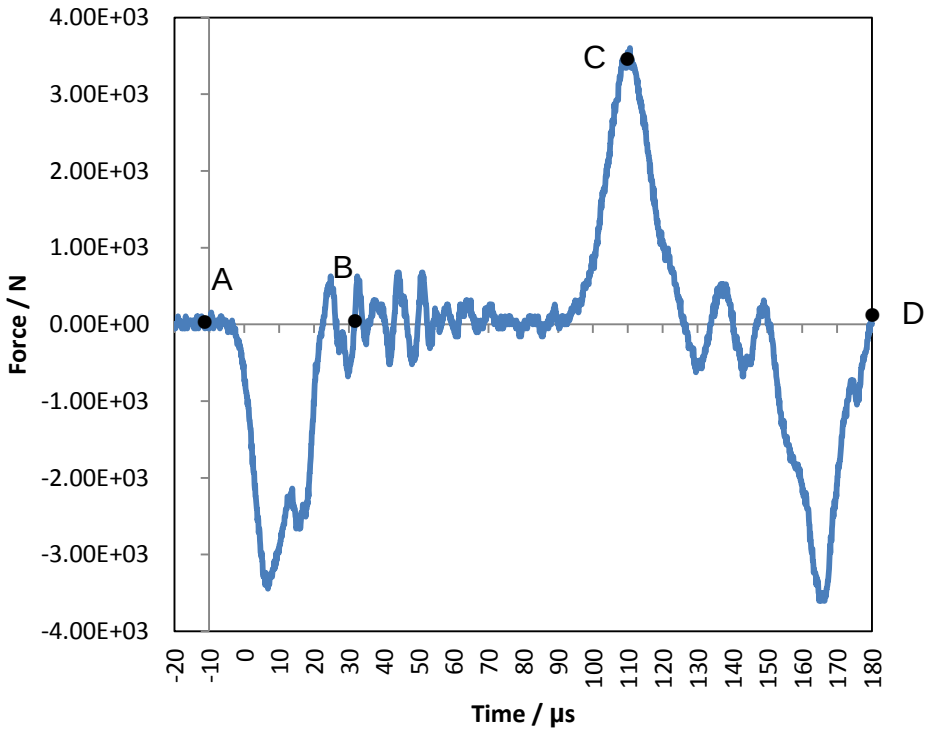

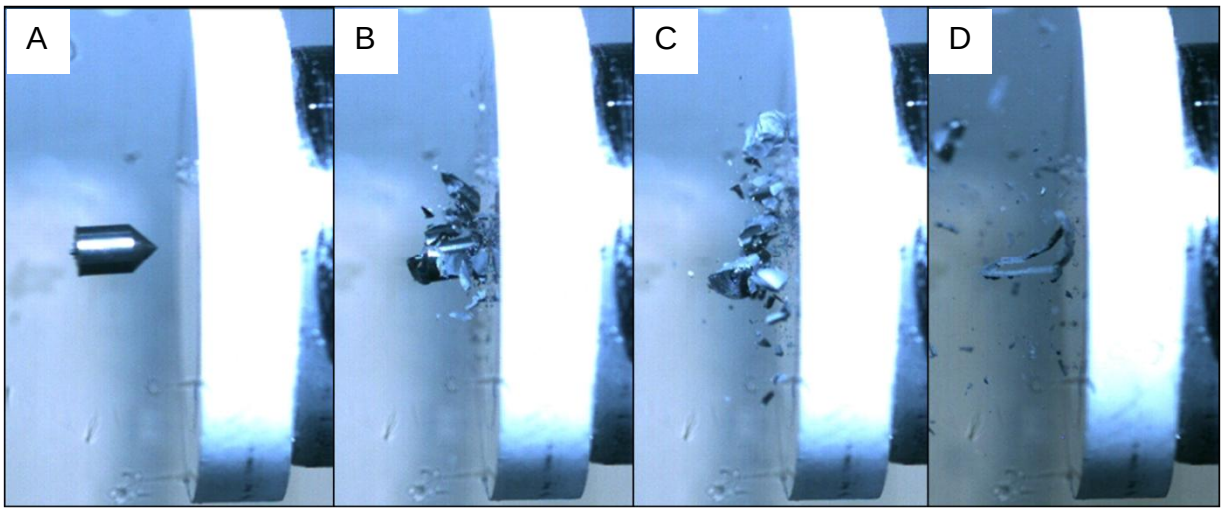

Figure 6.19 Force-time profile and the corresponding high speed photos at time A to D.

From the force-time profile in Figure 6.19, a compressive stress was applied on the sample during impact, which happened between A and B on the plot. The compression peak showed a double peak, which could be caused by crack generation. From B to C, the curve firstly fluctuated strongly, due to the continuous hitting by the projectile debris, and then a tensile stress was observed by the reflective load from the backing bar. From C to D and afterwards, the stress reflected back to the backing bar and the sample survived after the whole impact process. The fragmentation of the projectile was because of its lower hardness (12.2 GPa) compared to that of the ZTA samples (20.8 GPa)

6.2.2 Effect of zirconia phase transformation on the surface damage after impact testing

After impact testing with 100 m s^{-1} impact velocity, all the samples, alumina, 10% ZTA and 15% ZTA, survived with indented regions left at the impact point. By observing the sample surfaces, Figure 6.20, the size of the indentation of the alumina samples was slightly larger, ~1.8 mm diameter, than the observed indentation sizes of ~1.5 mm for the 10% and 15% ZTAs. Ring cracks, similar to Hertzian indented cracks, were observed on all the samples, these were caused by the blunted WC projectiles during the impacting process. In addition, some radial cracks emanating from the ring crack towards the outside of the samples were observed on the alumina and 10% ZTA samples, but not on the 15% ZTA. These radial cracks were considered to be critical to the failure of the sample, as their extensive propagation could lead to the breaking of the disc samples.

A line map curve showing the topographical change in the indentation area induced by the impact is displayed below the relevant optical microscopy image of each sample in Figure 6.20. The deepest point observed after the impact test for alumina was at -18 µm, whilst the 10% and 15% ZTA showed much flatter impact surfaces with the deepest point at around -10 µm; comparative details are listed in Table 6.4.

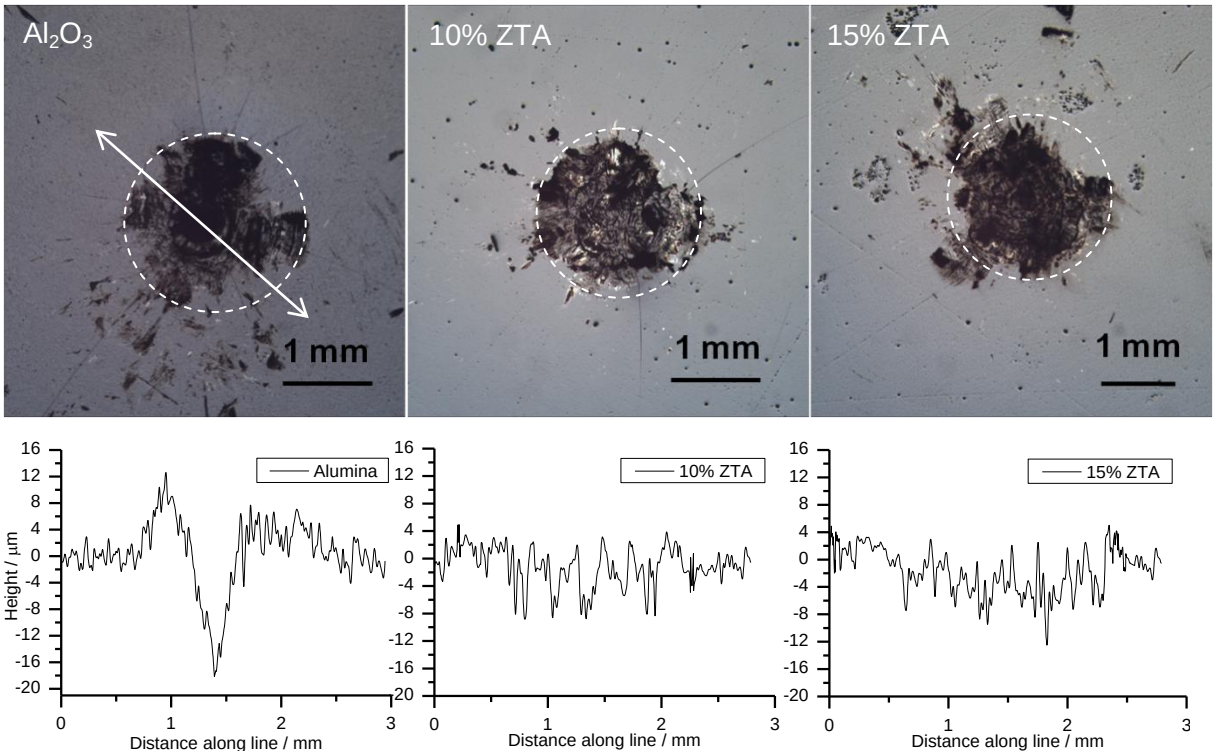

Fig. 6.20 Optical microscopy images showing the size and shape of indents caused by the projectile impact. The dotted circles indicate the surface micro-cracked region in each sample. The line scanning result for each sample shows the depth of the indentation along the line sketched on the image.

Table 6.4 Comparisons of the sizes of the impacted region and the depth of the indentations

	Alumina	10% ZTA	15% ZTA
Size of indentation / mm	1.8	1.4	1.5
Deepest point / µm	-18	-9	-12

From the above analysis, a significant difference in the indentation depth between alumina and ZTA materials was observed. However, in terms of microstructure and mechanical properties, the grain sizes were similar and the hardness of alumina was slightly higher. The main difference between the two materials was that the toughness of the ZTAs (5.4 MPa $m^{1/2}$) was~1.5 times higher than that of the alumina (3.5 MPa $m^{1/2}$). The volume expansion associated with the zirconia phase transformation could suppress the crack propagation and therefore increased the fracture toughness of the ZTA ceramics. This could also be the reason why there was reduced damage in the ZTA samples after the high strain rate impact testing. However, to verify this hypothesis, a study of the residual stress distribution and

plastic deformation in the impacted region, as well as the measurement of the phase transformation content was undertaken and the results are presented in section 6.2.3.

A large number of intergranular cracks were observed on the impacted surface inside the ring cracks for each sample, Figure 6.21. In addition, patterns of surface wear lines were identified on all the samples and were most obvious on the 15% ZTA. This could be formed by projectile debris which fragmented into very fine pieces travelling at high speed after impact and scratched the surfaces. The wear mechanisms could be plastic deformation controlled abrasive wear and micro fracture controlled chipping wear [122,127]. The ZTA samples showed dominant signs of abrasive wear, as the surface had no chips, whilst the alumina sample showed a combination of the two wear mechanisms, and more severe damage on the surface was observed. The different wear behaviour of the samples could be the reason for their different levels of surface damage after testing. It has been shown in Chapter 5 that the wear resistance of the ZTA materials is significantly higher than that of the alumina samples. This difference in wear resistance could indicate that the wear resistance of ceramic armours could be an important property to determine its performance under high strain rate impact.

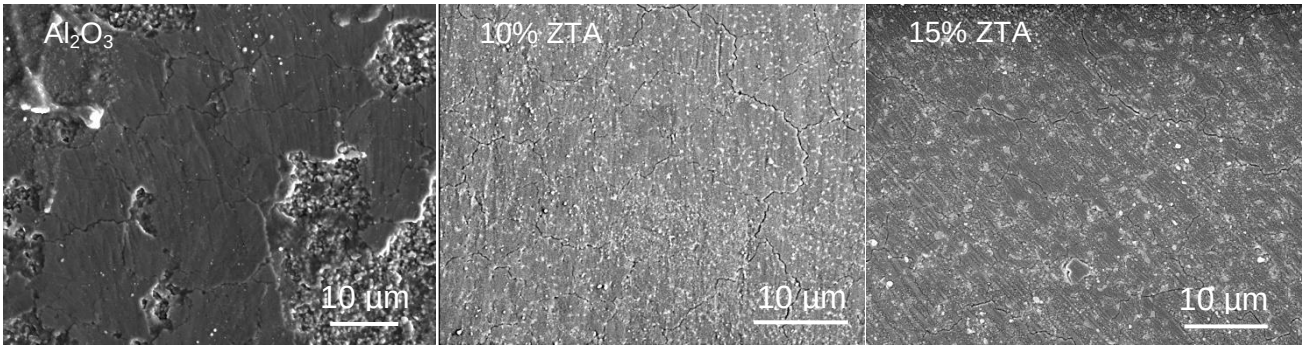

Figure 6.21 FEGSEM images of the impact tested sample surfaces.

The crack densities were calculated using Eqn. 3.2, see Chapter 3 and the comparison of the values for the three samples are shown in Figure 6.22. A significant reduction of the crack density from the alumina to the ZTA samples was observed. The crack density for the 15% 1.5Y-ZTA was also lower than that for the 10% ZTA. This result is consistent with the fact that the zirconia phase transformation could suppress the crack generation and propagation. With a lower

crack density, the ability to survive under the high strain rate impact is likely to be significantly improved.

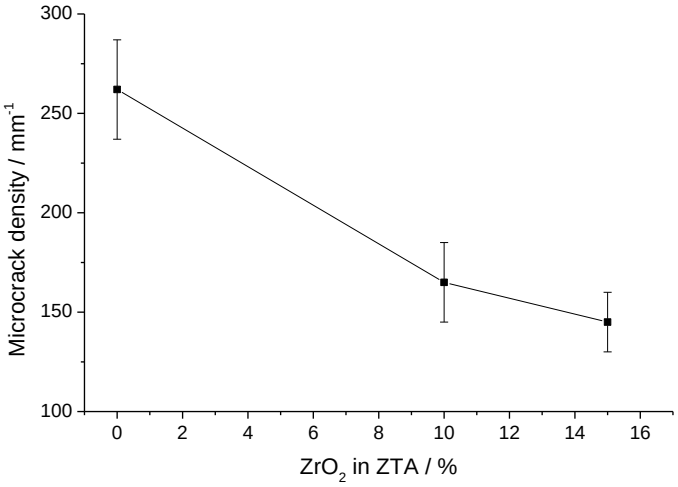

Figure 6.22 Crack densities of the 1.5Y-ZTA samples with the increased zirconia contents.

6.2.3 Effect of zirconia phase transformation on residual stress distribution and plastic deformation after impact testing

It is crucial to understand the residual stress distribution and plastic deformation condition on the samples after high strain rate testing, because they are responsible for the extent of the crack propagation and the absorption and distribution of the kinetic energy from the projectiles. Figure 6.23 shows the mapping results of the Cr^{3+} R1 peak shift from the alumina, 10% ZTA and 15% ZTA. The pixels in the maps were grey scaled according to the amount of peak shift measured, in which a black pixel represents the maximum negative peak shift observed (-6 cm^{-1}), whilst a white pixel indicates 0 shift. The black pixel with white lines represents positive peak shifts.

The alumina sample showed an increased negative shift of the peak position from outside of the impacted indentation (-0.5 cm^{-1}), to the centre of the indentation (-6 cm^{-1}), which corresponds to a hypostatic compressive stress change from -66 to -790 MPa. The stressed area was about 2 mm in diameter, similar to the measurement of the indent area using optical microscopy. Unlike the alumina, the peak shift in the impacted regions of the 10% and 15% ZTA samples was more

complicated. For the 10% ZTA, the peak shift changed from -1 cm^{-1} at the edge of the map area to the maximum value of ~-5 cm^{-1} at the edge of the indentation (as illustrated by the dotted circle). Interestingly, at the centre of the indentation, where the highest impact pressure was exerted, only a very limited negative shift was observed. The typical shift observed in the 10% ZTA indentation centre is in the range of 0 to about -2 cm^{-1}, which corresponds to a compressive residual stress of 0 to -260 MPa. In addition, a certain amount of positive shift, which indicates a tensile residual stress, was observed at some points (highlighted with the white line pattern in Figure 6.23). For 15% ZTA, the peak shift from the outside to the centre was very limited, i.e. from 0 to -2 cm^{-1}, moreover, a very significant region with tensile residual stress (approximately +130 MPa) was observed.

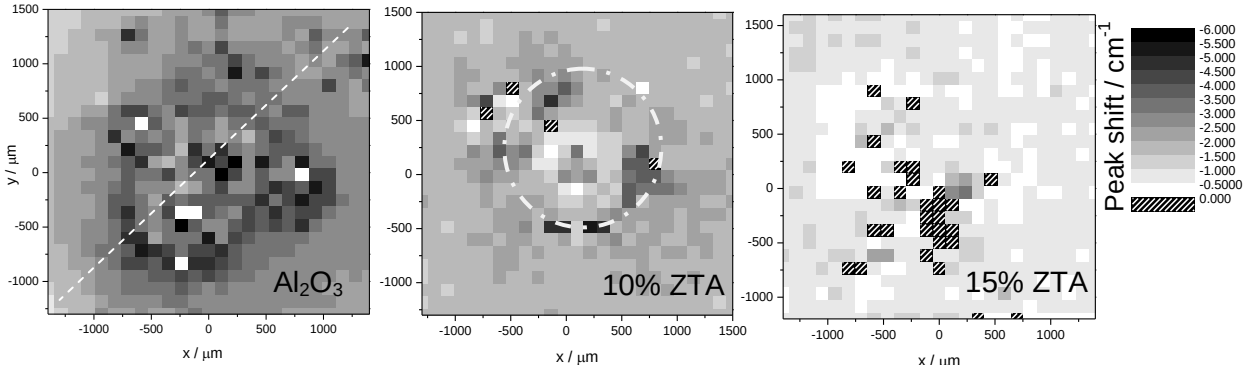

Figure 6.23 R1 fluorescence peak shift mapping on the impacted regions of the specimen: Alumina, 10% ZTA and 15% ZTA, the dashed line in the first image is the line mapping route in Figure 6.24.

Therefore, a significant difference in the residual stress state after the impact test was observed between the alumina and ZTA ceramics. For the alumina, the observed residual stress distribution was as expected, since the highest compressive strength was observed in the indentation centre as a result of the high speed impact. However, for the ZTA materials, previous studies [72,76] have proved that, during the zirconia phase transformation process, the volume expansion provides a local compressive stress to the surrounding alumina grains, and the latter provide an overall tensile stress to resist the force from the nearly uniformly distributed zirconia grains. As the Cr^{3+} mapping can only measure the residual stress in the alumina grains, it is very likely that the low compressive stress (and

even tensile residual stress) observed in the impact centre of the ZTA materials is due to the zirconia phase transformation that occurred during impact.

To further confirm the above assumption, the zirconia phase transformation in the mapped area was characterised. Due to the relatively low zirconia content, good quality Raman spectroscopy data could only be achieved by using a very long exposure time (60 s for each point, vs. 1 s for Cr^{3+} fluorescence spectroscopy). Therefore, a line map along the diagonal of the mapping area (along the dashed line shown in Figure 6.23) was carried out for a quantitative measurement of the zirconia phases. 25 points along the line, which was about 4 mm long, were scanned and the mapping was repeated 3 times for each 10 and 15% ZTA sample; the average results are plotted in Figure 6.24. Very significant zirconia phase transformation was observed in the impacted area, with about 50% monoclinic zirconia phase transformation for the 15% ZTA and 35% for the 10% ZTA. Higher transformability observed in the 15% ZTA led to a more significant reduction of the residual stress in the alumina grains and changed it from compression to tension, Figure 6.23. The reduction of tensile residual stress could help to reduce the microstructural deformation of the material and hence reduce the damaged area and damage level.

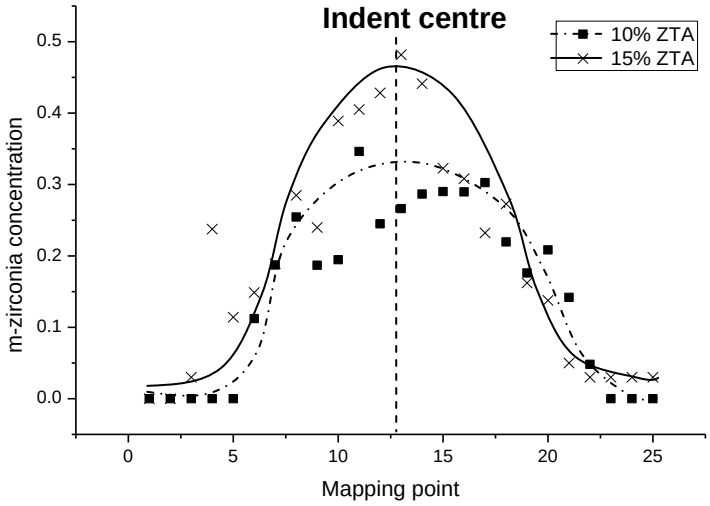

Figure 6.24 Line mapping across the indented area (the scanning path was noted in Figure 6.23 as a dashed line) showing the concentration of transformed monoclinic zirconia across the damaged area.

It has been shown that the zirconia phase transformation affects the residual stress on the impact surface; the plastic deformation was also found to be highly affected as shown in Figure 6.25, where the changes in the R1 peak width were mapped on the same area shown in Figure 6.23. A very large area in the alumina sample showed peak broadening from 17 to 35 cm^{-1}. The peak broadening regions for the ZTA samples were much smaller than those for the alumina. The different peak broadening conditions could be explained by the suppression of crack propagation and the energy absorption during the zirconia phase transformation process. As part of the kinetic energy from the high speed projectile was consumed by the former, the energy left to cause the plastic deformation was reduced, therefore, the dislocation density in the ZTAs was lower than that in alumina samples. The lower plastic deformation also resulted in reduced residual stress. With the smallest deformation area, residual stress and dislocation density, the 15% ZTA was considered to be the best material in terms of the high strain rate performance compared to the others investigated in this study.

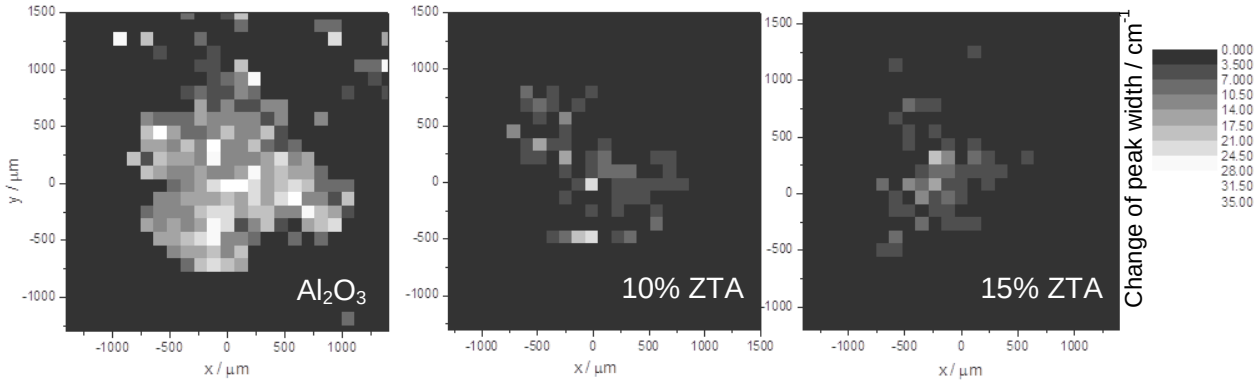

Figure 6.25 Map of the change of R1 fluorescence peak width on the impacted regions of the specimen: alumina, 10% ZTA and 15% ZTA.

6.2.4 Cross-section analysis

After the surface characterisation, the cross-sections of the tested samples were characterised using Raman and Cr^{3+} fluorescence spectroscopy. The micrograph of the cross-section of an alumina sample is shown in Figure 6.26 (a). A large number of cracks were observed below the surface. In addition, a plastic zone beneath the impacted region was observed, as highlighted in Figure 6.26 (a). This plastic zone

was easily observed mainly due to the extensive material pull-out, as shown in Figure 6.26 (b). Because the materials were highly deformed and a large microcrack network existed in the plastically deformed area, the materials were easily pulled out during polishing.

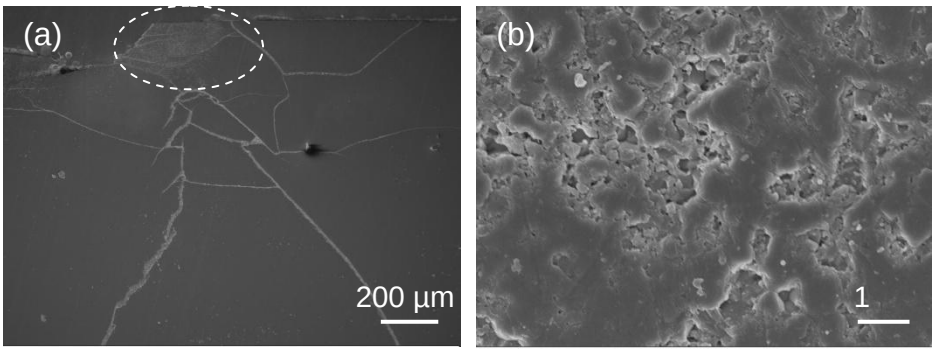

Figure 6.26 (a) SEM micrographs of the cross-section of an alumina specimen, the circle highlights the plastic zone formed by the impact; (b) materials pull-out on the plastic zone.

The cross section of the 10% and 15% ZTA samples are shown in Figure 6.27. A significant difference in the cross sections between the alumina and ZTAs is evident. No material pull out in the plastic zone was observed underneath the impact surface except for two to three large cracks forming a cone shape in the ZTA cross-sections. In addition, the extent of crack propagation was much suppressed in the ZTA samples compared to that in the alumina sample, which suggests that the identical impact speed caused much reduced damage.

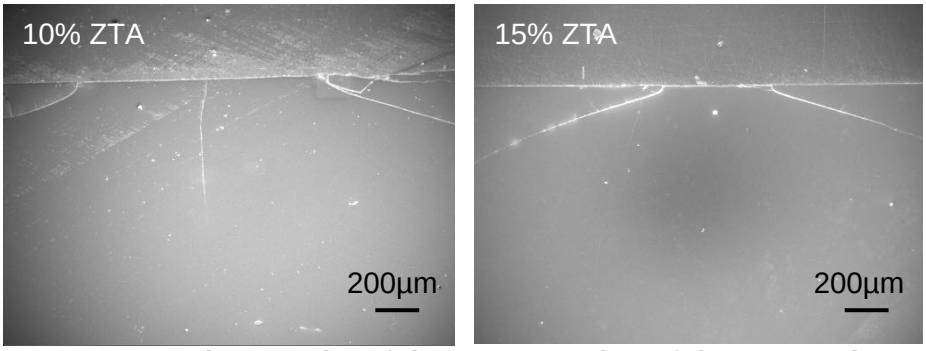

Figure 6.27 SEM micrographs of the cross-section of the 10% and 15% ZTA specimens

The Cr^{3+} fluorescence maps are shown in Figures 6.26 and 6.27,the peak shift map is shown in Figure 6.28. For the alumina sample, due to the polishing-induced

material pull out in the plastic zone, the compressive residual stress built up during the impact was released, therefore a lower negative peak shift was observed in the plastic zone compared to the other area underneath the impact surface. For the ZTA samples, no material pull out happened, suggesting that there was no significant fracture beneath the impact area, but plastic deformation could still exist. From the fluorescence mapping results, the both ZTA samples showed obvious signs of tensile stress areas beneath the impact surface, in which strong positive peak shift were observed. In addition, the 15% ZTA showed a larger and deeper area with tension. Comparing the stress maps with the SEM micrographs of the ZTA samples, it was found that, although no materials deformation or large degree of cracking was observed, plastic deformations still happened to form a plastic zone and induced the zirconia phase transformation, the latter generated a significant effect on the residual stress state of the impact affected regions.

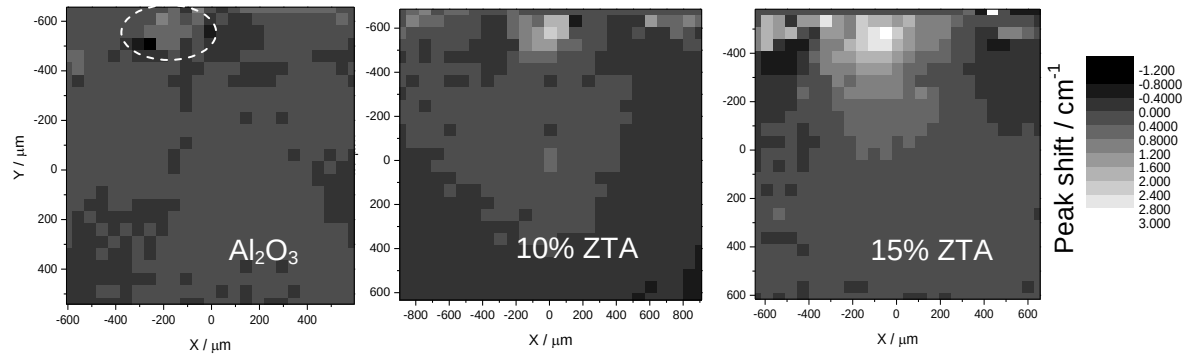

Figure 6.28 R1 fluorescence peak shift map on the cross-sections of the specimen: alumina, 10% ZTA and 15% ZTA, the dashed line circle highlights the position of the plastic zone in Figure 6.26.

The peak broadening of the cross-sections were mapped and are shown in Figure 6.29. It should be noted that the scale bars for the alumina and the ZTA samples are different due to the significantly different levels of the peak width change occurring during impact. The alumina sample showed the highest degree of peak broadening within the plastic zone, which was about 33 cm^{-1}increase in peak width. The peak broadening region in the alumina sample was found to overlap with the plastic zone and compressively stressed region shown in Figure 6.28. The 10% and 15% ZTA samples also showed regions with obvious peak broadening, confirming the existence of plastic zone, whilst their highest values were only about 11 cm^{-1} and 8

cm^{-1} respectively, which is much less compared to that observed in the alumina samples. The dislocations may have been able to induce the zirconia phase transformation, which inhibited further damage in the materials. The much lower level of peak broadening observed in the ZTA samples beneath the impact surface is consistent with the results observed on the impact surfaces, and therefore, further proved that the much reduced damage in the ZTA samples after impact may be derived from the impact triggered zirconia phase transformation. In addition, with the higher zirconia content, the protection from the zirconia phase transformation also increased.

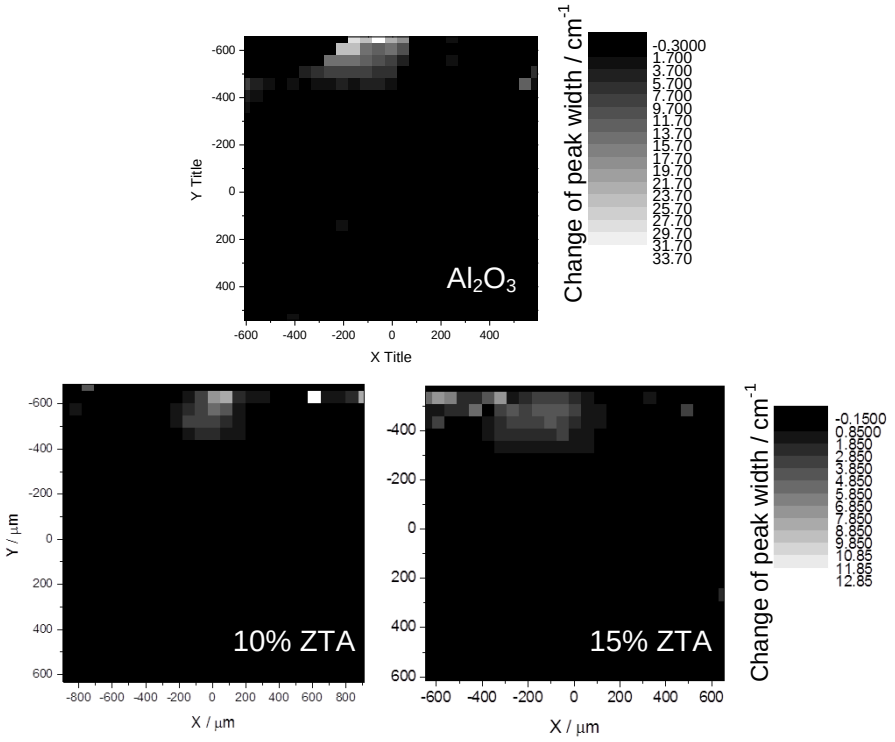

Figure 6.29 R1 fluorescence peak width change mapping on the cross-sections of the specimen: alumina, 10% ZTA and 15% ZTA.

To further confirm that the reduced level of the residual stress and dislocation density change observed from the ZTA samples originated from the zirconia phase transformation, the concentration of the transformed monoclinic zirconia phases on the cross-sections of the ZTA samples were mapped. The results are shown in Figure 6.30. Because the Cr^{3+} fluorescence map results showed that the residual stress and dislocation density change was concentrated on the region about 0-600 μm underneath the surface, the zirconia phase mapping was focused on this area of

interest. Very significant zirconia phase transformation was observed and the highest amount was about 45% for the 10% ZTA and 50% for the 15% ZTA. The phase transformation area was larger for the latter as well. The results confirmed the presence of zirconia phase transformation in the impact-affected region.

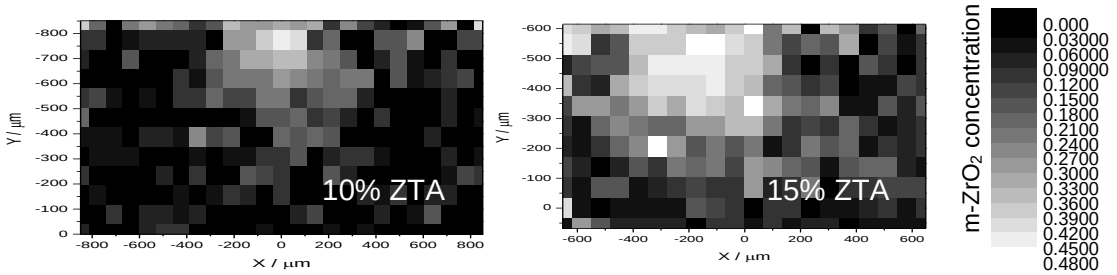

Figure 6.30 m-ZrO_2 concentration map on the cross-sections of the 10% and 15% ZTA specimens.

6.2.5 TEM study

Evidence from the Cr^{3+} fluorescence study suggested that plastic deformation in alumina underneath the impact site was almost absent in the ZTA specimens. An in depth TEM study was carried out on specimens collected by FIB from the region below the impacted region of the 15% ZTA sample to verify the observation. A slice shown in Figure 6.31 (a) was lifted from a region 20 μm below the impact region, which is within the plastic zone of the impact-tested specimen. Damage to the specimen due to ion beam impact in the FIB was avoided by using a very low beam current (100 pA) for final thinning of the electron transparent area of 15 ×5 μm. A significant number of zirconia grains, as the bright phases, were observed in the thinned area, Figure 6.31 (a), the larger grains are alumina. Polishing damage was restricted to within 200 nm from the surface, beyond that the microstructural changes were purely due to the high strain rate impact. Figure 6.31 (b) is the microstructure of the 15% ZTA. It can be observed that although the specimen was lifted from the impact region, minimal deformation was observed in the alumina grains. They were clean and only rare dislocations were noticed inside them. This observation was consistent with the Cr^{3+} fluorescence study, Figure 6.28. The grains shown with the arrows in Figure 6.31 (b) are the transformed zirconia grains. The concentration of the transformed grains was notably high in this specimen. Figure 6.31 (c) and (d) are the high magnification images of the transformed zirconia grains. TEM was performed primarily with a low condenser aperture to avoid transformation due to the

electron beam [128]. Several monoclinic laths were observed inside the ~200 nm zirconia grains. This observation again vindicated the observation from the fluorescence spectroscopy; formation of twins due to monoclinic transformation absorbs significant amount of energy. The strain energy for a normalized volume of the tetragonal phase has been predicted to be 9 MPa in contrast to 905 MPa under shear for monoclinic phase [129]. This large absorption of energy left very small shear available for plastic deformation in the alumina grains. This is believed to be the primary reason why plastic deformation was absent in the alumina grains in the ZTA, whilst the grains is the pure alumina experienced significant plastic deformation in the impact region, as shown in Figure 6.23.

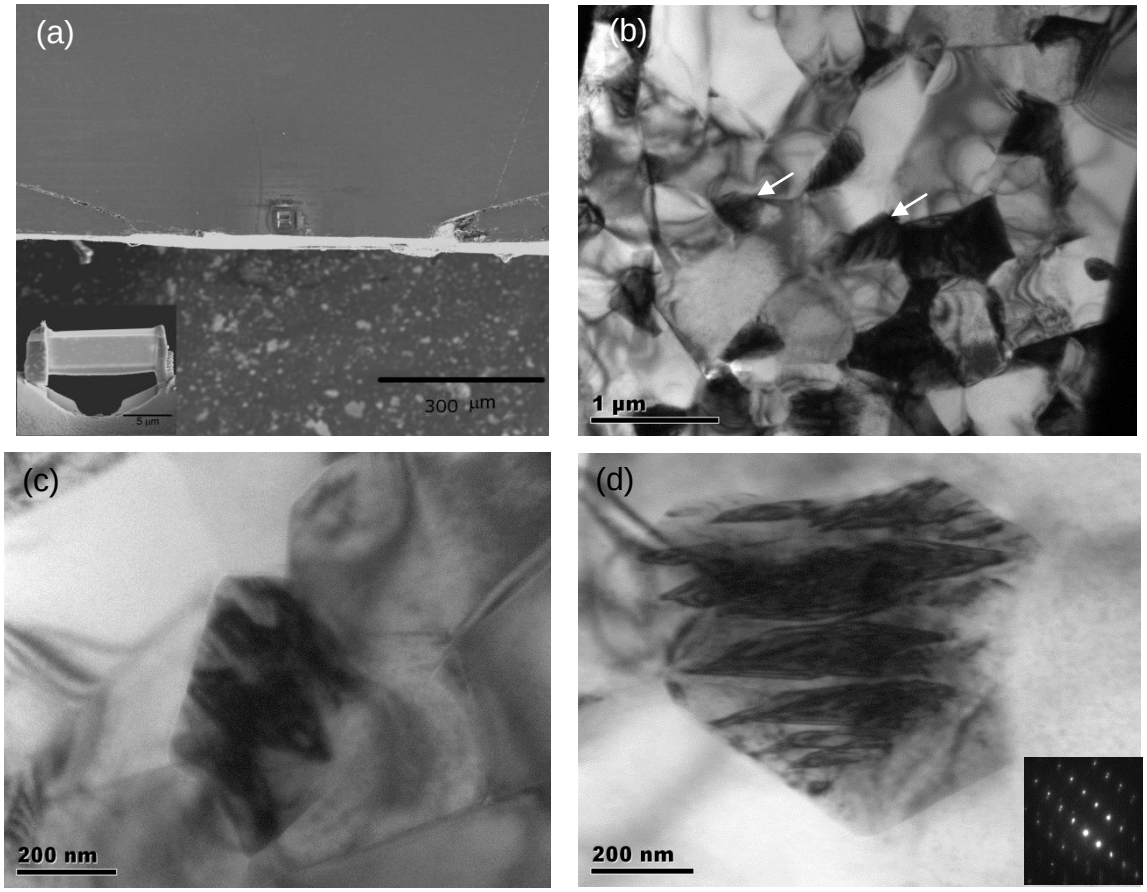

Figure 6.31 (a) SEM micrograph showing the location of the impact site of 15% ZTA specimen and the region from where the TEM specimen was lifted out (shown in inset) using FIB (b) TEM micrograph of showing clean alumina grains, whereas several zirconia grains, (b) and (c), were transformed to the monoclinic phase.

6.3 Gas Gun Impact Test with Different Speeds

From the previous gas gun impact tests on the alumina, 10% and 15% 1.5Y-ZTA samples at 100 m s^{-1} impact speed, the 15% ZTA samples showed potentially superior performance to defeat the high strain rate impact. In order to find out its limit to withstand the impact, higher impact speeds were used, viz. 130 and 150 m s^{-1}. In addition, nano 1.5YSZ samples were tested in this section to further understand the effect of zirconia phase transformation on the high strain rate performances upon impact. A summary of all the samples tested are listed in Table 6.5.

Table 6.5 Fracture conditions of the impact tested samples

Sample	Hardness / GPa	Toughness / MPa $m^{1/2}$	Impact speed / m s^{-1}	No. of samples tested	Condition after test
Alumina	20.3±0.4	3.0±0.4	100	3	Survived, with radial cracks
10 % ZTA	19.9±0.3	5.2±0.3	100	3	Survived, with radial cracks
15% ZTA	19.3±0.3	5.3±0.4	100	3	Survived
			130	3	1 survived, with radial cracks 2 broke into 2-3 pieces
			150	3	Broke into 4 pieces, showing very large cone crack
nano1.5YSZ (97% theor. density)	12.5±0.5	9.0±1.5	142	1	Survived, showing a very deep indent
			176	1	Broke

It was observed that under a higher impact speed, 130 m s^{-1}, only one in three 15% ZTA samples survived whilst the others were broken into several large pieces. With a further increase of the speed to 150 m s^{-1}, all the samples broke. This suggests that the 130 m s^{-1} could need to be a critical speed above which the energy from the impact was high enough to break the samples, whilst below which the samples could survive. The different behaviours of the materials at this speeds, i.e. some survived and some broke, could be related with their different inherent defect sizes in the impact region, which could have been caused by the processing or polishing. On the other hand, the nano 1.5YSZ samples survived at 142 m s^{-1}, although a very deep

indent was observed. The sample broke at the highest speed tested in this project, 176 m s^{-1}.

In this section, the surviving and broken samples of the 15% 1.5Y-ZTA were compared and characterised in detail. The breaking process during impact is studied in section 6.3.1. Then, the 15% samples that survived at different speeds, 100 and 130 m s^{-1}, are compared in terms of their stress distribution, dislocation density change and zirconia phase transformation conditions in section 6.3.2. In section 6.3.3, the surviving and broken samples tested under 130 and 150 m s^{-1} are compared and the crack densities at different impact speeds are studied. Finally, the nano 1.5YSZ sample that survived at 142 m s^{-1} is characterised in section 6.3.4.

6.3.1 Impact process recorded using high speed camera

A typical force-time profile of a 15% 1.5Y-ZTA sample tested at 130 m s^{-1} and the corresponding high speed photos are shown in Figure 6.32.

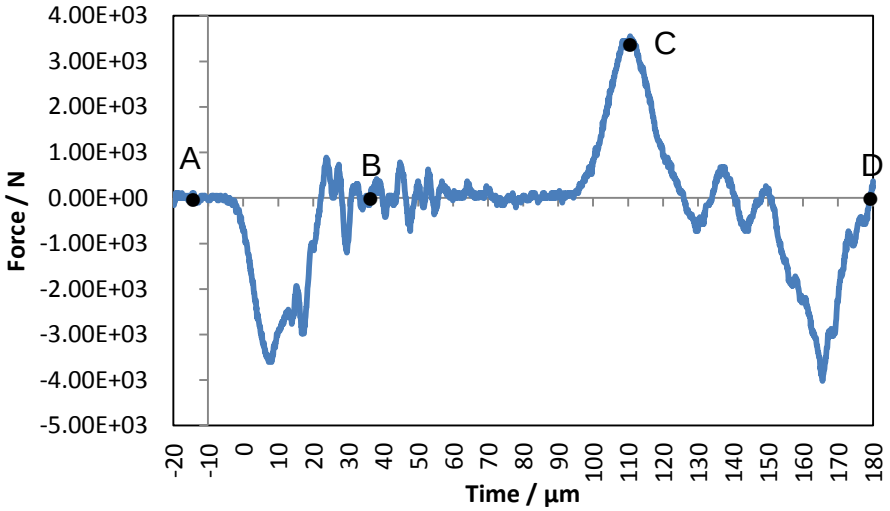

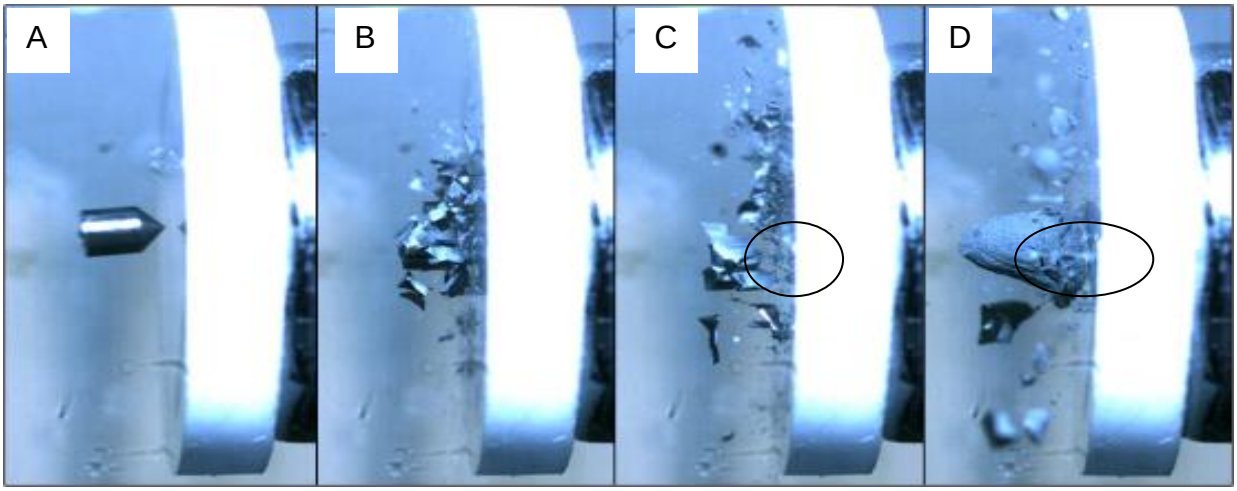

Figure 6.32 Force-time profile and the corresponding high speed photos at time A to D.

It was found that the cracks were generated during the impact process when a compressive stress was applied, as the double compressive peak was observed on the plot. After that, fracture started at the time C, at which the sample experienced a reflective tensile stress from the backing bar. By observing the samples after breaking, Figure 6.33, it was found that the fracture was caused by the propagation of the radial cracks, which initiated from the impact centre and propagated to the edge of the sample. The extensive propagation of the radial cracks resulted in the fragmentation of the impact tested samples.

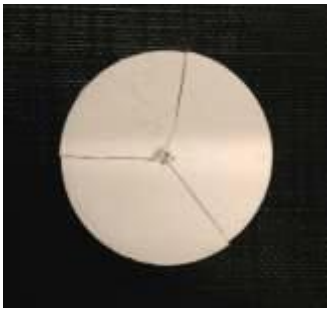

Figure 6.33 A broken sample after impact test.

6.3.2 Comparison of the surviving 15% 1.5Y-ZTA samples tested under 100 m s^{-1} and 130 m s^{-1}

The impact surface of the samples are shown in Figure 6.34. Both samples did not show deep indents as a result of the projectile impact, which could be due to the fragmentation of the projectile during impact. On the other hand, the sample with a

higher impact speed showed more severe surface damage, including large chips and radial cracks, which were not observed on the other sample tested at 100 m s^{-1}.

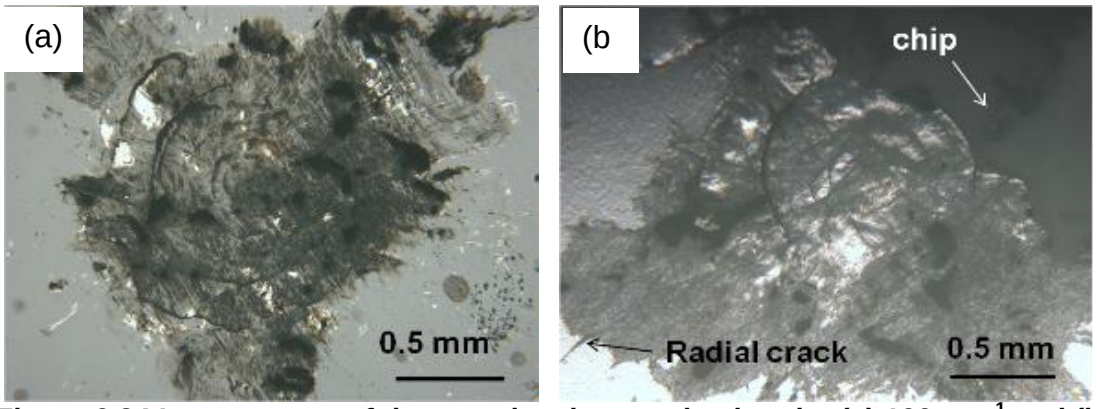

Figure 6.34 Impact areas of the samples that survived under (a) 100 m s^{-1} and (b) 130 m s^{-1} impact speeds. Large chips and radial cracks were observed on the sample (b).

The R1 fluorescence peak shift and peak broadening map of the above two samples are shown in Figures 6.35 and 6.36. The

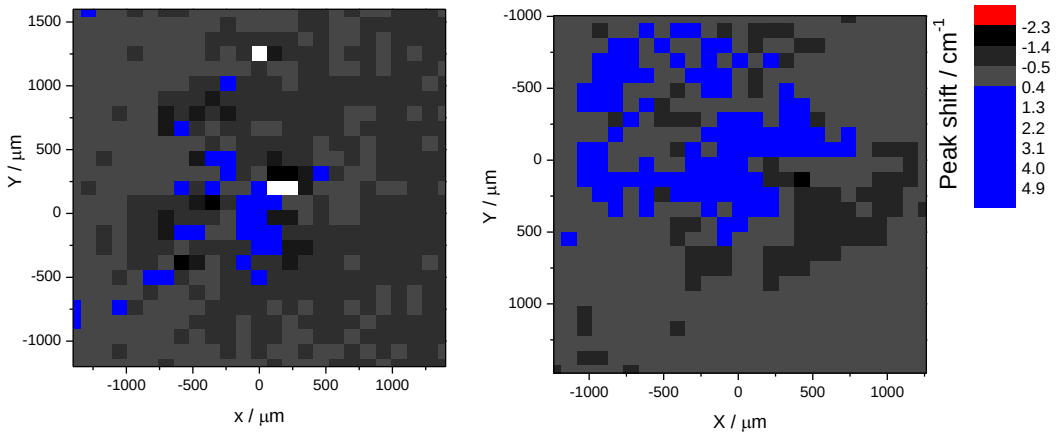

Figure 6.35 R1 fluorescence peak shift map of the impacted regions of the surviving 15% 1.5Y-ZTA tested at (a) 100 m s^{-1} and (b) 130 m s^{-1}.

Change of peak width / cm^{-1}

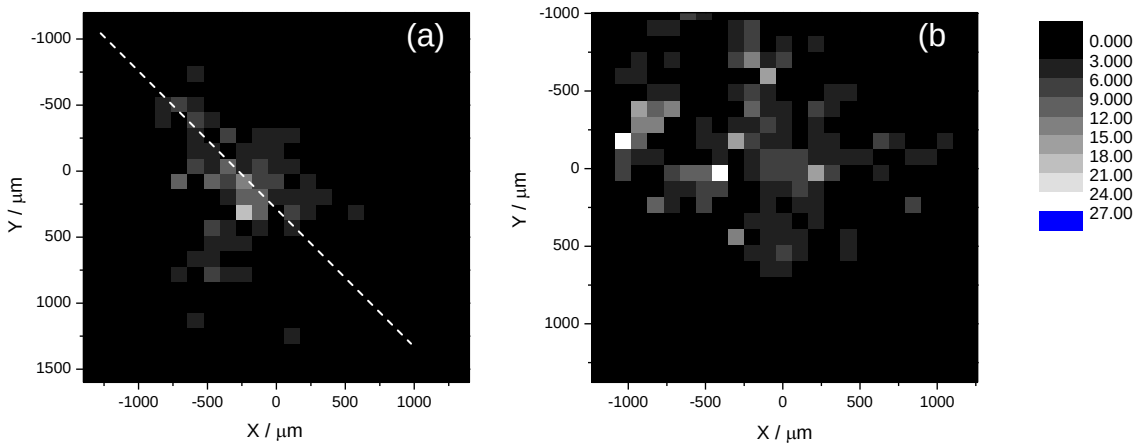

Figure 6.36 R1 fluorescence peak width change map of the impacted regions of the surviving 15% 1.5Y-ZTA tested at (a) 100 m s^{-1} and (b) 130 m s^{-1}.The dashed line in image (a) is the line mapping route used to generate Figure 6.37.

Line maps of the monoclinic zirconia contents of the two samples were constructed using Raman analysis and are shown in Figure 6.37. It was found that, despite the different impact speeds, the highest amount of zirconia phase transformation for both samples was around 50%, i.e. the value was not affected by the energy applied from the impact. This suggests that the highest zirconia phase transformability under high strain rate testing was reached in the 15% 1.5Y-ZTA samples. However, the sample with a higher impact speed showed a larger area in which the zirconia phase transformation had occurred, indicating that the energy from the impact was consumed by the zirconia transformation occurred in a larger area but not by increasing the transformability. The result suggests that the high strain rate performance of the ZTA materials could be further improved if the transformability of the material can be further increased, which could be achieved by changing the microstructures, such as increasing the zirconia grain size, whilst controlling the alumina grain size in ZTA, or, possibly, by reducing the yttria content further.

Indent centre

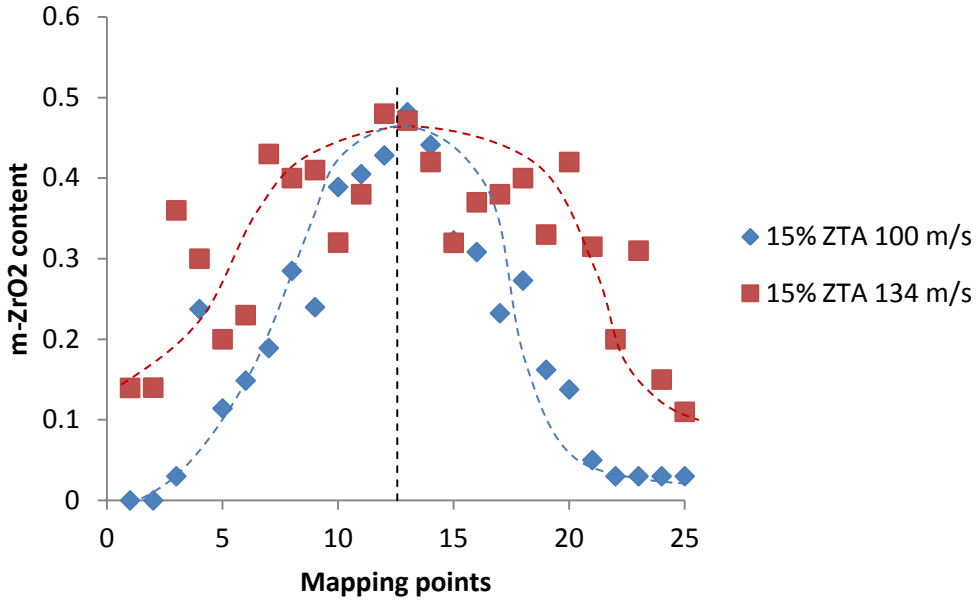

Figure 6.37 Line map across the indented area (the scanning path was noted in Figure 6.36 as a dashed line) showing the monoclinic zirconia contents along the scan line.

6.3.3 Comparison of the surviving and broken impact tested samples

The peak shift and peak broadening across the indent areas of the surviving and broken samples of 15% ZTA were line mapped, as shown in Figure 6.38. The surviving sample was tested at the impact speed of 130 m s^{-1}, whilst the two broken samples were tested at 130 m s^{-1} and 150m s^{-1}, respectively.

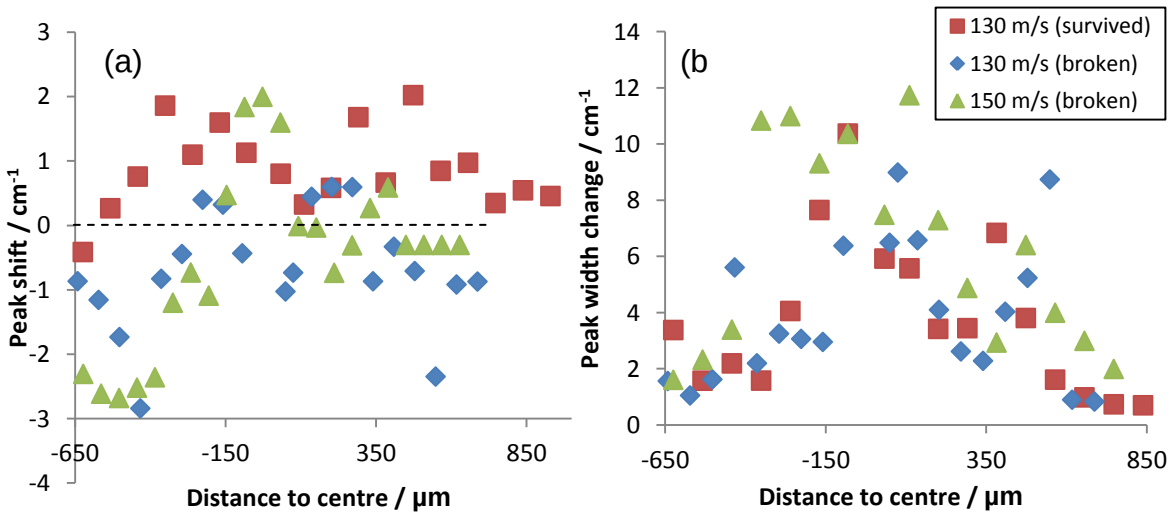

Figure 6.38 Line map across the indented area showing (a) the peak shift and (b) the peak width change across the indent.

It was found that the surviving sample showed mainly a positive peak shift in the indent, whilst for the broken samples, the peaks were mainly negatively shifted. The different peak shift suggested their different residual stresses, i.e. tension in the surviving sample and compression in the broken samples. It was already confirmed from the previous study that the tensile stresses were caused by the zirconia phase transformation, therefore, the amount of the zirconia phase transformation in the surviving and broken samples tested at the same speed, 130 m s^{-1}, could be different. This hypothesis was proved by the Raman analysis on the impact regions, as shown in Figure 6.39. A much higher degree of zirconia phase transformation was observed in the surviving sample. This result confirmed the finding in the SHPB testing study, i.e. the very quick fracture process consumed the energy from the impact, leading to much less energy being avoidable for the zirconia phase transformation. In addition, comparing the broken samples tested under different speeds, their peak shift results across the indents were very similar, indicating that the higher impact energy did not lead to a higher amount of zirconia to transform. In Figure 6.38 (b), the three samples showed no significant difference on the peak broadening, although the broken sample tested at 150 m s^{-1} showed a slightly higher degree of peak broadening than the others. It is considered that, in the alumina grains, the impact energy could be firstly consumed by the plastic deformation, resulting similar dislocation densities in the impact region. If the energy was not fully consumed, then crack propagation occurred and the sample fractured.

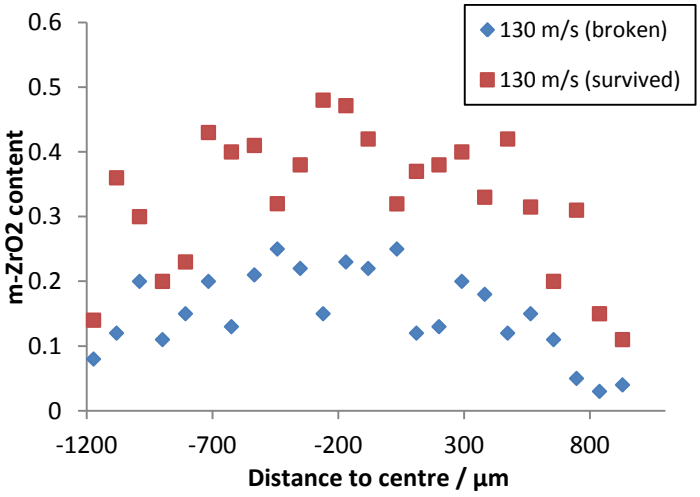

Figure 6.39 Monoclinic zirconia contents in the impact regions of the surviving and broken samples after impact tests under 130 m s^{-1}.

The crack density in the impact region of the 15% samples with different impact speeds were measured by FEGSEM using a similar method to that discussed in section 6.2.2. The results are shown in Figure 6.40. It was found that the crack density significantly increased with increasing impact speed, as expected, however, the crack density in the surviving and broken samples tested at the same speed were very similar, indicating that the cracks in the impact region was not the main reason that led to the failure of the samples. The radial cracking around the impact region should be the critical reason, as discussed in section 6.3.2. From Figure 6.40, the crack density of the 15% 1.5Y-ZTA at 150 m s^{-1} impact speed was of a similar value to that of the alumina sample at 100 m s^{-1} (in Figure 6.22). Less surface damage for the ZTA samples was, therefore, confirmed.

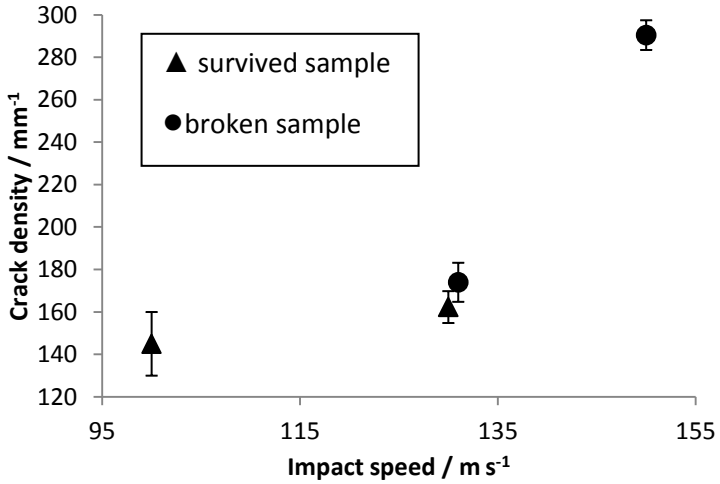

Figure 6.40 Variation of crack density with the impact speed for the 15% 1.5Y-ZTA.

6.3.4 Impact test on nano 1.5YSZ

In this project, only two large disc nano 1.5YSZ samples were tested in the gas gun impact test due to the consideration that materials with low hardness and high density were not suitable for armour applications. However, the nano 1.5YSZ samples survived at a higher impact speed, 142 m s^{-1}, than the much harder alumina and ZTA samples. On the impact surface, Figure 6.40 (a), a very deep indent, about 1-2 mm, was observed, this was because the WC projectile did not fragment but was only blunted during the impact due to the similar hardness of the two materials. The very deep indent suggests that the projectile penetration was very significant in the relatively soft material, which would not be beneficial to an amour material. On the other hand, the very deep projectile penetration caused only very local damage

without affecting the area away from the indent and did not lead to any radial cracks around the indent. By analysing the zirconia phases around and inside the indent, Figure 6.40 (b), very significant monoclinic zirconia was observed in the both locations, suggesting a very strong zirconia phase transformation effect. This could help to reduce the crack propagation and keep the damage local; therefore multihit capability could be improved. However, the zirconia was not considered as a good armour material due to the very deep projectile penetration and the higher density (6.01 g cm^{-3}) than the alumina (3.99 g cm^{-3}) and ZTA (4.20 g cm^{-3}) samples.

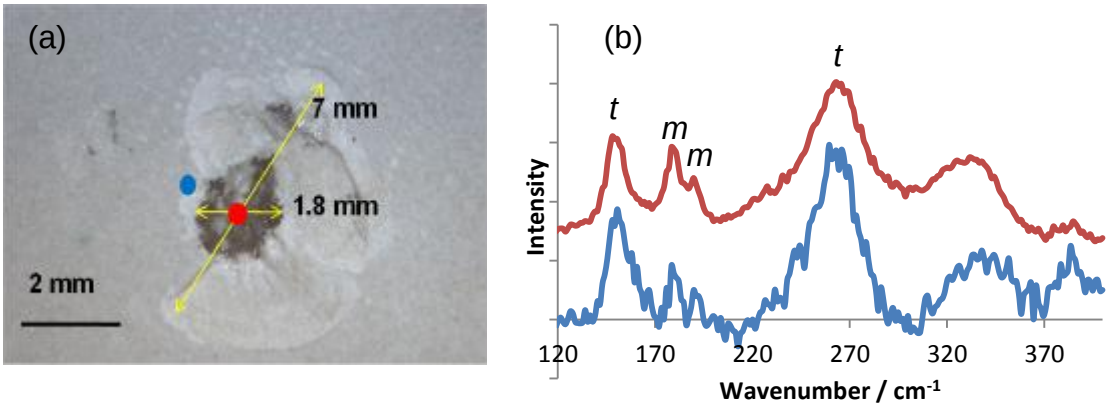

Figure 6.41 (a) Impact surface of the nano 1.5YSZ sample; (b) zirconia phase transformation on around (in blue) and inside (in red) the indent. The positions where the Raman spectra were collected are shown in image (a) as the blue and red dots.

6.4 Summary

- Using SHPB testing, it was found that the 15% ZTA could survive at 11 m s^{-1}, whilst the others were fragmented or chipped. The better high strain rate performance in withstanding the impact pressure and preventing fragmentation for the 15% samples were related with a combined effect from the high hardness, zirconia phase transformation toughening effect and high strength. With zirconia phase transformation, the energy from impact was consumed, also the volume expansion of the transformation zirconia grains caused a certain amount of tensile stress, which cancelled the compressive stress and reduced the stress change before and after testing. Both of the above reasons resulted in the survival of the 15% samples.

- However, the effect of zirconia phase transformation on the high strain rate performance was largely reduced when the samples were fragmented. It could be because the very strong fragmentation process lead to limited energy for sufficient phase transformation. By comparing the relationship between the fragment size and residual stress as well as fracture mode, it was found that the large fragments were intergranular fractured, with very low residual stress, whilst the small fragments were mainly transgranular fractured, leading to much higher residual stress. Fragmentation from large defect was considered to cause the intergranular fractured large fragments, whilst fragmentation from dislocations could result in the small fragments with transgranular fracture and ductile fracture surfaces.

- Using gas gun impact tests, the alumina, 10% ZTA and 15% ZTA were dynamically impacted using a sharpened WC projectile at 100 m s^{-1}. The damaging conditions of the impact surfaces and their cross-sections were analysed, much less surface damage and crack propagation was observed for the ZTA samples. The crack density on the impact region was measured for each sample using FEGSEM and the values for the ZTA samples were much lower than that for the alumina. Consistent with the finding in the SHPB testing, the tensile residual stress was observed on the ZTA samples due to the reduction of the compressive stress from the impact by the zirconia phase transformation. In addition the dislocation densities of the ZTA samples were lower compared to that of the alumina samples on the impact surface, as well as on the cross section. Comparing the three materials studied in this work, the 15% ZTA was found to be the most suitable material to resist projectile defeat due to less damage and smaller affected area on the surface, as well as lower residual stress and dislocation densities. The zirconia phase transformation worked to reduce the compressive stress and absorb the energy from the impacting, leading to less damage and deformation on the materials.

- By changing the impact speeds from 100 to 150 m s^{-1}, the impact speed limit for the 15% 1.5Y-ZTA samples was found to be 130 m s^{-1}. In addition, the

increased impact energy did not lead to an increased transformability of the samples, indicating that the limit of zirconia phase transformation was reached. Comparing the survived and broken samples tested under the same speeds, the compressive residual stress was much higher on the broken sample, due to the reduced degree of zirconia phase transformation. It is believed that the fracture process consumed a large amount of energy, leading to much less energy being available for zirconia phase transformation. The crack density on the impact region increased with the increasing impact speed, however, the highest crack density of the ZTA sample tested under 150 m s^{-1} was of a same level with that found on the alumina sample tested under 100 m s^{-1}, confirming the much less surface damage for the ZTA samples.

- It was found that a nano 1.5YSZ sample survived the 142 m s^{-1} impact. It was surprising that the impact caused only a small area of damage (but deep penetration) without affecting the material further away from the impacted area. This indicates that the zirconia phase transformation could significantly improve the multihit capability.

7 CONCLUSIONS

This project followeda research route shown in Figure 7.1. Firstly, fine grain sized alumina and ZTA materials were prepared, the processing routes of the samples with a range of grain sizes were developed. Then, the mechanical properties of these samples were studied in order to find out the effect of microstructure on the mechanical properties and find out the optimum materials for the high strain rate testing. The selected samples were finally tested under high strain rates and a series of post testing characterisation was carried out with the purpose of developing the understanding of the mechanism(s) by which ZTA ceramic armours defeat the high strain rate impact. The effect of zirconia phase transformation on the high strain rate performance of the samples was extensively studied. Both the mechanical property measurement and high strain rate testing also gave an instruction of the sample preparation, by which the materials with optimised microstructures could be produced.

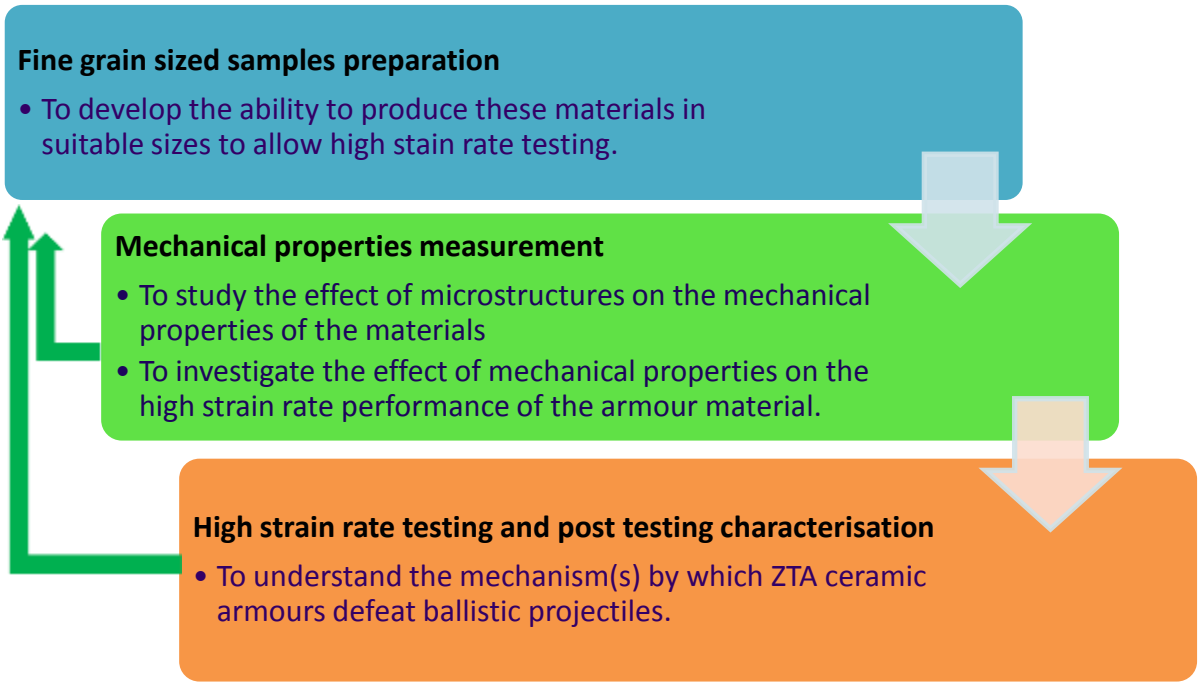

Figure 7.1 'Big picture' of the project

During the ceramic processing, fine grain sized alumina and nano ZTA samples were produced through die pressing of the spray freeze dried powders and different sintering techniques, including single and two-stage sintering. The alumina samples were successfully produced to achieve the grain sizes ranged from 0.6 to 1.6 μm with densities above 98%. The grain growth control effect for the two-stage sintering has been proved. The ZTA samples were also sintered using both single stage sintering and two-stage sintering. The samples sized ranged from 0.5 to 1.2 μm and density above 98% were prepared. The optimal sintering condition for each material was found.

The mechanical measurement results from this project suggest that nano ZTA ceramics with high zirconia phase transformation ability could be superior to the alumina samples for armour applications. For both materials, the fine and homogeneous microstructure assisted to increase its hardness and strength. Although a slightly lower hardness for ZTA was shown due to the addition of the less hard zirconia, its toughness was significantly improved by the zirconia phase transformation toughening effect. In addition, the toughness of the ZTA increased with the increasing zirconia grain size due to its higher phase transformability. This was confirmed to be caused by a larger transformation zone and better shielding effect on the cracks through Raman analysis. The wear resistance of the ZTAs with different zirconia contents was also improved with the increasing toughness. Comparisons of the mechanical properties of the ZTA samples suggest that a relatively coarse zirconia grain size (~200 nm) and a suitable zirconia composition (15% 1.5YSZ added in alumina matrix) optimised its properties including high hardness and toughness, as well as high strength and good wear resistance.

The residual stress distribution around indents of the alumina and ZTA samples were analysed in detail. The work helped to understand the effect of zirconia phase transformation on the residual stress distribution and dislocation density change under a high pressure static impact and after materials deformation. Although the effect from the zirconia phase transformation was not significant due to the very high stress from the indentation, the reduced residual stress and dislocation density was still observed. The microcrack density in the plastic zone was much less in the ZTA than in the alumina samples according to the TEM observation.

The high strain rate tests of the alumina and ZTA samples with different zirconia contents suggest that the 15% 1.5Y-ZTA displayed the best high strain rate performance in the compared samples. Using SHPB testing, it was found that the 15% ZTA showed a better performance in withstanding the impact pressure and preventing fragmentation. About 50% zirconia phase transformability was observed on the impact surface, which led to a reduction of the compressive stress from the impact. In addition, dislocations and twins were observed on the alumina and zirconia grains using TEM observation, the monoclinic phase of the zirconia grains was confirmed by the diffraction pattern on the grains.

However, the effect of zirconia phase transformation on the high strain rate performance was largely reduced when the samples were fragmented. It could because the fragmentation process released a lot of the stress from the impact, therefore, the zirconia phase transformation was reduced. By comparing the relationship between the fragment size and residual stress as well as fracture mode, it was found that the large fragments were intergranular fractured, with very low residual stress, whilst the small fragments were mainly transgranular fractured, leading to much higher residual stress. The different fracture modes were caused by the fragmentation process of the ZTA materials.

The results from the gas gun impact tests confirmed the finding in the SHPB tests, viz. the 15% ZTA showed an outstanding performance to withstand the high impact speed (100 $m\,s^{-1}$) compared to the alumina and 10% ZTA. The damaging conditions of the impact surfaces and their cross-sections were analysed; the 15% ZTA showed less damage and smaller affect area on the surface, as well as lower residual stress and dislocation densities. The zirconia phase transformation worked to reduce the compressive stress and absorb the energy from the impacting, leading to less damage and deformation on the materials.

By changing the impact speeds from 100 to 150 $m\,s^{-1}$, the impact speed limit for the 15% 1.5Y-ZTA samples was found to be 130 $m\,s^{-1}$. In addition, the increased impact energy did not lead to an increased transformability of the samples, indicating that the limit of zirconia phase transformation was reached. Comparing the survived and broken samples tested under the same speeds, the compressive residual stress was

much higher in the impact region of the broken sample, due to the reduced degree of zirconia phase transformation. It is believed that the fracture process consumed a large amount of energy, leading to much less energy being available for zirconia phase transformation, which was consistent with the finding in the SHPB testing.

It was found that a nano 1.5YSZ sample survived the 142 m s^{-1} impact and the impact caused only a small area of damage (but deep penetration) without affecting the material further away from the impacted area. This indicates that the zirconia phase transformation could significantly improve the multihit capability.

8 FURTHER WORK

- From the current work, nano ZTA showed significantly improved high strain rate performance in terms of the ability to prevent fragmentation, the extend of surface damage after high strain rate testing and multihit capability. It is worth proceeding to understand real ballistic testing to further evaluate the samples. This is being done as part of a follow-on project by another PhD student in the group at Loughborough University.

- Before ballistic testing, the first work to be carried out is to find out a suitable processing method. Due to the enlarged sample size of above 75 mm diameter and 10 mm thickness required by the ballistic testing, a large amount of powder is required and suitable die pressing and iso-pressing equipments for large sample preparation need to be used. Other issues to be concerned include: the green density of the samples and the density distribution of the green bodies; a slight modification of the sintering conditions could be necessary.

- In addition, the gas gun impact tests on the nano 1.5YSZ samples showed a extraordinary result that the samples withstood the very high impact speed, 142 m s^{-1}, without fragmentation. This result may be an indication of good multihit capability of this material. Although a deep projectile penetration was observed on the nano 1.5YSZ sample due to its low density, it is worth further investigation of whether there is a minimum thickness at which the ceramic tile could prohibit the projectile penetration as well as prevent crack propagation.

- It was also found that ZTA materials could be a suitable armour material. However, only three compositions were studied with regard to their mechanical properties and high strain rate performance, viz. 10%, 15% and 20% 1.5Y-ZTA. The 15% 1.5Y-ZTA is considered to be the best one in the three candidates. The author considers that there could be a composition in between 15 to 20%, which could provide even better performance on ballistic protection. Therefore, a further variation of the zirconia contents in the ZTA composite is suggested.

- In this project, fine grain sized alumina with grain sizes from 0.6 to 1.6 μm was produced. However, it is expected that a nano alumina with grain sizes around or lower than 100 nm could provide different mechanical properties and high strain rate performance. Samples with such a microstructure have been produced in Loughborough already; whilst the sample size has not been enlarge to a suitable size for the high strain rate testing yet. Therefore, a future work about the gas gun or ballistic testing of the nano alumina samples should be interesting.

REFERENCES

[1] Http://www.ceramicindustry.com/CDA/Archives/

[2] J. Briggs, Engineering Ceramics in Europe and the Usa: A Market and Strategic Study to the Year 2012, 2007.

[3] W.W. Chen, A.M. Rajendran, B. Song, X. Nie, Journal of the American Ceramic Society 90 (2007) 1005–1018.

[4] P. Karandikar, G. Evans, S. Wong, M.K. Aghajanian, in:, The 32nd International Conference on Advanced Ceramics and Composites, Daytona Beach, US, 2008.

[5] J. Karch, R. Brringer, H. Gleiter, Nature 330 (1987) 556–558.

[6] F. Wakai, Y. Kodama, S. Sakaguchi, N. Murayama, K. Izaki, K. Niihara, Nature 344 (1990) 421–423.

[7] M.V. Kremenchugskii, G.G. Savkin, V.I. Malinov, A.I. Rachkovskii, G.Y. Smorchkov, Nanotechnologies in Russia 3 (2008) 209–213.

[8] M. Flinders, D. Ray, A. Anderson, R. a. Cutler, Journal of the American Ceramic Society 88 (2005) 2217–2226.

[9] B. a Gama, T. a Bogetti, B.K. Fink, C.-J. Yu, T. Dennis Claar, H.H. Eifert, J.W. Gillespie Jr, Composite Structures 52 (2001) 381–395.

[10] J.M.K. Assis, F. Piorino Neto, F.C.L. Melo, M.C.A. Nono, Materials Science Forum 591/593 (2008) 436–440.

[11] X.F. Zhang, Y.C. Li, Design of Nanomaterials and Nanostructures 31 (2010) 1945–1952.

[12] M.L. Wilkins, International Journal of Engineering Science 16 (1978) 793–807.

[13] D.A. Shockey, A.H. Marchand, S.R. Skaggs, G.E. Cort, M.W. Burkett, R. Parker, International Journal of Impact Engineering 9 (1990) 263–275.

[14] R. Zaera, S. Sánchez-Sáez, J.L. Pérez-Castellanos, C. Navarro, Composites Part A: Applied Science and Manufacturing 31 (2000) 823–833.

[15] G. Subhash, S. Maiti, P.H. Geubelle, D. Ghosh, Journal of the American Ceramic Society 91 (2008) 2777–2791.

[16] J.J. Swab, International Journal of Applied Ceramic Technology 1 (2004) 219–225.

[17] D.W. Richerson, Modern Ceramic Engineering, Second Eddition, Marcel Dekker Inc., 2006.

[18] R. Klement, S. Rolc, R. Mikulikova, J. Krestan, Engineering Ceramics ’07: From Engineering To Functionality The Advanced Research Workshop Engineering Ceramics 2007 28 (2008) 1091–1095.

[19] P.J. Hazell, M.R. Edwards, H. Longstaff, J. Erskine, International Journal of Impact Engineering 36 (2009) 147–153.

[20] A. Krell, J. Klimke, T. Hutzler, Special Issue on Transparent Ceramics 29 (2009) 275–281.

[21] B.K. Fink, J.W. Gillespie Jr., ARL Technical Report, ARL-TR-2319.

[22] J. López-Puente, A. Arias, R. Zaera, C. Navarro, Fifth International Symposium on Impact Engineering 32 (2005) 321–336.

[23] R.G. O’Donnell, Journal of Materials Science Letters 10 (1991) 685–688.

[24] J.C. Lasalvia, Ceramic Transactions 134 (2002) 557–570.

[25] P. Lundberg, R. Renström, B. Lundberg, International Journal of Impact Engineering 24 (2000) 259–275.

[26] E. Straßburger, B. Lexow, O. Beffort, R. Jeanquartier, in:, 19th International Symposium on Ballistics 2001, Interlaken, Switzerland, 2001.

[27] J. Lankford, International Journal of Applied Ceramic Technology 1 (2004) 205–210.

[28] R. Feynman, Engineering and Science 23 (1960) 22–36.

[29] B. Bhushan, Handbook of Nanotechnology, Springer, Columbus, 2004.

[30] M. Wilson, K. Kannangara, G. Smith, M. Simmons, B. Raguse, in:, Nanotechnology: Basic Science and Emerging Technologies, Chapman & Hall/CRC, Boca Raton, 2002.

[31] V. Rotello, Nanoparticles: Building Blocks for Nanotechnology, Kluwer Academic / Plenum Publishers, pp. 1–19.

[32] M. Kohler, W. Fritzsche, Nanotechnology - An Introduction to Nano Structuring Techniques 2nd Ed, Wiley-VCH Verlag GmbH & Co. KGaA, Weinheim, 2004, pp. 1–43.

[33] M.J. Mayo, International Materials Reviews 41 (1996) 85–115.

[34] J. Binner, K. Annapoorani, A. Paul, I. Santacruz, B. Vaidhyanathan, Engineering Ceramics: From Engineering To Functionality, The Advanced Research Workshop, Engineering Ceramics 2007 28 (2008) 973–977.

[35] H. Hahn, R.S. Averback, Journal of the American Ceramic Society 74 (1991) 2918–2921.

[36] A. Paul, Processing and Properties of Nanostructured Zirconia Ceramics, PhD Thesis, 2009.

[37] G. Smith, Science in Parliament 61 (2004) 10–11.

[38] P. Boch, J. Niepce, Ceramic Materials, ISTE Ltd, 2007.

[39] http://fy.chalmers.se/~f10mh/CVD/aluminaintro.html.

[40] J.M. McHale, A. Auroux, A.J. Perrotta, A. Navrotsky, Science 277 (1997) 788–791.

[41] S. Blonski, S.H. Garofalini, Surface Science 295 (1993) 263–274.

[42] J.M. McHale, A. Navrotsky, A.J. Perrotta, J. Phys. Chem. B 101 (1997) 603–613.

[43] S.C. Liao, Y.J. Chen, B.H. Kear, W.E. Mayo, Nanostructured Materials 10 (1998) 1063–1079.

[44] A. Krell, P. Blank, Journal of the American Ceramic Society 78 (1995) 1118–1120.

[45] R. Rice, Journal of Materials Science Letters 13 (1994) 1408–1412.

[46] S.D. Skrovanek, R.C. Bradt, Journal of the American Ceramic Society 62 (1979) 215–216.

[47] C.B. Carter, M.G. Norton, Ceramic Materials: Science and Engineering, Springer, 2007.

[48] J.H. Miller, P.K. Liaw, ASM Handbook 8, 654–663.

[49] R.W. Armstrong, International Journal of Refractory Metals and Hard Materials 19 (2001) 251–255.

[50] N.J. Petch, R.W. Armstrong, Acta Materialia 37 (1989) 2279–2285.

[51] A. Muchtar, L.C. Lim, Acta Materialia 46 (1998) 1683–1690.

[52] R.W. Armstrong, Engineering Failure Analysis 28 (1987) 529–538.

[53] R. Rice, Materials Science Research 12 (1971) 791–796.

[54] J. Lankford, Journal of Materials Science 12 (1977) 791–796.

[55] J. Lankford, C.R. Blanchard, Journal of Materials Science 26 (1991) 3067–3072.

[56] L. Grabner, Journal of Applied Physics 49 (1978) 580–583.

[57] Q. Ma, D.R. Clarke, Journal of the American Ceramic Society 76 (1992) 1433–1440.

[58] S. Guo, R.I. Todd, Acta Materialia 59 (2011) 2637–2647.

[59] J. He, D.R. Clarke, Journal of the American Ceramic Society 78 (1995) 1347–1353.

[60] C. Sapphire, S.E. Molis, D.R. Clarke, 73 (n.d.).

[61] H.Z. Wu, S.G. Roberts, B. Derby, Acta Materialia 56 (2008) 140–149.

[62] S. Guo, R.I. Todd, Journal of the European Ceramic Society 30 (2010) 641–648.

[63] C.E.J. Dancer, H.M. Curtis, S.M. Bennett, N. Petrinic, R.I. Todd, Journal of the European Ceramic Society 31 (2011) 2177–2187.

[64] J. Wang, R. Stevens, Journal of Materials Science 24 (1989) 3421–3440.

[65] A. Paul, B. Vaidhyanathan, J. Binner, Advances in Applied Ceramics 110 (2011) 114–119.

[66] F.F. Lange, Journal of Materials Science 17 (1982) 235–239.

[67] K.T. Faber, A.G. Evans, Acta Materialia 31 (1983) 565–576.

[68] A.G. Evans, R.M. Cannon, Acta Materialia 34 (1986) 761–800.

[69] D. Casellas, M. Nagl, L. Llanes, M. Anglada, Journal of Materials Processing Technology 143-144 (2003) 148–152.

[70] P. Becher, Acta Materialia 34 (1986) 1885–1892.

[71] P. Becher, K. Alexander, A. Bleier, Journal of the American Ceramic Society 76 (1993) 657–663.

[72] V. Sergo, D. Clarke, W. Pompe, Journal of the American Ceramic Society 78 (1995) 633–640.

[73] J.F. Bartolomé, G. Bruno, a. H. DeAza, Journal of the European Ceramic Society 28 (2008) 1809–1814.

[74] V. Sergo, G. Pezzotti, O. Sbaizero, T. Nishida, Acta Materialia 46 (1998) 1701–1710.

[75] G.D. Portu, L. Micele, Y. Sekiguchi, G. Pezzotti, Acta Materialia 53 (2005) 1511–1520.

[76] G. Gregori, W. Burger, V. Sergo, Materials Science and Engineering: A 271 (1999) 401–406.

[77] R. L. Woodward, W. A. Gooch, JR, R. G. O'Donnell, W. J. Perciballi, International Journal of Impact Engineering 15 (1994) 605–618.

[78] J. Ding, T. Tsuzuki, P.G. Mccormick, Journal of the American Ceramic Society 79 (1996) 2956–2958.

[79] M. Mayo, R. Siegel, Y. Liao, W.D. Nix, Journal of Materials Research 7 (1992) 973–979.

[80] J. Eastman, R. Siegel, Organic Process Research & Development 31 (1989) 56–60.

[81] G. Skandan, H. Hahn, M. Roddy, W.R. Cannon, Journal of the American Ceramic Society 77 (1994) 1706–1710.

[82] J.A. Lewis, Journal of the American Ceramic Society 83 (2000) 2341–2359.

[83] Y. Hirata, M. Nakamura, M. Miyamoto, Y. Tanaka, X.H. Wang, Journal of the American Ceramic Society 89 (2006) 1883–1889.

[84] X.M. Wang, G. Lorimer, P. Xiao, Journal of the American Ceramic Society 88 (2005) 809–816.

[85] V. Shubin, P. Linse, Journal of Physical Chemistry 99 (1995) 1285–1291.

[86] P. Bowen, C. Carry, D. Luxembourg, H. Hofmann, Powder Technology 157 (2005) 100–107.

[87] J. Cesarano, I.A. Aksay, Journal of the American Ceramic Society 71 (1988) 250–255.

[88] J. Davies, J.G.P. Binner, Journal of the European Ceramic Society 20 (2000) 1539–1553.

[89] A. Tsetsekou, C. Agrafiotis, Journal of the European Ceramic 21 (2001) 363–373.

[90] J. Binner, B. Vaidhyanathan, Journal of the European Ceramic Society 28 (2008) 1329–1339.

[91] J.G.P. Binner, M.I. Santacruz, K. Annapoorani, Method for Concentrating Nanosuspensions, U.S. Patent Publ. No.WO 2006/136780 A2, 2006.

[92] J.G.P. Binner, Lecture Notes of Ceramic Materials'', 2009.

[93] H. Zhang, Am. Ceram. Soc. Bull. 75 (1996) 71–74.

[94] I.A. Aksay, F.F. Lange, B.I. Davis, Journal of the American Ceramic Society 66 (1983) 190.

[95] R. Siegel, S. Ramasamy, H. Hahn, Z. Zonghuan, L. Ting, Journal of Materials Research 3 (1988) 1367–1375.

[96] F.J. Schnettler, F.R. Monforte, W.W. Rhodes, Journal of Ceramic Science and Technology 4 (1968) 78-90.

[97] M. Jacquot, P. De Donato, O. Barres, M.. Pons, J. Scher, a Miclo, D. Poncelet, Powder Technology 128 (2002) 205–212.

[98] J.G.P. Binner, B. Vaidhyanathan, A. Paul, K. Annapoorani, B. Raghupathy, International Journal of Applied Ceramic Technology (2010) 1–17.

[99] M.N. Rahaman, Ceramic Processing and Sintering, Marcel Dekker Inc., 1995.

[100] K.H. Brosnan, G.L. Messing, D.K. Agrawal, Journal of the American Ceramic Society 90 (2007) 330–332.

[101] J. Li, Y. Ye, Journal of the American Ceramic Society 89 (2006) 139–143.

[102] I. Chen, X. Wang, Nature 404 (2000) 168–171.

[103] X.-H. Wang, P.-L. Chen, I.-W. Chen, Journal of the American Ceramic Society 89 (2006) 431–437.

[104] X.-H. Wang, X.-Y. Deng, H.-L. Bai, H. Zhou, W.-G. Qu, L.-T. Li, I.-W. Chen, Journal of the American Ceramic Society 89 (2006) 438–443.

[105] R.F. Cook, G.M. Pharr, Journal of the American Ceramic Society 73 (1990) 787–817.

[106] C.J. Wang, C.Y. Huang, Y.C. Wu, Ceramics International 35 (2009) 1467–1472.

[107] F.F. Lange, M.M. Hirlinger, Journal of the American Ceramic Society 67 (1983) 164–168.

[108] K. Bodišová, P. Šajgalík, D. Galusek, P. Švančárek, Journal of the American Ceramic Society 90 (2007) 330–332.

[109] J. Wang, R. Raj, Journal of the American Ceramic Society 74 (1991) 1959–1963.

[110] I. Santacruz, K. Anapoorani, J. Binner, Journal of the American Ceramic Society 91 (2008) 398–405.

[111] G.R. Anstis, P. Chantikul, B.R. Lawn, l D.B. Marshal, Journal of the American Ceramic Society 64 (1981) 533–538.

[112] T. Tani, Y. Miyamoto, M. Koizumi, Ceramics International 12 (1986) 33–37.

[113] J.. Calderon-Moreno, M. Popa, Materials Science and Engineering: A 319-321 (2001) 692–696.

[114] K. Kendalla, N.M. Alforda, S.R. Tana, J.D. Birchalla, Journal of Materials Research 1 (1986) 120–123.

[115] G. Katagiri, H. Ishida, A. Ishitani, Advances in Ceramics 24 (1988) 537–544.

[116] R.M. Mcmeeking, A.G. Evans, Journal of the American Ceramic Society 65 (1981) 242–246.

[117] E.E. Underwood, Quantitative Stereology, Addison-Wesley Publishing Co., Reading, Mass, 1970.

[118] H.G. Scott, Journal of Materials Science 10 (1975) 1527–1535.

[119] J. Wang, M. Rainforth, R. Stevens, Transactions and Journal of the British Ceramic Society 88 (1989) 1–6.

[120] A.A. Griffith, Philos. Trans. R. Soc. London A221 (1921) 163.

[121] F.F. Lange, Journal of Materials Science 17 (1982) 225–234.

[122] J.F. Bartolome, C. Pecharrom, J.S. Moya, A. Martin, J.Y. Pastor, J. Llorca, Journal of the European Ceramic Society 26 (2006) 2619–2625.

[123] G. Magnani, A. Brillante, Journal of the European Ceramic Society 25 (2005) 3383–3392.

[124] E.H. Yoffe, Philosophical Magazine A 46 (1982) 617–628.

[125] J.A. Muñoz-Tabares, E. Jiménez-Piqué, J. Reyes-Gasga, M. Anglada, Journal of the European Ceramic Society 32 (2012) 3919–3927.

[126] P.M. Kelly, C.J. Ball, Journal of the American Ceramic Society 69 (1986) 259–264.

[127] K. Cherif, B. Gueroult, Wear 199 (1996) 113–121.

[128] A. a. Sharif, M.L. Mecartney, Journal of the European Ceramic Society 24 (2004) 2041–2047.

[129] D.L. Porter, A.G. Evans, A.H. Heuer, Acta Metallurgica Et Materialia 27 (1979) 1649–1654.